

Dissertation zur Erlangung des Doktorgrades
der Fakultät für Chemie und Pharmazie
an der Ludwig-Maximilians-Universität München

Analysis of molecular forces transmitted by
Talin during muscle development *in vivo*

Sandra Beatrice Lemke

aus Boulder, Colorado, USA

2019

Erklärung

Diese Dissertation wurde im Sinne von § 7 der Promotionsordnung vom 28. November 2011 von Herrn Prof. Dr. Reinhard Fässler betreut.

Eidesstattliche Versicherung

Diese Dissertation wurde eigenständig und ohne unerlaubte Hilfe erarbeitet.

München, den 04.06.2019

Sandra B. Lemke

Dissertation eingereicht am: 26.04.2019

Erstgutachter: Prof. Dr. Reinhard Fässler

Zweitgutachter: Dr. Frank Schnorrer

Mündliche Prüfung am: 29.05.2019

Contents

| | |
|--|-----------|
| Summary | v |
| Abbreviations | vii |
| List of publications | xi |
| 1 Introduction | 1 |
| 1.1 Muscle-tendon system | 1 |
| 1.1.1 Muscle-tendon structure | 1 |
| 1.1.2 Sarcomere structure | 2 |
| 1.1.3 Mechanism of muscle contraction | 3 |
| 1.1.4 Regulation of muscle contraction | 4 |
| 1.2 <i>Drosophila</i> as a model system | 7 |
| 1.3 Muscle development in <i>Drosophila</i> | 7 |
| 1.3.1 Embryonic muscle development | 8 |
| 1.3.2 Pupal muscle development | 10 |
| 1.3.2.1 Abdominal muscle development | 10 |
| 1.3.2.2 Flight muscle development | 11 |
| 1.3.3 Forces during muscle development | 13 |
| 1.3.4 Myofibrillogenesis model | 14 |
| 1.4 Integrin-mediated adhesion | 16 |
| 1.4.1 Integrin receptor family | 17 |
| 1.4.2 Integrin regulation | 19 |
| 1.4.3 Focal adhesions | 20 |
| 1.4.4 Muscle attachment sites | 22 |
| 1.5 Talin – a major force transducer | 24 |
| 1.5.1 Talin domain structure | 25 |

| | | |
|------------|--|-----------|
| 1.5.2 | Talin interaction partners | 26 |
| 1.5.3 | Talin function in muscle attachment sites | 29 |
| 1.6 | Force measurements in biological systems | 30 |
| 1.6.1 | FRET-based molecular tension sensors | 33 |
| 1.6.2 | Förster resonance energy transfer (FRET) | 36 |
| 1.6.3 | Fluorescence lifetime imaging microscopy (FLIM) | 37 |
| 1.6.4 | Talin force measurements <i>in vitro</i> | 39 |
| 1.7 | CRISPR/Cas9-mediated genome engineering | 40 |
| 2 | Aim of thesis | 45 |
| 3 | Summary of publications | 47 |
| 3.1 | Paper I – A small proportion of Talin molecules transmit forces at developing muscle attachments <i>in vivo</i> | 47 |
| 3.2 | Paper II – Mechanical forces during muscle development | 49 |
| 3.3 | Paper III – <i>In Vivo</i> Imaging of Muscle-Tendon Morphogenesis in <i>Drosophila</i> Pupae | 51 |
| 3.4 | Paper IV – A transcriptomics resource reveals a transcriptional transition during ordered sarcomere morphogenesis in flight muscle | 53 |
| | Bibliography | 55 |
| | Acknowledgments | 69 |
| | Appendix | 71 |
| | Paper I – A small proportion of Talin molecules transmit forces at developing muscle attachments <i>in vivo</i> | 73 |
| | Paper I – Supporting Figures | 103 |
| | Paper II – Mechanical forces during muscle development. | 113 |
| | Paper III – <i>In Vivo</i> Imaging of Muscle-Tendon Morphogenesis in <i>Drosophila</i> Pupae. | 123 |
| | Paper IV – A transcriptomics resource reveals a transcriptional transition during ordered sarcomere morphogenesis in flight muscle. | 133 |

Summary

The muscle-tendon system built during the development of an animal is essential to allow the body to move, breath or keep the heart beating for a lifetime. The muscle is the most important force producing tissue in an animal and, at the same time, it is also dependent on forces built up in the muscle-tendon tissue, especially during its development. Using the *Drosophila* musculature as a model system, it had been shown that tension is built up in the muscle-tendon tissue during development and that this tension is required for myofibrillogenesis, the process of building myofibrils, which are long chains of the contractile units of muscles called sarcomeres.

The main focus of this thesis was to analyze how tension in tissues is transmitted across proteins at the molecular level to understand how proteins sense and respond to mechanical forces *in vivo*. As a model system, the developing *Drosophila* flight muscles were used that form in the pupal stage of the *Drosophila* life cycle. During development, these muscles attach to tendon cells and the connections between these two cells, called muscle attachment sites, need to bear the forces built up in the tissue. Muscle attachments are cell-extracellular matrix (ECM)-cell contacts that require receptor molecules in the cell membrane called integrins to connect the ECM between the cells with the contractile actin cytoskeleton inside the cells. Since integrins cannot directly connect to actin themselves, they require an adaptor protein called Talin that can bind to both integrin and actin filaments. Thus, Talin is in the ideal position to transmit and sense forces at muscle attachments.

Previous studies on Talin force transduction demonstrated that Talin indeed bears forces in the piconewton (pN) range using Förster resonance energy transfer (FRET)-based molecular tension sensors. However, these studies were based on analyzing Talin in focal adhesions in cells cultured *in vitro* in an artificial environment. Therefore, we aimed to analyze Talin force transmission for the first time *in vivo* in the natural mechanical environment in the intact organism.

In a first step, different FRET-based tension sensor modules and various control constructs were inserted in *Drosophila* into the endogenous *talin* (*rhea*) gene, taking advantage of the newly established clustered regularly interspaced short palindromic repeats/CRISPR-associated protein 9 (CRISPR/Cas9) system to achieve precise modification of the genome. After demonstrating that the Talin protein is still fully functional after insertion of the tension sensor modules, forces across Talin were first quantified—as a proof of concept—in primary muscle fibers *in vitro* using fluorescence lifetime imaging microscopy (FLIM) to measure FRET.

In a second step, forces transmitted by Talin at muscle attachments during flight muscle development were analyzed in detail in living pupae. We discovered that a surprisingly small proportion of Talin molecules at developing muscle attachments transmit forces at the same time (**Paper I**). Nevertheless, a large pool of Talin molecules need to be recruited to muscle attachment sites during development, as quantified by fluorescence correlation spectroscopy (FCS), to prepare for the forces generated by active muscle contractions in the adult fly. If the accumulation of Talin at flight muscle attachments is reduced during development by RNA interference (RNAi), the muscle attachments rupture in young adults, likely during the first flight attempts. In conclusion, recruitment of a high number of Talin molecules during development is physiologically relevant to enable the muscle to adapt to sudden changes in tissue forces, likely by dynamically sharing the load among the Talin molecules. This mechanical adaptation concept is important to ensure that the muscle-tendon connections are stable and last for a lifetime.

During the course of the thesis, I also discovered that flight muscles contract spontaneously during development. Characterization of these contractions in wild-type animals compared to a knockdown condition provided a functional readout for myofibrillogenesis during development (**Paper IV**). Furthermore, a review article on the role of mechanical forces during muscle development (**Paper II**) and a video article explaining how to perform *in vivo* imaging in *Drosophila* pupae (**Paper III**) were published.

Abbreviations

| | |
|--------------------|---|
| aa | amino acid |
| ABS | actin binding site |
| ACh | acetylcholine |
| ADP | adenosine diphosphate |
| AFM | atomic force microscopy |
| AMP | adult muscle precursor |
| APF | after puparium formation |
| Arp3 | actin-related protein 3 |
| ATP | adenosine triphosphate |
| βTD | β tail domain |
| CFP | cyan fluorescent protein |
| CRISPR/Cas9 | clustered regularly interspaced short palindromic repeats/CRISPR-associated protein 9 |
| DD | dimerization domain |
| DLC1 | deleted in liver cancer 1 |
| DNALig4 | DNA ligase 4 |
| ECM | extracellular matrix |
| EGF | epidermal growth factor |
| EM | electron microscopy |
| F40 | flagelliform |
| FAK | focal adhesion kinase |
| FCS | fluorescence correlation spectroscopy |
| FERM | 4.1 protein, ezrin, radixin, moesin |
| FGF | fibroblast growth factor |

| | |
|--|---|
| FL | ferredoxin-like |
| FLIM | fluorescence lifetime imaging microscopy |
| FRAP | fluorescence recovery after photobleaching |
| FRET | Förster resonance energy transfer |
| GFP | green fluorescent protein |
| h APF | hours after puparium formation |
| HDR | homology directed repair |
| HP | villin headpiece |
| HPst | stabilized villin headpiece |
| IBS | integrin binding site |
| <i>if</i> | <i>inflated</i> |
| Kank2 | KN motif and ankyrin repeat domain-containing protein 2 |
| <i>mew</i> | <i>multiple edematous wings</i> |
| mRNA | messenger RNA |
| mTFP1 | monomeric teal fluorescent protein 1 |
| <i>mys</i> | <i>myospheroid</i> |
| NHEJ | non-homologous end joining |
| NMR | nuclear magnetic resonance |
| PCR | polymerase chain reaction |
| PDMS | polydimethylsiloxane |
| P_i | inorganic phosphate |
| pN | piconewton |
| PS | position specific |
| PSI | plexin/semaphorin/integrin |
| PtdIns(4,5)P₂ | phosphatidylinositol 4,5-bisphosphate |
| PtdInsP kinase Iγ | phosphatidylinositol 4-phosphate 5-kinase type I γ |
| RGD | arginine-glycine-aspartate |
| RIAM | Rap1-GTP-interacting adaptor molecule |
| RNAi | RNA interference |
| sgRNA | single guide RNA |

| | |
|--------------|---|
| TCSPC | time-correlated single-photon counting |
| TIAM1 | T-lymphoma invasion and metastasis-inducing protein 1 |
| VASP | vasodilator-stimulated phosphoprotein |
| WASH | Wiskott-Aldrich syndrome protein (WASP)-homolog |
| WASP | Wiskott-Aldrich syndrome protein |
| WT | wild-type |
| YFP | yellow fluorescent protein |
| YPet | yellow fluorescent protein for energy transfer |
| Zasp | Z-band alternatively spliced PDZ-motif protein |

List of publications

This thesis is based on the following publications:

Paper I: Lemke, S. B.* , Weidemann, T., Cost, A.-L., Grashoff, C.* and Schnorrer, F.* (2019). A small proportion of Talin molecules transmit forces at developing muscle attachments in vivo. *PLoS Biology*, 17(3):e3000057.

Paper II: Lemke, S. B.* and Schnorrer, F.* (2017). Mechanical forces during muscle development. *Mechanisms of Development*, 144(Pt A):92-101.

Paper III: Lemke, S. B.* and Schnorrer, F.* (2018). *In Vivo* Imaging of Muscle-Tendon Morphogenesis in *Drosophila* Pupae. *Journal of Visualized Experiments*, (132):e57312.

Paper IV: Spletter, M. L.* , Barz, C., Yeroslaviz, A., Zhang, X., Lemke, S. B., Bonnard, A., Brunner, E., Cardone, G., Basler, K., Habermann, B. H., Schnorrer, F.* (2018). A transcriptomics resource reveals a transcriptional transition during ordered sarcomere morphogenesis in flight muscle. *eLife*, 7:e34058.

* corresponding authors

1 Introduction

1.1 Muscle-tendon system

Animals—from jellyfish to human—use muscles to move their body. Muscles keep our human heart beating and enable us to breathe and walk. To achieve locomotion, muscle contractions, leading to shortening of the muscles, move our skeleton with the help of tendons that connect the muscles with the skeleton. Similarly, the movement of insects is powered by muscles that are stably connected to the exoskeleton by tendon cells. Evolution has created different muscle types specialized for their respective functions, however, the basic functional principle and their main components are conserved.

1.1.1 Muscle-tendon structure

A muscle consists of multiple myofibers, which are large syncytial cells that span the muscle and contain many myofibrils (Figure 1.1). These myofibrils span the entire myofiber from one end to the other and consist of sarcomeres, which are the contractile

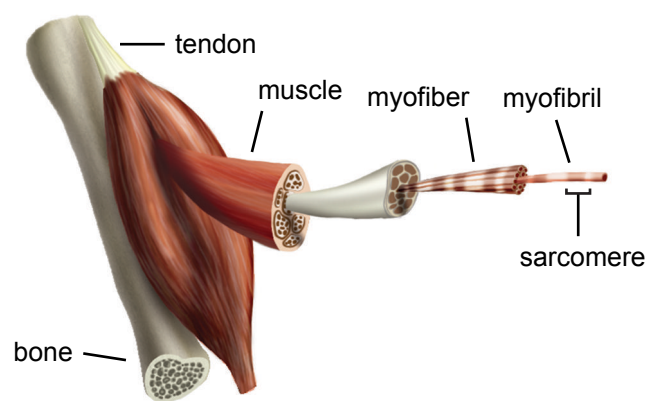


Figure 1.1: Muscle-tendon structure. Muscles are attached to bones via tendons and consist of large cells called myofibers. These myofibers contain many myofibrils, which consist of the contractile units called sarcomeres. Adapted with permission from Myhre and Pilgrim (2012).

units of the muscle. The microscopic contractions of hundreds of sarcomeres in series within a myofibril lead to shortening of the muscle on the macroscopic scale. To create a targeted and productive motion, this movement is transferred to the bone via tendons.

1.1.2 Sarcomere structure

The contractile units of the muscle, the sarcomeres, consist of three main filaments: the thick, the thin, and the connecting filaments. The thick filaments consist of bipolar muscle myosin filaments centered around the M-line (Figure 1.2). The motor domains of these muscle myosin filaments drive muscle contractions by moving along the thin filaments, which consist of actin filaments decorated with tropomyosin and troponin.

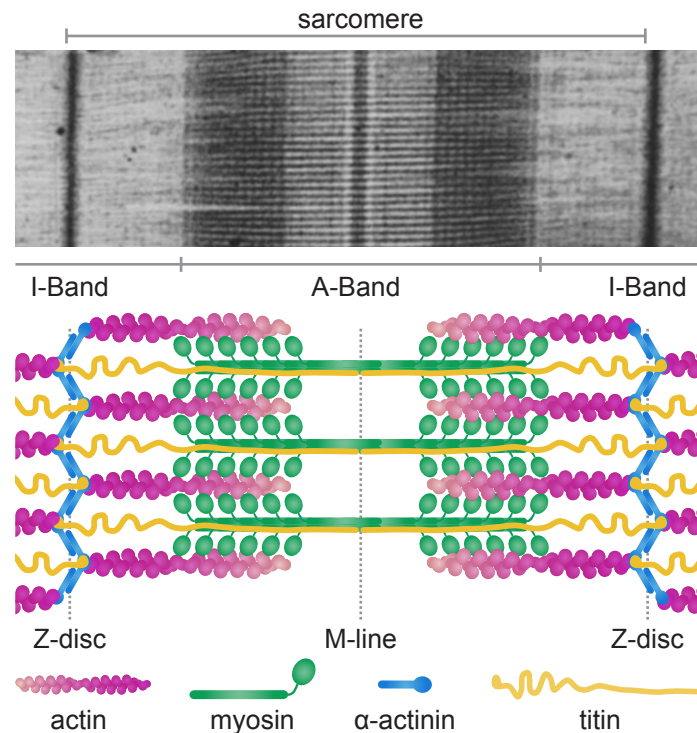


Figure 1.2: Sarcomere structure. An electron microscopy (EM) image of a sarcomere from a sectioned frog muscle is shown together with a schematic representation of the sarcomere. Light regions in the EM image centered around the Z-discs are called I-bands and the dark region centered around the M-line is called A-band. The A-band contains the myosin thick filaments that slide towards the Z-discs along the actin thin filaments, thereby shortening the sarcomere. Actin filaments are crosslinked at the Z-disc by α -actinin and the connecting filament (built by titin) connects the Z-disc with the thick filament. EM image reproduced with permission from Huxley (1967).

These actin filaments are cross-linked by α -actinin at their plus ends and thereby anchored to the Z-disc. The connecting filament built by titin, a gigantic elastic protein, connects the Z-disc with the middle of the thick filament at the M-line, ensuring that the thick filaments stay in the center of the sarcomere during contraction and relaxation. The region that contains the thick filaments is called A-band and the region around the Z-disc with only thin filaments is called I-band. Upon muscle contraction, the thick filaments slide on the thin filaments (sliding filament theory) and thus, the I-band shortens and the Z-discs move closer together, thereby shortening the sarcomere and hence the entire muscle.

1.1.3 Mechanism of muscle contraction

In the 1960's, the mechanism of muscle contraction was studied extensively and, as a result, Huxley (1969) proposed a model for the contraction mechanism that is now

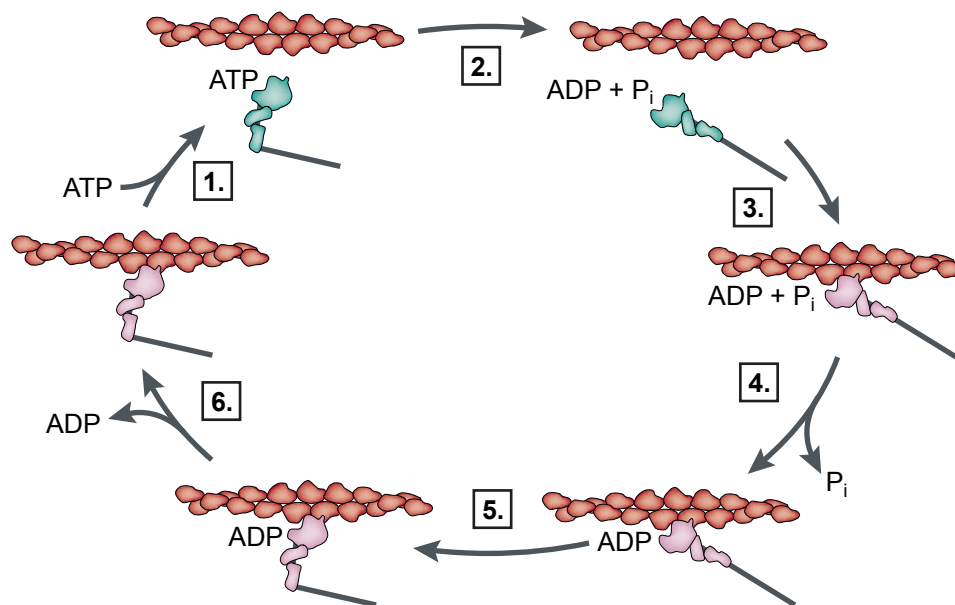


Figure 1.3: Muscle contraction: the swinging cross-bridge model. During muscle contraction adenosine triphosphate (ATP) is hydrolyzed in the following cycle generating movement of myosin (green in actin dissociated state and pink in actin associated state) along actin filaments (red): **1.** ATP binds to myosin resulting in dissociation from actin. **2.** ATP is hydrolyzed to adenosine diphosphate (ADP) + inorganic phosphate (P_i). **3.** Myosin binds to actin. **4.** P_i is released. **5.** Powerstroke: A conformational change in myosin displaces the actin filament. **6.** ADP is released. Actin and myosin head are drawn to scale. Adapted with permission from Spudich (2001).

known as the swinging cross-bridge model. Cross-bridges could be observed early on in electron microscopy (EM) images of muscle sections as connections between thick and thin filaments (Huxley, 1957). They turned out to be the myosin heads of the thick filament bound to the actin thin filaments in the A-band of the sarcomere. Since then, the mechanism of muscle contraction has been elucidated in detail (Lymn and Taylor, 1971; Yount et al., 1971; Sheetz and Spudich, 1983; Dominguez et al., 1998; Shih et al., 2000): Myosin without adenosine triphosphate (ATP) binds tightly to actin (Figure 1.3). Upon ATP binding, myosin is released from the actin filament and hydrolysis of ATP to adenosine diphosphate (ADP) and inorganic phosphate (P_i) leads to a conformational change in myosin and rebinding to the actin filament. Upon release of P_i , myosin displaces the actin filament and ADP is released, while the myosin head remains bound to actin. A new ATP molecule is required to restart the cycle.

1.1.4 Regulation of muscle contraction

To ensure that myofibrils contract in a synchronous fashion and exactly when required, the process of muscle contraction is precisely regulated. Generally, the signal for a muscle to contract comes from a motor neuron and is transferred to the muscle via a neuromuscular junction (Figure 1.4). This junction is a specialized synapse that forms between the tip of a motor neuron and the muscle membrane. As long as there is no action potential coming from the neuron, Ca^{2+} ions are stored in the sarcoplasmic reticulum, a membrane-bound organelle in muscle cells. In the absence of Ca^{2+} , troponin and tropomyosin bound to the actin thin filaments of the sarcomeres block the myosin head binding sites. Thus, the sarcomeres cannot contract and the muscle is relaxed. However, when the motor neuron sends a signal to the muscle to contract, an action potential arrives at the neuromuscular junction and leads to release of the neurotransmitter acetylcholine (ACh) into the synaptic cleft between the neuron and the muscle. ACh then binds to receptors on the postsynaptic side and activates sodium ion channels leading to an action potential in the sarcolemma. The sarcolemma is the plasma membrane of the muscle cell that extensively invaginates into the cytoplasm forming a network of tubules, called T-tubules. The action potential travels along these T-tubules to the sarcoplasmic reticulum, which then releases Ca^{2+} into the cytoplasm. Upon binding of the Ca^{2+} ions to troponin, troponin and tropomyosin move, making the myosin binding sites on the actin thin filaments in the sarcomere accessible. Hence,

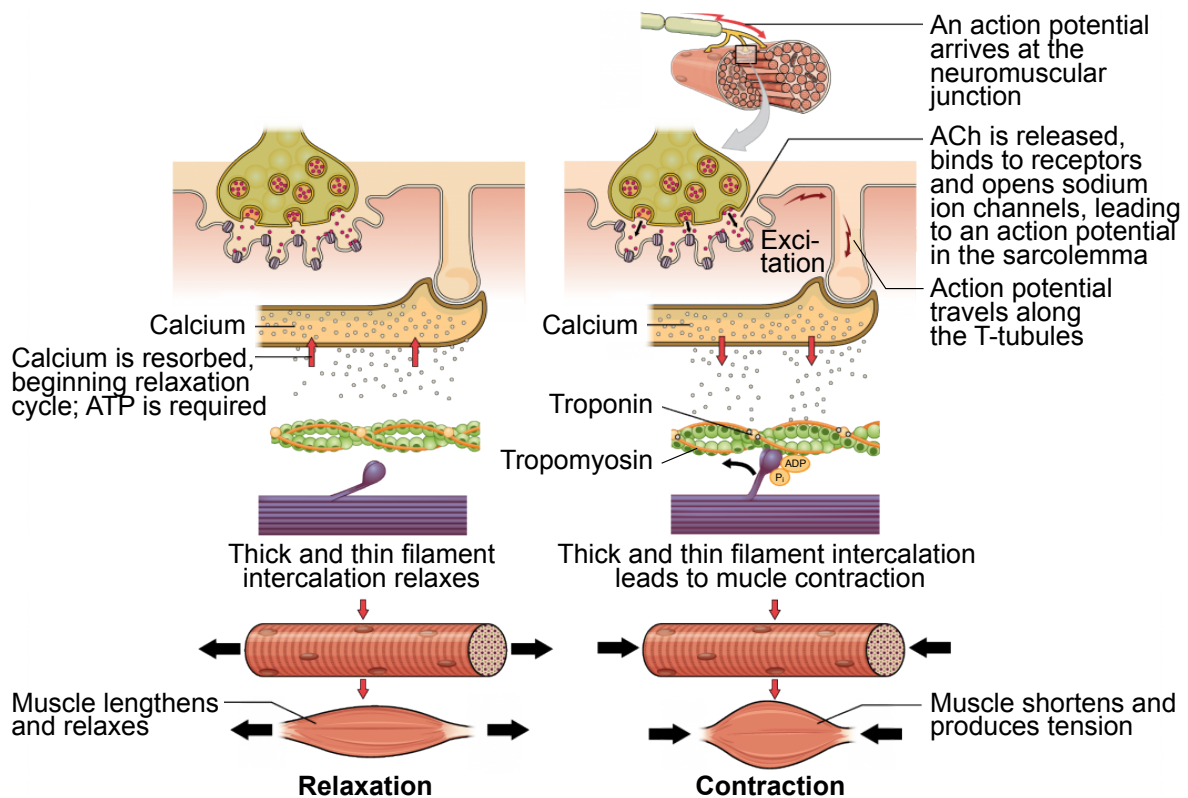


Figure 1.4: Neuronal regulation of muscle contraction. Muscle contraction is regulated by motor neuron signaling. Action potentials coming from the neuron activate muscle contraction by triggering the release of Ca^{2+} into the cytoplasm of the muscle. Upon binding of Ca^{2+} to troponin, myosin binds to actin, which leads to intercalation of the thin and thick filaments and thus, to muscle contraction. ACh: acetylcholine. Adapted with permission from Biga et al. (2018).

the myosin motor domains can bind to the actin filaments and initiate the contraction cycle as described in Chapter 1.1.3. As a result, the muscle contracts only if triggered by the motor neuron.

Specialized muscle types, for example flight muscles in insects, can have an additional layer of regulation. To power flight, flight muscles contract with a very high frequency of around 200 Hz (Dudley, 2002). To achieve powerful contractions at such a high frequency, an additional regulatory system is needed in these muscles. In flight muscles, this is achieved by an asynchronous stretch activation mechanism: Two sets of muscles, the dorsoventral and the dorsolongitudinal flight muscles, are arranged orthogonally to each other in the thorax of insects (Figure 1.5A). Contraction of the dorsoventral muscles leads to a deformation of the thorax, which leads to stretching of the dorsolongitudinal

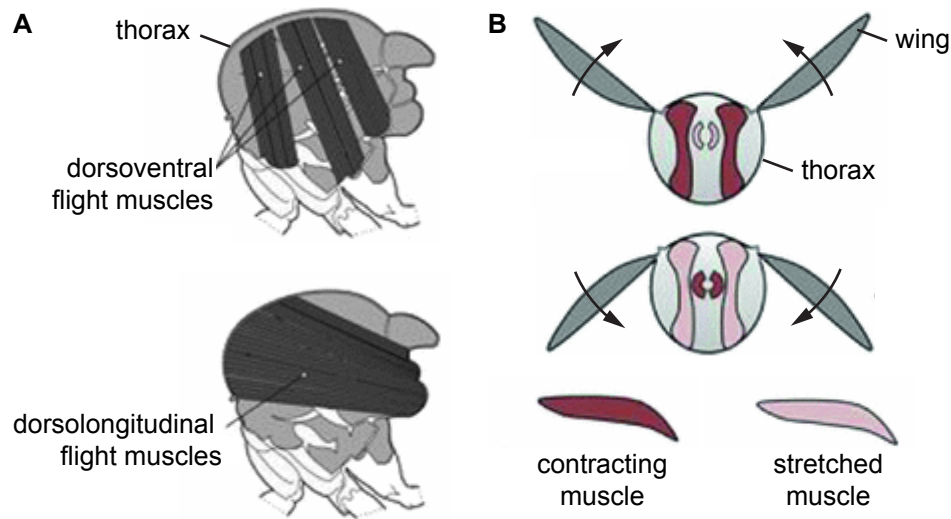


Figure 1.5: Stretch activation mechanism of flight muscles. **A.** Schematic drawing of a *Drosophila* thorax containing dorsoventral and dorsolongitudinal flight muscles arranged orthogonally to each other. Anterior is to the left, dorsal to the top. **B.** Schematic drawing of the insect flight apparatus during asynchronous contraction cycles that power flight. While the dorsoventral muscles contract the thorax is deformed, stretching the dorsolongitudinal muscles and allowing the wings to move upwards. The dorsolongitudinal muscles then contract, thereby stretching the thorax dorsoventrally. This allows the wings to move downwards. Finally, the stretched dorsoventral muscles contract again and thereby complete the cycle. Anterior is facing the reader, dorsal is to the top. Adapted with permission from Cleri (2016).

muscles (Figure 1.5B). Stretching of these muscles induces contraction, which in turn deforms the thorax, thereby stretching the dorsoventral muscles, which then contract again. This cycle of contraction, deformation and stretching creates an oscillator that can achieve high frequencies determined by its mechanical properties. Since there is a hinge mechanism between the dorsal and the ventral thorax cuticle plates, the wings move up and down as the thorax is deformed. Like this, insect flight is powered by very fast muscle contractions, which require the input from motor neurons only as a permissive signal to release Ca^{2+} and keep it at a constant high. However, the ATP-consuming fast cycling of Ca^{2+} between the cytoplasm and the sarcoplasmic reticulum is not required. Therefore, the stretch activation mechanism is very energy efficient, permitting extended flight times, and it allows the generation of maximum forces per muscle weight.

Both the muscle-tendon structure and the regulatory mechanisms of the muscle contractions are put into place during development. For example, to build myofibrils, a myofiber faces the challenge to assemble contractile myofibrils that span the myofiber

exactly from one end to the other like a tense rubber band. The myofibril can be tens of centimeters long, yet it consists of very small building blocks, the sarcomeres, which are only about 3 μm long. The number of sarcomeres assembled into a myofibril needs to be exactly right, so that the contractions of the myofibrils lead to shortening of the muscle to achieve productive movement. Developmental problems like this and many more can be addressed by studying *Drosophila melanogaster* as a model system.

1.2 *Drosophila* as a model system

Drosophila is an ideal model system to study mechanisms of muscle development, because the general developmental process and also the components of sarcomeres are highly conserved between humans and *Drosophila*. In addition, the *Drosophila* life cycle takes only ten days, genetics is easily accessible and many genetic tools are available and readily shared in the *Drosophila* community. Furthermore, genome engineering using the clustered regularly interspaced short palindromic repeats/CRISPR-associated protein 9 (CRISPR/Cas9)-system allows precisely targeted modification of the genome (see Chapter 1.7). Furthermore, fluorescence microscopy methods can be easily applied to study muscle development in the living organism or in fixed and dissected samples.

1.3 Muscle development in *Drosophila*

During the *Drosophila* life cycle, muscles are formed twice (Figure 1.6). A first set of muscles is formed during embryonic development. These muscles allow the larvae to hatch and then crawl and feed before undergoing pupation. In a process called metamorphosis, the musculature is then degraded and completely remodeled to form the musculature of the adult fly during the pupal stage. Just like vertebrates including humans, flies make many different muscle types that are optimized to fulfill their respective function, for example: continuous beating of the heart muscle for a good supply of nutrients during the entire life span, fast and repeated contractions of the flight muscles to power insect flight, quick one-time contractions of the jump muscles to mediate an escape response, or targeted and well-coordinated contractions of leg muscles for walking.

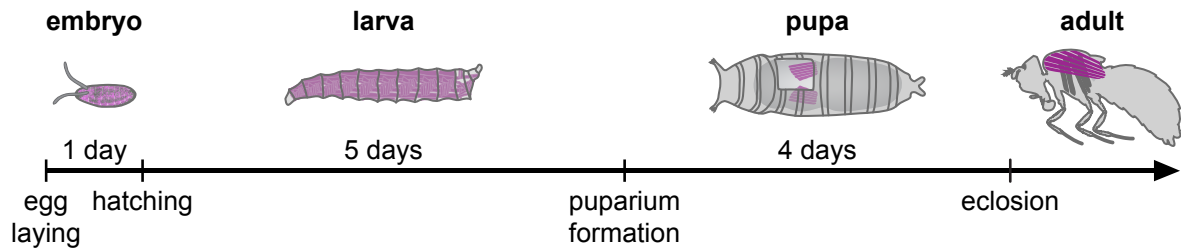


Figure 1.6: Muscle development during the *Drosophila* life cycle. The *Drosophila* life cycle is split into four stages: the embryonic, larval, pupal, and adult stage. During the embryonic stage (1 day) the muscles for the larval stage are built. Using these muscles the larvae hatch and then feed to support growth (5 days). As the larvae grow the musculature grows with it until the pupal stage, during which the musculature is remodeled and the adult muscles are formed (4 days). As examples, the body wall muscles are indicated in magenta in the embryonic and larval stage, and the flight muscles in the pupal and adult stage.

1.3.1 Embryonic muscle development

The musculature required for hatching and crawling during the larval stage is formed during embryogenesis. At the end of embryogenesis, each body segment contains a stereotypical pattern of muscles (Figure 1.7). For example, the abdominal segments A2 to A7 all contain 30 muscles per hemisegment, divided into dorsal, lateral, and ventral muscle groups.

The muscles are derived from the mesoderm, which is specified by the transcription factor Twist and enters the interior of the embryo during gastrulation. During a process called germband elongation, the mesoderm elongates together with the surrounding tissues. The mesoderm in each embryonic segment differentiates into promuscular clusters, each giving rise to one progenitor cell surrounded by fusion competent myoblasts.

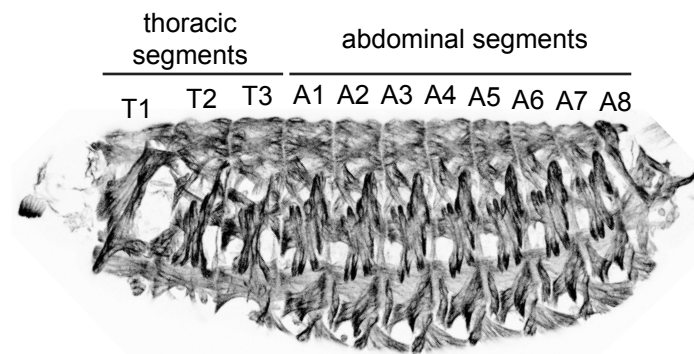


Figure 1.7: Embryonic musculature in a late stage embryo. Body wall musculature stained with β 3-Tubulin antibody. Each body segment has a stereotypical set of muscles. Anterior is to the left, dorsal to the top.

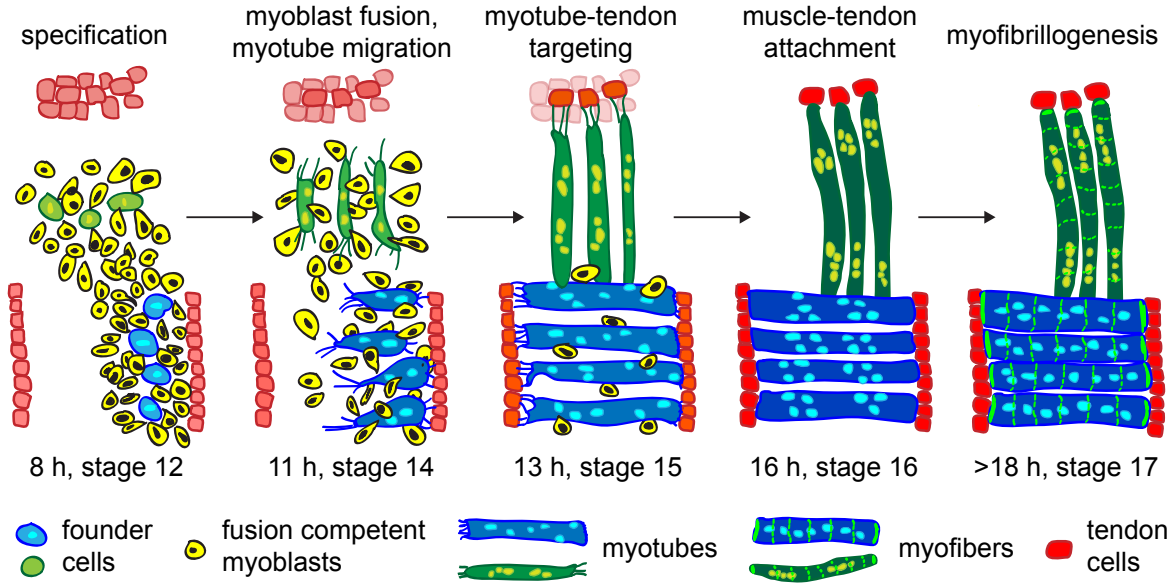


Figure 1.8: Embryonic muscle development. During embryonic stages 12 to 17, the embryonic musculature is formed. Fusion competent myoblasts fuse to founder cells, which each give rise to one specific muscle. As an example, three lateral transverse muscles (green) and four ventral longitudinal muscles (blue) are shown. The resulting myotubes migrate towards the tendon precursors and start to form muscle-tendon attachments, while more myoblasts fuse. Finally, the attached myotubes differentiate into myofibers by undergoing myofibrillogenesis and thereby becoming contractile. Adapted with permission from Weitkunat and Schnorrer (2014).

The progenitor cell then divides asymmetrically giving rise to a founder cell and either another founder cell, a pericardial cell or an adult muscle precursor (AMP) cell (de Jossineau et al., 2012). In the hemisegments A2 to A7 a total of 30 founder cells are specified in this way, each containing the identity information for one muscle.

The process of making a contractile muscle fiber out of each founder cell takes about 10-12 hours during embryonic development (Figure 1.8). First, fusion competent myoblasts fuse to founder cells resulting in the formation of multinucleated myotubes. The tips of the myotubes then migrate towards the tendon precursors while more myoblasts fuse to the myotubes. Upon reaching their tendon targets, the myotubes interact with the tendon precursors leading to their terminal differentiation and stable muscle-tendon attachments are formed. Finally, the myotubes become innervated and undergo sarcomerogenesis, thereby transitioning to the myofiber stage. During sarcomerogenesis, myofibrils, consisting of sarcomeres chained together, are built. Thus, the resulting myofibers gain the ability to contract, allowing the larva to hatch from the eggshell.

During the larval stages, the larva uses the muscles to crawl and feed. As a result, the larva grows dramatically and the muscles need to grow with it about ten times in length (Weitkunat and Schnorrer, 2014). During growth, new sarcomeres are added to the muscles, likely at the ends of the myofibrils (Bai et al., 2007). After going through the larval stages L1, L2, and L3, the so-called wandering L3 larva finds a good spot for pupation.

1.3.2 Pupal muscle development

During metamorphosis at the pupal stage, the musculature is completely remodelled and a new musculature is formed with each muscle tailored to the requirements of the adult fly, for example, flight muscles allowing fast and powerful contractions powering flight, jump muscles allowing an effective escape response, and leg muscles allowing efficient walking (Figure 1.9). The adult muscles are built using twist-expressing AMPs that are derived from the embryonic mesoderm and are set aside during embryonic development. At the larval stage, these AMPs proliferate and then form adult muscles *de novo* or using larval muscles as templates during metamorphosis.

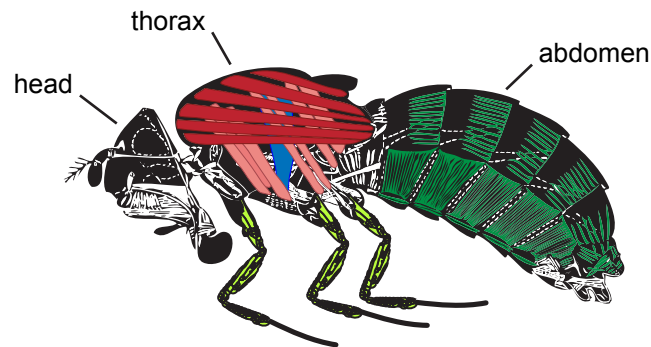


Figure 1.9: Adult musculature. Scheme showing different muscles in a sagittal section through an adult fly. In the thorax, indirect flight muscles consisting of the dorsolongitudinal muscles (red) and dorsoventral muscles (rose), and the jump muscle (blue) are highlighted. Legs muscles are shown in light green and abdominal muscles in dark green. Anterior is to the left, dorsal to the top. Adapted with permission from Miller (1950).

1.3.2.1 Abdominal muscle development

Abdominal muscles are an example for adult muscles that form without requiring a larval muscle as a template (Figure 1.10). AMPs proliferate and migrate along growing neural branches to their future positions within each abdominal segment (Currie and Bate,

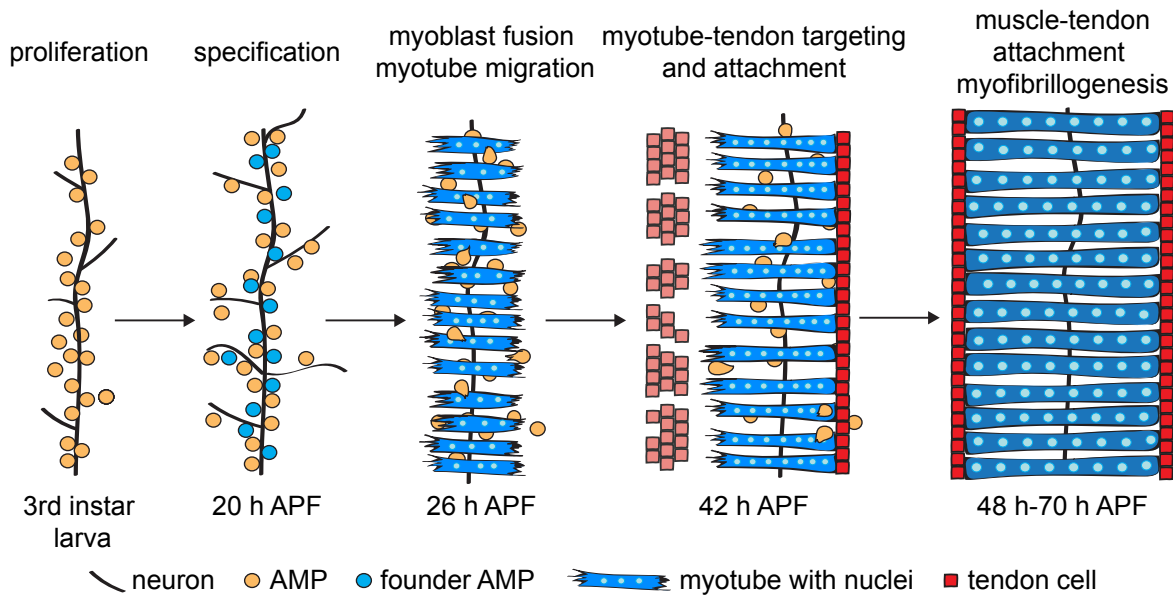


Figure 1.10: Abdominal muscle development. For forming the adult abdominal musculature, adult muscle precursors (AMPs) proliferate and migrate along growing neurons in the abdominal segments. From the pool of AMPs, founder cells are specified that each give rise to one muscle. The remaining AMPs become fusion competent myoblasts and fuse to founder cells, thereby giving rise to myotubes which migrate and attach to tendon cells both on their posterior and their anterior end. Finally, the myotubes undergo myofibrillogenesis and become contractile myofibers. h APF: hours after puparium formation. Adapted with permission from Weitkunat and Schnorrer (2014).

1991). Initially, the AMPs are indistinguishable but with the help of fibroblast growth factor (FGF)-signaling, founder cells are specified and the remaining AMPs become fusion competent myoblasts at the early pupal stage (Dutta et al., 2005). Similar to the embryonic muscle development, the myoblasts then fuse to the founder AMPs resulting in the formation of myotubes that migrate both anteriorly and posteriorly towards their tendon targets. Upon attaching posteriorly and then anteriorly to the tendon cells, the myotubes undergo myofibrillogenesis. Immature myofibrils align laterally forming cross-striated tubular muscles (Weitkunat et al., 2017).

1.3.2.2 Flight muscle development

The flight muscles were the main model system used in this thesis. Therefore, their development will be described in more detail in this chapter. The dorsolongitudinal flight muscles are an example for muscles that form by fusion of myoblasts to larval templates. These myoblasts already proliferate during the larval stage while they are

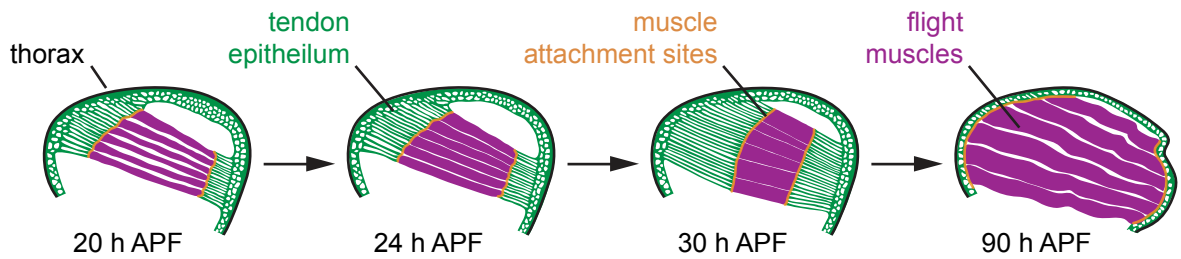


Figure 1.11: Flight muscle development. Schemes of the developing dorsolongitudinal flight muscles in the pupal thorax are shown. By 20 h APF, the forming myotubes have initiated contact with the epithelial tendon cells. While the muscle attachment sites mature the myotubes compact and the tendon epithelium forms long cellular extensions. At 30 h APF, the maximally compacted stage is reached. Finally, the flight muscles grow to fill the entire thorax by the end of the pupal development, at 90 h APF.

associated with the wing imaginal disc. During early pupal development, the myoblasts migrate to three larval templates and fuse to them. Fusion of more myoblasts leads to splitting of the templates and a total of six myotubes are formed on each side of the pupal thorax. The tips of these myotubes migrate towards their tendon-targets while forming dynamic filopodia and attachment formation is initiated at around 13h APF (Weitkunat et al., 2014). This process requires Kontiki, a transmembrane protein that is recruited to the muscle tips (Weitkunat et al., 2014).

After the initial contact of the myotube with the tendon cells, extracellular matrix (ECM) components are deposited at the maturing muscle attachment sites. Concomitantly, integrins, which are the major cell-ECM adhesion receptors, are recruited to the muscle attachment sites. While the attachments mature, the myotubes compact and initiate myofibrillogenesis. Simultaneously, the tendon epithelium forms long cellular extensions by 30 h APF (Figure 1.11). As a result, tension is built up in the muscle-tendon tissue (Weitkunat et al., 2014). After the compaction phase, the muscle fibers grow and mature until they fill the entire thorax at the end of the pupal stage at 90 h APF (Figure 1.11).

Myofibrillogenesis can be divided into three major phases during flight muscle development (Spletter et al., 2018): In a first phase, immature myofibrils are assembled that consist of $\approx 1.8 \mu\text{m}$ long immature sarcomeres. All ≈ 2000 myofibrils that will make up the mature muscle fiber are already present in their immature form at 30 h APF. In a second phase, more sarcomeres are added to the immature myofibrils, roughly tripling the number of sarcomeres per myofibril from ≈ 80 to ≈ 230 in less than a day

of development until 48 h APF. By 60 h APF the final number of ≈ 270 sarcomeres per myofibril is reached. In a third phase, the sarcomeres mature and grow both in width and length until they reach their final size of $\approx 3.2 \mu\text{m}$ in the adult stage. No new myofibrils are added during the second and third phase and, as opposed to the myofibrils in the abdominal muscles, which laterally align and connect to form a tubular structure, the myofibrils in flight muscles do not align.

In the final structure, each myofibril has to have exactly the right length, i.e. the right number of sarcomeres, to reach exactly from one muscle attachment to the other. Additionally, the sarcomeres need to have a stereotyped size to guarantee optimal contraction forces. Only if this is the case, a contraction of the individual sarcomeres leads to muscle shortening, which creates a productive and powerful movement. Thus, the myofibrillogenesis process needs to be well controlled and defects in flight muscle sarcomerogenesis lead to flightless animals.

1.3.3 Forces during muscle development

To achieve changes in shape of a cell or an entire tissue, mechanical forces need to be generated during morphogenesis. For example, the tips of the myotubes that migrate towards their tendon targets need to dynamically attach to their surrounding and pull themselves forward. Similar to the leading edge of migrating cells, flight muscle myotubes form a specialized and polarized cytoskeleton with dynamic filopodia that explore the environment at the myotube tips (Weitkunat et al., 2014). Likewise, the epithelial tendon cells form filopodia that strongly interdigitate with the filopodia on the myotube tips to initiate the muscle attachment process. As the attachment matures, the length and number of filopodia is reduced and a stable attachment is formed.

At the same time, the myotubes compact and the tendon epithelium forms long cellular extensions that have a very straight appearance (see Figure 1.11). This observation sparked the idea that there might be tension built up in the muscle-tendon tissue. Indeed, laser microdissection experiments revealed that tissue tension increases from 13 to 22 h APF (Weitkunat et al., 2014). Importantly, if the tendons are severed early during development or the attachment is weakened by genetic means, myofibrillogenesis is severely compromised. Thus, mechanical tension built up in the muscle-tendon tissue is essential for myofibrillogenesis and hence for the formation of a functioning muscle.

1.3.4 Myofibrillogenesis model

Based on the finding that tension in the muscle-tendon system is essential for myofibrillogenesis, a tension-driven myofibrillogenesis model was proposed (Figure 1.12) (Lemke and Schnorrer, 2017). This model combines two previous models, the premyofibril

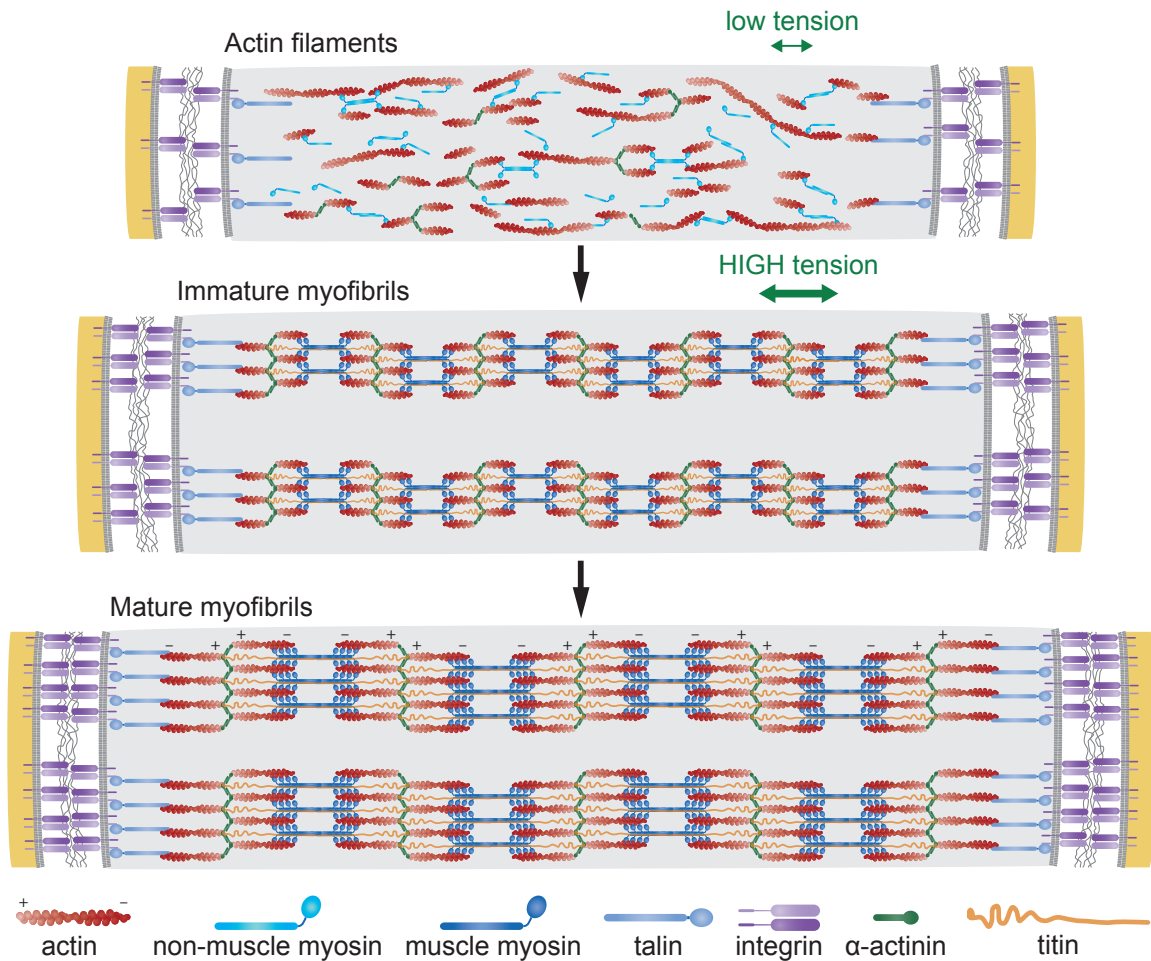


Figure 1.12: Tension-driven myofibrillogenesis model. Early in development when tissue tension is low, actin filaments (red) are formed that are not yet striated but oriented mostly along the long axis of the muscle (grey). The actin filaments loosely interact with non-muscle myosin (light blue). As tissue tension increases, immature myofibrils form, which are striated, contain muscle myosin (dark blue), and are connect via talin (blue) and integrin (violet) to the tendon cells (yellow) at both ends of the muscle. The actin filaments are crosslinked by α -actinin (green) at the forming sarcomeric Z-discs and titin (orange) connects the Z-disc with the myosin filaments. In a last step, the immature myofibrils mature with the sarcomeres growing both in length and width. There are no new myofibrils added in the maturation phase. Adapted from Lemke and Schnorrer (2017).

model (Rhee et al., 1994; Sparrow and Schöck, 2009; White et al., 2014) and the I-Z-I body, self-assembly model (Holtzer et al., 1997; Ehler et al., 1999), and adds the aspect of mechanical forces.

The premyofibril model is based on the observation of premyofibrils in avian cardiac muscle cells and mouse skeletal muscle cells (Rhee et al., 1994; White et al., 2014; Fenix et al., 2018). These premyofibrils contain actin and non-muscle myosin but no muscle myosin, yet. As the premyofibrils mature, they become nascent myofibrils in which the non-muscle myosin is replaced by muscle myosin and additional sarcomere components are recruited. The mature myofibrils contain only muscle myosin and no non-muscle myosin. The premyofibrils were mostly observed at the edges or tips of cultured cells and thus presumably move inwards as they mature.

In contrast, the I-Z-I body, self-assembly model is based on the observation that myofibrils can assemble within hours without the previous assembly of premyofibrillar structures (Holtzer et al., 1997; Ehler et al., 1999). This view is supported by the observation that muscle myosin can assemble into aligned antiparallel mini-filaments in the absence of actin filaments or Z-discs and that they can self-assemble into myofibrils together with so-called I-Z-I bodies. These I-Z-I bodies consist of α -actinin, titin, and actin filaments (also see Figure 1.2) and are first irregular in shape. As they are incorporated into myofibrils, they become more regular and the thin filament length becomes more stereotypical. These structures are then called I-Z-I brushes and form the sarcomere together with the thick filaments (consisting of muscle myosin) that assemble into A-bands (Holtzer et al., 1997).

Based on the insights gained from studying the *Drosophila* flight muscle myofibrillogenesis an updated model was proposed. The major observations important for the new model are (1) that myofibrillogenesis progresses homogeneously along the entire muscle fiber and (2) that mechanical tension is required for myofibrillogenesis (Weitkunat et al., 2014). The first observation is well in agreement with the finding that actin order increases homogeneously along the muscle fiber as determined by polarization-resolved microscopy (Loison et al., 2018). These observations support a self-organization model for myofibrillogenesis rather than growth of premyofibrils from the tips or edges of the cells that mature as they move further inwards. Nevertheless, mature myofibrils are certainly formed out of immature myofibrils, but these already reach from one end to other at a very early stage (Figure 1.12) (Loison et al., 2018).

The self-assembly process of these immature myofibrils needs to be directed such that the myofibrils form along the long axis of the muscle and not in any other direction, and the myofibril length needs to be exactly right. Only if both these requirements are fulfilled, the contraction of the mature sarcomeres can lead to a productive shortening of the muscle. Mechanical tension is likely an important cue for both requirements: First, tension in the muscle-tendon tissue builds up along the long axis of the muscle fiber (Weitkunat et al., 2014) and thus can guide the formation of actin filaments that are preferentially oriented (Figure 1.12). Passive tension along the immature myofibril could stabilize fibrils that are oriented correctly, are properly attached, and have the right length. Fibrils that are too long, too short or in the wrong orientation could all be disassembled based on only one cue, the tension. This mechanism could explain how the perfectly regular myofibrils are assembled that make up the mature muscle (Figure 1.12).

How the tissue tension is transmitted and sensed at the molecular level, however remains an open question. The ideal candidate for transmitting and sensing forces at the muscle-tendon interface is the integrin adhesion complex. Integrins are transmembrane proteins that connect the ECM to the intracellular actin cytoskeleton with the help of the major adaptor protein Talin (Figure 1.12). The main aim of this thesis was to analyze how forces are transmitted by Talin before and during myofibrillogenesis. Therefore, integrins and Talin will be introduced in detail in the following chapters.

1.4 Integrin-mediated adhesion

Integrins are the major cell-ECM-receptors that are used by cells to hold on to their environment. Integrins are transmembrane proteins consisting of an α - and a β -subunit that form a heterodimer (Figure 1.13). At the extracellular side, integrins have large domains that bind to ECM-components, whereas, at the intracellular side, integrins only have a very short cytoplasmic tail, yet it contains many protein binding sites. In this way, integrins can recruit a large number of proteins that form the intracellular adhesion complex. One of the major proteins recruited to integrins is Talin, which binds to an NPXY motif in the β -integrin cytoplasmic tail and connects integrins to the intracellular actin cytoskeleton (Figure 1.13).

Integrin function is essential both in *Drosophila* and in vertebrates. Knockout of the main β -integrin in *Drosophila*— β PS encoded by *myspheroid* (*mys*)—leads to

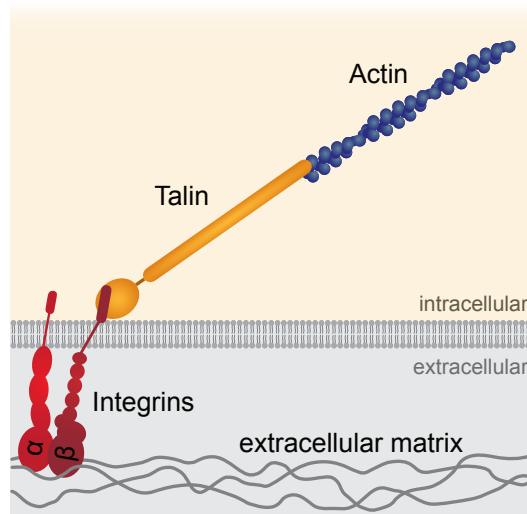


Figure 1.13: The integrin-actin linkage. Integrin heterodimers bind to both extracellular matrix (ECM) components and to a large number of proteins at the intracellular side. One of these proteins is Talin, which provides the major linkage to the actin cytoskeleton.

embryonic lethality (Wright, 1960; Bunch et al., 1992). The mutant embryos show various morphological defects including an abnormal musculature. Similarly, $\beta 1$ -integrin mutant mice die very early during embryonic development, shortly after implantation into the uterus (Fässler and Meyer, 1995). If $\beta 1$ -integrin is eliminated specifically in skeletal muscle during development, the mice die at birth displaying strong musculature defects including myoblast fusion defects (Schwander et al., 2003). Hence, integrin function is essential for development in general and for muscle development in particular, both in *Drosophila* and vertebrates.

1.4.1 Integrin receptor family

Vertebrates express a large family of integrins. Their genome contains 8 different β -integrins ($\beta 1$ -8) and 18 different α -integrins ($\alpha 1$ -11, αv , αIIb , αD , αE , αL , αM , and αX), which can form heterodimers in specific combinations (Figure 1.14). Each heterodimer has a particular specificity for an extracellular matrix component to which it can bind. A fairly large group of heterodimers bind to the peptide sequence arginine-glycine-aspartate (RGD), which is found in extracellular matrix proteins like fibronectin. A second group interacts with laminins and a third group with collagens in the extracellular matrix. Finally, there is a group of integrin heterodimers that are specific to leukocytes.

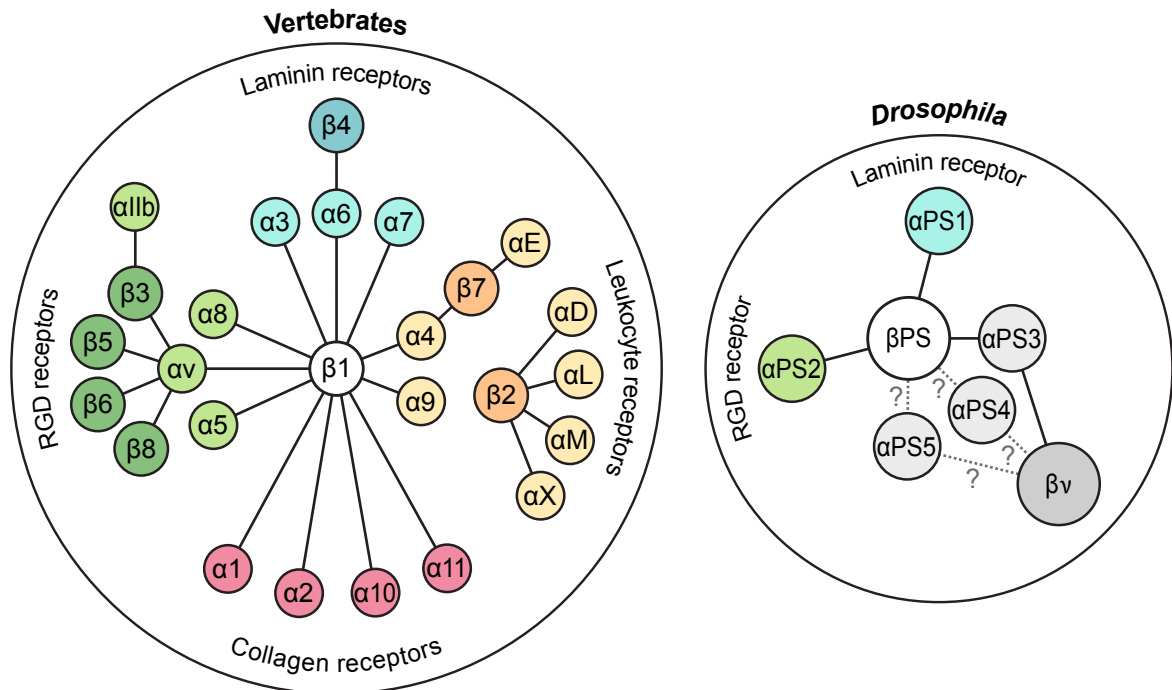


Figure 1.14: The vertebrate vs. the *Drosophila* integrin family. In vertebrates, there are at least 8 different β -integrins and 18 different α -integrins that heterodimerize in various combinations (black lines). In *Drosophila*, there are only two β -integrins and five α -integrins, with α PS1 β PS and α PS2 β PS being the most prominent heterodimers. Color coding indicates functional similarity. *Drosophila* integrin subunits colored in gray do not have an obvious vertebrate orthologs. Dashed lines indicate that heterodimerization is assumed based on the similarity of α PS3, α PS4, and α PS5. The vertebrate scheme was adapted with permission from Barczyk et al. (2013) and the *Drosophila* scheme was drawn based on information summarized by Narasimha and Brown (2013).

In *Drosophila*, integrins are conserved, but a smaller number of family members makes the system more accessible and therefore easier to study. There are only two different β -integrins (β PS and β ν) and five different α -integrins (α PS1-5) (Figure 1.14). β PS (position specific) is the main β -integrin in *Drosophila* and it is most closely related to the vertebrate β 1-integrin (Takada et al., 2007). As mentioned above, knock-out of the β PS encoding gene *mysospheroid* (*mys*) is embryonic lethal (Wright, 1960; Bunch et al., 1992). The musculature of these embryos is severely compromised as muscles lose their attachments and round up. Therefore, the gene was named *mysospheroid* after the spheroid appearance of the rounded-up muscles. In contrast, knock-out flies for the other β -integrin subunit, β ν , are viable and fertile (Devenport and Brown, 2004). However, when both β -integrins are removed the β PS-phenotype becomes more

severe, especially in the developing gut, where $\beta\nu$ is mainly expressed. Thus, $\beta\nu$ can partially compensate for the loss of β PS, but nevertheless, β PS is the major β -integrin in *Drosophila* that is ubiquitously expressed.

Of the five α -subunits in *Drosophila*, α PS1 is most closely related to vertebrate subunits α 3, α 6, and α 7 and shares with these subunits the ability to bind to laminins (Figure 1.14) (Hynes and Zhao, 2000). The gene coding for α PS1 is called *multiple edematous wings* (*mew*) due to a wing blistering phenotype that occurs if mutant cell clones are induced in the wing (Brower et al., 1995). Complete knock-out of *mew*, however, leads to larval lethality.

Drosophila α PS2 is most closely related to the vertebrate subunits $\alpha\nu$, α 5, and α 8 and binds RGD motifs just like the vertebrate homologs (Hynes and Zhao, 2000) (Figure 1.14). The gene coding for α PS2 is called *inflated* (*if*) because the original mutant allele isolated in 1918 caused wing blisters that made the wings look inflated (Weinstein, 1918). However, this allele was not a null allele. α PS2 null animals die as embryos displaying a muscle detachment phenotype as severe as β PS knock-out embryos (Brabant and Brower, 1993). Compared to this, the *mew* (α PS1) phenotype is rather mild as the embryos do not show any muscle detachment phenotype and larvae are even able to hatch.

This difference can likely be explained by compensation of the loss of α PS1 by another α -subunit, either α PS2 or one of the three remaining α -subunits, α PS3-5. These three α -subunits do not have an obvious vertebrate homolog; they are, however, very similar to each other and therefore α PS4 and α PS5 are thought to be recent gene duplications of α PS3 (Narasimha and Brown, 2013). α PS3 has been shown to interact both with β PS and $\beta\nu$ and it has been inferred that α PS4 and α PS5 can do the same (Figure 1.14).

In conclusion, in *Drosophila*, a complete integrin null animal can be generated by knocking out only the two genes encoding the β -subunits, β PS and $\beta\nu$ (Devenport and Brown, 2004). Furthermore, knock-out of the individual α -subunits causes subsets of the complete integrin null phenotype, depending on where these α -subunits are predominantly expressed and on redundancy between the α -subunits.

1.4.2 Integrin regulation

Integrin-mediated adhesion has to be tightly regulated. For example, a migrating cell has to activate integrins at its front to adhere to the extracellular matrix that it encounters and at the same time deactivate integrins at its rear allowing the cell to let go and move

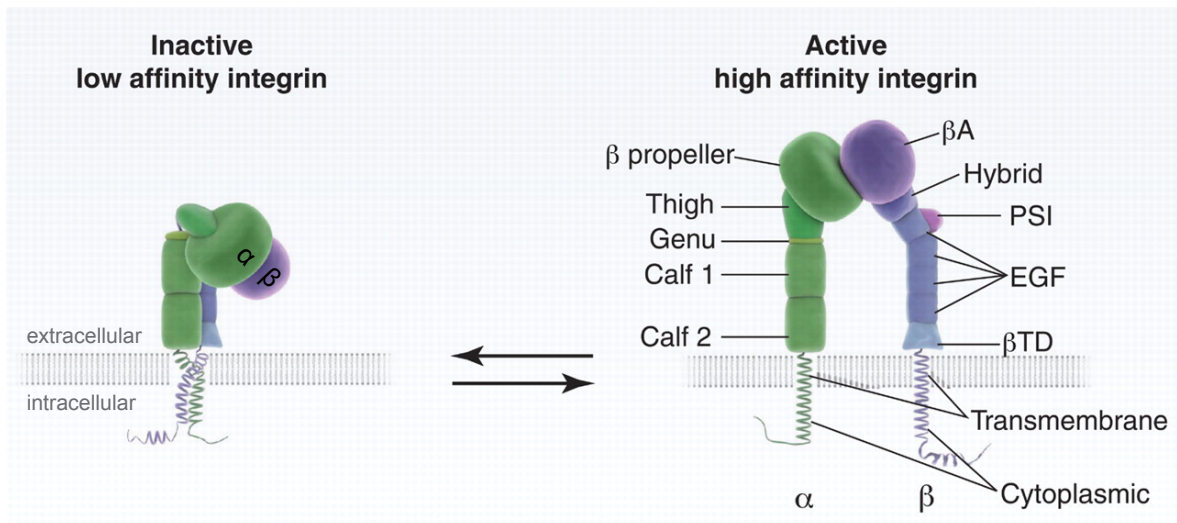


Figure 1.15: Integrin structure and regulation. Integrins are transmembrane proteins with large extracellular domains and short cytoplasmic tails. α -integrins consist of a β -propeller domain that is also called the head, a thigh domain, and two calf domains that form the so-called leg. β -integrins consist of a β A-domain, which is connected by a hybrid domain to a plexin/semaphorin/integrin (PSI)-domain, four epidermal growth factor (EGF)-domains, and a β tail domain (β TD)-domain that is just next to the membrane. In the inactive, low affinity conformation, the integrin heterodimer is bent and the transmembrane domains interact. In the active, high affinity conformation, the extracellular domain is in an extended open conformation with separated legs and transmembrane domains. Adapted from Moser et al. (2009). Reprinted with permission from AAAS.

forward. Inactive integrins have a conformation that has a low affinity for extracellular matrix components (Su et al., 2016). In this conformation, the transmembrane domains bind to each other and the extracellular domains of the α - and β -subunit are bent. It is therefore called bent closed conformation (Figure 1.15) (Gottschalk, 2005). Signals both from the outside ("outside-in") or from the inside ("inside-out") can activate integrins and convert them to a high affinity state. In this conformation, the extracellular domains are extended, the so-called legs of the extracellular domains are separated and also the transmembrane domains dissociate from each other (Figure 1.15). This conformation is called the extended open conformation.

1.4.3 Focal adhesions

Integrins recruit a large number of proteins to sites of cell-ECM adhesion and the entire complex is called a focal adhesion. The core element are the integrin transmembrane

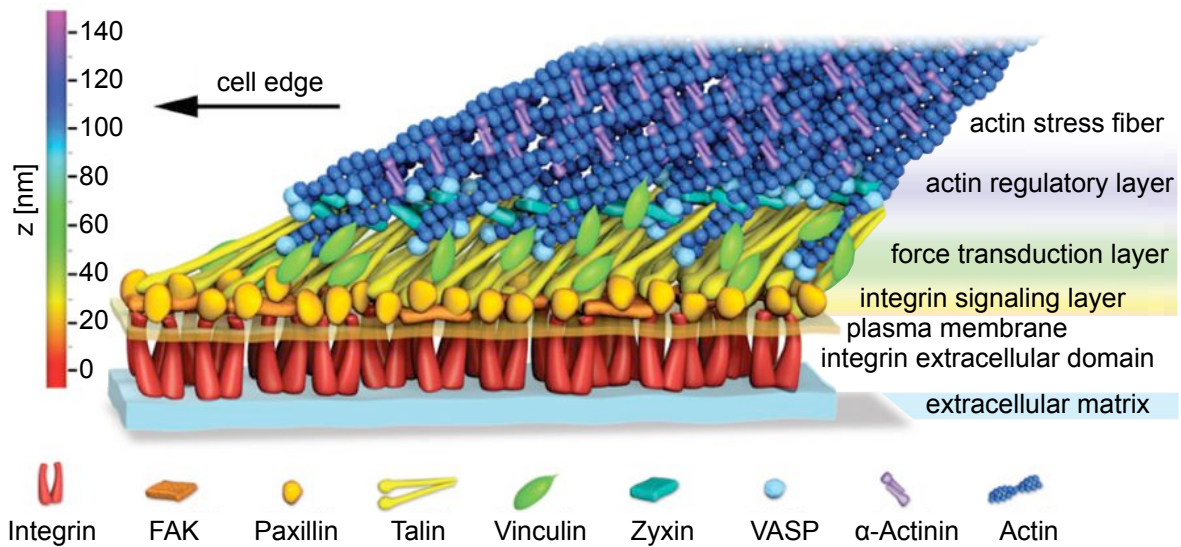


Figure 1.16: Focal adhesion structure. Superresolution microscopy revealed that focal adhesions have a layered structure. The distance of the respective focal adhesion proteins from the extracellular matrix is color-coded. Adapted with permission from Kanchanawong et al. (2010).

proteins, however, they can recruit more than 150 proteins directly or indirectly on their intracellular side. These proteins fulfill various signaling functions including chemical signaling and mechanotransduction, thus they can translate a mechanical stimulus into a chemical response.

Focal adhesion proteins are organized in a layered structure with the mechanotransducer protein Talin in a central position (Figure 1.16) (Kanchanawong et al., 2010). Talin consists of a head domain and a long rod domain. The head domain interacts with the integrin cytoplasmic tail directly at the membrane. The Talin rod domain extends about 30 nm away from the membrane, where it binds to actin crosslinked by α -actinin. At the interface between the actin stress fiber and the focal adhesion, actin regulatory proteins like Zyxin and vasodilator-stimulated phosphoprotein (VASP) are recruited, which form an actin regulatory layer (Figure 1.16). Vinculin, a protein that can bind both Talin and actin, is recruited to Talin in a force-dependent manner, thereby reinforcing the Talin-actin interaction in the force transduction layer below the actin regulatory layer. Finally, integrin signaling proteins like focal adhesion kinase (FAK) and Paxillin are recruited in close proximity to the plasma membrane creating an integrin signaling layer (Figure 1.16).

It is debated in the field how closely focal adhesions, which have mainly been studied *in vitro* in cultured cells, resemble adhesion structures *in vivo*. One of the main differences for cells on a cell culture dish compared to cells *in vivo* are the mechanical properties of their environment. While cells in culture encounter a flat and stiff surface that tends to induce the formation of strong actin stress fibers and large focal adhesions, cells *in vivo* experience a three-dimensional and generally much softer environment (Barnes et al., 2017). In this environment, cells make different kinds of adhesions and can migrate faster, therefore the adhesions need to be more dynamic (Cukierman et al., 2001). An exception are muscle attachment sites that are very large and stable integrin-mediated adhesion structures. Since the main objective of this thesis was to study how mechanical forces are transmitted in adhesion structures *in vivo*, muscle attachment sites were chosen as a model system.

1.4.4 Muscle attachment sites

Muscle attachment sites are integrin-based adhesions that have been studied in detail in the *Drosophila* embryo. The muscles building the body wall musculature of the embryo attach either directly to a so-called tendon cell or the muscles attach to each other end-to-end and in addition to tendon cells, thereby creating three-way connections (Figure 1.17A). The tendon cells are epithelial cells that are part of the

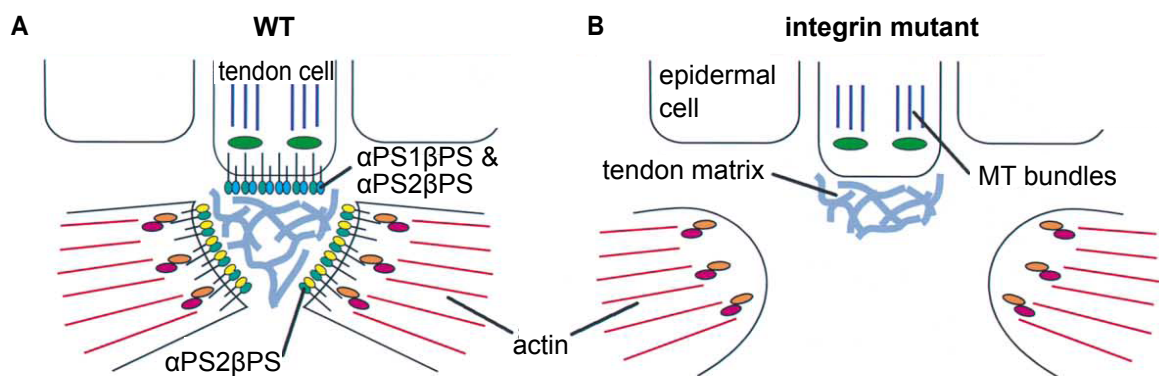


Figure 1.17: Integrin-dependent muscle attachment in the *Drosophila* embryo. **A.** Scheme of a wild-type (WT) muscle attachment site between two muscle cells and a tendon cell. Expression of different integrin heterodimers is indicated. **B.** Scheme of a muscle attachment site lacking integrins. Even though some tendon matrix is deposited correctly, the muscles lose attachment and round up, because they cannot adhere to the matrix. Adapted with permission from Bökel and Brown (2002).

epithelial monolayer forming the larval cuticle. The connection between the muscle and tendon cells is not a direct cell-cell contact but rather a cell-ECM-cell contact. ECM components like Tiggrin, Thrombospondin (both RGD-containing matrix proteins), Laminin, Perlecan, and M-spondin are deposited at muscle attachment sites and integrins expressed by the tendon and muscle cells bind to these extracellular matrix components (Fogerty et al., 1994; Umemiya et al., 1997; Bunch et al., 1998; Martin et al., 1999; Friedrich et al., 2000; Chanana et al., 2007; Subramanian et al., 2007). While both the tendon and the muscle cells express β PS, the tendon cells express both α -subunits α PS1 and α PS2, whereas the muscle cells express only α PS2 (Figure 1.17A) (Maartens and Brown, 2015).

If β PS integrin is removed, both α PS1 β PS and α PS2 β PS are lacking, and hence the muscles lose their attachment and round up (Wright, 1960; Bunch et al., 1992) (Figure 1.17B). In contrast, if only α PS1 is removed, the muscles stay attached and some larvae are even able to hatch from the eggshell (Brabant and Brower, 1993). This phenotype is well in agreement with the expression pattern of the two integrin heterodimers, as α PS2 β PS remains functional and can compensate the loss of α PS1 β PS in tendon cells. Compared to the mild phenotype of α PS1 depletion, removal of α PS2 causes a strong phenotype including muscle detachment that is comparable to the β PS loss-of-function phenotype (Brower et al., 1995). This phenotype can also be explained by the integrin expression pattern, because loss of α PS2 β PS in muscles cannot be compensated (Figure 1.17).

Apart from integrins, also other components that have been studied in focal adhesions play an important role in muscle attachment sites. For example, Talin is an essential component of muscle attachment sites (Brown et al., 2002), just like of focal adhesions. Its structure and function in muscle attachment sites is described in detail in Chapter 1.5.

Since the loss of major muscle attachment components is embryonic or larval lethal, the function of integrins and associated proteins during adult muscle development (see Figures 1.9, 1.10, and 1.11) is less well studied. Recently, however, muscle attachment sites forming at the tips of adult flight muscles during the pupal stage of *Drosophila* have been studied in some detail (Green et al., 2018). Interestingly, adult muscle attachment sites have a layered structure similar to focal adhesions (see Figure 1.16). At the tips of the myofibrils, the membrane of muscles form interdigitations with the tendon cells that they are attached to (Figure 1.18). In direct proximity of the membrane, an integrin signaling layer is formed that contains integrins and tightly associated proteins,

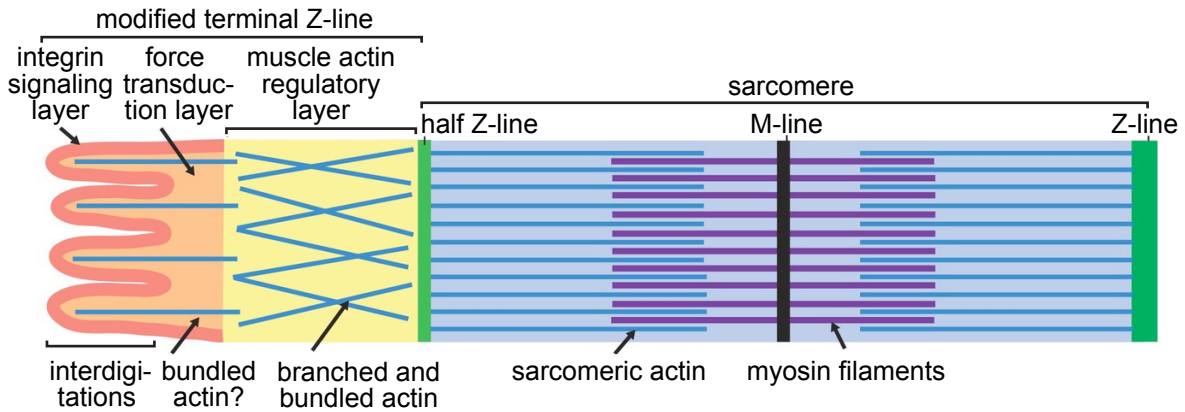


Figure 1.18: Integrin-dependent muscle attachment in adult flies. Scheme of a *Drosophila* flight muscle attachment site. The end of a single myofibril with its terminal sarcomere (blue) is depicted. The modified terminal Z-line consists of four layers: The integrin signaling layer (red) contains proteins that are closely associated with the cell membrane, for example the N-terminal end of Talin but very little actin. The C-terminal end of Talin and Vinculin are found both in the integrin signaling layer and in the force transduction layer (orange). The muscle actin regulatory layer (yellow) also contains Vinculin and in addition Filamin, Arp3, and WASH. The following half Z-line (green) contains high amounts of α -Actinin and Z-band alternatively spliced PDZ-motif protein (Zasp). Adapted with permission from Green et al. (2018).

including Talin’s N-terminal head domain. Talin’s C-terminal end is found in a force transduction layer, where also actin and Vinculin are present. The force transduction layer is followed by a novel layer, termed muscle actin regulatory layer, that differs from the actin regulatory layer found in focal adhesions in that it contains actin-related protein 3 (Arp3) and Wiskott-Aldrich syndrome protein (WASP)-homolog (WASH), an Arp2/3-regulator. Finally, a half Z-line, containing high levels of α -Actinin and Z-band alternatively spliced PDZ-motif protein (Zasp), connects the muscle attachment to the first sarcomere of the myofibril. The similarities between focal adhesions and muscle attachments make muscle attachment sites a good model system to investigate how findings based on studying focal adhesions *in vitro* can be transferred to an *in vivo* system.

1.5 Talin – a major force transducer

Talin is the major adaptor protein connecting integrins bound to the extracellular matrix to actin in the cell interior. Therefore, Talin is an obvious candidate for transmitting

mechanical forces at the molecular level at muscle attachment sites and was hence the main focus of this thesis. It is an essential protein both in *Drosophila* and vertebrates. While *Drosophila* has only one Talin gene, vertebrates have two isoforms, Talin-1 and Talin-2.

Knock-out of the Talin-encoding gene in *Drosophila*, named *rhea* after a flightless bird, leads to an equally severe embryonic lethal phenotype as knock-out of the integrins, including the muscle detachment phenotype (Brown et al., 2002). Thus, Talin is essential for integrin function in general and for integrin-mediated muscle attachment in particular.

Similarly, Talin-1 mutant mice die by embryonic day 9.5 displaying a phenotype during gastrulation after implanting into the uterus (Monkley et al., 2000). Thus, Talin-2 cannot compensate entirely for the loss of Talin-1. If Talin-1 is specifically ablated in skeletal muscle during development, the mice show a progressive myopathy phenotype (Conti et al., 2008). However, in contrast to the β 1-integrin skeletal muscle mutant mice (Schwander et al., 2003), they survive to adulthood. Thus, Talin-2 likely partially compensates for the loss of Talin-1 in muscles but is unable to prevent progressive failure of muscle-tendon attachment. If both Talin-1 and Talin-2 are eliminated in skeletal muscle, the mice die shortly after birth, similar to the skeletal muscle-specific β 1-integrin knockout mice (Conti et al., 2009). In conclusion, Talin function is conserved from *Drosophila* to vertebrates.

1.5.1 Talin domain structure

Talin is an about 270 kD protein that consists of a head domain and an extended rod domain, which are connected by a unstructured linker region (Figure 1.19). The about 50 kD head domain contains an atypical 4.1 protein, ezrin, radixin, moesin (FERM) domain. Instead of its domains F1, F2, and F3 being organized in a cloverleaf shape, they are organized in a linear fashion with an additional F0 domain juxtaposed to the F1 domain (Goult et al., 2010c). In addition, the F1 domain has an unstructured loop inserted (F1-loop). The about 220 kD rod domain consists of 13 helical bundles (R1 to R13) and a dimerization domain (DD) at its C-terminus. Each helical bundle is made up of 4-5 amphipathic helices, whose structures have been determined by a combination of limited proteolysis, nuclear magnetic resonance (NMR), and x-ray crystallography (Papagrigoriou et al., 2004; Gingras et al., 2007, 2009; Goult et al., 2009, 2010b, 2013).

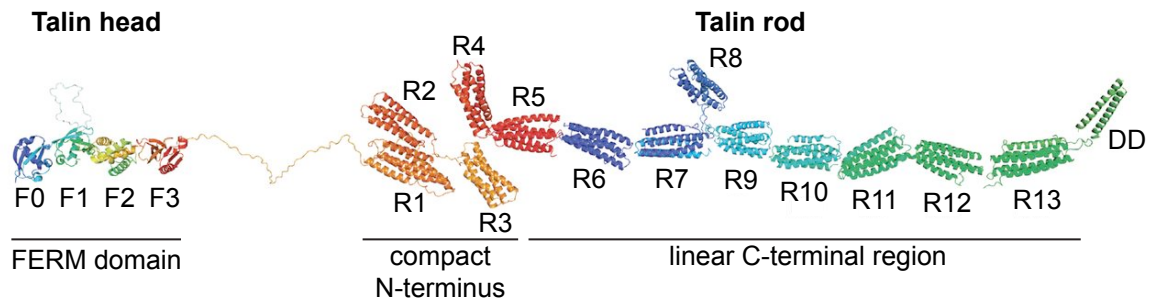


Figure 1.19: Talin structure. Model of the Talin structure with the head domain consisting of a 4.1 protein, ezrin, radixin, moesin (FERM) domain (F0-F3) and the rod domain consisting of 13 helical bundles (R1-R13, each containing 4-5 α -helices) and a C-terminal dimerization domain (DD). The dimerization domain consists of a single α -helix and is depicted here as an antiparallel dimer. Adapted with permission from Goult et al. (2013).

R1 to R4 are arranged in a compact fashion with R1 and R2 interacting directly with each other. Domains R3 and R4 have their N- and C-termini on the same side of the helical bundle and are therefore arranged in a compact way. Domains R5 to R13 have their N- and C-termini on opposite sides and are therefore chained together in a linear fashion with the exception of R8 (Figure 1.19).

1.5.2 Talin interaction partners

Talin interacts with the integrin cytoplasmic tail via two integrin binding sites (IBSs) (Figure 1.20) (Horwitz et al., 1986; Knezevic et al., 1996). One integrin binding site, IBS1, is in the Talin head domain within the FERM-subdomain F3 (Calderwood et al., 1999, 2002). In addition, the head domain, particularly the unstructured loop in the F1 domain and the domains F2 and F3, contains positively charged residues that can bind to negatively charged phosphatidylinositol 4,5-bisphosphate (PtdIns(4,5)P₂) in the plasma membrane. This interaction is essential for integrin activation (Goult et al., 2010a). A second integrin binding site is in the rod domains R11 and R12 (Tremuth et al., 2004). Both IBS1 and IBS2 are sufficient to recruit Talin to integrin in the plasma membrane in flies, however only IBS1 can activate integrins, thereby reinforcing the attachment (Ellis et al., 2011). In focal adhesions, it has been shown by super-resolution microscopy that the Talin head is close to the membrane while the Talin rod extends away from the membrane (Kanchanawong et al., 2010). Thus, IBS1 in the head domain is thought to be the major integrin binding site.

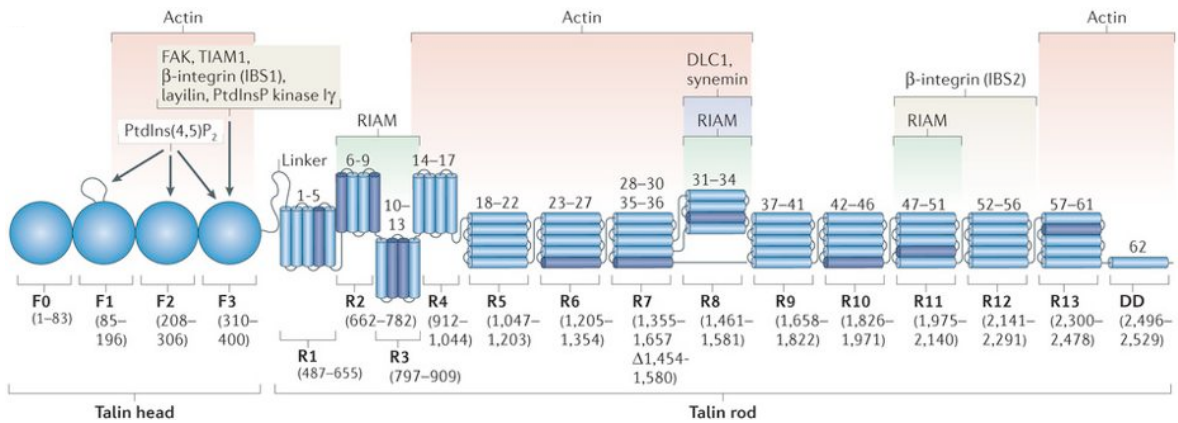


Figure 1.20: Talin interaction partners. Talin domain organisation model with an overview of Talin interaction partner binding sites. The Talin head domain is depicted as spheres corresponding to the FERM domains, F0 to F3. The rod domain consisting of 62 α -helices is depicted as numbered cylinders that are bundled in the rod domains R1 to R13. Helix 62 is the dimerization domain (DD). Aminoacid numbers of the FERM and rod domains are indicated for vertebrate Talin-1. Binding sites are marked for β -integrin (IBS1 and IBS2), actin, phosphatidylinositol 4,5-bisphosphate (PtdIns(4,5)P₂), focal adhesion kinase (FAK), T-lymphoma invasion and metastasis-inducing protein 1 (TIAM1), layilin, phosphatidylinositol 4-phosphate 5-kinase type I γ (PtdInsP kinase I γ), Rap1-GTP-interacting adaptor molecule (RIAM), deleted in liver cancer 1 (DLC1), and synemin. Vinculin binding sites are represented in dark blue. Adapted with permission from Calderwood et al. (2013).

Three actin binding sites (ABSs) were identified in Talin, one in the head domain (ABS1) and two in the rod domain (ABS2 and ABS3) (Figure 1.20) (Hemmings et al., 1996; Lee et al., 2004; Gingras et al., 2007; Atherton et al., 2015). ABS3 (R13-DD) likely provides the primary mechanical linkage to actin filaments (Gingras et al., 2007; Franco-Cea et al., 2010). ABS2 encompassing domains R4 to R8 is likely only activated after force is applied to Talin via IBS1 and ABS3. In the absence of force, R3 and R9 reduce actin binding to ABS2 (Atherton et al., 2015). Within an established adhesion, ABS2 and ABS3 likely act in concert, which is consistent with the observation that molecular forces at the N-terminal end of the Talin rod between IBS1 and ABS2/ABS3 are higher than the forces measured more C-terminally between ABS2 and ABS3 (Ringer et al., 2017). It is less clear what the role of ABS1 is. It is unlikely that it provides a stable linkage to actin as super-resolution microscopy revealed that actin is more than 30 nm away from the Talin head (Kanchanawong et al., 2010). Recently, it has been shown that the Talin head has a role in capping actin filaments to prevent further actin polarization (Ciobanasu et al., 2018). Thus, ABS1 may have a regulatory role rather than providing a stable mechanical linkage to actin.

Eleven Vinculin binding sites are located in the Talin rod (Figure 1.20) (Gingras et al., 2005). Vinculin binds to Talin with its head and to actin with its tail and is therefore able to reinforce adhesion by recruiting more actin filaments (Ziegler et al., 2008). The Vinculin binding sites on Talin each consist of one amphipathic helix that is part of a helical bundle in the rod. In the absence of force, the Vinculin binding sites are mostly inaccessible because they are buried in the hydrophobic core of the rod domains (Papagrigoriou et al., 2004). Increasing mechanical tension on Talin leads to sequential unfolding of the rod domains and, as a consequence, more and more Vinculin binding sites become exposed (del Rio et al., 2009). R3 unfolding is particularly easy, because 4-helix bundles are generally weaker than 5-helix bundles and, in addition, the hydrophobic core of R3 is destabilized by three threonine residues (Goult et al., 2013; Mykuliak et al., 2018). Therefore, R3 already starts to unfold if forces as low as 5 piconewton (pN) are applied (Yao et al., 2014). Thus, Vinculin is likely first recruited to R3 and, as more tension is built up on Talin, more Vinculin can bind to other Vinculin binding sites, thereby reinforcing adhesion in a mechanosensitive manner.

In addition to interacting with other proteins, Talin also interacts with itself. The Talin head domain F3 can bind to the rod domain R9 (Goksoy et al., 2008), thereby rendering IBS1 inaccessible. The autoinhibition of cytosolic Talin needs to be relieved in order for Talin to be recruited to integrins in the plasma membrane. Binding of Rap1-GTP-interacting adaptor molecule (RIAM) to Talin rod domains R2, R3, R8, and R11 can activate Talin and thereby recruit it to integrins and in turn activate integrins (Figure 1.20) (Goult et al., 2013). Interestingly, all domains that contain a RIAM binding site also contain Vinculin binding sites, however RIAM binds to the rod domains in their folded conformation, while Vinculin binding sites are buried and only become accessible upon mechanical Talin engagement. Therefore, it is thought that RIAM first binds to Talin recruiting it to the membrane and then Vinculin displaces RIAM as Talin becomes mechanically engaged at the adhesion.

Other known interactors of Talin are FAK, a tyrosine kinase that regulates adhesion dynamics (Lawson et al., 2012); T-lymphoma invasion and metastasis-inducing protein 1 (TIAM1), a Rac exchange factor (Wang et al., 2012); layilin, a hyaluronan receptor (Wegener et al., 2008); phosphatidylinositol 4-phosphate 5-kinase type I γ (PtdInsP kinase I γ) (de Pereda et al., 2005); deleted in liver cancer 1 (DLC1), a RHO GTPase-activating protein (Li et al., 2011), and synemin, an intermediate filament protein present in muscle tissues (Sun et al., 2008) (Figure 1.20). In addition,

it has recently been shown that KN motif and ankyrin repeat domain-containing protein 2 (Kank2) interacts with the Talin rod domains R7 and R8, competing with actin binding to ABS2 and thereby reducing force transmission across Talin and allowing adhesions to slide rather than being fixed in one position (Sun et al., 2016).

1.5.3 Talin function in muscle attachment sites

Talin is an essential component of muscle attachment sites and Talin depletion leads to muscle detachment and other muscle-related phenotypes both in *Drosophila* (Brown et al., 2002) and in vertebrates (Conti et al., 2008, 2009). Since Talin is a very versatile protein, it is, however, difficult to know how Talin functions exactly at muscle attachment sites. Questions arising are: which interaction partners (described in Chapter 1.5.2) do actually bind to Talin at the muscle attachment sites and if they bind, which of the many binding sites are used? This question is particularly important to answer for this thesis regarding the integrin and actin binding sites in Talin, because molecular force measurements can only be successful if it is known where to expect forces in the protein of choice. The highest forces in Talin are expected between the major integrin and actin binding sites. The region between these two binding sites should be exposed to forces generated by actomyosin that are transmitted across Talin to integrins and via the extracellular matrix to the tendon cells.

Similar to Talin in focal adhesions (see Chapter 1.4.3) (Kanchanawong et al., 2010), Talin in muscle attachment sites is thought to be bound to integrin mainly via IBS1

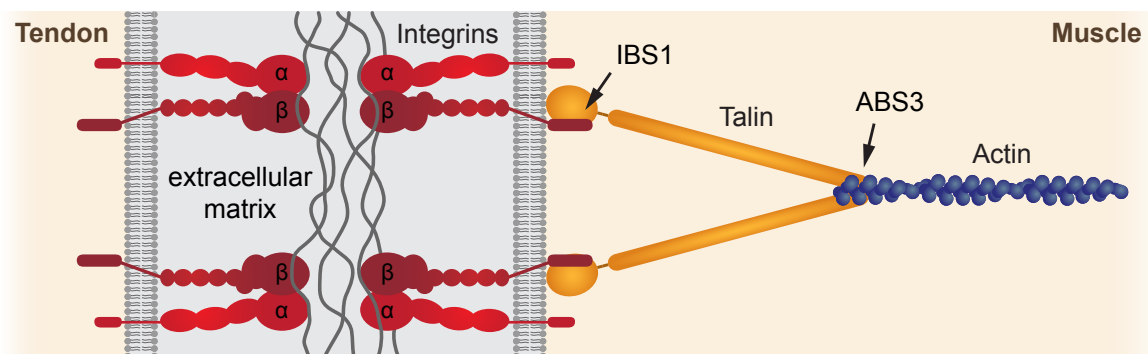


Figure 1.21: Model of Talin at muscle attachment sites. Scheme of the cell-ECM-cell contact between a tendon and a muscle cell. Talin is depicted bound to integrin via integrin binding site 1 (IBS1) and bound to actin via actin binding site 3 (ABS3), which are thought to be the major integrin and actin binding sites.

in the Talin head domain and to actin mainly via ABS3 at the end of the rod domain (Figure 1.21). IBS1 is most likely the main integrin binding site in muscle attachment sites, and not IBS2, based on the following lines of evidence: (1) Klapholz et al. (2015) tagged the integrin cytoplasmic tail endogenously with green fluorescent protein (GFP) at the C-terminus in close proximity to the Talin-binding NPXY motif. Furthermore, Talin was tagged by inserting mCherry into the Talin rod right after IBS2. When co-expressing the tagged proteins, Förster resonance energy transfer (FRET) could be observed between the two fluorophores in adhesions in the wing tissue but not at muscle attachment sites. Thus, IBS2 is in close proximity to integrin in the wing tissue but not at muscle attachment sites. (2) Super resolution microscopy confirmed that the mCherry signal from Talin IBS2 is indeed separated from the GFP-signal from the integrin cytoplasmic tail at muscle attachment sites (Klapholz et al., 2015). Therefore, IBS1 is thought to be the major integrin binding site and IBS2 likely only transiently binds integrin at muscle attachment sites and thereby might help recruit Talin to the attachment sites independently from IBS1 (Ellis et al., 2011).

The statement that ABS3 is the major actin binding site in muscle attachments is based on the following lines of evidence: (1) Franco-Cea et al. (2010) showed that point mutations in ABS3 or in the dimerization domain of the Talin rod lead to muscle shortening and detachment, demonstrating that ABS3 is essential for Talin function in muscle attachment sites. (2) Using a series of Talin truncation alleles, Klapholz et al. (2015) demonstrated that full length Talin including ABS3 is required for normal muscle attachment in *Drosophila*. If Talin is truncated just before ABS3, embryos display a serious muscle shortening phenotype, even though a connection to actin can still be made with the help of Vinculin. Whether ABS2 is present or absent does not affect the severity of the phenotype. However, if Talin is truncated such that no Vinculin binding sites are left, the muscles detach and round up completely as in *talin* null embryos. Thus, ABS3 is essential for Talin function in muscle attachment sites and its loss can neither be fully rescued by ABS2 nor by Vinculin binding to Talin rod.

1.6 Force measurements in biological systems

It has recently become more and more evident that mechanical forces play a key role for the behavior of cells in tissues during development and homeostasis. For example, stem cells can differentiate into different cell types based on the stiffness of their

environment (Engler et al., 2006). In a soft environment like the brain, the stem cells tend to differentiate into neurons; in a stiff environment like the bone, stem cells rather differentiate into osteoblasts, whereas in an environment with intermediate stiffness, the stem cells tend to differentiate into muscle cells. Furthermore, the direction of mechanical tension in a tissue can be used as a cue by a myotube to assemble myofibrils along its long axis during development (Weitkunat et al., 2014). Cells generate mechanical forces to constantly probe the mechanical properties of their environment and respond to it accordingly. Therefore, it is an important question how cells generate and sense mechanical forces.

A number of techniques have become available to study forces in biological systems (Figure 1.22). To measure the forces that cells exert on their environment, traction force microscopy measurements can be performed. To that end, cells are placed on a polydimethylsiloxane (PDMS) substrate shaped into micropillars (Figure 1.22A). Depending on the forces generated by cells adhering to the micropillars, the pillars bend more or less extremely. If the stiffness and height of the pillars are known, the absolute value of the traction force generated by the cells can be calculated from the displacements of the top ends of the micropillars and a traction force map can be generated (reviewed in Ribeiro et al., 2016). This technique is well suited to study forces generated by cultured cells, however forces in intact organisms cannot be analyzed.

To measure forces in living organisms, tissues can be probed by cutting small lesions into a tissue using a laser and then following the tissue's response by live imaging microscopy (Figure 1.22B). Cutting the tissue can be achieved by a strong UV or infrared laser that is carefully adjusted to cut the tissue cleanly without causing unnecessary damage to cells in the vicinity. If the tissue of interest is under tension, a hole will open up at the site of the cut as the tissue recoils. The higher the initial recoil velocity, the higher is the tissue tension, therefore the velocity of the tissue recoil can be quantified as a proxy for tension. In principle, it would be possible to calculate absolute values for tissue tension with this method, but it is often not feasible because it is challenging to determine the viscoelastic properties of a tissue *in vivo*. Nevertheless, laser cutting is a powerful technique to analyze tension in tissues *in vivo* (Hutson et al., 2003; Rauzi et al., 2008; Weitkunat et al., 2014) and also in subcellular structures like actin stress fibers, microtubules or keratin filament bundles (Colombelli et al., 2005, 2009; Latorre et al., 2018).

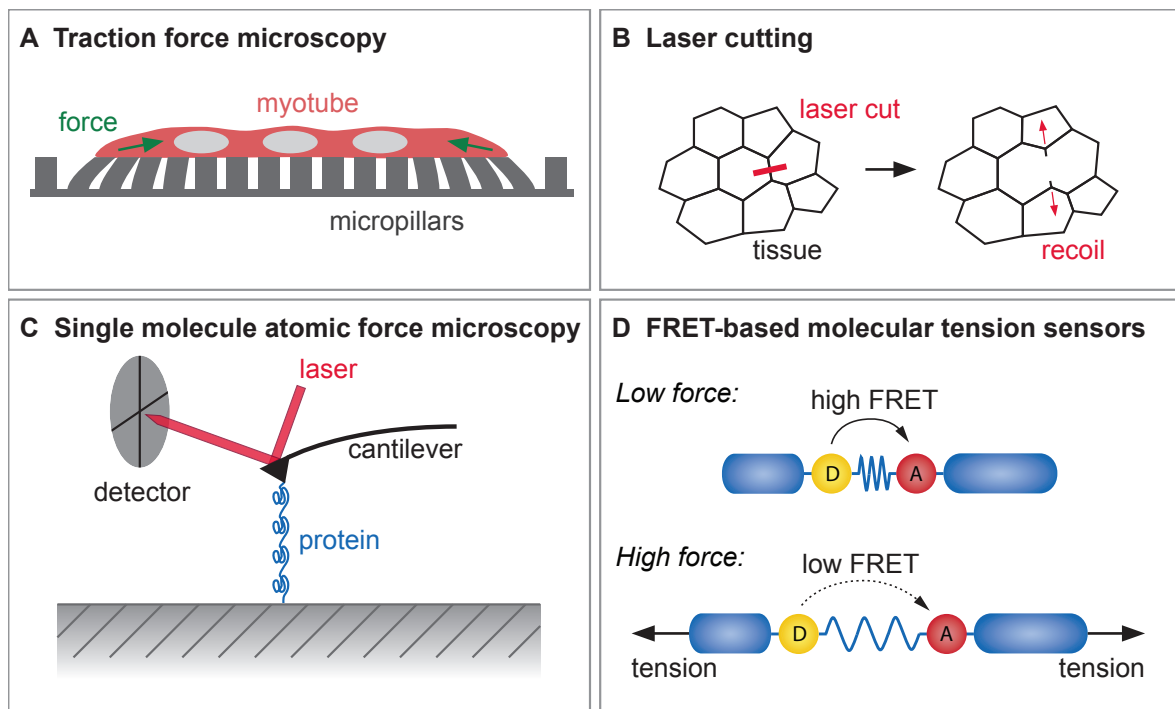


Figure 1.22: Overview of methods used to measure forces in biological systems. **A.** Traction force microscopy: Cells plated on micropillars attach to them and deflect them. The deflection can be quantified to calculate the tension generated by the cells. **B.** Laser cutting: A tissue is cut by a laser and the recoil of the tissue is quantified to measure tissue tension. **C.** Single molecule atomic force microscopy (AFM): Individual proteins are suspended between a substrate and a cantilever. As the cantilever moves away from the substrate forces on the protein increase and the cantilever bends. The degree of bending can be measured with a laser and a split photodetector to quantify the forces applied to the protein of interest. **D.** Förster resonance energy transfer (FRET)-based molecular tension sensors: A sensor module is inserted into the protein of interest that consists of a donor, a flexible spring-like linker peptide and an acceptor. In low-force conditions FRET is high and in high force conditions the sensor module opens, thus the FRET efficiency is low. Adapted from Lemke and Schnorrer (2017).

In addition to traction force microscopy or laser cutting, which can only measure cell- or tissue-level tension, other techniques are required to measure forces at the molecular level. Single-molecule AFM is well suited to study how individual protein molecules react to forces in the pN range and in particular what forces are required to unfold a protein domain of interest (reviewed in Hughes and Dougan, 2016). To that end, the protein of interest is purified and then attached to a rigid substrate with one end and to the tip of a cantilever with the other end (Figure 1.22C). Then, the distance between the cantilever and the substrate is slowly increased, thereby increasing the forces acting

on the protein, which leads to bending of the cantilever. The degree of bending of the cantilever can be measured by a laser beam reflected off the back of the cantilever onto a split photodetector. This kind of detector can precisely measure the degree of deviation of the laser from the center and from this information force-extension traces are generated. Unfolding of a protein domain leads to a characteristic drop in force as the domain extends and can thereby be identified in the force-extension traces. Thus, single-molecule AFM is well suited to study mechanosensitive proteins that change their conformation upon application of force (Mykuliak et al., 2018).

To study forces on proteins in their natural environment inside living organisms, however, different methods are required. In the last decade, FRET-based molecular tension sensors have been developed that can be genetically encoded and thereby expressed directly in cultured cells and even in intact organisms (Figure 1.22D). The application of such a sensor to measure molecular forces *in vivo* was the main aim of this thesis, therefore, FRET-based molecular tension sensors will be described in detail in the next chapter.

1.6.1 FRET-based molecular tension sensors

A range of FRET-based molecular tension sensor modules have been developed in recent years to analyze the forces proteins are exposed to and respond to in biological systems. These tension sensor modules consist of a donor and an acceptor fluorophore that are connected by a short mechanosensitive linker (Figure 1.23A). In the absence of tension, the fluorophores are close together and therefore the FRET efficiency between the fluorophores is high. When tension is transmitted across the sensor module, the mechanosensitive linker unfolds and extends, and thus the FRET efficiency decreases (Grashoff et al., 2010). The linker has to be chosen such that it can reversibly extend under force and refold upon force release. This can, for example, be achieved by a DNA hairpin; however, a sensor with DNA can only be assembled *in vitro* and cannot be genetically encoded. Therefore, these sensors can only be used to measure forces outside cells. Usually, these DNA-based sensors are connected to a ligand of choice, for example an RGD peptide, and are coated on the cell culture substrate. Then, forces transmitted by a receptor, for example integrin, can be measured *in vitro* (Zhang et al., 2014b).

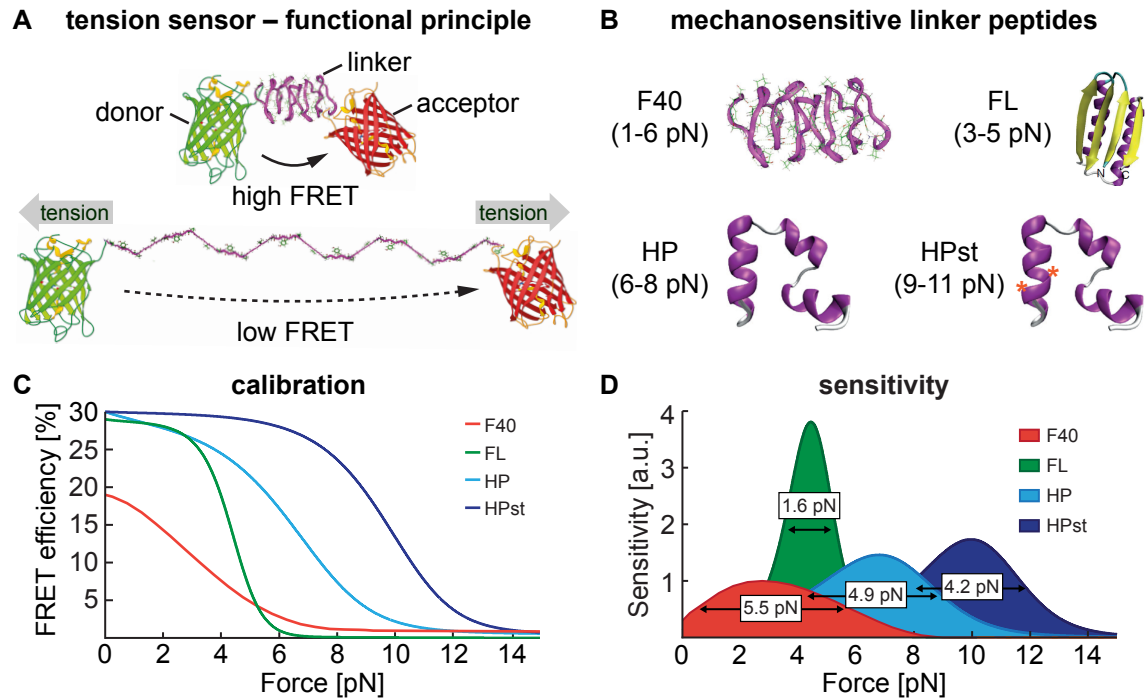


Figure 1.23: Genetically-encoded FRET-based tension sensors. **A.** Functional principle of FRET-based molecular tension sensor modules: In the absence of force a donor and an acceptor fluorophore connected by a mechanosensitive linker are in close proximity and therefore undergo high FRET. Under tension, the linker extends and the tension can be detected as a reduction in FRET efficiency. The extension of the spider silk derived flagelliform linker peptide is shown as an example. **B.** Structural models of four mechanosensitive linker peptides as examples: flagelliform (F40), ferredoxin-like (FL), villin headpiece (HP), and stabilized villin headpiece (HPst) peptide. Force ranges leading to unfolding are indicated. **C.** FRET-force calibration curves of tension sensor modules with the linker peptides shown in B are displayed. Note the differences in starting FRET efficiency, the relative shift of the transitions and the differing sharpness of the transitions. **D.** Sensitivity of the sensor modules as determined by single-molecule calibration. Structural models in A and B were compiled with permission from Becker et al. (2003); Freddolino et al. (2010); Fang et al. (2013) and graphs in C and D were adapted with permission from Ringer et al. (2017).

To visualize molecular forces inside living cells or entire organisms, the entire sensor module including the mechanosensitive linker needs to be genetically encodable, such that it can be inserted into any protein of interest by molecular biology techniques and by genome engineering (see Chapter 1.7). Therefore, peptides that unfold in a defined force regime have been used in the field as mechanosensitive linkers (Figure 1.23B). One example is the 40 amino acid (aa)-long flagelliform (F40) peptide derived from spider silk (Becker et al., 2003). Its fold resembles a molecular spring that gradually extends

at forces of 1-6 pN (Figure 1.23C). Therefore, sensor modules with the F40 peptide can be used to detect very low forces in the pN range, but the transition from closed to open is not very sharp and the starting FRET efficiency of the closed sensor is only moderately high (Figure 1.23C and D) (Grashoff et al., 2010). In contrast, the 82 aa-long ferredoxin-like (FL) peptide consisting of a compact fold of two α -helices and four β -strands displays a very sharp transition from closed to open at 3-5 pN (Fang et al., 2013). Therefore, it is well suited for measuring forces in the low pN range with a high sensitivity (Ringer et al., 2017). Another mechanosensitive linker peptide is the 35 aa-long villin headpiece (HP) peptide that consists of three α -helices (Freddolino et al., 2010). Its fold is slightly more resistant to force and therefore only opens up at 6-8 pN (Austen et al., 2015). With two point mutations, the fold becomes even more stabilized so that it only opens up at 9-11 pN. The stabilized villin headpiece (HPst) peptide sensor is currently the genetically encodable sensor with the highest force range. The sensor modules with the HP or the HPst peptide display a high starting FRET efficiency of about 30%, thus they have a high dynamic range similar to the FL sensor module.

The four mechanosensitive linker peptide sensors introduced here are particularly valuable if used in combination. For example, if the HP sensor opens but the HPst sensor does not, one can conclude that the sensors are exposed to forces between 7 and 10 pN, whereas an individual sensor can just indicate whether forces are higher than the respective force threshold required for opening this particular sensor or not.

Apart from the choice of the mechanosensitive linker, it is also important to use an efficient pair of fluorophores as donor and acceptor in the sensor module. Most importantly, the emission spectrum of the donor needs to overlap with the absorption spectrum of the acceptor to allow a high FRET efficiency (see Chapter 1.6.2). Furthermore, the fluorophores need to be bright and photostable to achieve bright images and to avoid photobleaching. Commonly used FRET pairs are cyan fluorescent protein (CFP)/yellow fluorescent protein (YFP) and GFP/mCherry. In this thesis, the FRET pair yellow fluorescent protein for energy transfer (YPet)/mCherry was used, because this pair was shown to have a high FRET efficiency when connected with the HP peptide (Austen et al., 2015), and YPet is well suited for fluorescence lifetime imaging microscopy (FLIM), a method with which FRET can be determined very precisely (see Chapter 1.6.3).

1.6.2 Förster resonance energy transfer (FRET)

FRET is an electrodynamic process that allows energy to transfer from one fluorophore (the donor) to another (the acceptor) in a radiation-free manner (Figure 1.24A). For FRET to occur, the donor needs to be excited by absorbing a photon and the acceptor needs to be in its ground state. Then, the energy can be transferred from the donor to the acceptor without the appearance of a photon by a dipole-dipole interaction. Finally, the acceptor emits a photon that is red-shifted compared to the photon absorbed by the donor.

The rate of the energy transfer depends on the spectral overlap between the emission spectrum of the donor and the absorption spectrum of the acceptor (Figure 1.24B), the emission efficiency of the donor known as quantum yield, the orientation of the fluorophores towards each other and, most importantly, the distance between the fluorophores (Lakowicz, 2006).

FRET can occur at distances in the range of about 1-10 nm, but the efficiency of the transfer strongly depends on the distance between the donor and the acceptor.

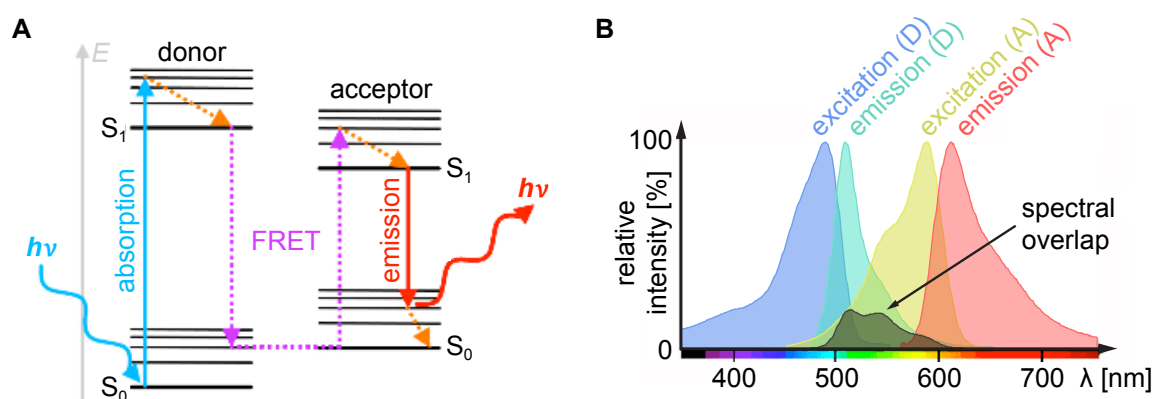


Figure 1.24: Basic principles of FRET. **A.** Jablonski diagram illustrating the process of FRET. A photon ($h\nu$) is first absorbed by the donor fluorophore and thereby an electron is raised from the ground state S_0 to the excited state S_1 (blue arrow). After radiation-free vibrational relaxation (orange dotted arrow) to the ground level of the excited state the energy is transferred from the donor to the acceptor fluorophore via FRET (purple dotted arrows). When the electron in the excited state of the acceptor relaxes back to the ground state, a red-shifted photon is emitted (red arrow). **B.** Excitation and emission spectra of a donor (D) and acceptor (A) pair. The spectral overlap that allows FRET is shown as the product of the donor emission and the acceptor excitation. The spectra used as an example are from the FRET pair GFP/mCherry. Jablonski diagram adapted with permission from Hochreiter et al. (2015) and GFP/mCherry spectra plotted with data from <https://www.chroma.com/spectra-viewer>.

Equation 1.1 shows the dependency of the FRET efficiency E on the distance between the donor and the acceptor r and the Förster distance R_0 . The Förster distance is the distance at which the fluorophores have a FRET efficiency of 50%, which is specific for each FRET pair.

$$E = \frac{R_0^6}{R_0^6 + r^6} \quad (1.1)$$

Equation 1.2 shows the dependency of the Förster distance on the spectral overlap of the fluorophore pair J , the quantum yield of the donor Q_D in absence of an acceptor and the refractive index of the medium n . The Förster distance also depends on the orientation of the fluorophores towards each other described by the factor κ^2 . Usually, $\kappa^2 = 2/3$ is assumed, which is valid for random averaging of relative orientations.

$$R_0^6 \propto \frac{\kappa^2 Q_D J}{n^4} \quad (1.2)$$

Since the FRET efficiency is inversely proportional to r^6 (Equation 1.1), a change in FRET efficiency is a very sensitive readout for changes in distance. Most fluorescent protein FRET pairs have R_0 values in the range of 4-6 nm, so distances in the range of about 2-9 nm can be measured by FRET (Hochreiter et al., 2015). These distances are very similar to the size of proteins, for example the Talin head is about 4 nm \times 10 nm in size (Goult et al., 2010c). Therefore, FRET is very well suited to measure distances within proteins and between proteins. In FRET-based tension sensors, the sensitive readout of distance by FRET is used to draw conclusions on the forces acting on the sensor based on a calibration measurement (see Figure 1.23). Similarly, FRET can be used to detect protein cleavage or conformational changes for example upon binding of a metabolite or another protein. In conclusion, FRET-based techniques are a very versatile and powerful tools to address a broad range of biological questions.

1.6.3 Fluorescence lifetime imaging microscopy (FLIM)

FLIM is a method suitable to determine FRET accurately experimentally. The fluorescence lifetime is defined as the time that it takes after excitation of fluorophores until 50% of the excited molecules have relaxed back to the ground state. In the absence of FRET, the relaxation happens predominantly by emitting a photon, i.e. through

fluorescence. If FRET occurs, the excited state of the donor fluorophore can relax back to ground state either by fluorescing itself or by transferring the energy to an acceptor fluorophore by FRET (Lakowicz, 2006). The higher the rate of FRET $k_T(r)$, the faster the donor fluorophore returns to the ground state and therefore, the fluorescence lifetime of a donor in presence of an acceptor τ_{DA} becomes shorter than the lifetime of the donor alone τ_D according to Equation 1.3.

$$\tau_{DA} = \frac{1}{\tau_D^{-1} + k_T(r)} \quad (1.3)$$

This effect can be used to determine the FRET efficiency according to Equation 1.4 by measuring the lifetimes τ_D and τ_{DA} .

$$E = 1 - \frac{\tau_{DA}}{\tau_D} \quad (1.4)$$

To determine the fluorescence lifetime of a fluorophore by FLIM, the sample is excited with a pulsed laser with pulse widths in the ps time range. Using a time-correlated single-photon counting (TCSPC) detector the arrival times of individual emitted photons after each laser pulse can be detected and—after collecting many individual photons—a histogram of the arrival times, i.e. a fluorescence decay curve, can be generated. If the excited state of the fluorophore decays following a single exponential, as it is the case for YPet, the fluorescence decay curve can be fit with a mono-exponential decay to determine the lifetime. The TCSPC detector used in this thesis has a 0.08 ns time resolution to detect photons between laser pulses every 12.5 ns (80 MHz repetition rate).

An alternative method to determine FRET is to measure the intensity in the acceptor channel upon excitation of the donor and compare it to the intensity in the donor channel. This method is known as ratiometric FRET. The advantage of this method is that measurements are very fast. However, apart from data acquisition being slower, FLIM has several advantages compared to ratiometric FRET: Bleed-through of donor emission into the acceptor channel is not an issue, because only the donor channel needs to be recorded for FLIM. Furthermore, FLIM is independent of fluorescence intensity and therefore, variations in laser power or sample brightness (within the imaged area or between experiment days) do not affect the FLIM measurement. Thus, FLIM is a highly reproducible method to determine FRET efficiencies in biological samples and was therefore applied in this thesis to determine the FRET efficiency of a

genetically-encoded Talin tension sensor at developing *Drosophila* muscle attachment sites.

1.6.4 Talin force measurements *in vitro*

When this project was started, FRET-based tension sensors had not been applied to measure forces *in vivo* in an intact organism. Studies at the time were mainly focusing on establishing FRET-based tension sensor techniques *in vitro* in cultured cells and on studying the mechanobiology of adhesion structures like focal adhesions or cadherin-based cell-cell contacts in this model system (Grashoff et al., 2010; Borghi et al., 2012; Conway et al., 2013; Morimatsu et al., 2013; Austen et al., 2015).

Grashoff et al. (2010) had developed a Vinculin tension sensor to analyze the forces transmitted by Vinculin in focal adhesions. To this end, a sensor module consisting of monomeric teal fluorescent protein 1 (mTFP1), the F40 linker peptide and Venus was inserted into Vinculin between its Talin-binding head domain and its actin-binding tail domain. The sensor module was calibrated by single-molecule fluorescence force spectroscopy using optical tweezers and it was determined that this sensor module is sensitive to 1-6 pN. Using this calibration, it was concluded that Vinculin is exposed to about 2.5 pN force on average in stable focal adhesions. This value, however, has to be considered as a lower border for estimating the average forces per Vinculin molecule, because individual molecules could experience forces higher than 6 pN that cannot be detected by this sensor. Furthermore, Grashoff et al. (2010) showed that Vinculin forces depend on the state of the focal adhesions: Vinculin experiences highest average forces early during focal adhesion assembly and lower forces during focal adhesion disassembly.

The Grashoff group applied the same method to measure forces transmitted by Talin in focal adhesions (Austen et al., 2015; Ringer et al., 2017). During the course of this project three new tension sensor modules were developed based on the HP peptide (6-8 pN), the HPst peptide (9-11 pN), and the FL peptide (3-5 pN) (see Chapter 1.23) and the fluorophores mTFP1/Venus were replaced by YPet/mCherry. Simultaneously, an alternative Talin FRET-sensor was developed by Kumar et al. (2016).

With these new tools in hand, the Grashoff group showed that Talin molecules experience forces of 7-10 pN and a proportion of the molecules even forces higher than 10 pN in focal adhesions (Austen et al., 2015). Depletion of Vinculin in these cells leads to a reduction in average force on Talin, showing that Vinculin adds more force to

Talin, likely through binding to the Talin rod and linking more actin filaments to Talin. However, also in the absence of Vinculin, Talin still transmits force by binding to actin directly. Furthermore, it was shown that mechanical engagement of the Talin rod is required to strengthen and grow focal adhesions, allowing cells to spread depending on the degree of the substrate rigidity. Through this mechanism, Talin contributes to extracellular rigidity sensing and allows cells to respond to changes in the rigidity of their environment.

More recently, it was shown that forces in the Talin rod are not distributed equally but rather form a gradient along the rod (Ringer et al., 2017). This was demonstrated by comparing different tension sensor modules inserted into two different positions within the Talin protein: (1) between Talin head and rod, and (2) in the Talin rod between ABS2 and ABS3. The HP sensor module (sensitive to 6-8 pN) inserted into the first position indicated forces above 7 pN but could not detect any force in the second position. In contrast, the FL sensor module (sensitive to 3-5 pN) reported forces also in the second position. In conclusion, the Talin rod experiences forces higher than 7 pN at its N-terminal end and lower forces between 4-7 pN more towards the C-terminus between ABS2 and ABS3. Forces in these two positions could even be measured simultaneously in one sample by applying a multiplexing approach based on dual-color FLIM.

1.7 CRISPR/Cas9-mediated genome engineering

To enable force measurements across Talin *in vivo* in *Drosophila*, tension sensor modules were inserted into the endogenous *talin* (*rhea*) gene by CRISPR/Cas9-mediated genome engineering during the course of this thesis. The CRISPR/Cas9-system is a powerful method to modify the genome of living organisms. It is based on a defense system used by bacteria to cut intruding viral DNA in pieces, and has been engineered to achieve efficient genome editing (Jinek et al., 2012; Cong et al., 2013).

The major feature of the CRISPR/Cas9-system is that it creates double strand breaks in genomic DNA in a targeted manner. This can be achieved by only two components: the nuclease Cas9 and a sgRNA (Figure 1.25A). The sgRNA binds to Cas9 and provides sequence specificity with a 20 nucleotide stretch that needs to match the target DNA in order for Cas9 to cut. The double strand break is then repaired by the target cell's DNA repair machinery using either the non-homologous end joining (NHEJ) pathway

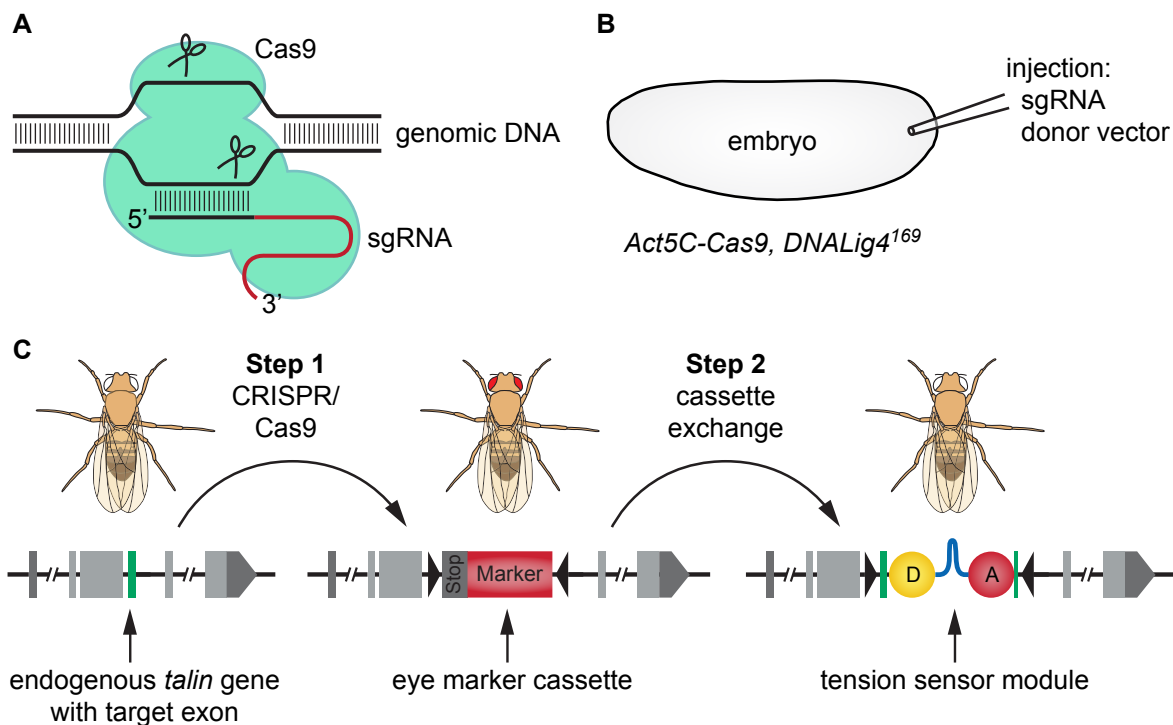


Figure 1.25: CRISPR/Cas9-mediated genome engineering. **A.** Scheme of the Cas9 nuclease bound to genomic DNA. It is targeted to a specific DNA sequence with the help of a single guide RNA (sgRNA) that forms a 20 nucleotide-long DNA-RNA hybrid with the target DNA sequence. Upon successful base pairing, Cas9 cleaves the DNA, creating a double strand break. **B.** Setup of a *Drosophila* CRISPR/Cas9-mediated genome engineering experiment. Embryos ubiquitously expressing Cas9 under the Act5C-promotor and carrying the DNA ligase 4 null allele *DNALig4¹⁶⁹* are injected with sgRNA and a donor vector containing the desired modified DNA sequence to be inserted into the genome. Injections are performed close to the posterior pole of the embryo where the germline develops to favor targeting of the germline. **C.** Schematic representation of a two-step genome engineering strategy using the insertion of a tension sensor module into the *talin* (*rhea*) locus as an example. See text for details.

or the homology directed repair (HDR) pathway (Sander and Joung, 2014). The NHEJ pathway repairs the double strand break without the requirement of a template. Instead short homologous sequences at the loose ends are used to anneal and religate them. However, this process is error-prone and often leads to small deletions or insertions, so-called indels. This property of the NHEJ pathway can be exploited to create mutants of a gene of interest by causing a frameshift.

If larger modifications are desired, the HDR pathway can be exploited. This pathway repairs a double strand break by using a template, which is usually the homologous

chromosome, and thereby achieves error-free repair. However, if a modified template is provided, it can be used by the HDR repair pathway instead of the homologous chromosome. The modified template can, for example, be provided in the form of a plasmid containing a modified DNA sequence surrounded by sufficient homologous DNA. The modification can be as small as a single point mutation or large stretches of DNA can be deleted or inserted, for example the sequence of a fluorescent protein to tag the protein of interest at the endogenous locus.

To facilitate the delivery of the components of the CRISPR/Cas9-system in *Drosophila*, a fly line that expresses Cas9 ubiquitously under the Act5C-promoter has been created (Figure 1.25B) (Port et al., 2014). Additionally, DNALig4, a DNA ligase important for NHEJ, was mutated in these flies to favor HDR over NHEJ repair (Beumer et al., 2013; Carroll and Beumer, 2014; Zhang et al., 2014a). Components that need to be designed and prepared specifically for each gene targeting experiment, i.e. the sgRNA and the template containing donor vector, can then be injected into these Cas9-expressing, *DNALig4*¹⁶⁹ mutant embryos (Figure 1.25B).

A major bottleneck in CRISPR/Cas9-mediated genome engineering is the identification of successful targeting events. If there is no visual effect that can be scored, successful targeting events have to be identified by polymerase chain reaction (PCR) screening. Especially if the targeting efficiency is rather low, it can require hundreds of PCRs to identify a single successful event. Therefore, a two-step strategy was developed in the Schnorrer group that allows the use of visual markers to screen the flies (Zhang et al., 2014a) (Figure 1.25C). In the first step, the CRISPR/Cas9-system is used to introduce a marker cassette into the gene of interest. This cassette contains a fluorescent-red eye marker that can be used to identify successfully targeted flies simply by visual inspection under a fluorescent binocular microscope. Furthermore, the cassette contains a splice acceptor followed by a stop codon to truncate the expressed messenger RNA (mRNA), thereby creating a loss of function allele. In addition, the cassette is flanked by attP sites. In the second step, these attP sites are used to easily replace the marker cassette by ϕ C31-mediated cassette exchange with any desired DNA sequence that has been flanked by attB sites. In conclusion, this two-step genome engineering strategy is a very versatile and efficient method to achieve targeted modifications of the genome in *Drosophila*.

In this thesis, this strategy was used to introduce different tension sensor modules and control constructs into the endogenous *talin* gene at two positions: at the linker region

between Talin head and rod, and at the C-terminus for controls (Figure 1.25C). Each position had to be targeted only once by the CRISPR/Cas9-system and then several different sensor modules and control constructs could each be introduced simply by performing step two repeatedly. In conclusion, the CRISPR/Cas9-system allows precise modifications of the genome, tailored specifically to address the respective biological question of interest, which was a key factor for the success of this thesis.

2 Aim of thesis

At the start of this thesis, a Förster resonance energy transfer (FRET)-based Talin tension sensor had just been developed to measure forces transmitted by Talin in focal adhesions *in vitro* in the Grashoff group. In parallel, it was discovered in the Schnorrer group that tension built up in the muscle-tension tissue in *Drosophila* is required for ordered sarcomerogenesis. Therefore, we decided to apply the tension sensor technique to measure forces transmitted across Talin *in vivo* at muscle attachment sites in *Drosophila*.

The **first aim** of this thesis was to introduce tension sensor modules into the *talin* gene in the *Drosophila* genome using the CRISPR/Cas9 system and then verify whether the Talin protein is still functional with the inserted tension sensor module. The **second aim** was to establish *Drosophila* Talin tension sensor measurements *in vivo* using fluorescence lifetime imaging microscopy (FLIM) to measure the FRET efficiency of the sensor in living whole mount pupae. The **third aim** was to apply the tension sensors to quantify forces transmitted by Talin during muscle development *in vivo*.

The results of this work were published in **Paper I**. Additionally, using the fly stocks generated initially as controls for tension sensor measurements, spontaneous contractions of developing flight muscles were discovered, characterized and published in **Paper IV**. Furthermore, a review about forces during muscle development was written (**Paper II**) and a video article explaining how to perform live imaging in *Drosophila* pupae was published (**Paper III**).

3 Summary of publications

3.1 Paper I – A small proportion of Talin molecules transmit forces at developing muscle attachments *in vivo*

Lemke, S. B., Weidemann, T., Cost, A.-L., Grashoff, C. and Schnorrer, F.

Cells in an organism need to be able to sense and react to mechanical forces, which shape tissues during morphogenesis and control cell fate decisions. In previous studies, forces acting on proteins in cells had been studied by introducing Förster resonance energy transfer (FRET)-based molecular tension sensor modules into the protein. At the start of this project, such a sensor had just been created for Talin, an essential adhesion protein (Austen et al., 2015). However, this Talin tension sensor had only been applied to measure forces in mammalian fibroblasts cultured *in vitro* and thus in an artificial mechanical environment.

In this paper, we reported the introduction of FRET-based tension sensor modules into Talin in *Drosophila* to be able to characterize the forces transmitted by Talin molecules in their natural environment in the living organism for the first time. As a model system, we chose the developing flight muscle-tendon system, because it had already been shown that tension is built up in this tissue and that this tension is essential for myofibrillogenesis. First, we demonstrated that the flies with a tension sensor module inserted into the essential protein Talin are viable. The Talin tension sensor localizes normally to muscle attachments, the flies have a normal sarcomere morphology, can fly and the dynamics of the Talin tension sensor protein remain unaffected by the insertion of the sensor module as demonstrated by fluorescence recovery after photobleaching (FRAP). Thus, the Talin tension sensor protein is fully functional.

As a proof of concept, we quantified forces across Talin by measuring FRET by fluorescence lifetime imaging microscopy (FLIM) in primary muscle fibers that were differentiated *in vitro*. We found that our *Drosophila* Talin tension sensor reports forces in adhesions at the tips of these fibers similar to the previously developed Talin tension sensor in focal adhesions of mammalian fibroblasts *in vitro*.

We then aimed to quantify forces transmitted by Talin *in vivo*, focusing particularly on flight muscle development between 18 h and 30 h after puparium formation (APF), because during this phase, the developing muscles gradually compact and the tendon epithelium forms long, straight, cellular extensions. Concomitantly, the muscle attachments mature. It had been shown previously that tissue tension is built up from 13 h to 22 h APF (Weitkunat et al., 2014). By performing laser cutting experiments at 20 h and 30 h APF both in the tendon tissue and in the muscle tissue in living whole-mount pupae, we showed that the tissue tension remains high until 30 h APF.

After having established that tension is built up in the muscle-tendon tissue, we performed Talin tension sensor measurements in a time course from 18 h to 30 h APF. We found that a surprisingly small proportion of Talin molecules (<15%) at muscle attachments experience detectable forces and that the proportion even decreases from 20 h to 30 h APF.

To estimate whether the total Talin-mediated tissue stress is still significant despite the small proportion of mechanically engaged molecules, we quantified the absolute amount of Talin present at developing muscle attachment sites by fluorescence correlation spectroscopy (FCS) *in vivo*. We found that the local Talin concentration increases about 5-fold from 20 h to 30 h APF, thus Talin could contribute significantly to tissue stress by its strong recruitment to the developing muscle attachments.

Intrigued by the large pool of Talin molecules at developing muscle attachments of which only a small proportion transmit force, we investigated the physiological relevance of the high Talin accumulation during development. If Talin levels are reduced towards the end of the pupal development by RNA interference (RNAi), the muscle attachments rupture in young adults, likely during their first flight attempts. Thus, an accumulation of high Talin levels during development is required for building stable muscle attachments that withstand the forces generated by muscle contractions in the adults. In conclusion, we discovered a new mechanical adaptation concept that allows animals to build stable adhesions that can dynamically adapt to high tissue forces such that they last for a lifetime.

3.2 Paper II – Mechanical forces during muscle development

Lemke, S. B. and Schnorrer, F.

As part of a special issue on the roles of physical forces in development, we reviewed the literature on the role of forces during muscle development in general and myofibril formation in particular, and proposed a tension-driven self-organization model for myofibrillogenesis. Furthermore, we discussed possible force bearing proteins in muscles and summarized techniques that allow quantification of forces at the cell and tissue level, and at the molecular level.

The developmental problem that muscles need to solve is to assemble sarcomeres, the contractile units of muscles, into myofibrils that have exactly the right length to span the muscle from one end to the other. Only if this is achieved during development, contraction of the sarcomeres, leading to shortening of the myofibrils, will in turn lead to shortening of the muscle to create a productive movement. The building blocks, the sarcomeres, are very short (about 3 μm) compared to the length of the structure that they need to build, the myofibrils (for example, about 1 mm in *Drosophila* flight muscles or even longer in vertebrates). Since the muscle cannot simply measure its length, it is an intriguing question how development solves this 'dimension problem' of myofibril formation.

We proposed a tension-driven self-organization mechanism, which achieves simultaneous assembly of all myofibrils in a muscle using tissue tension as a cue both for length and orientation of the forming myofibrils. We integrated the idea of tension as cue with concepts from previously proposed myofibrillogenesis models.

To use tension as a cue, muscle cells need to be able to sense tension and therefore it is an important question which proteins are exposed to mechanical forces that could act as mechanosensors. In this context, we discussed the recent literature on integrins and on titin. Integrins are cell surface receptors that bind to the extracellular matrix (ECM) and are connected indirectly to the intracellular actin cytoskeleton or more specifically, to myofibrils in muscle cells. Titin is a so-called connecting filament that stably connects components of the sarcomere and is thought to bear passive tension in myofibrils. At the time of writing the review, direct evidence for tension on these two proteins in

muscles *in vivo* was lacking, but we summarized the evidence in the literature that strongly suggested that integrins and titin bear force *in vivo*.

Finally, we introduced techniques that can be used to measure tension in biological systems experimentally. For measuring forces generated by cells or cell sheets *in vitro*, traction force microscopy is a powerful tool. Measuring tension in a tissue *in vivo* in a living organism, however, requires different techniques: for example, cutting the tissue with a laser and following the tissue recoil by live imaging. Measuring forces at the molecular level requires yet another set of tools: it can be achieved by single molecule atomic force microscopy (AFM) for purified proteins *in vitro* or by introducing genetically-encoded Förster resonance energy transfer (FRET)-based tension sensors into proteins in cells in culture or even in intact organisms.

In conclusion, the development of the muscle-tendon tissue is strongly dependent on mechanical forces and we are only starting to appreciate the importance of mechanotransduction in biology. Hopefully, in the future, the development of more tools to visualize and to manipulate forces *in vivo*, will help to unravel the mechanisms that are used during the development of organs, like muscles, to sense and respond to mechanical forces.

3.3 Paper III – *In Vivo* Imaging of Muscle-Tendon Morphogenesis in *Drosophila* Pupae

Lemke, S. B. and Schnorrer, F.

The development of a musculature is essential for animals to allow them to move around, breath or keep their heart beating for a lifetime. Since most components of the sarcomere, the contractile units of the muscle, and developmental concepts are conserved from invertebrates to humans, *Drosophila* can be used as a powerful model system to gain insights into muscle-tendon morphogenesis.

In this article, we provided a detailed protocol and showed in a video how to perform *in vivo* imaging in *Drosophila* pupae, focusing on the musculature of the adult that develops during the pupal stage. Briefly, prepupae (very young pupae that are 0-1 h old) are collected and aged to the desired time point. The pupae are then prepared for live imaging by cutting a small window into the pupal case above the structure of interest, for example above the developing flight muscles in the thorax. After mounting the pupae on a custom-made slide with a groove to accommodate the pupae and covering the windows in their pupal cases with 50% glycerol and a coverslip, the pupae can be imaged for hours or even days on a fluorescence microscope.

We compiled an extensive list of fluorescently tagged protein markers that can be used to for studying muscle-tendon morphogenesis *in vivo*, including markers overexpressed by the GAL4-UAS-system and endogenously tagged markers. Furthermore, we provided example movies to showcase what can be achieved by *in vivo* imaging in *Drosophila*. We showed examples of long-term movies following muscle-tendon morphogenesis over many hours of development and short movies optimized to capture muscle contractions occurring during muscle development with sub-second time resolution.

In conclusion, the presented protocol will facilitate extensive *in vivo* studies of the developing muscle-tendon system and—with small modifications—also other tissues in living whole-mount pupae. With more and more endogenously tagged proteins becoming available, live imaging according to the presented protocol will be a powerful tool to investigate the dynamics of many proteins in their physiological environment.

3.4 Paper IV – A transcriptomics resource reveals a transcriptional transition during ordered sarcomere morphogenesis in flight muscle

Spletter, M. L., Barz, C., Yeroslaviz, A., Zhang, X., Lemke, S. B., Bonnard, A., Brunner, E., Cardone, G., Basler, K., Habermann, B. H., Schnorrer, F.

To build muscles during development the expression of the respective components of the sarcomeres (the contractile units of muscles) has to be carefully timed. To study how the expression of proteins is timed to built sarcomeres and assemble them into myofibrils (long chains of sarcomeres spanning the muscle), mRNA sequencing was performed in a time course during *Drosophila* flight muscle development, generating a valuable transcriptomics resource published with this paper.

Clustering of expression profiles revealed different phases of expression during muscle development and a particularly strong transition in expression was observed after 30 hours after puparium formation (h APF). To correlate these expression profiles with different stages of muscle development, a detailed analysis of flight muscle myofibrillogenesis, including the quantification of sarcomere length, number of sarcomeres per myofibril and the number of myofibrils per myofiber, was carried out. It revealed that myofibrils are assembled in three consecutive phases: In the first phase, short immature sarcomeres are assembled into immature myofibrils. Strikingly, all the about 2000 myofibrils that make up the adult muscle are already laid out at 30 h APF. In the second phase, new sarcomeres are added to increase the length of each of the myofibrils with the increasing length of the muscle fibers. Nearly all sarcomeres are added by 48 h APF in an immature form. During the third and final phase from 48 h APF to 90 h APF, the sarcomeres mature and grow both in length and diameter to reach their final size. The strong transition in expression profiles after 30 h APF correlates well with the shift from assembling immature myofibrils to adding sarcomeres and strong growth and thus likely reflects the need for a strong upregulation of the expression of sarcomeric components.

My contribution to the paper was the discovery and characterization of spontaneous twitching during flight muscle development. From 30 h APF to 48 h APF, an increasing frequency of spontaneous muscle twitching events can be observed, demonstrating that

the immature myofibrils are already contractile at this developmental stage. After 48 h APF, the twitch events become less frequent until none could be observed anymore at 72 h APF, likely because the myofibrils acquire a regulatory stretch-activation mechanism at this stage. Therefore, they stop contracting spontaneously in the absence stretch, which induces contraction in adult flight muscles allowing a high wingbeat frequency during flight.

Furthermore, I used the twitching behavior of the developing flight muscles as a functional readout for an RNA interference (RNAi) condition. When knocking down *Salm*, a transcription factor that controls the expression of a large set of sarcomeric components, the flight muscles still twitch at 48 h APF, albeit with a lower frequency. At 72 h APF, however, they fail to stop twitching and instead show uncoordinated contractions, indicating that myofibril maturation is disrupted and that the stretch-activation mechanism is likely not acquired in this condition.

In conclusion, analyzing the spontaneous twitching behavior of developing flight muscles as a functional readout of myofibrillogenesis nicely complemented the detailed analysis of the transcriptome and accurate quantification of the sarcomere morphology presented in this paper. In the future, the functional consequences of more RNAi conditions or mutants could be analyzed with the same strategy.

Bibliography

- Atherton, P., Stutchbury, B., Wang, D.-Y., Jethwa, D., Tsang, R., Meiler-Rodriguez, E., Wang, P., Bate, N., Zent, R., Barsukov, I. L., Goult, B. T., Critchley, D. R., and Ballestrem, C. (2015). Vinculin controls talin engagement with the actomyosin machinery. *Nature Communications*, 6(1):10038.
- Austen, K., Ringer, P., Mehlich, A., Chrostek-Grashoff, A., Kluger, C., Klingner, C., Sabass, B., Zent, R., Rief, M., and Grashoff, C. (2015). Extracellular rigidity sensing by talin isoform-specific mechanical linkages. *Nature Cell Biology*, 17(12):1597–1606.
- Bai, J., Hartwig, J. H., and Perrimon, N. (2007). SALS, a WH2-Domain-Containing Protein, Promotes Sarcomeric Actin Filament Elongation from Pointed Ends during *Drosophila* Muscle Growth. *Developmental Cell*, 13(6):828–842.
- Barczyk, M., Bolstad, A. I., and Gullberg, D. (2013). Role of integrins in the periodontal ligament: organizers and facilitators. *Periodontology 2000*, 63(1):29–47.
- Barnes, J. M., Przybyla, L., and Weaver, V. M. (2017). Tissue mechanics regulate brain development, homeostasis and disease. *Journal of Cell Science*, 130(1):71–82.
- Becker, N., Oroudjev, E., Mutz, S., Cleveland, J. P., Hansma, P. K., Hayashi, C. Y., Makarov, D. E., and Hansma, H. G. (2003). Molecular nanosprings in spider capture-silk threads. *Nature Materials*, 2(4):278–283.
- Beumer, K. J., Trautman, J. K., Mukherjee, K., and Carroll, D. (2013). Donor DNA Utilization during Gene Targeting with Zinc-finger Nucleases. *G3-Genes, Genomes, Genetics*.
- Biga, L. M., Dawson, S., Harwell, A., Hopkins, R., Kaufmann, J., LeMaster, M., Matern, P., Morrison-Graham, K., Quick, D., Runyeon, J., and Whittier, L. (2018). *Anatomy & Physiology*. Pressbooks.
- Bökel, C. and Brown, N. H. (2002). Integrins in development: moving on, responding to, and sticking to the extracellular matrix. *Developmental Cell*, 3(3):311–321.

- Borghgi, N., Sorokina, M., Shcherbakova, O. G., Weis, W. I., Pruitt, B. L., Nelson, W. J., and Dunn, A. R. (2012). E-cadherin is under constitutive actomyosin-generated tension that is increased at cell-cell contacts upon externally applied stretch. *Proceedings of the National Academy of Sciences*, 109(31):12568–12573.
- Brabant, M. C. and Brower, D. L. (1993). PS2 Integrin Requirements in Drosophila Embryo and Wing Morphogenesis. *Developmental Biology*, 157(1):49–59.
- Brower, D. L., Bunch, T. A., Mukai, L., Adamson, T. E., Wehrli, M., Lam, S., Friedlander, E., Roote, C. E., and Zusman, S. (1995). Nonequivalent requirements for PS1 and PS2 integrin at cell attachments in Drosophila: genetic analysis of the alpha PS1 integrin subunit. *Development*, 121(5):1311–1320.
- Brown, N. H., Gregory, S. L., Rickoll, W. L., Fessler, L. I., Prout, M., White, R. A. H., and Fristrom, J. W. (2002). Talin is essential for integrin function in Drosophila. *Developmental Cell*, 3(4):569–579.
- Bunch, T. A., Graner, M. W., Fessler, L. I., Fessler, J. H., Schneider, K. D., Kerschen, A., Choy, L. P., Burgess, B. W., and Brower, D. L. (1998). The PS2 integrin ligand tiggerin is required for proper muscle function in Drosophila. *Development*, 125(9):1679–1689.
- Bunch, T. A., Salatino, R., Engelsgerd, M. C., Mukai, L., West, R. F., and Brower, D. L. (1992). Characterization of mutant alleles of myospheroid, the gene encoding the beta subunit of the Drosophila PS integrins. *Genetics*, 132(2):519–528.
- Calderwood, D. A., Campbell, I. D., and Critchley, D. R. (2013). Talins and kindlins: partners in integrin-mediated adhesion. *Nature Reviews Molecular Cell Biology*, 14(8):503–517.
- Calderwood, D. A., Yan, B., de Pereda, J. M., Alvarez, B. G., Fujioka, Y., Liddington, R. C., and Ginsberg, M. H. (2002). The phosphotyrosine binding-like domain of talin activates integrins. *The Journal of Biological Chemistry*, 277(24):21749–21758.
- Calderwood, D. A., Zent, R., Grant, R., Rees, D. J., Hynes, R. O., and Ginsberg, M. H. (1999). The Talin head domain binds to integrin beta subunit cytoplasmic tails and regulates integrin activation. *The Journal of Biological Chemistry*, 274(40):28071–28074.
- Carroll, D. and Beumer, K. J. (2014). Genome engineering with TALENs and ZFNs: Repair pathways and donor design. *Methods (San Diego, Calif.)*.

-
- Chanana, B., Graf, R., Koledachkina, T., Pflanz, R., and Vorbrüggen, G. (2007). α PS2 integrin-mediated muscle attachment in *Drosophila* requires the ECM protein Thrombospondin. *Mechanisms of Development*, 124(6):463–475.
- Ciobanasu, C., Wang, H., Henriot, V., Mathieu, C., Fente, A., Csillag, S., Vigouroux, C., Faivre, B., and Le Clainche, C. (2018). Integrin-bound talin head inhibits actin filament barbed-end elongation. *The Journal of Biological Chemistry*, 293(7):2586–2596.
- Cleri, F. (2016). Of Limbs, Wings and Fins. In *The Physics of Living Systems*, pages 423–473. Springer, Cham.
- Colombelli, J., Besser, A., Kress, H., Reynaud, E. G., Girard, P., Caussinus, E., Haselmann, U., Small, J. V., Schwarz, U. S., and Stelzer, E. H. K. (2009). Mechanosensing in actin stress fibers revealed by a close correlation between force and protein localization. *Journal of Cell Science*, 122(10):1665–1679.
- Colombelli, J., Reynaud, E. G., Rietdorf, J., Pepperkok, R., and Stelzer, E. H. K. (2005). In vivo selective cytoskeleton dynamics quantification in interphase cells induced by pulsed ultraviolet laser nanosurgery. *Traffic (Copenhagen, Denmark)*, 6(12):1093–1102.
- Cong, L., Ran, F. A., Cox, D., Lin, S., Barretto, R., Habib, N., Hsu, P. D., Wu, X., Jiang, W., Marraffini, L. A., and Zhang, F. (2013). Multiplex Genome Engineering Using CRISPR/Cas Systems. *Science*, 339(6121):819–823.
- Conti, F. J., Felder, A., Monkley, S., Schwander, M., Wood, M. R., Lieber, R., Critchley, D., and Müller, U. (2008). Progressive myopathy and defects in the maintenance of myotendinous junctions in mice that lack talin 1 in skeletal muscle. *Development*, 135(11):2043–2053.
- Conti, F. J., Monkley, S. J., Wood, M. R., Critchley, D. R., and Müller, U. (2009). Talin 1 and 2 are required for myoblast fusion, sarcomere assembly and the maintenance of myotendinous junctions. *Development*, 136(21):3597–3606.
- Conway, D. E., Breckenridge, M. T., Hinde, E., Gratton, E., Chen, C. S., and Schwartz, M. A. (2013). Fluid shear stress on endothelial cells modulates mechanical tension across VE-cadherin and PECAM-1. *Current Biology*, 23(11):1024–1030.
- Cukierman, E., Pankov, R., Stevens, D. R., and Yamada, K. M. (2001). Taking Cell-Matrix Adhesions to the Third Dimension. *Science*, 294(5547):1708–1712.
- Currie, D. A. and Bate, M. (1991). The development of adult abdominal muscles in *Drosophila*: myoblasts express twist and are associated with nerves. *Development*, 113(1):91–102.

- de Joussineau, C., Bataillé, L., Jagla, T., and Jagla, K. (2012). Diversification of Muscle Types in *Drosophila*: Upstream and Downstream of Identity Genes. *Current Topics in Developmental Biology*, 98:277–301.
- de Pereda, J. M., Wegener, K. L., Santelli, E., Bate, N., Ginsberg, M. H., Critchley, D. R., Campbell, I. D., and Liddington, R. C. (2005). Structural basis for phosphatidylinositol phosphate kinase type I γ binding to talin at focal adhesions. *Journal of Biological Chemistry*, 280(9):8381–8386.
- del Rio, A., Perez-Jimenez, R., Liu, R., Roca-Cusachs, P., Fernandez, J. M., and Sheetz, M. P. (2009). Stretching single talin rod molecules activates vinculin binding. *Science*, 323(5914):638–641.
- Devenport, D. and Brown, N. H. (2004). Morphogenesis in the absence of integrins: mutation of both *Drosophila* β subunits prevents midgut migration. *Development*, 131(21):5405–5415.
- Dominguez, R., Freyzon, Y., Trybus, K. M., and Cohen, C. (1998). Crystal Structure of a Vertebrate Smooth Muscle Myosin Motor Domain and Its Complex with the Essential Light Chain: Visualization of the Pre-Power Stroke State. *Cell*, 94(5):559–571.
- Dudley, R. (2002). *The Biomechanics of Insect Flight*. Form, Function, Evolution. Princeton University Press.
- Dutta, D., Shaw, S., Maqbool, T., Pandya, H., and Vijayraghavan, K. (2005). *Drosophila* Heartless Acts with Heartbroken/Dof in Muscle Founder Differentiation. *PLOS Biology*, 3(10):e337.
- Ehler, E., Rothen, B. M., Hammerle, S. P., Komiyama, M., and Perriard, J. C. (1999). Myofibrillogenesis in the developing chicken heart: assembly of Z-disk, M-line and the thick filaments. *Journal of Cell Science*, 112(10):1529–1539.
- Ellis, S. J., Pines, M., Fairchild, M. J., and Tanentzapf, G. (2011). In vivo functional analysis reveals specific roles for the integrin-binding sites of talin. *Journal of Cell Science*, 124(Pt 11):1844–1856.
- Engler, A. J., Sen, S., Sweeney, H. L., and Discher, D. E. (2006). Matrix elasticity directs stem cell lineage specification. *Cell*, 126(4):677–689.
- Fang, J., Mehlich, A., Koga, N., Huang, J., Koga, R., Gao, X., Hu, C., Jin, C., Rief, M., Kast, J., Baker, D., and Li, H. (2013). Forced protein unfolding leads to highly elastic and tough protein hydrogels. *Nature Communications*, 4(1):2974.

-
- Fässler, R. and Meyer, M. (1995). Consequences of lack of beta 1 integrin gene expression in mice. *Genes & Development*, 9(15):1896–1908.
- Fenix, A. M., Neininger, A. C., Taneja, N., Hyde, K., Visetsouk, M. R., Garde, R. J., Liu, B., Nixon, B. R., Manalo, A. E., Becker, J. R., Crawley, S. W., Bader, D. M., Tyska, M. J., Liu, Q., Gutzman, J. H., and Burnette, D. T. (2018). Muscle-specific stress fibers give rise to sarcomeres in cardiomyocytes. *eLife*, 7:1111.
- Fogerty, F. J., Fessler, L. I., Bunch, T. A., Yaron, Y., Parker, C. G., Nelson, R. E., Brower, D. L., Gullberg, D., and Fessler, J. H. (1994). Tiggrin, a novel Drosophila extracellular matrix protein that functions as a ligand for Drosophila alpha PS2 beta PS integrins. *Development*, 120(7):1747–1758.
- Franco-Cea, A., Ellis, S. J., Fairchild, M. J., Yuan, L., Cheung, T. Y., and Tanentzapf, G. (2010). Distinct developmental roles for direct and indirect talin-mediated linkage to actin. *Developmental Biology*, 345(1):64–77.
- Freddolino, P. L., Harrison, C. B., Liu, Y., and Schulten, K. (2010). Challenges in protein folding simulations: Timescale, representation, and analysis. *Nature Physics*, 6(10):751–758.
- Friedrich, M. V. K., Schneider, M., Timpl, R., and Baumgartner, S. (2000). Perlecan domain V of Drosophila melanogaster. *European Journal of Biochemistry*, 267(11):3149–3159.
- Gingras, A. R., Bate, N., Goult, B. T., Hazelwood, L., Canestrelli, I., Grossmann, J. G., Liu, H., Putz, N. S. M., Roberts, G. C. K., Volkman, N., Hanein, D., Barsukov, I. L., and Critchley, D. R. (2007). The structure of the C-terminal actin-binding domain of talin. *The EMBO Journal*, 27(2):458–469.
- Gingras, A. R., Ziegler, W. H., Bobkov, A. A., Joyce, M. G., Fasci, D., Himmel, M., Rothemund, S., Ritter, A., Grossmann, J. G., Patel, B., Bate, N., Goult, B. T., Emsley, J., Barsukov, I. L., Roberts, G. C. K., Liddington, R. C., Ginsberg, M. H., and Critchley, D. R. (2009). Structural Determinants of Integrin Binding to the Talin Rod. *Journal of Biological Chemistry*, 284(13):8866–8876.
- Gingras, A. R., Ziegler, W. H., Frank, R., Barsukov, I. L., Roberts, G. C. K., Critchley, D. R., and Emsley, J. (2005). Mapping and consensus sequence identification for multiple vinculin binding sites within the talin rod. *Journal of Biological Chemistry*, 280(44):37217–37224.
- Goksoy, E., Ma, Y.-Q., Wang, X., Kong, X., Perera, D., Plow, E. F., and Qin, J. (2008). Structural Basis for the Autoinhibition of Talin in Regulating Integrin Activation. *Molecular Cell*, 31(1):124–133.

- Gottschalk, K.-E. (2005). A Coiled-Coil Structure of the α IIb β 3 Integrin Transmembrane and Cytoplasmic Domains in Its Resting State. *Structure*, 13(5):703–712.
- Goult, B. T., Bate, N., Anthis, N. J., Wegener, K. L., Gingras, A. R., Patel, B., Barsukov, I. L., Campbell, I. D., Roberts, G. C. K., and Critchley, D. R. (2009). The structure of an interdomain complex that regulates talin activity. *Journal of Biological Chemistry*, 284(22):15097–15106.
- Goult, B. T., Bouaouina, M., Bate, N., Patel, B., Gingras, A. R., Grossmann, J. G., Roberts, G. C. K., Calderwood, D. A., Critchley, D. R., and Barsukov, I. L. (2010a). Structure of a double ubiquitin-like domain in the talin head: a role in integrin activation. *The EMBO Journal*, 29(6):1069–1080.
- Goult, B. T., Gingras, A. R., Bate, N., Barsukov, I. L., Critchley, D. R., and Roberts, G. C. K. (2010b). The domain structure of talin: Residues 1815–1973 form a five-helix bundle containing a cryptic vinculin-binding site. *FEBS Letters*, 584(11):2237–2241.
- Goult, B. T., Kopp, P. M., Bate, N., Grossmann, J. G., Roberts, G. C. K., Critchley, D. R., and Barsukov, I. L. (2010c). The Structure of the talin head reveals a novel extended conformation of the FERM domain. *Structure*, 18(10):1289–1299.
- Goult, B. T., Zacharchenko, T., Bate, N., Tsang, R., Hey, F., Gingras, A. R., Elliott, P. R., Roberts, G. C. K., Ballestrem, C., Critchley, D. R., and Barsukov, I. L. (2013). RIAM and Vinculin Binding to Talin Are Mutually Exclusive and Regulate Adhesion Assembly and Turnover. *Journal of Biological Chemistry*, 288(12):8238–8249.
- Grashoff, C., Hoffman, B. D., Brenner, M. D., Zhou, R., Parsons, M., Yang, M. T., McLean, M. A., Sligar, S. G., Chen, C. S., Ha, T., and Schwartz, M. A. (2010). Measuring mechanical tension across vinculin reveals regulation of focal adhesion dynamics. *Nature*, 466(7303):263–266.
- Green, H. J., Griffiths, A. G., Ylänne, J., and Brown, N. H. (2018). Novel functions for integrin-associated proteins revealed by analysis of myofibril attachment in *Drosophila*. *eLife*, 7:197.
- Hemmings, L., Rees, D. J., Ohanian, V., Bolton, S. J., Gilmore, A. P., Patel, B., Priddle, H., Trevithick, J. E., Hynes, R. O., and Critchley, D. R. (1996). Talin contains three actin-binding sites each of which is adjacent to a vinculin-binding site. *Journal of Cell Science*, 109(11):2715–2726.

-
- Hochreiter, B., Garcia, A., and Schmid, J. (2015). Fluorescent Proteins as Genetically Encoded FRET Biosensors in Life Sciences. *Sensors*, 15(10):26281–26314.
- Holtzer, H., Hijikata, T., Lin, Z. X., Zhang, Z. Q., Holtzer, S., Protasi, F., Franzini-Armstrong, C., and Sweeney, H. L. (1997). Independent assembly of 1.6 microns long bipolar MHC filaments and I-Z-I bodies. *Cell Structure and Function*, 22(1):83–93.
- Horwitz, A., Duggan, K., Buck, C., Beckerle, M. C., and Burridge, K. (1986). Interaction of plasma membrane fibronectin receptor with talin—a transmembrane linkage. *Nature*, 320(6062):531–533.
- Hughes, M. L. and Dougan, L. (2016). The physics of pulling polyproteins: a review of single molecule force spectroscopy using the AFM to study protein unfolding. *Reports on Progress in Physics*, 79(7):076601.
- Hutson, M. S., Tokutake, Y., Chang, M.-S., Bloor, J. W., Venakides, S., Kiehart, D. P., and Edwards, G. S. (2003). Forces for Morphogenesis Investigated with Laser Microsurgery and Quantitative Modeling. *Science*, 300(5616):145–149.
- Huxley, H. E. (1957). The double array of filaments in cross-striated muscle. *The Journal of Biophysical and Biochemical Cytology*, 3(5):631–648.
- Huxley, H. E. (1967). Recent X-ray Diffraction and Electron Microscope Studies of Striated Muscle. *The Journal of General Physiology*, 50(6):71–83.
- Huxley, H. E. (1969). The Mechanism of Muscular Contraction. *Science*, 164(3886):1356–1366.
- Hynes, R. O. and Zhao, Q. (2000). The evolution of cell adhesion. *The Journal of Cell Biology*, 150(2):F89–96.
- Jinek, M., Chylinski, K., Fonfara, I., Hauer, M., Doudna, J. A., and Charpentier, E. (2012). A programmable dual-RNA-guided DNA endonuclease in adaptive bacterial immunity. *Science*, 337(6096):816–821.
- Kanchanawong, P., Shtengel, G., Pasapera, A. M., Ramko, E. B., Davidson, M. W., Hess, H. F., and Waterman, C. M. (2010). Nanoscale architecture of integrin-based cell adhesions. *Nature*, 468(7323):580–584.
- Klapholz, B., Herbert, S. L., Wellmann, J., Johnson, R., Parsons, M., and Brown, N. H. (2015). Alternative mechanisms for talin to mediate integrin function. *Current Biology*, 25(7):847–857.

- Knezevic, I., Leisner, T. M., and Lam, S. C. (1996). Direct binding of the platelet integrin α IIb β 3 (GPIIb-IIIa) to talin. Evidence that interaction is mediated through the cytoplasmic domains of both α IIb and β 3. *Journal of Biological Chemistry*, 271(27):16416–16421.
- Kumar, A., Ouyang, M., Van den Dries, K., McGhee, E. J., Tanaka, K., Anderson, M. D., Groisman, A., Goult, B. T., Anderson, K. I., and Schwartz, M. A. (2016). Talin tension sensor reveals novel features of focal adhesion force transmission and mechanosensitivity. *The Journal of Cell Biology*, 213(3):371–383.
- Lakowicz, J. R. (2006). *Principles of Fluorescence Spectroscopy*. Springer US, Boston, MA, third edition.
- Latorre, E., Kale, S., Casares, L., Gómez-González, M., Uroz, M., Valon, L., Nair, R. V., Garreta, E., Montserrat, N., del Campo, A., Ladoux, B., Arroyo, M., and Trepate, X. (2018). Active superelasticity in three-dimensional epithelia of controlled shape. *Nature*, 563(7730):203–208.
- Lawson, C., Lim, S.-T., Uryu, S., Chen, X. L., Calderwood, D. A., and Schlaepfer, D. D. (2012). FAK promotes recruitment of talin to nascent adhesions to control cell motility. *The Journal of Cell Biology*, 196(2):223–232.
- Lee, H.-S., Bellin, R. M., Walker, D. L., Patel, B., Powers, P., Liu, H., García-Alvarez, B., de Pereda, J. M., Liddington, R. C., Volkmann, N., Hanein, D., Critchley, D. R., and Robson, R. M. (2004). Characterization of an Actin-binding Site within the Talin FERM Domain. *Journal of Molecular Biology*, 343(3):771–784.
- Lemke, S. B. and Schnorrer, F. (2017). Mechanical forces during muscle development. *Mechanisms of Development*, 144(Pt A):92–101.
- Lemke, S. B. and Schnorrer, F. (2018). In Vivo Imaging of Muscle-tendon Morphogenesis in *Drosophila* Pupae. *Journal of Visualized Experiments*, (132):e57312.
- Lemke, S. B., Weidemann, T., Cost, A.-L., Grashoff, C., and Schnorrer, F. (2019). A small proportion of Talin molecules transmit forces at developing muscle attachments in vivo. *PLOS Biology*, 17(3):e3000057.
- Li, G., Du, X., Vass, W. C., Papageorge, A. G., Lowy, D. R., and Qian, X. (2011). Full activity of the deleted in liver cancer 1 (DLC1) tumor suppressor depends on an LD-like motif that binds talin and focal adhesion kinase (FAK). *Proceedings of the National Academy of Sciences of the United States of America*, 108(41):17129–17134.

-
- Loison, O., Weitkunat, M., Kaya-Çopur, A., Alves, C. N., Matzat, T., Spletter, M. L., Luschnig, S., Brasselet, S., Lenne, P.-F., and Schnorrer, F. (2018). Polarization-resolved microscopy reveals a muscle myosin motor-independent mechanism of molecular actin ordering during sarcomere maturation. *PLoS Biology*, 16(4):e2004718.
- Lymn, R. W. and Taylor, E. W. (1971). Mechanism of adenosine triphosphate hydrolysis by actomyosin. *Biochemistry*, 10(25):4617–4624.
- Maartens, A. P. and Brown, N. H. (2015). The many faces of cell adhesion during *Drosophila* muscle development. *Developmental Biology*, 401(1):62–74.
- Martin, D., Zusman, S., Li, X., Williams, E. L., Khare, N., DaRocha, S., Chiquet-Ehrismann, R., and Baumgartner, S. (1999). wing blister, A New *Drosophila* Laminin α Chain Required for Cell Adhesion and Migration during Embryonic and Imaginal Development. *The Journal of Cell Biology*, 145(1):191–201.
- Miller, A. (1950). The internal anatomy and histology of the imago of *Drosophila melanogaster*. In Demerec, M., editor, *Biology of Drosophila*, pages 420–534.
- Monkley, S. J., Zhou, X. H., Kinston, S. J., Giblett, S. M., Hemmings, L., Priddle, H., Brown, J. E., Pritchard, C. A., Critchley, D. R., and Fässler, R. (2000). Disruption of the talin gene arrests mouse development at the gastrulation stage. *Developmental Dynamics*, 219(4):560–574.
- Morimatsu, M., Mekhdjian, A. H., Adhikari, A. S., and Dunn, A. R. (2013). Molecular Tension Sensors Report Forces Generated by Single Integrin Molecules in Living Cells. *Nano Letters*, 13(9):3985–3989.
- Moser, M., Legate, K. R., Zent, R., and Fässler, R. (2009). The Tail of Integrins, Talin, and Kindlins. *Science*, 324(5929):895–899.
- Myhre, J. L. and Pilgrim, D. B. (2012). At the Start of the Sarcomere: A Previously Unrecognized Role for Myosin Chaperones and Associated Proteins during Early Myofibrillogenesis. *Biochemistry Research International*, 2012(1):712315–16.
- Mykuliak, V. V., Haining, A. W. M., von Essen, M., del Río Hernández, A., and Hytönen, V. P. (2018). Mechanical unfolding reveals stable 3-helix intermediates in talin and α -catenin. *PLoS Computational Biology*, 14(4):e1006126.
- Narasimha, M. and Brown, N. H. (2013). Integrins and Associated Proteins in *Drosophila* Development. In *Madame Curie Bioscience Database*. Landes Bioscience.

- Papagrigoriou, E., Gingras, A. R., Barsukov, I. L., Bate, N., Fillingham, I. J., Patel, B., Frank, R., Ziegler, W. H., Roberts, G. C., Critchley, D. R., and Emsley, J. (2004). Activation of a vinculin-binding site in the talin rod involves rearrangement of a five-helix bundle. *The EMBO Journal*, 23(15):2942–2951.
- Port, F., Chen, H.-M., Lee, T., and Bullock, S. L. (2014). Optimized CRISPR/Cas tools for efficient germline and somatic genome engineering in *Drosophila*. *Proceedings of the National Academy of Sciences*, 111(29):E2967–76.
- Rauzi, M., Verant, P., Lecuit, T., and Lenne, P.-F. (2008). Nature and anisotropy of cortical forces orienting *Drosophila* tissue morphogenesis. *Nature Cell Biology*, 10(12):1401–1410.
- Rhee, D., Sanger, J. M., and Sanger, J. W. (1994). The premyofibril: Evidence for its role in myofibrillogenesis. *Cell Motility and the Cytoskeleton*, 28(1):1–24.
- Ribeiro, A. J. S., Denisin, A. K., Wilson, R. E., and Pruitt, B. L. (2016). For whom the cells pull: Hydrogel and micropost devices for measuring traction forces. *Methods (San Diego, Calif.)*, 94:51–64.
- Ringer, P., Weißl, A., Cost, A.-L., Freikamp, A., Sabass, B., Mehlich, A., Tramier, M., Rief, M., and Grashoff, C. (2017). Multiplexing molecular tension sensors reveals piconewton force gradient across talin-1. *Nature Methods*, 14(11):1090–1096.
- Sander, J. D. and Joung, J. K. (2014). CRISPR-Cas systems for editing, regulating and targeting genomes. *Nature Biotechnology*, 32(4):347–355.
- Schwander, M., Leu, M., Stumm, M., Dorchies, O. M., Ruegg, U. T., Schittny, J., and Müller, U. (2003). $\beta 1$ Integrins Regulate Myoblast Fusion and Sarcomere Assembly. *Developmental Cell*, 4(5):673–685.
- Sheetz, M. P. and Spudich, J. A. (1983). Movement of myosin-coated fluorescent beads on actin cables in vitro. *Nature*, 303(5912):31–35.
- Shih, W. M., Gryczynski, Z., Lakowicz, J. R., and Spudich, J. A. (2000). A FRET-Based Sensor Reveals Large ATP Hydrolysis-Induced Conformational Changes and Three Distinct States of the Molecular Motor Myosin. *Cell*, 102(5):683–694.
- Sparrow, J. C. and Schöck, F. (2009). The initial steps of myofibril assembly: integrins pave the way. *Nature Reviews Molecular Cell Biology*, 10(4):293–298.

-
- Spletter, M. L., Barz, C., Yeroslaviz, A., Zhang, X., Lemke, S. B., Bonnard, A., Brunner, E., Cardone, G., Basler, K., Habermann, B. H., and Schnorrer, F. (2018). A transcriptomics resource reveals a transcriptional transition during ordered sarcomere morphogenesis in flight muscle. *eLife*, 7:e34058.
- Spudich, J. A. (2001). The myosin swinging cross-bridge model. *Nature Reviews Molecular Cell Biology*, 2(5):387–392.
- Su, Y., Xia, W., Li, J., Walz, T., Humphries, M. J., Vestweber, D., Cabañas, C., Lu, C., and Springer, T. A. (2016). Relating conformation to function in integrin $\alpha 5\beta 1$. *Proceedings of the National Academy of Sciences of the United States of America*, 113(27):E3872–E3881.
- Subramanian, A., Wayburn, B., Bunch, T., and Volk, T. (2007). Thrombospondin-mediated adhesion is essential for the formation of the myotendinous junction in *Drosophila*. *Development*, 134(7):1269–1278.
- Sun, N., Critchley, D. R., Paulin, D., Li, Z., and Robson, R. M. (2008). Identification of a repeated domain within mammalian α -synemin that interacts directly with talin. *Experimental Cell Research*, 314(8):1839–1849.
- Sun, Z., Tseng, H.-Y., Tan, S., Senger, F., Kurzawa, L., Dedden, D., Mizuno, N., Wasik, A. A., They, M., Dunn, A. R., and Fässler, R. (2016). Kank2 activates talin, reduces force transduction across integrins and induces central adhesion formation. *Nature Cell Biology*, 18(9):941–953.
- Takada, Y., Ye, X., and Simon, S. (2007). The integrins. *Genome Biology*, 8(5):215.
- Tremuth, L., Kreis, S., Melchior, C., Hoebeke, J., Rondé, P., Plançon, S., Takeda, K., and Kieffer, N. (2004). A fluorescence cell biology approach to map the second integrin-binding site of talin to a 130-amino acid sequence within the rod domain. *The Journal of Biological Chemistry*, 279(21):22258–22266.
- Umemiya, T., Takeichi, M., and Nose, A. (1997). M-spondin, a novel ECM protein highly homologous to vertebrate F-spondin, is localized at the muscle attachment sites in the *Drosophila* embryo. *Developmental Biology*, 186(2):165–176.
- Wang, S., Watanabe, T., Matsuzawa, K., Katsumi, A., Kakeno, M., Matsui, T., Ye, F., Sato, K., Murase, K., Sugiyama, I., Kimura, K., Mizoguchi, A., Ginsberg, M. H., Collard, J. G., and Kaibuchi, K. (2012). Tiam1 interaction with the PAR complex promotes talin-mediated Rac1 activation during polarized cell migration. *The Journal of Cell Biology*, 199(2):331–345.

- Wegener, K. L., Basran, J., Bagshaw, C. R., Campbell, I. D., Roberts, G. C. K., Critchley, D. R., and Barsukov, I. L. (2008). Structural Basis for the Interaction between the Cytoplasmic Domain of the Hyaluronate Receptor Layilin and the Talin F3 Subdomain. *Journal of Molecular Biology*, 382(1):112–126.
- Weinstein, A. (1918). Coincidence of Crossing over in DROSOPHILA MELANOGASTER (AMPELOPHILA). *Genetics*, 3(2):135–172.
- Weitkunat, M., Brasse, M., Bausch, A. R., and Schnorrer, F. (2017). Mechanical tension and spontaneous muscle twitching precede the formation of cross-striated muscle in vivo. *Development*, 144(7):1261–1272.
- Weitkunat, M., Kaya-Çopur, A., Grill, S. W., and Schnorrer, F. (2014). Tension and force-resistant attachment are essential for myofibrillogenesis in Drosophila flight muscle. *Current Biology*, 24(7):705–716.
- Weitkunat, M. and Schnorrer, F. (2014). A guide to study Drosophila muscle biology. *Methods (San Diego, Calif.)*, 68(1):2–14.
- White, J., Barro, M. V., Makarenkova, H. P., Sanger, J. W., and Sanger, J. M. (2014). Localization of sarcomeric proteins during myofibril assembly in cultured mouse primary skeletal myotubes. *Anatomical record (Hoboken, N.J. : 2007)*, 297(9):1571–1584.
- Wright, T. R. F. (1960). The phenogenetics of the embryonic mutant lethal myspheroid, in *Drosophila melanogaster*. *Journal of Experimental Zoology*, 143(1):77–99.
- Yao, M., Goult, B. T., Chen, H., Cong, P., Sheetz, M. P., and Yan, J. (2014). Mechanical activation of vinculin binding to talin locks talin in an unfolded conformation. *Scientific Reports*, 4(1):4610.
- Yount, R. G., Ojala, D., and Babcock, D. (1971). Interaction of P-N-P and P-C-P analogs of adenosine triphosphate with heavy meromyosin, myosin, and actomyosin. *Biochemistry*, 10(13):2490–2496.
- Zhang, X., Koolhaas, W. H., and Schnorrer, F. (2014a). A Versatile Two-Step CRISPR- and RMCE-Based Strategy for Efficient Genome Engineering in Drosophila. *G3-Genes, Genomes, Genetics*, 4(12):2409–2418.
- Zhang, Y., Ge, C., Zhu, C., and Salaita, K. (2014b). DNA-based digital tension probes reveal integrin forces during early cell adhesion. *Nature Communications*, 5(1):5167.

Ziegler, W. H., Gingras, A. R., Critchley, D. R., and Emsley, J. (2008). Integrin connections to the cytoskeleton through talin and vinculin. *Biochemical Society Transactions*, 36(2):235.

Acknowledgments

First of all, I want to say thank you to Frank who always supported me from the beginning of my Master thesis and all the way through my PhD. Thank you for encouraging me to go to conferences right from the beginning and for always being ready to discuss my results in many one-on-one meetings lasting for hours and hours, but also for giving me the freedom and trusting me to make my own plans and decisions in my everyday lab life.

I want to thank the Schnorrer group for a great working atmosphere and for always being ready to teach me something I did not know yet, right from the start when I joined the group (basically almost dropping their pipettes mid-way through an experiment). Special thanks goes to Manu for sharing all her experience on flight muscle development with me, to Xu for teaching me how to CRISPR and to Maria and Wouter for sharing the office with me and being always ready to discuss my results. Furthermore, I want to thank Maria for helping me improve my English by answering any kind of language question. Thank you to Bettina and Nicole for countless embryo injections. A big thank you also goes to Aynur who stayed with me in Munich after Frank's move to Marseille and gave me a lot of good advice. And finally, apart from all the science, I learned more about pregnancy and young kinds in the Schnorrer lab than I could have ever imagined without actually having kids myself :)

I want to thank Carsten and his group for becoming my second home. I never felt like I was left just by myself after the Schnorrer group in Munich disbanded. Thank you, Carsten, for always pointing out a positive way to view my results and for even paying my position for quite some time. I greatly appreciate that and definitely don't take it for granted. I want to thank my 'Fliegenkammerle' colleague Lisa and now also Christoph and Verena for making the office a great place to be at even without windows. I thank Anna-Lena for putting countless hours into the development of our analysis software and for in-depth discussions on biexponential fitting that my story greatly benefited from, resulting in a co-authorship on my paper. Thank you to Anna for always keeping

all the strings together in the Grashoff lab and finally, I want to thank all the former members of the Grashoff lab, especially Kathi for sharing her work on the Talin tension sensor with me before publication, Carleen for the original development of the analysis software and Pia, who was not only a colleague, but also became a good friend and got me excited about beach volleyball.

I am indebted to Reinhard Fässler for agreeing to be my 'Doktorvater', for his supportive attitude towards my project and myself, for providing access to the microscopes that I spent countless hours using, and for allowing me to stay as a guest in the department to finish my paper and thesis.

I thank my TAC committee, consisting of Frank, Carsten, Reinhard, and Stefan Luschnig who came all the way from Zürich, and later Münster, to be part of my TAC committee meetings. For me, these meetings were always a great opportunity to look back at all the results collected in the last year and discuss how to go on from there.

I want to thank my collaboration partner Thomas Weidemann for teaching me how to do FCS, for making it work together with me in a difficult sample and for being my sparring partner in countless discussions about how to best analyze the FCS data.

I thank Jürg Müller for letting me store my fly stocks in his incubators and for providing fly food in the final phase of my PhD in Munich.

Last but not least, I want to thank my husband and my family. Michi, you have a big part in making my time as a PhD student a part of my life that I will be happy to look back to. And thank you to my family for always supporting my choices what routes to follow in my life.

Appendix

The appendix includes reprints of the **Papers I to IV**.

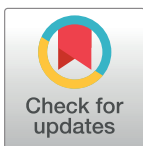
RESEARCH ARTICLE

A small proportion of Talin molecules transmit forces at developing muscle attachments in vivo

Sandra B. Lemke^{1*}, Thomas Weidemann¹, Anna-Lena Cost^{1,2}, Carsten Grashoff^{1,2*}, Frank Schnorrer^{1,3*}

1 Max Planck Institute of Biochemistry, Martinsried, Germany, **2** University of Münster, Institute for Molecular Cell Biology, Münster, Germany, **3** Aix Marseille University, CNRS, IBDM, Marseille, France

* frank.schnorrer@univ-amu.de (FS); grashoff@uni-muenster.de (CG); lemke@biochem.mpg.de (SBL)



Abstract

Cells in developing organisms are subjected to particular mechanical forces that shape tissues and instruct cell fate decisions. How these forces are sensed and transmitted at the molecular level is therefore an important question, one that has mainly been investigated in cultured cells in vitro. Here, we elucidate how mechanical forces are transmitted in an intact organism. We studied *Drosophila* muscle attachment sites, which experience high mechanical forces during development and require integrin-mediated adhesion for stable attachment to tendons. Therefore, we quantified molecular forces across the essential integrin-binding protein Talin, which links integrin to the actin cytoskeleton. Generating flies expressing 3 Förster resonance energy transfer (FRET)-based Talin tension sensors reporting different force levels between 1 and 11 piconewton (pN) enabled us to quantify physiologically relevant molecular forces. By measuring primary *Drosophila* muscle cells, we demonstrate that *Drosophila* Talin experiences mechanical forces in cell culture that are similar to those previously reported for Talin in mammalian cell lines. However, in vivo force measurements at developing flight muscle attachment sites revealed that average forces across Talin are comparatively low and decrease even further while attachments mature and tissue-level tension remains high. Concomitantly, the Talin concentration at attachment sites increases 5-fold as quantified by fluorescence correlation spectroscopy (FCS), suggesting that only a small proportion of Talin molecules are mechanically engaged at any given time. Reducing Talin levels at late stages of muscle development results in muscle–tendon rupture in the adult fly, likely as a result of active muscle contractions. We therefore propose that a large pool of adhesion molecules is required to share high tissue forces. As a result, less than 15% of the molecules experience detectable forces at developing muscle attachment sites at the same time. Our findings define an important new concept of how cells can adapt to changes in tissue mechanics to prevent mechanical failure in vivo.

OPEN ACCESS

Citation: Lemke SB, Weidemann T, Cost A-L, Grashoff C, Schnorrer F (2019) A small proportion of Talin molecules transmit forces at developing muscle attachments in vivo. *PLoS Biol* 17(3): e3000057. <https://doi.org/10.1371/journal.pbio.3000057>

Academic Editor: Simon M. Hughes, King's College London, UNITED KINGDOM

Received: September 27, 2018

Accepted: March 8, 2019

Published: March 27, 2019

Copyright: © 2019 Lemke et al. This is an open access article distributed under the terms of the [Creative Commons Attribution License](https://creativecommons.org/licenses/by/4.0/), which permits unrestricted use, distribution, and reproduction in any medium, provided the original author and source are credited.

Data Availability Statement: All relevant data are within the paper and its Supporting Information files.

Funding: This work was supported by the EMBO Young Investigator Program (to FS), the European Research Council under the European Union's Seventh Framework Programme (FP/2007-2013)/ERC Grant 310939 (to FS), the Max Planck Society (to SBL, TW, A-LC, CG, and FS), the Centre National de la Recherche Scientifique (CNRS) (to FS), the excellence initiative Aix-Marseille

University AMIDEX (ANR-11-IDEX-0001-02, to FS), the LabEX-INFORM (ANR-11-LABX-0054, to FS), the ANR-ACHN 'Muscle Forces' (to FS), the Human Frontiers Science Program (HFSP-CDA-50/2009, to FS), the Bettencourt Foundation (to FS), the Boehringer Ingelheim Fonds (to SBL), the German Research Council (DFG) priority program SPP1782 (to CG) and FOR1756 (to SBL and FS). The funders had no role in study design, data collection and analysis, decision to publish, or preparation of the manuscript.

Competing interests: The authors have declared that no competing interests exist.

Abbreviations: C-F40-TS, Talin control sensor with F40-sensor module; C-mCh, Talin with C-terminal mCherry; C-stTS, Talin control sensor with HPst-sensor module; C-TS, Talin control sensor with HP-sensor module; C-YPet, Talin with C-terminal YPet; CPP, counts per particle; CRISPR/Cas9, clustered regularly interspaced short palindromic repeats/CRISPR-associated protein 9; FCS, fluorescence correlation spectroscopy; F40, flagelliform peptide; F40-TS, Talin tension sensor with F40-sensor module; FCS, fluorescence correlation spectroscopy; FLIM, fluorescence lifetime imaging microscopy; FRAP, fluorescence recovery after photobleaching; FRET, Förster resonance energy transfer; h APF, hours after puparium formation; HP, Villin headpiece peptide; HPst, stable Villin headpiece peptide; I-mCh, Talin with internal mCherry; I-YPet, Talin with internal YPet; pN, piconewton; RNAi, RNA interference; RT, room temperature; sgRNA, single guide RNA; TCSPC, time-correlated single photon counting; stTS, Talin tension sensor with HPst-sensor module; *tal**in-IR*, *tal**in* RNA interference; TS, Talin tension sensor with HP-sensor module; WT, wild type; YPet, yellow fluorescent protein for energy transfer.

Author summary

Cells in our body are constantly exposed to mechanical forces, which they need to sense and react to. In previous studies, fluorescent force sensors were developed to demonstrate that individual proteins in adhesion structures of a cell experience forces in the piconewton (pN) range. However, these cells were analyzed in isolation in an artificial plastic or glass environment. Here, we explored forces on adhesion proteins in their natural environment within a developing animal and used the muscle–tendon tissue in the fruit fly *Drosophila* as a model system. We made genetically modified fly lines with force sensors or controls inserted into the gene that produces the essential adhesion protein Talin. Using these force sensor flies, we found that only a small proportion of all the Talin proteins (<15%) present at developing muscle–tendon attachments experience detectable forces at the same time. Nevertheless, a large amount of Talin is accumulated at these attachments during fly development. We found that this large Talin pool is important to prevent rupture of the muscle–tendon connection in adult flies that produce high muscle forces during flight. In conclusion, we demonstrated that a large pool of Talin proteins is required for stable muscle–tendon attachment, likely with the individual Talin molecules dynamically sharing the mechanical load.

Introduction

The shape of multicellular organisms critically depends on the presence of mechanical forces during development [1,2]. Forces not only generate form and flows within tissues [3,4] but can also control cell fate decisions [5,6] and trigger mitosis [7]. There are various ways to quantify forces at the cellular or tissue level [8,9]; however, mechanical forces experienced by proteins in cells have only recently become quantifiable with the development of Förster resonance energy transfer (FRET)-based molecular tension sensors [10]. These sensors contain a donor and an acceptor fluorophore connected by a mechanosensitive linker peptide, which reversibly unfolds and extends when experiencing mechanical forces. As a result, such sensors report forces as a decrease in FRET efficiency caused by an increase in distance between the fluorophores. Since previous studies analyzed molecular forces using in vitro cell culture systems [11–17] and insights from in vivo experiments are still limited [18–21], it remains largely open how mechanical loads are processed at the molecular level in tissues of living organisms.

Integrins are a major and highly conserved force-bearing protein family. They connect the actomyosin cytoskeleton to the extracellular matrix and are essential for numerous mechanically regulated processes in vivo or in vitro [22,23]. However, in vivo it is particularly unclear how integrin-based structures are mechanically loaded because forces have so far only been analyzed in focal adhesions, which are typically not found in soft tissues [11–13,17]. Therefore, we chose to investigate *Drosophila* muscle attachment sites in vivo, which experience high mechanical forces during development [24] and depend on integrin-based attachment of muscle fibers to tendon cells [22,25]. For the molecular force measurements, we selected the integrin activator and mechanotransducer Talin, which is essential for all integrin-mediated functions and binds with its globular head domain to the tail of β -integrin and with its rod domain to actin filaments [26,27]. Thus, Talin is in the perfect position to sense mechanical forces across integrin-dependent adhesive structures. In contrast to measurements performed previously in vitro [12], we find that less than 15% of the Talin molecules experience significant forces at developing muscle attachments in vivo, suggesting that high tissue forces are sustained by recruiting a large excess of Talin molecules to muscle attachments. Reducing the

Talin levels leads to rupture of muscle attachments in response to high forces during adult muscle contractions. This demonstrates the significance of high Talin levels for the robustness of muscle attachments under peak mechanical load.

Results

A *Drosophila* Talin tension sensor

To enable quantitative force measurements, we generated various *Drosophila* Talin tension sensor and control flies by modifying the endogenous *talin (rhea)* gene using a two-step strategy based on clustered regularly interspaced short palindromic repeats (CRISPR)/CRISPR-associated protein 9 (Cas9) genome engineering and ϕ C31-mediated cassette exchange (Fig 1A, S1 Fig) [28]. This strategy enabled us to generate an entire set of Talin tension sensor fly lines with yellow fluorescent protein for energy transfer (YPet) and mCherry FRET pairs and 3 different mechanosensitive linker peptides [11,13], Flagelliform (F40), Villin headpiece peptide (HP), and HP's stable variant (HPst), reporting forces of 1–6 piconewton (pN), 6–8 pN, and 9–11 pN, respectively (Fig 1B). The sensor modules were inserted both internally between the Talin head and rod domains (F40-TS, TS, stTS) at the analogous position used in mammalian Talin to report forces in vitro [11,17] and C-terminally as a zero-force control (C-F40-TS, C-TS, C-stTS). Furthermore, the individual fluorescent proteins were inserted at both positions as controls (I-YPet, I-mCh, C-YPet, C-mCh). All stocks are homozygous viable and fertile and do not display any overt phenotype indicating that the Talin tension sensor proteins are functional.

To assess the functionality of Talin-TS more rigorously, we first analyzed Talin-TS localization in adult hemithoraxes and found that Talin-TS localizes to myofibril tips as expected (Fig 2A–2D). Second, we performed western blot analysis and found the expected band shifts for tension sensor module incorporation into Talin protein isoforms (Fig 2E). Third, we quantified sarcomere length in flight muscles and found the expected length of 3.2 μ m in wild-type (WT) [29] and *talin-TS* flies (Fig 2F–2H). Fourth, we tested flight ability [30] and found that neither the insertion of the sensor module nor the individual fluorescent proteins into the

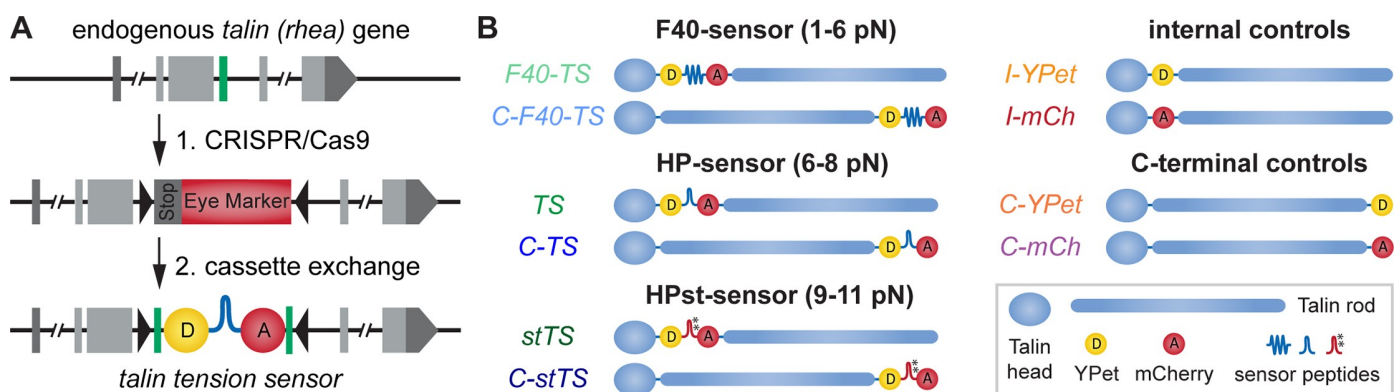


Fig 1. Talin tension sensor generation. (A) Two-step genome engineering strategy of the *talin (rhea)* gene. Step 1: Cas9-mediated insertion of an eye marker cassette replacing the target exon (green). Step 2: ϕ C31-mediated cassette exchange restoring the original exon and including a tension sensor. See S1 Fig for details. (B) Overview of Talin tension sensor and control flies. Sensors with 3 different mechanosensitive linker peptides, F40, HP, and HPst, were generated. Respective force regimes are indicated. Each sensor was inserted internally (F40-TS, TS, stTS) or at the C-terminus (C-F40-TS, C-TS, C-stTS). Controls with the individual fluorescent proteins were also generated (I-YPet, I-mCh, C-YPet, C-mCh). C-F40-TS, Talin control sensor with F40-sensor module; C-mCh, Talin with C-terminal mCherry; C-stTS, Talin control sensor with HPst-sensor module; C-TS, Talin control sensor with HP-sensor module; C-YPet, Talin with C-terminal YPet; CRISPR/Cas9, clustered regularly interspaced short palindromic repeats/CRISPR-associated protein 9; F40, Flagelliform peptide; F40-TS, Talin tension sensor with F40-sensor module; HP, Villin headpiece; HPst, stable Villin headpiece; I-mCh, Talin with internal mCherry; I-YPet, Talin with internal YPet; pN, piconewton; stTS, Talin tension sensor with HPst-sensor module; TS, Talin tension sensor with HP-sensor module; YPet, yellow fluorescent protein for energy transfer.

<https://doi.org/10.1371/journal.pbio.3000057.g001>

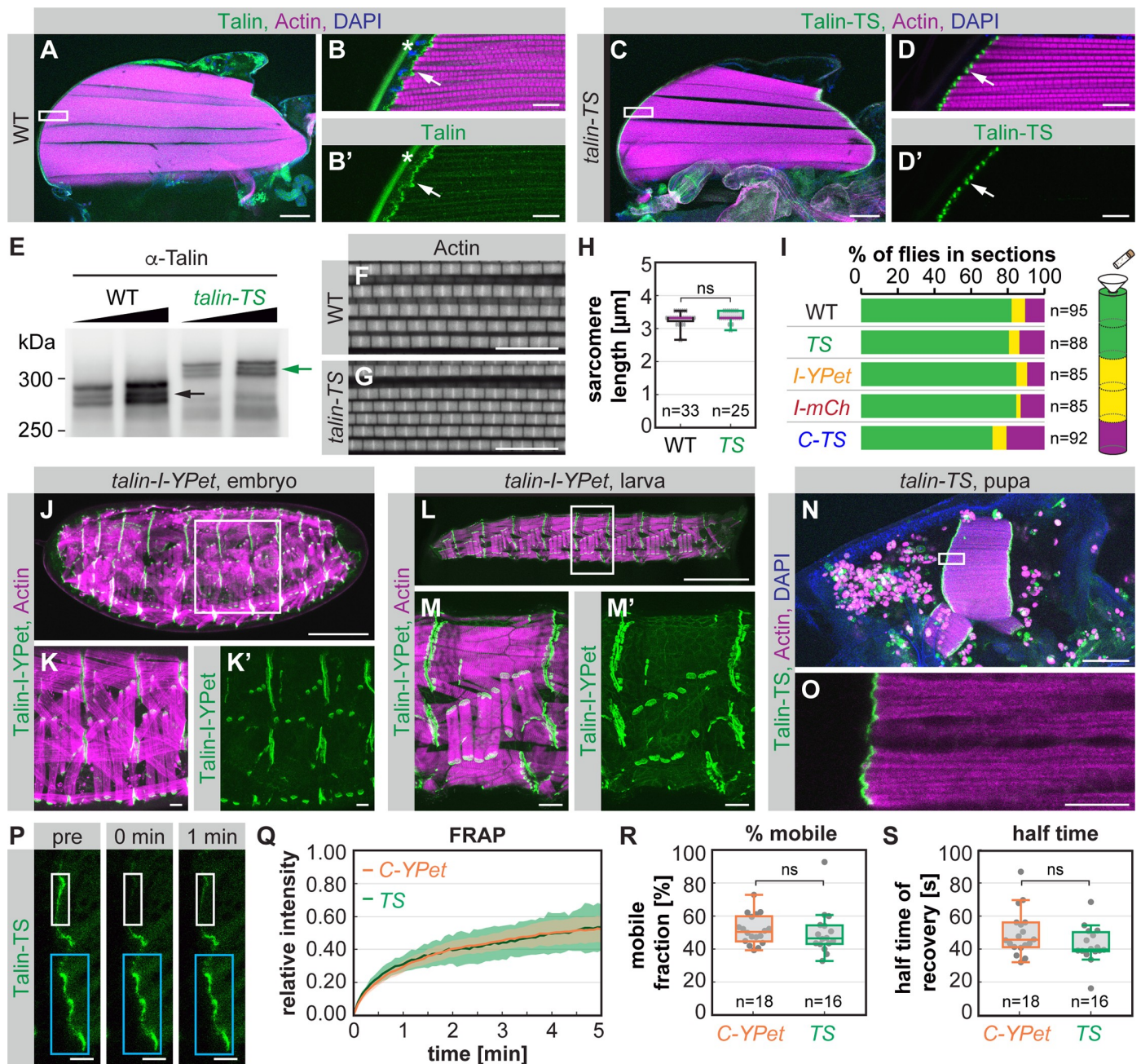


Fig 2. Verification of Talin tension sensor protein functionality. (A–B) WT adult hemithorax stained with Talin antibody, phalloidin (actin), and DAPI. White box in A indicates zoom-in area shown in B and B'. Note the Talin localization at myofibril tips (arrow). The star indicates background fluorescence from the cuticle. (C–D) *tal**in-TS* adult hemithorax showing Talin-TS localization at myofibril tips (arrow). (E) Western blot of whole fly extract from WT and *tal**in-TS* flies probed with Talin antibody. Note the up-shift of all Talin-TS bands (green arrow) compared to WT (black arrow). (F–H) Phalloidin stainings of adult hemithoraxes showing normal sarcomere morphology in WT (F) and *tal**in-TS* (G) flies, and normal sarcomere length (H) (Mann Whitney test, ns: $p > 0.05$). (I) Flight test (two-way ANOVA, no significant differences compared to WT in 6 replicates). (J–O) Talin-I-YPet or Talin-TS expression at different stages of development. Live images of a stage 17 *tal**in-I-YPet* embryo (J–K) and an L3 larva (L–M) co-expressing *Mef2-GAL4*, *UAS-mCherry-Gma* as a muscle actin marker. (Because the actin marker contains mCherry, we used Talin-I-YPet here to avoid signal overlap in the mCherry channel.) A 32 h APF *tal**in-TS* pupa (N–O) stained with phalloidin and DAPI. (P–S) Talin dynamics analyzed by FRAP at flight muscle attachment sites in 24 h APF pupae. Fluorescence intensity was followed in a bleached region (white boxes in P) in comparison to a control region (cyan boxes in P). Time point 0 is directly after bleaching. Talin-TS shows the same recovery dynamics as C-YPet (Q, mean and standard deviation). The mobile fraction (R) and the half time of recovery (S) are indistinguishable (Kolmogorov-Smirnov test, ns: $p > 0.05$). Scale bars are 100 μ m in A, C, J, M, and N, 10 μ m in B, D, F, G, K, O, and P, and 1 mm in L. Underlying data can be found in [S1 Data](#). C-TS, Talin control sensor with HP-sensor module; C-YPet, Talin with C-terminal YPet; fluorescence recovery after photobleaching; h APF, hours after puparium formation; HP, Villin headpiece; I-mCh, Talin with internal mCherry; I-YPet, Talin with internal YPet; ns, not significant; TS, Talin tension sensor with HP-sensor module; WT, wild type; YPet, yellow fluorescent protein for energy transfer.

<https://doi.org/10.1371/journal.pbio.3000057.g002>

internal position nor the insertion of the sensor module at the C-terminus causes flight defects (Fig 2I). Fifth, we confirmed that Talin-TS (or Talin-I-YPet) is expressed correctly at all developmental stages (embryo, larva, and pupa) and is detected most prominently at muscle attachment sites as previously reported for endogenous Talin (Fig 2J–2O) [31]. Finally, we assessed the molecular dynamics of Talin-TS at flight muscle attachments using fluorescence recovery after photobleaching (FRAP). We compared the internal tension sensor to Talin-C-YPet, which is tagged at a functionally verified position [32], and found that internal tagging of Talin does not alter its molecular dynamics. Both the mobile fraction as well as the recovery half time are indistinguishable from C-terminally tagged Talin (Fig 2P–2S). Together, these data demonstrate that the tension sensor module is properly incorporated into Talin and the resulting protein is functional. Thus, Talin-TS is suitable for the quantification of mechanical tension across Talin in any tissue and at any developmental stage of *Drosophila* in vivo.

Forces across *Drosophila* Talin in primary muscle fiber cultures

To ensure that our approach is comparable to previous Talin force measurements in cultured mammalian cells, we established muscle fiber cultures by incubating primary myoblasts in vitro for 5 to 7 d [33,34]. Isolated myoblasts from *talin-I-YPet* embryos differentiated into striated, often multinucleated muscle fibers and efficiently adhered to the underlying plastic substrate (Fig 3A and 3B). In these cells, Talin-I-YPet localizes to adhesions at the fiber tips and at myofibril ends as well as to costameres, which connect myofibrils at the sarcomeric Z-discs to the cell membrane [35]. Primary muscle fibers generated from *talin-I-YPet*, *talin-TS*, and *talin-C-TS* embryos display similar morphologies (Fig 3C–3E) and contract spontaneously (S1 Movie). Adhesions at the fiber tips do not move during these contractions, whereas costameres are mobile and thus are not fixed to the plastic substrate (Fig 3F).

For establishing force measurements using these primary fiber cultures, we performed fluorescence lifetime imaging microscopy (FLIM) to determine the FRET efficiency of the Talin tension sensor containing the HP-sensor module (TS) compared to the zero-force control (C-TS). We created distinct masks for Talin FRET signals either in the entire fiber or specifically in cell-substrate adhesions at the fiber tips or in costameres along myofibrils (Fig 3G–3J). Consistent with previous Talin force measurements in cultured fibroblasts [11,17], we observed a reduction in FRET efficiency of TS compared to the control C-TS within the entire fiber, indicating that Talin indeed experiences mechanical forces in these adherent, primary muscle fibers (Fig 3K). As expected, we find higher average forces across Talin at muscle-substrate adhesions compared to the rest of the cell. In costameres, which are not fixed to the plastic substrate, the FRET efficiency of TS is indistinguishable from the control, indicating that forces across Talin at costameres are lower and do not exceed 6 to 8 pN (Fig 3K). Together, these data demonstrate that the *Drosophila* Talin-TS reports similar Talin forces at adhesions of cultured muscle fibers as were previously described for Talin in focal adhesions of mammalian fibroblasts [11,12,17].

Tissue forces during *Drosophila* muscle–tendon development in vivo

To quantify forces across Talin in vivo, we chose the developing muscle–tendon attachments of the flight muscles as a model system, which critically depend on integrin and Talin function [24,31]. At 20 hours after puparium formation (h APF), the developing myotubes have initiated contact with the tendon epithelium, and immature muscle attachment sites are formed (Fig 4A). While they mature, the myotubes compact and the tendon epithelium forms long cellular extensions. By 30 h APF, the myotubes have reached their maximally compacted stage (Fig 4A) and have initiated myofibrillogenesis. Thereafter, the muscles elongate and grow to

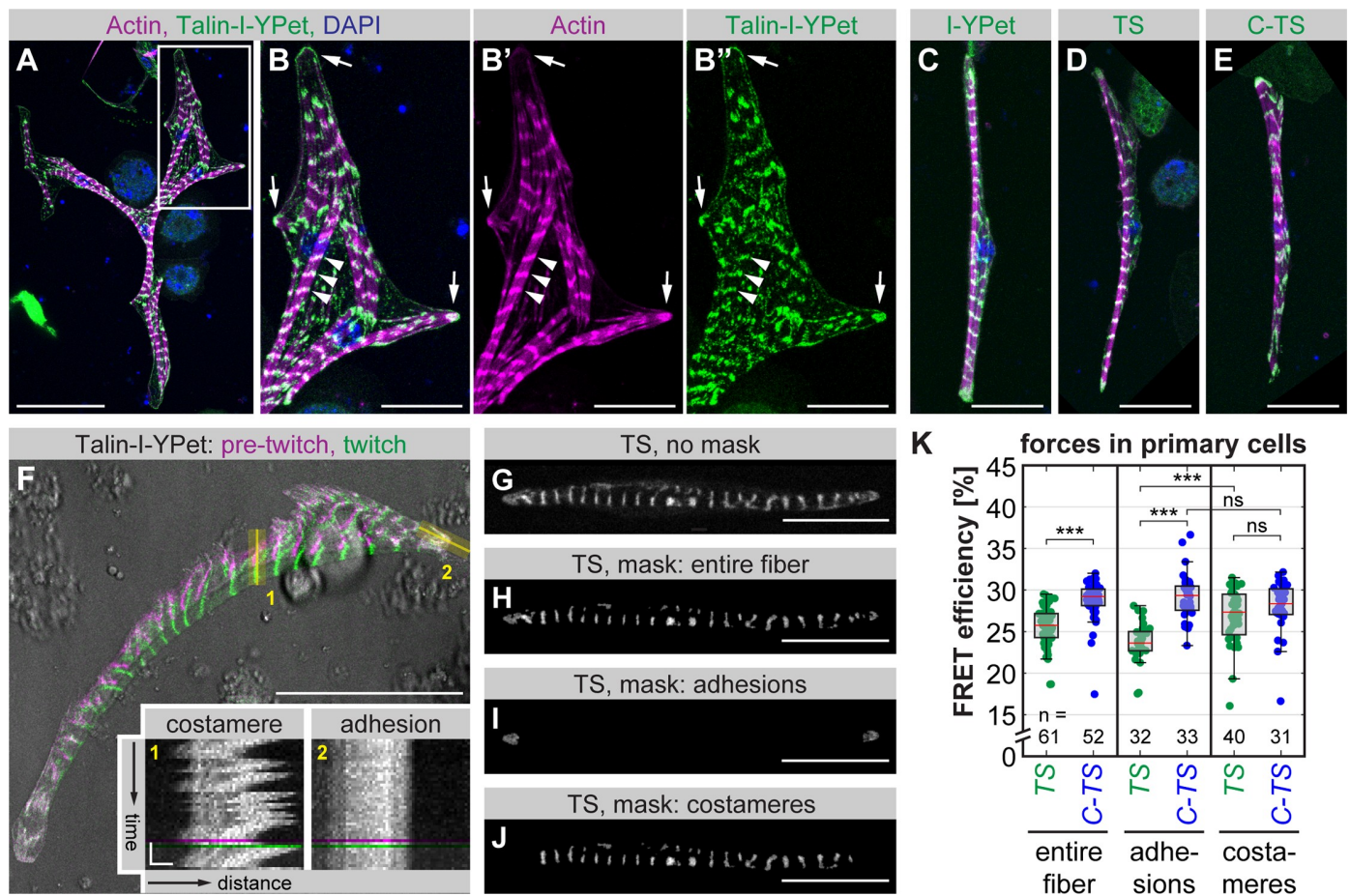


Fig 3. Talin-TS reveals forces in primary muscle fibers. (A–B) Primary myoblasts isolated from *talin-I-YPet* embryos were differentiated and stained with phalloidin and DAPI on day 6. White box in A indicates zoom-in area in B. In differentiated muscle fibers, Talin-I-YPet localizes to adhesions at fiber tips (arrows) and to costameres along myofibrils (arrowheads). (C–E) Primary muscle fibers differentiated from *talin-I-YPet* (C), *talin-TS* (D), or *talin-C-TS* (E) embryos stained with phalloidin (magenta) and DAPI (blue) show similar morphologies and Talin localization (green). (F) Transmission light image (grey) of a twitching primary muscle cell overlaid with Talin-I-YPet signal pre-twitch (magenta) and during the twitch (green), and kymographs of the regions indicated in yellow. Note that costameres move with contractions, while adhesions are fixed to the substrate. See [S1 Movie](#). (G–J) Masking of cells for force analysis. From the original image (G), masks from the entire fiber (H), from adhesions at fiber tips (I), or from costameres (J) were created. (K) Talin forces measured by FLIM-FRET. A decrease in FRET efficiency of Talin-TS (TS) compared to the C-terminal zero-force control (C-TS) indicates force. Note that Talin in adhesions but not in costameres experiences a significant amount of force (Kolmogorov-Smirnov test, *** $p < 0.001$, ns: $p > 0.05$). Scale bars are 50 μm in A and F and 20 μm in B–E and G–J. Scale bars in kymographs in F are 10 s and 2 μm . Underlying data can be found in [S1 Data](#). C-TS, Talin control sensor with HP-sensor module; FLIM, fluorescence lifetime imaging microscopy; FRET, Förster resonance energy transfer; HP, Villin headpiece; I-YPet, Talin with internal YPet; ns, not significant; TS, Talin tension sensor with HP-sensor module; YPet, yellow fluorescent protein for energy transfer.

<https://doi.org/10.1371/journal.pbio.3000057.g003>

fill the entire thorax by the end of the pupal stage [29]. Previous studies using laser-induced microlesions in developing tendons had shown that increasing mechanical tension is built up in the muscle–tendon tissue from 18 h to 22 h APF and that this tension is required for ordered myofibrillogenesis [24,36]. However, tissue tension at the maximally compacted stage of the muscle fibers at 30 h APF had not been analyzed yet. Therefore, we cut the tendon cells at 20 h and 30 h APF and performed time-lapse imaging to quantify the tendon tissue recoil. As a proxy for tissue tension, we calculated the initial recoil velocity from the first 2 frames after the cut (300 ms) and found that it remains high at 30 h APF (Fig 4B–4G, S2 Movie and S3 Movie).

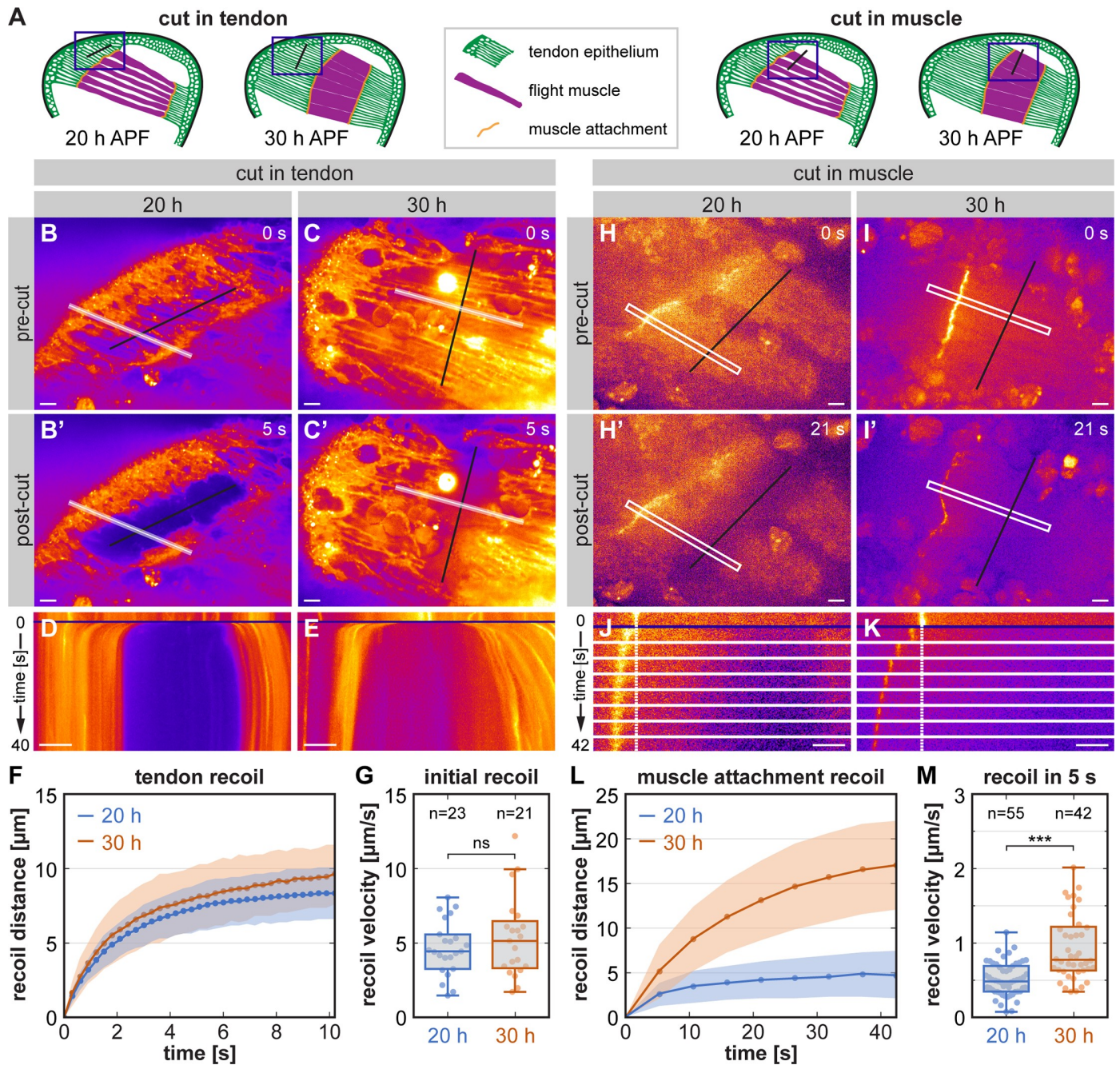


Fig 4. The muscle-tendon system is exposed to high tissue tension during development. (A) Schemes of developing flight muscles in the pupal thorax at 20 h and 30 h APF. Blue boxes indicate the areas imaged during the laser cutting experiments. Black lines indicate the positioning of the laser cuts either in the tendon epithelium or the muscle. (B-E) Stills from movies of *stripe-GALA*, *Mef2-GALA*, *UAS-brainbow* pupae expressing palmitoylated mCherry in the tendon and muscle tissue (B-C). B' and C' show the tissue recoil after laser cutting the tendon tissue (black line). White lines in B and C indicate areas analyzed in kymographs in D and E highlighting the tissue recoil. Time resolution is 300 ms. See S2 and S3 Movies. (F-G) Quantification of the tendon tissue recoil (F; mean as dots and standard deviation as shaded area) and the initial recoil velocity calculated from the first 2 frames after the cut (G). (Kolmogorov-Smirnov test, ns: $p > 0.05$). (H-K) Stills from movies of pupae expressing Talin-I-YPet as a marker for muscle attachment sites (H-I). H' and I' show the recoil of the muscle attachment after laser cutting the muscle in a 10- μm -thick z-stack (black line). White boxes in H and I indicate areas shown in a time course in J and K. Dashed white lines mark the position of the muscle attachments before the cut. Time resolution is 5.3 s. See S6 and S7 Movies. (L-M) Quantification of the muscle attachment recoil (L; mean as dots and standard deviation as shaded area) and the recoil velocity calculated from the pre-cut image and the first frame after the cut (M). (Kolmogorov-Smirnov test, *** $p < 0.001$). Scale bars are 10 μm . Underlying data can be found in S1 Data. h APF, hours after puparium formation; I-YPet, Talin with internal YPet; ns, not significant; YPet, yellow fluorescent protein for energy transfer.

<https://doi.org/10.1371/journal.pbio.3000057.g004>

To ensure that the high tissue tension is also present in the muscle fibers, we cut the muscle at 20 h and 30 h APF (Fig 4A). Cutting the muscle fibers in a single focal plane is not sufficient to cut the entire fiber in two. However, laser lesions in the muscle induce muscle contractions at 30 h APF but not at 20 h APF (S2 Fig, S4 Movie and S5 Movie). This demonstrates that the immature myofibrils present at 30 h APF are contractile and are stably connected to muscle attachments. A similar observation was made before in *Drosophila* abdominal muscles, in which laser-induced lesions cause a Ca^{2+} pulse that triggers contraction of the immature myofibrils [37]. To sever the entire muscle fibers, we cut repeatedly in a 10- μm -thick z-stack and tracked the recoil of the muscle attachments at 20 h and 30 h APF (Fig 4H–4L, S6 Movie and S7 Movie). Due to the z-stack acquisition, our time resolution was limited to 5 s, and therefore we could not determine the initial recoil velocity precisely. Instead, we quantified the average recoil velocity in the first 5 s and found that it increases from 20 h to 30 h APF, suggesting an overall increase in muscle fiber tension between 20 h and 30 h APF (Fig 4M). In conclusion, tissue tension in the muscle–tendon system remains high and possibly increases further from 20 h to 30 h APF, both in the tendon and the muscle tissue.

Forces across *Drosophila* Talin in vivo

After establishing that tissue forces build up in the muscle–tendon system and remain high until 30 h APF, we measured Talin forces between 18 h and 30 h APF in living pupae at the anterior muscle attachment sites of the dorsal-longitudinal flight muscles using the HP-sensor module (Fig 5A and 5B and workflow in S3 Fig). For calculating the FRET efficiency, we determined the fluorescence lifetime of only the donor in flies expressing YPet at the internal position of Talin (S4A Fig). In addition, we excluded the possibility that FRET between neighbouring molecules (intermolecular FRET) affects our measurements throughout the entire time course (Fig 5C) and confirmed that our lifetime measurements are independent of signal intensity (S4B Fig). We noted that the FRET efficiency of the zero-force control sensor slightly increases over the time course, possibly because the increasing crowding at the attachments restricts the conformational freedom of the sensor and thus may favor FRET (Fig 5D). Therefore, we measured the FRET efficiency of the control sensor in addition to the tension sensor at all developmental time points. In this way, we detected a significant drop in FRET efficiency for Talin-TS compared to the control Talin-C-TS at 18 to 28 h APF (Fig 5D). The FRET efficiency reduction at muscle attachment sites was significantly smaller compared to the *in vitro* measurements of cultured muscle fibers (Fig 3K) or of cultured mammalian fibroblasts [11]. At 30 h APF, no difference in FRET efficiencies was detected, suggesting that there is little or no tension across Talin at this time point. Together, these data suggest that only a small percentage of Talin molecules at muscle attachments experience forces above 6 pN at 18 to 28 h APF. The remaining molecules could either bear no force or forces below 6 pN that cannot be detected by the HP-sensor module. Contrary to our expectation, the average force across Talin decreases during muscle compaction while tissue tension builds up and myofibrils are assembled.

To substantiate these findings, we compared flies carrying the HP-based Talin sensor (6–8 pN) to those with the stable variant HPst (9–11 pN), which only differs in 2 point mutations. We found similar and highly reproducible differences in FRET efficiency (Fig 5E, S4C Fig) indicating that, at 20 to 24 h APF, some Talin molecules even experience forces of ≥ 10 pN at muscle attachment sites. Comparison of TS to its stable variant (stTS) revealed a significant difference in FRET efficiency at 20 h APF, while the respective zero-force controls were indistinguishable (Fig 5E). This demonstrates that a proportion of the mechanically engaged Talin molecules experience a range of forces between 7 and 10 pN at muscle–tendon attachments *in vivo*, further emphasizing that the observed differences are force specific.

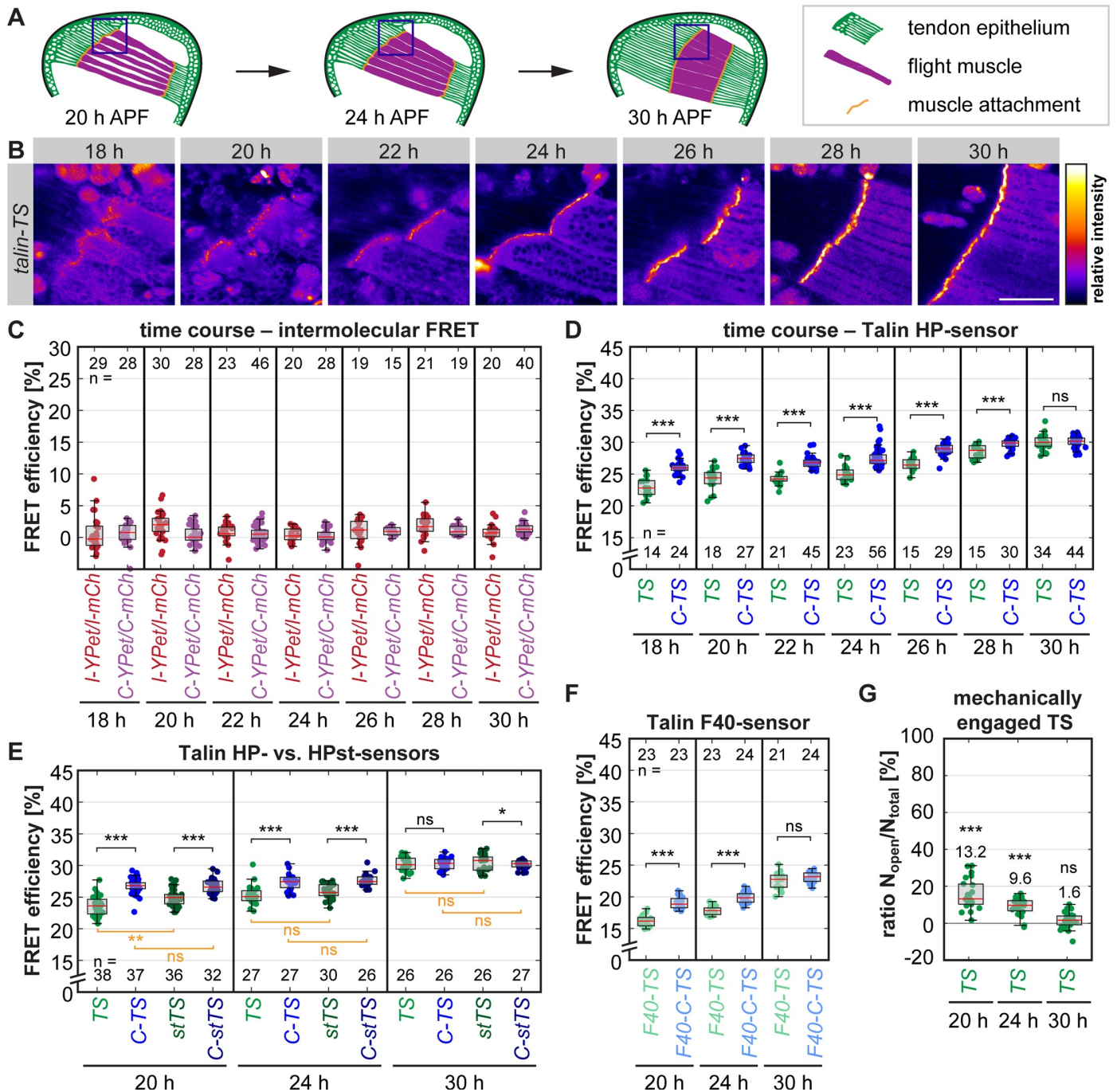


Fig 5. A small proportion of Talin molecules at muscle attachment sites in vivo are mechanically engaged. (A) Schemes of flight muscle development in the pupal thorax at 20, 24, and 30 h APF. Blue boxes indicate areas imaged for force measurements (see B). (B) Images showing Talin-TS localization to maturing muscle attachment sites. Scale bar is 50 μ m. (C) Intermolecular FRET control data measured by FLIM-FRET in a time course comparing heterozygous I-YPet/I-mCh or C-YPet/C-mCh pupae to homozygous I-YPet or C-YPet pupae (set to 0), respectively. Intermolecular FRET is negligible at all time points. (D) Talin forces measured by FLIM-FRET using the HP-sensor module (6–8 pN). A decrease in FRET efficiency of Talin-TS compared to the C-terminal zero-force control (C-TS) indicates force. Note that the average force per molecule is highest in the beginning of the time course. (E) Comparisons of TS (6–8 pN) and stTS (9–11 pN) to the C-terminal zero-force controls, C-TS and C-stTS. Note that both sensors indicate forces across Talin at 20 h and 24 h APF (significance indicated in black). Direct comparisons between TS and stTS or the controls are indicated in orange. Note the increase in FRET of stTS compared to TS at 20 h APF. (F) Talin force measurements using the F40-sensor module (1–6 pN). (G) Proportion of mechanically engaged TS determined as the ratio of open (N_{open}) versus total (N_{total}) sensor using biexponential fitting. Significance is indicated in comparison to zero-force control level (set to 0). The raw data are the same as in D. (Kolmogorov-Smirnov test, *** $p < 0.001$, ** $p < 0.01$, * $p < 0.05$; ns: $p > 0.05$). Underlying data can be found in [S1 Data](#). C-mCh, Talin with C-terminal mCherry; C-stTS, Talin control sensor with HPst-sensor module; C-TS, Talin

control sensor with HP-sensor module; C-YPet, Talin with C-terminal YPet; F40, Flagelliform peptide; F40-C-TS, Talin control sensor with F40-sensor module; F40-TS, Talin tension sensor with F40-sensor module; FLIM, fluorescence lifetime imaging microscopy; FRET, Förster resonance energy transfer; F40, Flagelliform peptide; h APF, hours after puparium formation; HP, Villin headpiece; HPst, stable Villin headpiece; I-mCh, Talin with internal mCherry; I-YPet, Talin with internal YPet; ns, nonsignificant; pN, piconewton; stTS, Talin tension sensor with HPst-sensor module; TS, Talin tension sensor with HP-sensor module; YPet, yellow fluorescent protein for energy transfer.

<https://doi.org/10.1371/journal.pbio.3000057.g005>

To test whether the remaining Talin molecules experience forces that are too low to be detected by the HP or HPst sensor modules, we generated flies with the F40 sensor module, which is sensitive to forces of 1 to 6 pN [13]. Again, we quantified a decrease in FRET efficiency relative to the control at 20 h and 24 h APF, but FRET efficiency differences remained small, and no change was observed at 30 h APF (Fig 5F). Thus, a large proportion of the Talin molecules at muscle attachment sites are not exposed to detectable mechanical forces during development.

To quantify the proportion of mechanically engaged Talin molecules at 20 h and 24 h APF, we applied biexponential fitting to our FLIM data and calculated the ratio of open versus closed sensor (Fig 5G, see Methods for details). This analysis revealed that only 13.2% and 9.6% of all Talin molecules are mechanically engaged at 20 h and 24 h APF, which contrasts in vitro measurements of focal adhesions that are characterized by a Talin engagement ratio of about 70% [12].

Each mechanically engaged Talin molecule needs to be bound to an integrin, therefore we tested whether the integrin levels at muscle attachment sites may be limiting the amount of force-bearing Talin molecules. However, integrins and Talin are present at comparable levels at muscle attachment sites at 20 h and 30 h APF (S5 Fig). Thus, it is unlikely that a lack of integrins is the primary reason for the surprisingly small proportion of Talin molecules experiencing detectable forces.

Talin concentration at developing muscle attachments

As Talin is thought to play an important mechanical role during tissue formation, we wanted to test whether such a small proportion of mechanically engaged Talin molecules in vivo could still contribute a significant amount of tissue-level tension. We therefore quantified the absolute amount of Talin molecules present at muscle attachment sites by combining in vivo fluorescence correlation spectroscopy (FCS) with quantitative confocal imaging (see workflow in S6A–S6D Fig). From FCS measurements in the muscle interior, we calculated the counts per particle (CPP) value, i.e. the molecular brightness of a single Talin-I-YPet particle in each pupa. Because such a particle may correspond to a Talin monomer or dimer, we compared the Talin-I-YPet brightness to the brightness of free monomeric YPet expressed in flight muscles and found no significant difference (Fig 6A). We conclude that Talin is mostly monomeric in the muscle interior.

Next, we calculated the Talin concentration at muscle attachment sites by calibrating confocal images using the molecular brightness (CPP) information from the FCS measurements. Using a dilution series of Atto488, we ascertained that the fluorescence intensity increases linearly with the concentration over multiple orders of magnitude in our confocal images (S6E Fig). The resulting images with pixel-by-pixel Talin concentration values (Fig 6B) indicate an average concentration at the muscle attachment of 5.9 μM (20 h), 10.9 μM (24 h), and 30.9 μM (30 h) (Fig 6C). Thus, the local concentration of Talin molecules increases approximately 2-fold from 20 h to 24 h APF and 5-fold to 30 h APF, indicating that Talin may contribute to the high tissue stress by its strong recruitment to maturing muscle attachment sites.

To confirm this hypothesis, we estimated the density of Talin molecules on the membrane by dividing the number of Talin molecules per pixel by the estimated membrane area in the

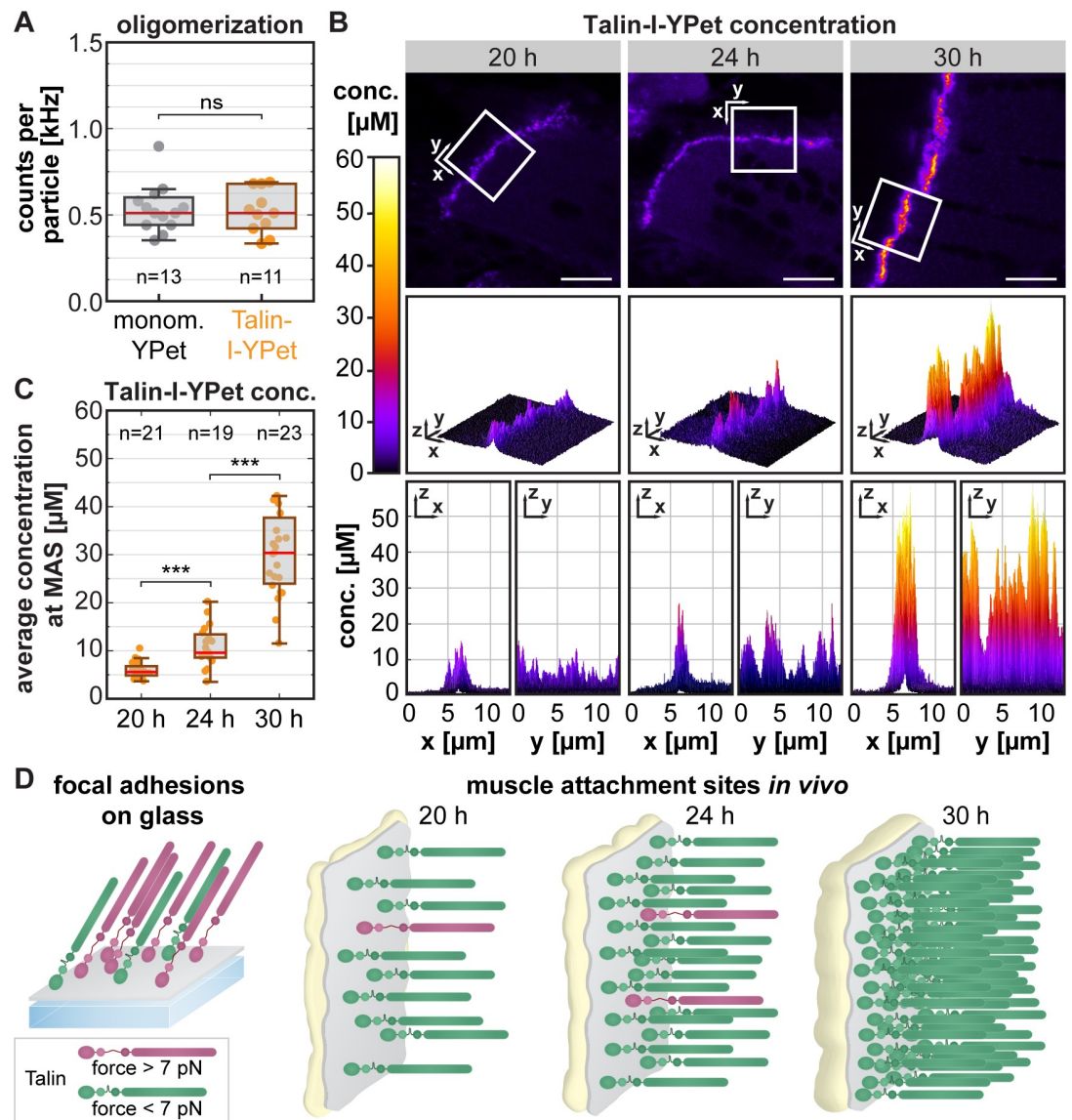


Fig 6. Talin concentration at muscle attachment sites increases 5-fold during attachment maturation. (A) Degree of Talin oligomerization measured by in vivo FCS in the muscle interior. Brightness (in CPP) of monomeric free YPet compared to Talin-I-YPet particles. Note that Talin-I-YPet particles are as bright as monomeric YPet, thus Talin-I-YPet is also monomeric (Kolmogorov-Smirnov test; ns; $p > 0.05$). (B) Absolute Talin-I-YPet concentration measured by FCS in combination with quantitative confocal imaging. Representative calibrated concentration images are shown for 20, 24, and 30 h APF. The boxes mark the area shown in the graphs below from different perspectives as indicated. Scale bars are 10 μm . (C) Quantification of the average Talin-I-YPet concentration at the MASs per image. Note that the concentration increases about 2-fold from 20 h to 24 h APF and 5-fold to 30 h APF. (Kolmogorov-Smirnov test, *** $p < 0.001$) (D) Model of mechanical Talin engagement. In focal adhesions, 70% of the Talin molecules are under force [12], whereas at developing MAS in vivo, less than 15% are mechanically engaged at any given time. As more Talin is recruited during muscle attachment maturation, the proportion of mechanically engaged Talin molecules decreases even further. Underlying data can be found in [S1 Data](#). conc., concentration; CPP, counts per particle; FCS, fluorescence correlation spectroscopy; h APF, hours after puparium formation; I-YPet, Talin with internal YPet; MAS, muscle attachment site; ns, nonsignificant; YPet, yellow fluorescent protein for energy transfer.

<https://doi.org/10.1371/journal.pbio.3000057.g006>

confocal volume (Fig 6D, see [Methods](#) for details). This resulted in about 400, 700, and 2,300 Talin molecules per μm^2 at 20, 24, and 30 h APF, respectively, which corresponds to 20 nm \times 20 nm space per molecule at 30 h APF. This space can easily accommodate the size of a

Talin head domain (about 4 nm × 10 nm) [38], and the estimated density is comparable to previous studies of integrins in focal adhesions [39].

By combining our force quantifications with the estimated Talin density at muscle attachment sites, we calculated the Talin-mediated tissue stress to be in the order of 0.4 to 0.5 kPa at 20 h to 24 h APF (see [Methods](#) for details). These values are remarkably close to a previously published stress estimate of 0.16 kPa determined by traction force microscopy in focal adhesions of cultured cells [40]. Thus, Talin does contribute a significant amount of tissue stress despite the small proportion of mechanically engaged molecules ([Fig 6D](#)).

High Talin levels are required to resist muscle contractions

To investigate the physiological relevance of the high Talin levels at muscle attachments, we aimed to reduce the Talin concentration. The simplest way would be to examine heterozygous animals with only 1 functional Talin copy. However, crossing *talin-I-YPet* to a *talin* null allele resulted only in a minor reduction of Talin levels (to about 80% of the WT level) at 20 h and 30 h APF muscle attachments ([S7A–S7E Fig](#)). Consequently, we did not detect any significant differences in the molecular forces across Talin in these heterozygous animals ([S7F Fig](#)).

Hence, we applied RNA interference (RNAi) to reduce Talin levels. As knockdown of Talin with a general muscle GAL4 driver—such as *Mef2-GAL4*—is embryonic lethal [30], we used the late flight-muscle-specific *Act88F-GAL4* driver [41]. *Act88F-GAL4*-driven *talin* RNAi (*talin-IR*) resulted in a reduction of Talin levels to about 50% at flight muscle attachments at 90 h APF, which is shortly before the adult flies eclose ([Fig 7A–7E](#)). Apart from the reduced Talin levels, the muscle attachments look normal, and all flight muscles remain attached at 90 h APF.

As flight muscles at 90 h APF display a wavy shape and their cuticle has not hardened yet, we instead performed force measurements in adult flies, which have straightened flight muscles and are ready to fly. Talin force measurements in adult flight muscle attachments revealed a significant reduction in FRET efficiency for Talin-TS compared to the zero-force control. This indicates that a proportion of the Talin molecules indeed experience forces above 6 to 8 pN in adults under resting nonflying conditions ([Fig 7F, S8 Fig](#)) and the additional Talin could buffer peak muscle forces during flight.

To test this hypothesis, we investigated whether the reduction of Talin levels by RNAi has consequences during adult stages when flies actively fly and thus produce very high forces on muscle attachments. Indeed, *talin* knockdown flies display a muscle detachment phenotype, whereas in control flies, all muscles remain attached ([Fig 7G–7J](#)). In conclusion, high Talin levels are required for stable muscle attachments that withstand the high forces generated by active muscle contractions in adult animals.

Discussion

Our findings highlight the importance of investigating tissues in their natural mechanical environment in vivo. While the forces per Talin molecule and the tissue stress in vivo are in the same order of magnitude as in previous in vitro studies of focal adhesions [11,12,40], a surprisingly small proportion of Talin molecules (<15%) experience detectable forces during muscle development in vivo. An obvious question arising, therefore, is: what are the other Talin molecules doing at muscle attachment sites, for which we cannot detect significant mechanical forces? Likely, the pool of mechanically engaged Talin molecules exchanges dynamically with the other Talin molecules present at the muscle attachment site. Talin molecules may even remain anchored to integrin and actin, without actomyosin pulling on them continuously. Such a dynamic system would allow the rapid adjustment to changes in tissue forces and

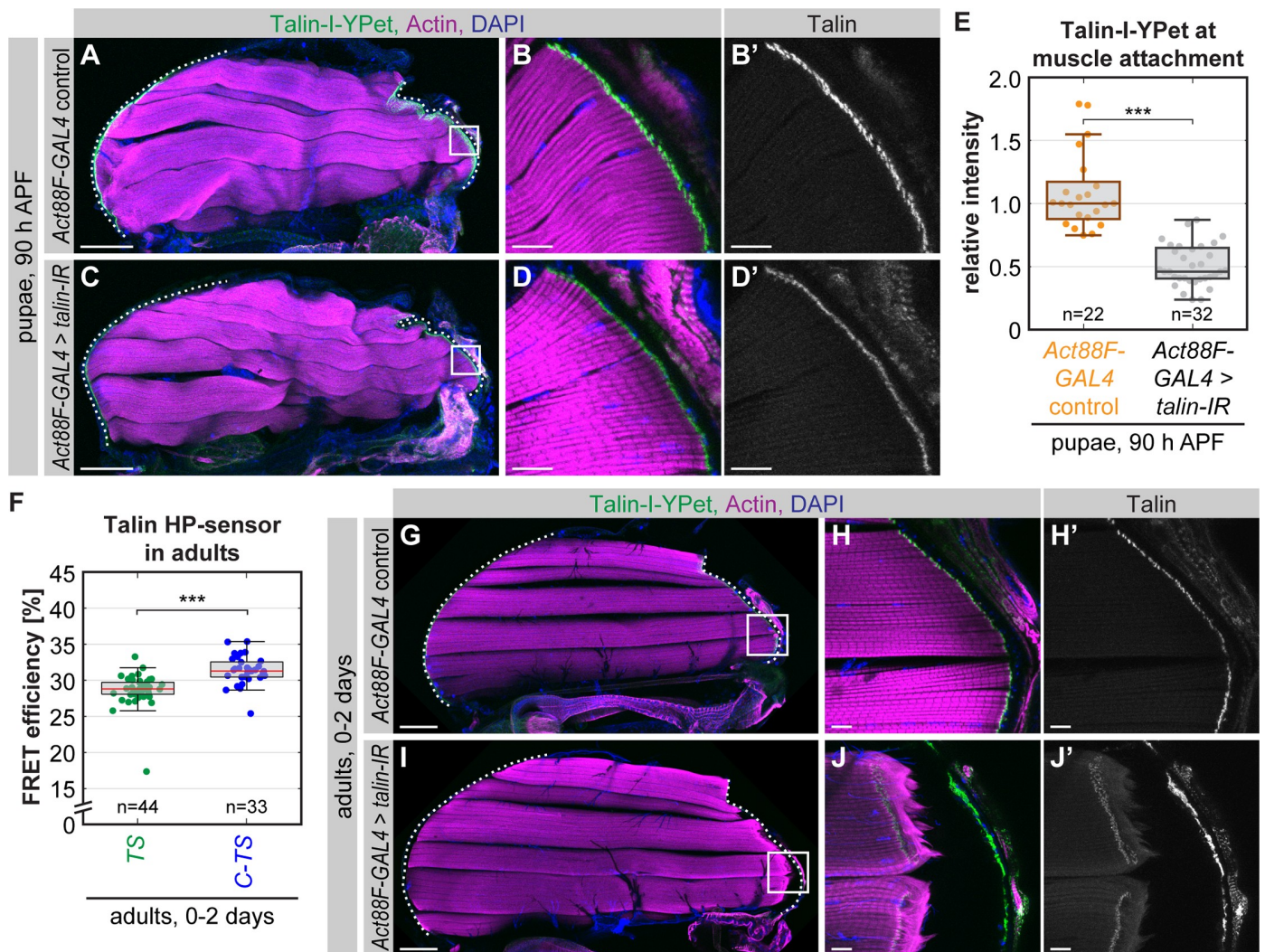


Fig 7. Reduced Talin levels lead to muscle attachment rupture in adults. (A–D) Talin knockdown in 90 h APF pupae. *Act88F-GAL4*; *talin-I-YPet* flies were crossed to *UAS-talin-IR* or WT flies as a control. Hemithoraxes of 90 h APF pupae were stained with phalloidin (actin) and DAPI. White boxes in A and C indicate zoom-in areas shown in B and D. The dotted lines highlight the cuticle. (E) Quantification of Talin-I-YPet intensity at muscle attachment sites. Median control intensity was set to 1. (Kolmogorov-Smirnov test, *** $p < 0.001$). (F) Talin forces in living whole-mount adults measured by FLIM-FRET. (Kolmogorov-Smirnov test, *** $p < 0.001$). (G–J) Talin knockdown phenotype in adults. Control and RNAi adult hemithoraxes were dissected and stained with phalloidin (actin) and DAPI. White boxes in G and I indicate zoom-in areas shown in H and J. The dotted lines highlight the cuticle. Note the ruptured muscle attachment in the *tal* knockdown condition. Scale bars are 100 μ m in A, C, G, and I and 10 μ m in B, D, H, and J. Underlying data can be found in [S1 Data](#). C-TS, Talin control sensor with HP-sensor module; FLIM, fluorescence lifetime imaging microscopy; FRET, Förster resonance energy transfer; h APF, hours after puparium formation; HP, Villin headpiece; I-YPet Talin with internal YPet; *tal*-IR, *tal* RNA interference; TS, Talin tension sensor with HP-sensor module; WT, wild-type; YPet, yellow fluorescent protein for energy transfer.

<https://doi.org/10.1371/journal.pbio.3000057.g007>

thereby prevent rupture of the muscle–tendon attachment upon a sudden increase in tissue stress. In line with this hypothesis, we demonstrated that a high Talin level is particularly important when active muscle contractions result in high forces on the attachments.

Talin was just recently proposed to act as a “shock absorber” based on cell culture experiments [26]. In focal adhesions of cultured cells, the length of Talin can fluctuate dynamically on the time scale of seconds, with Talin being transiently extended from 50 nm up to 350 nm [42]. This can be explained by reversible folding and unfolding of some of the 13 helical bundles in the Talin rod upon actomyosin-dependent stretching of Talin. The hypothesis that

Talin acts as a shock absorber is consistent with our finding that only some molecules experience forces at the same time under baseline conditions, whereas additional molecules may dampen a force increase. A similar force-induced reversible unfolding mechanism was recently proposed for particular immunoglobulin domains in the giant sarcomeric protein titin during muscle contraction cycles at estimated forces of 6 to 8 pN [43]. Thus, it is conceivable that muscle attachments prepare for peak forces during muscle contraction cycles by the recruitment of large amounts of Talin during development.

In addition, the unfolding of the Talin rod domains makes binding sites accessible, leading to the recruitment of vinculin [44]. Magnetic tweezer-based in vitro studies suggested that the rod domain R3 unfolds at about 5 pN [45] and the remaining rod domains unfold when forces larger than 8 pN are applied [46]. Our in vivo force measurements are consistent with those observations suggesting that low pN forces change the Talin structure and make vinculin binding sites accessible, thereby allowing a mechanotransduction response.

Previous estimates of forces transmitted by integrins based on studies of focal adhesions in vitro cover a wide range of forces. Studies using extracellular sensors with synthetic integrin ligands (that report forces based on double-stranded DNA rupture) suggest that integrins can experience very high forces in cells plated on glass (more than 54 pN) [47,48]. However, other data generated with FRET-based extracellular sensors suggest that about 70% of the integrins in focal adhesions experience low forces (less than 3 pN) [49]. These in vitro systems have the advantage that they are accessible for precise manipulations; however, the artificial mechanical environment may have a strong impact on the amount of force experienced by the individual proteins and the number of molecules that are mechanically engaged. Our study provides, to our knowledge, the first insights into molecular forces acting on integrin-mediated attachments in vivo. Here, we focused on developing muscle attachments in pupae; however, our newly established Talin tension sensor fly lines should enable future force measurements in all integrin-based processes in *Drosophila* leading to more insights into mechanobiology in vivo.

In this study, we found that only a small proportion of Talin molecules (<15%) are experiencing forces higher than 6 to 8 pN at developing muscle attachments and thus hypothesize that tissues prevent mechanical failure in vivo with the following mechanism: a large pool of molecules dynamically share the mechanical load, such that a sudden increase in tissue tension can be rapidly buffered by mechanically engaging additional molecules already present at the attachment site. These additional molecules could either be unbound and then rapidly recruited or already bound but not yet under force. Mechanical failure of integrin-mediated attachments in vivo needs to be avoided at all cost, particularly in muscle fibers or cardiomyocytes, to prevent fatal consequences for the animal. Therefore, creating a mechanical buffer system to withstand peak forces is an important concept for the survival of animals.

Methods

Fly strains

All fly work was performed at 27°C to be consistent with previously published work, unless otherwise stated. For details on the genome engineering strategy resulting in Talin tension sensor and control stocks generated in this study (*talín-F40-TS*, *talín-C-F40-TS*, *talín-TS*, *talín-C-TS*, *talín-stTS*, *talín-C-stTS*, *talín-I-YPet*, *talín-C-YPet*, *talín-I-mCh*, and *talín-C-mCh*), see below. Muscles were labelled using *Mef2-GAL4* [50] with *UAS-mCherry-Gma* [51]. To label the tendon and muscle tissue simultaneously, *Mef2-GAL4* and *stripe-GAL4* [52] were used in combination with *UAS-brainbow* [53]. For quantifying Talin-GFP levels, a MiMIC GFP-trap line was used [54]; for Integrin-GFP levels, a homozygous viable GFP knockin line was used [55]. The deficiency line *rhea*⁷⁹ was used as a *talín* null allele [31]; to achieve Talin knockdown,

Act88F-GAL4 [41] was crossed to *UAS-talin-IR* (TF40399, obtained from the VDRC stock center [56]) at 25°C.

Generation of tension sensor and control stocks

Tension sensor and control stocks were generated by combining CRISPR/Cas9-mediated genome engineering with ϕ C31-mediated cassette exchange as described previously [28]. See S1 Fig for a detailed depiction of the two-step strategy. For step 1, single guide RNAs (sgRNAs) were designed with the help of an online tool maintained by the Feng Zhang lab (<http://crispr.mit.edu/>) [57] and transcribed in vitro. After testing sgRNA cutting efficiency in Cas9-expressing S2-cells [58], 2 sgRNAs (70 ng/ μ L) were injected into *Act5C-Cas9*, *DNAI4¹⁶⁹* embryos together with the dsRed donor vector (500 ng/ μ L) containing a dsRed eye marker cassette flanked by attP sites and homology arms. Successful homologous recombination events were identified by screening for red fluorescent eyes and verified by PCR and sequencing. “Ends-in” events were excluded. We call the resulting fly lines *talin-I-dsRed* and *talin-C-dsRed*. For step 2, vasa- ϕ C31 plasmid (200 ng/ μ L) was injected together with attB-donor vector (150 ng/ μ L). Successful exchange events were identified by screening for the absence of dsRed, and correct orientation of the cassette was verified by PCR.

Adult hemithorax staining

Adult hemithoraxes were dissected and stained similar to as previously described [59]. Specifically, the wings and abdomen were cut off the thorax of adult flies with fine scissors, and the thoraxes were fixed for 15 min in 4% PFA in relaxing solution (20 mM sodium phosphate buffer [pH 7.0], 5 mM MgCl₂, 5 mM ATP, 5 mM EGTA, 0.3% Triton-X-100). After washing once with PBST (PBS with 0.3% Triton-X-100), the thoraxes were placed on double-sided tape, and the legs were cut off. Next, the thoraxes were cut sagittally with a microtome blade (dorsal to ventral). The thorax halves were placed in PBST, washed once, and blocked in normal goat serum (1:30) for 30 min at room temperature (RT) on a shaker. Primary antibodies (anti-Talin antibody: 1:500, 1:1 mixture of E16B and A22A, DSHB) were incubated overnight at 4°C on a shaker. Hemithoraxes were then washed 3 times 10 min in PBST at RT and stained with secondary antibody (Alexa488 goat antimouse IgG, 1:500, Molecular Probes) and phalloidin (Rhodamine or Alexa647 conjugate, 1:500 or 1:200, respectively, Molecular Probes) in PBST for 2 h at RT in the dark. After washing 3 times with PBST for 5 min, hemithoraxes were mounted in Vectashield containing DAPI with 2 spacer coverslips on each side. YPet signal after fixation was bright enough for imaging without further amplification.

Dissection of pupae

At 32 h APF, pupae were freed from the pupal case and dissected in PBS in a silicone dish using insect pins [59]. The head and the sides were cut using fine scissors to remove the ventral half of the pupa. Next, the thorax was cut sagittally, and the thorax halves were cut off the abdomen and placed in fixing solution (4% PFA in PBST) for 15 min. The thorax halves were then stained with phalloidin and DAPI like the adult hemithoraxes but without shaking and were mounted using 1 spacer coverslip. At 90 h APF, pupae were dissected like adults after freeing them from the pupal case (see above).

Imaging of stainings

Samples were imaged on a Zeiss LSM 780 scanning confocal microscope with Plan Aplanachromat objectives (10 \times air, NA 0.45 for overview images and 40 \times oil, NA 1.4 for detail images).

For thick samples, a z-stack was acquired and maximum-projected using the ImageJ variant Fiji [60].

Sarcomere length quantification

Sarcomere length was quantified as previously described using the Fiji plug-in MyofibrilJ (<https://imagej.net/MyofibrilJ>) [29]. Briefly, an area with straight, horizontal myofibrils is analyzed by Fourier transformation to find the periodicity of the sarcomeres. One area was analyzed for each hemithorax stained with phalloidin and imaged at 40× and zoom 4.

Western blotting

Western blotting was performed according to standard procedures. Specifically, 15 flies each were homogenized in 100 μ L 6× SDS loading buffer (250 mM Tris [pH 6.8], 30% glycerol, 1% SDS, 500 mM DTT) and heated to 95°C for 5 min. The amount of 200 μ L water was added, and the equivalent of 0.5 fly (10 μ L) and 1 fly (20 μ L), respectively, were loaded onto a NuPAGE Novex 3–8% Tris-Acetate Gel. The transfer to the membrane was carried out overnight with 20 V at 4°C. The membrane was blocked (5% blotting grade blocker, BioRad) and then incubated overnight at 4°C with a 1:1 mixture of anti-Talin antibodies E16B and A22A (1:1,000 in block). For detection, HRP antimouse antibody and Immobilon Western Chemiluminescent HRP Substrate (Millipore) were used.

Flight assays

Male flies (1–3 d old, aged at 25°C) were thrown into a 1 m × 8 cm plexiglass cylinder with 5 marked sections [56]. Flightless flies fall to the bottom of the tube immediately, whereas strong fliers land in the top 2 sections and weak fliers in the third and fourth section. Flight assays were performed in triplicates with 10–20 males each and were repeated twice.

Live imaging of embryos and larvae

Embryos from the cross *yw; talin-I-YPet* to *w; Mef2-GAL4; UAS-mCherry-Gma* were collected on apple juice agar plates for 24 h and dechorionated in 50% bleach (0.024% hypochlorite) for 3 min. Living embryos were mounted in 50% glycerol before imaging. L3 larvae from the same cross were immobilized by immersing them in 60°C water for about 1 s [30] and mounted using a plexiglass slide with a groove and 1 spacer coverslip on each side in 50% glycerol. Five-by-1-tile scan z-stacks were acquired using a 10× objective to image the entire larva.

Sample preparation for live imaging of pupae and adult flies

White pre-pupae were collected and aged at 27°C to the desired time point. Before imaging, a window was cut into the pupal case above the thorax, and the pupae were mounted on a custom-made slide with a groove as previously described [61].

Living adults (0–2 d after eclosion) were mounted similarly: after cutting off the legs to prevent the flies from moving too much, up to 5 flies were each placed in a small drop of 50% glycerol (with 0.13% Triton to ensure that the fluid can wet the water-repellent surface of the cuticle) on a coverslip on their dorsal sides. The wings were then spread out in the drops on the coverslip, and the flies were aligned in a row anterior to posterior. Next, the coverslip was flipped over and placed on a custom-made slide with a groove and 2 spacer coverslips, such that the groove accommodated all 5 flies. In this way, the anterior muscle attachment sites of the dorsal most flight muscles can be imaged directly through the adult cuticle. The flies on

each slide were imaged immediately after mounting to minimize the amount of time that they had spent confined to the slide before the measurement.

FRAP

Living 24 h APF *talin-C-YPet* or *talin-TS* pupae were imaged at 25°C on a Leica SP8 scanning confocal microscope equipped with an argon laser. A 63× water objective (HC PL APO CS, NA 1.2) was used at zoom 2 to image flight muscle attachment sites first for 5 frames before the bleach (512 × 512 px), then a region of interest (ROI; 120 × 40 px) was bleached for 1 frame using all 4 argon laser lines (458 nm, 476 nm, 488 nm, and 514 nm), and finally the fluorescence recovery was followed for 61 frames with a 5 s time resolution. The resulting 5-min movies were analyzed with the Fiji plug-in FRAP profiler (http://worms.zoology.wisc.edu/ImageJ/FRAP_Profiler.java) by comparing the bleached region to a control region of the muscle attachment to correct for gradual bleaching during image acquisition. FRAP curves were each normalized (1 = pre-bleach intensity; 0 = intensity directly after bleaching) and then fit with a single exponential, yielding the recovery half time and the mobile fraction. Movies in which the attachment moved out of plane or out of the bleached region were excluded from the analysis. The experiment was performed on 3 independent experiment days.

Isolation and differentiation of primary muscle fibers

Primary cells were isolated from *Drosophila* embryos and differentiated as previously described [33,34] with the following modifications: embryos (5–7 h old, aged at 25°C) were collected from smaller cages on only one 9-cm molasses plate per genotype. Embryos were homogenized with a Dounce homogenizer using a loose-fit pestle in 4 mL Schneider's *Drosophila* medium (Gibco 21720–024, lot 1668085) and, after several washing steps (using 2 mL medium), were resuspended to a concentration of 3×10^6 cells/mL. Finally, cells were plated in 8-well ibidi dishes (1 cm² plastic bottom for microscopy with ibiTreat surface) coated with vitronectin (optional) at a density of $3\text{--}9 \times 10^5$ cells/cm² and differentiated for 5 to 7 d at 25°C in a humid chamber.

Fixation, staining, and imaging of primary muscle fibers

Primary muscle fibers were fixed on day 6 after isolation with 4% PFA in PBS for 10 min at RT on a shaker. Phalloidin-staining (Alexa647-conjugate; Molecular Probes) was performed overnight in the dark at 4°C. Fixed cells were imaged in PBS on a Zeiss LSM 780 with a 40× oil objective (Plan Aplanachromat, NA 1.4). Live imaging of twitching primary cells was performed on a Leica SP5 confocal with a 63× water objective (HCX PL APO 63×/1.2 W CORR λ_{BL}), acquiring the transmission light channel and the YPet channel simultaneously.

Tissue tension analysis by laser cutting

Laser cutting and imaging was performed similar to a previous study on a custom-built setup with a spinning disc unit and a UV laser (355 nm, 100 mW nominal power) [37]. Here, flight muscles and the connected tendon tissue were imaged at 20 h and 30 h APF in *stripe-GAL4*, *Mef2-GAL4*, *UAS-brainbow* pupae expressing palmitoylated mCherry as a marker in the tendon and muscle tissue or in *talin-I-YPet* pupae with Talin-I-YPet as marker for muscle attachment sites. For performing line cuts in a single z-plane, movies were acquired with a 300-ms time resolution for 150 frames (45 s) using a 40× water objective (NA 1.1, Leica). After the first 10 frames, an 80- to 100- μ m-long line was cut (UV laser pulse repetition rate: 1 kHz, 2 pulses every 0.5 μ m) into the tendon or muscle tissue, and the recoil was followed over time. For

performing line cuts in a 10- μm -thick z-stack in the muscle fibers, z-stack movies were acquired with a z-spacing of 1 μm and an exposure time of 300 ms per slice, resulting in 5.3 s acquisition time per stack. A total of 10 frames were acquired (42.5 s). During the second frame, 5 line cuts were performed, thereby cutting the tissue every 2 μm in z. A single z-plane of the resulting movie was chosen to analyze the tissue recoil.

To quantify the tissue recoil, a line (20 px width) was drawn along the direction of the movement in Fiji, and a kymograph with the average intensity along the line over time was created using the plug-in KymographBuilder [62]. In the kymograph, the movement of the tendon tissue or the muscle attachment was tracked manually by using the multipoint tool and the measure function. The initial recoil velocity of the tendon tissue was calculated from the first 2 frames after the cut. The recoil velocity of the muscle attachment after cutting the muscle in a z-stack was calculated from the position of the attachment in the first frame after the cut (at 5.3 s) compared to the position before the cut.

FLIM

Primary muscle fibers and pupae were imaged live on a Leica SP5 microscope equipped with a pulsed white light laser (NKT Photonics, 80 MHz), a time-correlated single photon counting (TCSPC)-FLIM detector (FLIM X16, LaVision BioTec), and a 545/30 nm emission filter (Chroma). Primary muscle fibers were imaged with a 63 \times water objective (HCX PL APO 63 \times /1.2 W CORR λ_{BL}), and pupae were imaged with a 40 \times water objective (HC PL APO 40 \times /1.1 W CORR CS2). Photon arrival times were detected with a resolution of 0.08 ns in a 12.5 ns time window between laser pulses.

FLIM-FRET data analysis

The FLIM data were analyzed using a custom-written MATLAB (MathWorks) program [11,12]. First, an intensity image was created to manually draw an ROI around the target structure (adhesions/costameres in primary cells or muscle attachment sites in pupae, also see S3 Fig). To create a binary mask of the target structure, Multi-Otsu thresholding with 3 classes was applied to the signal in the ROI blurred with a median filter (3 \times 3 pixels), and holes in the mask containing the brightest class were filled. Photon arrival times of all photons inside the mask were plotted in a histogram, and the tail of the curve was fitted with a monoexponential decay yielding the fluorescence lifetime τ . Fits with more than 5% relative error in lifetime determination were excluded from further analysis. For dimmer samples (primary fiber cultures and intermolecular FRET pupae), we used a 10% relative error cut-off. The FRET efficiency E was calculated according to the following formula, with τ_{DA} being the lifetime of the donor in presence of the acceptor and τ_D the lifetime of the donor alone:

$$E = 1 - \frac{\tau_{DA}}{\tau_D} \quad (1)$$

For all measurements, τ_D was determined as the median lifetime of Talin-I-YPet in the same experimental conditions. Experiments were repeated 2 to 5 times on different experiment days with 10 to 15 pupae/cells imaged per genotype and day.

Calculation of the proportion of mechanically engaged Talin

We determined the number of mechanically engaged (= open) tension sensor N_{open} relative to the total number of molecules N_{total} at the muscle attachment site using biexponential fitting similar to as previously described [12]. Briefly, we assumed that the fluorescence decay from a tension sensor FLIM measurement can be described by 2 lifetimes: the lifetime of the open

sensor τ_{noFRET} and the lifetime of the closed sensor undergoing FRET τ_{FRET} . The lifetime of the open sensor τ_{noFRET} approximately corresponds to the lifetime of the donor alone, because of the large contour length increase upon opening of the sensor. Thus, we determined the lifetime τ_{noFRET} by using a monoexponential fit on Talin-I-YPet data as described above. The lifetime τ_{FRET} was determined from zero-force control (Talin-C-TS) data. Since the Talin-C-TS sample contains fully fluorescent sensor (τ_{FRET}) and sensor with nonfluorescent mCherry acceptor (τ_{noFRET}), we used a biexponential fit with fixed τ_{noFRET} to determine τ_{FRET} . The 2 lifetimes τ_{noFRET} and τ_{FRET} were then fixed and used to fit Talin-TS and Talin-C-TS data biexponentially, thereby determining the relative contributions of photons from molecules with these two lifetimes. From this, the relative number of molecules with τ_{noFRET} and τ_{FRET} was calculated, taking into account that FRET reduces the number of photons detected in the donor channel. Finally, the ratio N_{open}/N_{total} was determined by normalizing the Talin-TS values to the respective Talin-C-TS values.

Relative quantification of protein levels

For the relative quantification of Talin-GFP and Integrin-GFP (β PS-GFP, Mys-GFP) levels at flight muscle attachments, living 20 h and 30 h APF pupae (mounted as described above) were imaged on a Zeiss LSM 780 scanning confocal microscope with a 40 \times oil objective (Plan Aplanachromat, NA 1.4) using the same laser power and gain settings for Talin- and Integrin-GFP pupae. Muscle attachments were traced manually with the free-hand selection tool in Fiji using a fixed line width (40 px for 20 h APF and 20 px for 30 h APF). The intensity in the area along the line was averaged for each pupa. For each experiment day, the median Talin-GFP intensity of all pupae was set to 1, and the relative Integrin-GFP intensity was calculated. Finally, the data from 3 independent experiment days were merged. Because the Talin-GFP allele is not homozygous viable, both the Talin-GFP and the Integrin-GFP flies were crossed to WT flies for this experiment.

For quantifying Talin-I-YPet levels in heterozygous pupae, *tal**in*-I-YPet flies were crossed to *tal**in* null flies (deficiency *rhea*⁷⁹) [31], and homozygous *tal**in*-I-YPet animals were used as a control. In addition to images acquired on the Zeiss LSM 780 microscope as described above, confocal images from the corresponding FLIM data set (S7F Fig) were used for quantification.

For quantifying Talin-I-YPet levels at muscle attachments at 90 h APF upon *tal**in* knock-down with *Act88F*-GAL4, z-stacks were acquired on the Zeiss LSM 780 microscope with a 10 \times air objective (Plan Aplanachromat objectives, NA 0.45). In a maximum-projected image of the thorax, anterior and posterior flight muscle attachments were traced manually with the free-hand selection tool in Fiji using a line width of 4 px. For this experiment, the flies were crossed at 25 $^{\circ}$ C because at 27 $^{\circ}$ C *Act88F*-GAL4 is detrimental.

FCS

Living *tal**in*-I-YPet pupae were analyzed at 20, 24, and 30 h APF by a combination of confocal microscopy (LSM 780, Zeiss) and FCS using a 40 \times water objective (C-Aplanachromat 40 \times /1.20 W Korr UV-VIS-IR) and the built-in GaAsP detector in single photon counting mode. Prior to the experiment, the correction collar and pinhole position were adjusted with fluorescent Rhodamine 6G in aqueous solution (30 nM in Tris [pH 8]) using the same type of cover glass (Marienfeld, High Precision, 18 \times 18 mm, 170 \pm 5 μ m thickness) as for mounting the pupae [61]. To calibrate the detection volume (excitation 514 nm laser light), we measured FCS (120 s recordings) at 3 different positions 20 μ m above the cover glass surface. Autocorrelation curves were analyzed with our open-source software *PyCorrFit* [63] (version 1.0.1, available online at <http://pycorrfit.craban.de/>). For fitting Rhodamine 6G data, we used a model

accounting for triplet transitions and three-dimensional diffusion (denoted “T-3D” in *PyCorrFit*). The detection volume V_{eff} was calculated based on the measured diffusion time (τ_{diff}) and the published diffusion coefficient $D = 414 \mu\text{m}^2/\text{s}$ [64]:

$$V_{eff} = S \cdot (4\pi \cdot D \cdot \tau_{diff})^{3/2} \quad (2)$$

For all measurements, the axis ratio of the detection volume $S = 5$ was consistently fixed [65].

In living pupae, fluorescent proteins (YPet or Talin-I-YPet) were measured by FCS using a park and probe procedure [66]: in images, 3 positions in the muscle interior next to the muscle attachment site were manually selected for FCS (10× 40 s recordings). For fitting of Talin-I-YPet autocorrelation curves (time bins > 1 μs), a two-component three-dimensional diffusion model with 2 nonfluorescent dark states (denoted “T+T+3D+3D” in *PyCorrFit*) was applied. Transient dark states were assigned either to triplet transitions (τ_{trip1} , T_1) in the time range of 1–20 μs and photochemical flickering (τ_{trip2} , T_2) in the time range of about 200–600 μs [67]. The first diffusion time was assigned to protein diffusion in the muscle interior, whereas the second diffusion term was merely a descriptive term accounting for slow long-tail behaviour that cannot be avoided in a crowded intracellular environment [66]. Autocorrelation curves derived from visibly unstable intensity traces were excluded from further analysis. Due to the high endogenous expression levels, the contribution of noncorrelated background was negligible. Thus, the molecular brightness, i.e., the CPP value, of Talin-I-YPet was determined by dividing the average intensity I (brackets indicate the average) by the number of molecules in the focal volume N , which is dependent on the autocorrelation amplitude $G(0)$ of the autocorrelation function $G(\tau)$ and the dark fractions T_1 and T_2 from the fit:

$$CPP = \frac{\langle I \rangle}{N} = \langle I \rangle \cdot G(0) \cdot (1 - T_1 - T_2) \quad (3)$$

Because freely diffusing YPet diffuses faster than Talin-I-YPet, the signal fluctuations related to flickering and diffusion cannot be distinguished in YPet measurements. Therefore, the autocorrelation curves of free YPet were fitted by a simplified model function accounting only for transient triplet states and 2 diffusive terms, of which the first combines contributions of both protein diffusion and flickering (denoted “T-3D-3D” in *PyCorrFit*). To estimate true particle numbers, we corrected for triplet transitions and flickering globally by using the average fractions T_1 and T_2 from corresponding Talin-I-YPet measurements performed with the same excitation power density:

$$CPP_{YPet} = \frac{\langle I \rangle}{\langle N \rangle} = \langle I \rangle \cdot \langle G(0) \rangle \cdot (1 - \langle T_{1,Talin-I-YPet} \rangle - \langle T_{2,Talin-I-YPet} \rangle) \quad (4)$$

The diffusion constant of freely expressed YPet was in good agreement to other fluorescent proteins in the cytoplasm of living cells, suggesting that the point spread function positioned in the muscle cell is still diffraction limited. This finding justifies the external calibration of the detection volume by Rhodamine 6G.

Calibration of confocal images

For quantification of the absolute Talin-I-YPet concentration at muscle–tendon attachment sites, the developing flight muscles were imaged in photon counting mode (512 × 512 px, pixel dwell time $PT = 50 \mu\text{s}$). Saturation of the detector was carefully avoided by keeping $I(x,y)$ below 2 MHz. The counts in each pixel of an image were calibrated by the molecular brightness (CPP) value determined for Talin-I-YPet in the interior of the same muscle fiber by FCS [66]. Due to the monomeric state of Talin-I-YPet, intensity values stored in each pixel $I(x,y)$

could be directly transformed into numbers of Talin molecules:

$$N(x, y) = \frac{I(x, y)}{CPP \cdot PT} \quad (5)$$

Using the Avogadro constant (N_A) and the detection volume (V_{eff}) as determined by Rhodamine 6G measurements, we then calculated concentration maps:

$$c(x, y) = \frac{N(x, y)}{N_A \cdot V_{eff}} \quad (6)$$

Finally, the muscle attachment sites were isolated in the Talin-I-YPet concentration maps by creating a mask with the same thresholding algorithm as used for FLIM-FRET. The concentration values were averaged across pixels within the mask resulting in a mean concentration value per pupa.

A prerequisite for this approach is that the count values per pixel in the acquired confocal images increase linearly with the concentration of the analyte. To test this, we made an Atto488 1:10 dilution series and acquired confocal images 50 μm into a drop of each dilution on a coverslip (covered to prevent evaporation). Quantification of the images indeed revealed a linear relationship between the photon count values and the analyte concentration over 5 orders of magnitude. Thus, low photon count values from Talin-I-YPet in the muscle interior can be directly compared to the high photon count values at the muscle attachment sites.

Estimation of Talin density and tissue stress

To estimate Talin density on the membrane from pixel-by-pixel concentration values, we divided the average number of molecules in the focal volume at the muscle attachment sites by the membrane area in the focal volume. The focal volume was determined by Rhodamine 6G FCS measurements as described above. For the shape of the focal volume, we assumed an ellipsoid with the long axis (z) being 5 times the short axis ($x = y$). Therefore, for a focus volume of 0.32 fL, the membrane area in the z - y plane is 0.63 μm^2 . Taking into account that there are 2 membranes (one from the tendon and one from the muscle) and that the membrane is not flat (ruffles approximately increase the area 2-fold as determined from EM images [68]), the total membrane area in the focal volume is about 2.5 μm^2 .

To estimate Talin-mediated tissue stress, we calculated *force threshold of sensor* \times *Talin density* \times *proportion of mechanically engaged Talin* = 7 pN \times 400 molecules/ μm^2 \times 13.2% = 0.37 kPa for 20 h APF; and 7 pN \times 700 molecules/ μm^2 \times 9.6% = 0.47 kPa for 24 h APF. Note that these values are lower estimates because individual molecules might experience forces higher than 7 pN.

Statistics

Box plots display the median as a horizontal line, and the box denotes the interquartile range. Whiskers extend to 1.5 times the interquartile range from the median and are shortened to the adjacent data point (Tukey). In addition, all data points are shown as dots. Tests used for statistical evaluation are indicated in the figure legends. All data and statistical tests are listed in [S1 Data](#).

Code availability

FLIM-FRET data were analyzed using custom-written MATLAB (MathWorks) code as published previously [11,12]. The code is available upon request.

Supporting information

S1 Fig. Talin tension sensor genome engineering. (A) Top: Gene model of *talin* (*rhea*, *isoform RF*) with the insertion sites (green) in the linker region between Talin head and rod (internal) and at the C-terminus. The gene *CG6638* immediately follows *talin* and therefore was also included. Middle: Tension sensor allele with the sensor module inserted into the target exon in the linker region of Talin. attR sites left in the surrounding introns are shown in light blue. Bottom: C-terminal control sensor allele with the sensor module inserted at the C-terminus of Talin. Gene models are drawn to scale. (B) Scheme showing how tension sensor alleles were generated. Step 1: The target exon in the linker region (green) was replaced by a splice acceptor (SA)-3×Stop-SV40 terminator (pA)-3×P3>dsRed-pA cassette flanked by attP sites (P) using the CRISPR/Cas9 system. Specifically, a dsRed donor vector containing 1.5 to 2.0 kb homology arms was injected into *Act5C*-Cas9 expressing embryos (also carrying a *DNAlig4*¹⁶⁹ mutation to favor homology-directed repair over nonhomologous end-joining [28]) together with 2 in vitro-transcribed sgRNAs (target sites in blue). Successful targeting was identified by screening for fluorescent red eyes. Step 2: ϕ C31-mediated cassette exchange was performed to replace the dsRed cassette by the original target exon including a tension sensor module consisting of YPet, a flexible, calibrated, mechanosensitive linker peptide (dark blue), and mCherry (mCh). To this end, a tension sensor donor vector including flanking attB sites (B) was injected together with *vasa*- ϕ C31 plasmid. Thereby, the tension sensor was inserted seamlessly into the gene (after Talin amino acid 456) except for 2 attR sites (R) in the flanking introns. Successful exchange events were identified by screening for the absence of fluorescent red eyes [28]. Control fly lines with 1 fluorophore and fly lines with different tension sensor modules were generated by repeating step 2 with different donor vectors. (C) Scheme showing how C-terminal zero-force sensor alleles were generated using the same strategy. However, at the C-terminus, 3 exons (green) were replaced by the dsRed cassette in the first step, because the last intron in *talin* is small and the gene *CG6638* follows immediately after *talin*. All 3 exons were put back in the second step together with the sensor module resulting in 1 attR site in a *talin* intron and 1 in an *CG6638* intron. Respective controls with the individual fluorophores were also generated. CRISPR/Cas9, clustered regularly interspaced short palindromic repeats/CRISPR-associated protein 9; mCh, mCherry; sgRNA, single guide RNA. (TIF)

S2 Fig. Laser cutting induces contractions in 30 h APF flight muscles. (A–B) Stills from movies of *talin-I*-YPet pupae before and after an incomplete cut of the muscle in a single z-plane. Black lines mark the position of the laser cuts, and white lines indicate areas analyzed in kymographs in C and D. (C–D) Kymographs showing muscle attachment movement. Dashed lines mark the position of the muscle attachments before the cut (at 0 s). Time resolution is 300 ms. Scale bars are 10 μ m. See S4 and S5 Movies. h APF, hours after puparium formation. (TIF)

S3 Fig. FLIM workflow to determine FRET efficiencies. (A) Living *talin-TS* or control pupae were prepared for imaging by opening a window in the pupal case above the thorax containing the developing flight muscles (magenta) [61]. (B) FLIM was performed on a confocal microscope equipped with a pulsed laser (indicated by green peak) for exciting the donor fluorophore (YPet) and a TCSPC detector for recording photon arrival times (indicated by yellow dot). (C) A YPet intensity image created from the FLIM data was used to manually draw an ROI containing the anterior muscle attachment sites of the dorsal-longitudinal flight muscles close to the surface of the thorax. From this ROI, a mask for the muscle attachment sites was created by Multi-Otsu thresholding. (D) Photon arrival times of all photons inside the mask

were plotted in a histogram. The tail of the curve was fitted by a monoexponential decay to determine the lifetime τ . By comparing the lifetime of the Talin tension sensor τ_{DA} with the lifetime of respective donor-only control τ_D , the FRET efficiency E was calculated. (E) Interpretation of FRET results: a high FRET efficiency indicates mostly closed sensor modules and therefore low force; vice versa, a low FRET efficiency indicates mostly open sensor modules and therefore high force. FLIM, fluorescence lifetime imaging microscopy; FRET, Förster resonance energy transfer; ROI, region of interest; TCSPC, time-correlated single photon counting; YPet, yellow fluorescent protein for energy transfer. (TIF)

S4 Fig. Control measurements for Talin forces detected at muscle attachment sites in vivo.

(A) Lifetime data of donor-only controls at the internal position of Talin (I-YPet) (B) Lifetime data for I-YPet, C-YPet, TS, and C-TS at 24 h APF for each pupa plotted against the average intensity inside its muscle attachment site mask. Red dotted line represents median lifetime value. No correlation between lifetime and intensity could be detected (Pearson correlation coefficient r with 95% confidence interval and p -values are indicated). (C) Reproducibility of FLIM-FRET measurements performed in different years: TS and its stable variant stTS show a reproducible decrease in FRET efficiency compared to the C-terminal zero-force controls C-TS and C-stTS at 20 h APF (Kolmogorov-Smirnov test, $***p < 0.001$, $**p < 0.01$, ns: $p > 0.05$). Underlying data can be found in [S1 Data](#). C-TS, Talin control sensor with HP-sensor module; C-stTS, Talin control sensor with HPst-sensor module; C-YPet, Talin with C-terminal YPet; FLIM, fluorescence lifetime imaging microscopy; FRET, Förster resonance energy transfer; h APF, hours after puparium formation; HP, Villin headpiece; HPst, stable Villin headpiece; I-YPet, Talin with internal YPet; ns, nonsignificant; stTS, Talin tension sensor with HPst-sensor module; TS, Talin tension sensor with HP-sensor module; YPet, yellow fluorescent protein for energy transfer. (TIF)

S5 Fig. Integrin levels are comparable to Talin levels at muscle attachment sites. (A–D)

Live imaging of flight muscle attachment sites at 20 h and 30 h APF. Pupae expressing Talin-GFP (A and C) were compared to pupae expressing Integrin-GFP (β PS-GFP) (B and D). Yellow shaded areas in A'–D' indicate attachment regions in which GFP intensity was quantified. Scale bars are 10 μ m. (E) Quantification of Talin- and Integrin-GFP intensity at muscle attachment sites. Median Talin-GFP intensity was set to 1 for 20 h APF and 30 h APF. (Kolmogorov-Smirnov test, $***p < 0.001$, $**p < 0.01$). Underlying data can be found in [S1 Data](#). GFP, green fluorescent protein; h APF, hours after puparium formation. (TIF)

S6 Fig. Quantitative imaging workflow and control measurements for FCS. (A) Living

talin-I-YPet pupae were prepared for quantitative imaging by opening a window in the pupal case above the thorax containing the developing flight muscles (magenta) [61]. (B) A confocal image and 3 FCS measurements were acquired using the same detector on a confocal microscope. (C) Autocorrelation curves from the FCS measurements were fit to obtain a CPP value for each pupa. (D) The CPP value was used to calibrate each image resulting in a pixel-by-pixel concentration image. This image was used to manually draw an ROI around the muscle attachment site. From this ROI, a muscle attachment mask was created automatically by Multi-Otsu thresholding. Finally, the average concentration at the attachment was calculated from the pixel values inside the mask for each pupa. (E) Pixel-by-pixel photon count values measured in confocal images of an Atto488 dye dilution series (mean with standard deviation). Note that the number of detected photons increases linearly with the concentration of the dye

for the entire range measured. Thus, the high intensities at muscle attachment sites can be directly compared to low intensities in the muscle interior of the same confocal image. Underlying data can be found in [S1 Data](#). CPP, counts per particle; FCS, fluorescence correlation spectroscopy; ROI, region of interest.

(TIF)

S7 Fig. Talin levels at muscle attachment sites are only slightly reduced in heterozygous pupae. (A–D) Live imaging of flight muscle attachment sites of homozygous *talin-I-YPet* pupae (2 copies) and heterozygous *talin-I-YPet/rhea⁷⁹* pupae (1 copy). Scale bars are 10 μm . (E) Quantification of Talin-I-YPet (I-YPet) intensities at muscle attachment sites. Median intensity of homozygous pupae was set to 1 for 20 h and 30 h APF. Note that the Talin levels are only reduced to 80% and not 50% in heterozygous pupae. (F) Talin force measurements in homozygous and heterozygous tension sensor (TS) and zero-force control (C-TS) pupae. (Kolmogorov-Smirnov test, $***p < 0.001$, $*p < 0.05$; ns: $p > 0.05$). Underlying data can be found in [S1 Data](#). C-TS, Talin control sensor with HP-sensor module; h APF, hours after puparium formation; HP, Villin headpiece; I-YPet, Talin with internal YPet; ns, nonsignificant; *rhea⁷⁹*, *talin* deficiency; TS, Talin tension sensor with HP-sensor module; YPet, yellow fluorescent protein for energy transfer.

(TIF)

S8 Fig. Control measurements for Talin forces detected at muscle attachment sites in adult flies. (A) Lifetime data of donor-only control at the internal position of Talin (I-YPet) in adults. The measured lifetime is slightly lower than in pupae at 18–30 h APF ([S4A Fig](#)), likely due to the short background lifetime of the adult cuticle that is just above to the muscle attachment sites. (B) Intermolecular FRET control data comparing heterozygous I-YPet/I-mCh or C-YPet/C-mCh pupae to homozygous I-YPet or C-YPet pupae, respectively. Underlying data can be found in [S1 Data](#). C-mCh, Talin with C-terminal mCherry; C-YPet, Talin with C-terminal YPet; FRET, Förster resonance energy transfer; h APF, hours after puparium formation; I-mCh, Talin with internal mCherry; I-YPet, Talin with internal YPet; YPet, yellow fluorescent protein for energy transfer.

(TIF)

S1 Movie. Live imaging of primary muscle fibers. Movie of the twitching primary muscle fiber shown in [Fig 3F](#). Talin-I-YPet signal (green) is overlaid with the transmission light channel (grey) acquired simultaneously. The length of the movie is 1 min with a time resolution of 1.29 s played at 10 \times speed. Scale bar is 10 μm . I-YPet, Talin with internal YPet; YPet, yellow fluorescent protein for energy transfer.

(AVI)

S2 Movie. Tendon tissue laser cutting at 20 h APF. Movie of the *stripe-GAL4*, *Mef2-GAL4*, *UAS-brainbow* pupa shown in [Fig 4B](#). The black line indicates the position of the cut. The length of the movie is 45 s with a time resolution of 300 ms played at 5 \times speed. Scale bar is 10 μm . h APF, hours after puparium formation.

(AVI)

S3 Movie. Tendon tissue laser cutting at 30 h APF. Movie of the *stripe-GAL4*, *Mef2-GAL4*, *UAS-brainbow* pupa shown in [Fig 4C](#). The black line indicates the position of the cut. The length of the movie is 45 s with a time resolution of 300 ms played at 5 \times speed. Scale bar is 10 μm . h APF, hours after puparium formation.

(AVI)

S4 Movie. Muscle laser cutting in a single z-plane at 20 h APF. Movie of the *talin-I-YPet* pupa shown in [S2A Fig](#). The black line indicates the position of the cut. Note that there is no contraction of the muscle induced after the cut. The length of the movie is 45 s with a time resolution of 300 ms played at 5× speed. Two consecutive frames each were averaged to reduce file size. Scale bar is 10 μm. h APF, hours after puparium formation.
(AVI)

S5 Movie. Muscle laser cutting in a single z-plane at 30 h APF. Movie of the *talin-I-YPet* pupa shown in [S2B Fig](#). The black line indicates the position of the cut. Note that the muscle contracts after the cut, showing that the immature myofibrils at this stage are already contractile. The length of the movie is 45 s with a time resolution of 300 ms played at 5× speed. Two consecutive frames each were averaged to reduce file size. Scale bar is 10 μm. h APF, hours after puparium formation.
(AVI)

S6 Movie. Muscle laser cutting in a z-stack at 20 h APF. Movie of the *talin-I-YPet* pupa shown in [Fig 4H](#). The black line indicates the position of the z-stack cut. Note that the muscle attachment recoils away from the cut. The length of the movie is 42.5 s with a time resolution of 5.3 s played at 20× speed. Scale bar is 10 μm. h APF, hours after puparium formation.
(AVI)

S7 Movie. Muscle laser cutting in a z-stack at 30 h APF. Movie of the *talin-I-YPet* pupa shown in [Fig 4I](#). The black line indicates the position of the z-stack cut. Note that the muscle attachment recoils away from the cut. The length of the movie is 42.5 s with a time resolution of 5.3 s played at 20× speed. Scale bar is 10 μm. h APF, hours after puparium formation.
(AVI)

S1 Data. All individual data points and statistical evaluation of the data shown in this manuscript.
(XLSX)

Acknowledgments

The authors are indebted to Carleen Kluger (initial software development for FLIM-FRET data analysis), Paul Müller (PyCorrFit software development), Andreas Bausch and Pablo Fernandez (generous access to and advice on how to use the laser cutting setup), the MPI-Biochemistry imaging core facility, Bettina Stender, Nicole Plewka, Christophe Pitaval and Céline Guichard (fly embryo injections), Xu Zhang (two-step CRISPR/RMCE protocol), Petra Schwille (access to FCS-equipment), and Reinhard Fässler (continuous support).

Author Contributions

Conceptualization: Sandra B. Lemke, Carsten Grashoff, Frank Schnorrer.

Data curation: Sandra B. Lemke.

Formal analysis: Sandra B. Lemke, Thomas Weidemann, Anna-Lena Cost.

Funding acquisition: Carsten Grashoff, Frank Schnorrer.

Investigation: Sandra B. Lemke.

Methodology: Sandra B. Lemke, Thomas Weidemann, Anna-Lena Cost.

Software: Anna-Lena Cost.

Supervision: Frank Schnorrer.

Visualization: Sandra B. Lemke.

Writing – original draft: Sandra B. Lemke, Frank Schnorrer.

Writing – review & editing: Sandra B. Lemke, Thomas Weidemann, Anna-Lena Cost, Carsten Grashoff, Frank Schnorrer.

References

1. Heisenberg C-P, Bellaïche Y. Forces in tissue morphogenesis and patterning. *Cell*. Elsevier; 2013; 153: 948–962. <https://doi.org/10.1016/j.cell.2013.05.008> PMID: 23706734
2. Lecuit T, Lenne P-F, Munro E. Force generation, transmission, and integration during cell and tissue morphogenesis. *Annu Rev Cell Dev Biol*. 2011; 27: 157–184. <https://doi.org/10.1146/annurev-cellbio-100109-104027> PMID: 21740231
3. Behrndt M, Salbreux G, Campinho P, Hauschild R, Oswald F, Roensch J, et al. Forces Driving Epithelial Spreading in Zebrafish Gastrulation. *Science*. 2012; 338: 257–260. <https://doi.org/10.1126/science.1224143> PMID: 23066079
4. Rauzi M, Lenne P-F, Lecuit T. Planar polarized actomyosin contractile flows control epithelial junction remodelling. *Nature*. 2010; 468: 1110–1114. <https://doi.org/10.1038/nature09566> PMID: 21068726
5. Engler AJ, Sen S, Sweeney HL, Discher DE. Matrix elasticity directs stem cell lineage specification. *Cell*. 2006; 126: 677–689. <https://doi.org/10.1016/j.cell.2006.06.044> PMID: 16923388
6. Maître J-L, Turlier H, Illukkumbura R, Eismann B, Niwayama R, Nédélec F, et al. Asymmetric division of contractile domains couples cell positioning and fate specification. *Nature*. 2016; 536: 344–348. <https://doi.org/10.1038/nature18958> PMID: 27487217
7. Nicklas RB. The forces that move chromosomes in mitosis. *Annu Rev Biophys Biophys Chem*. 1988; 17: 431–449. <https://doi.org/10.1146/annurev.bb.17.060188.002243> PMID: 3293594
8. Nerger BA, Siedlik MJ, Nelson CM. Microfabricated tissues for investigating traction forces involved in cell migration and tissue morphogenesis. *Cell Mol Life Sci*. 2017; 74: 1819–1834. <https://doi.org/10.1007/s00018-016-2439-z> PMID: 28008471
9. Lemke SB, Schnorrer F. Mechanical forces during muscle development. *Mech Dev*. 2017; 144: 92–101. <https://doi.org/10.1016/j.mod.2016.11.003> PMID: 27913119
10. Freikamp A, Cost A-L, Grashoff C. The Piconewton Force Awakens: Quantifying Mechanics in Cells. *Trends Cell Biol*. 2016; 26: 838–847. <https://doi.org/10.1016/j.tcb.2016.07.005> PMID: 27544876
11. Austen K, Ringer P, Mehlich A, Chrostek-Grashoff A, Kluger C, Klingner C, et al. Extracellular rigidity sensing by talin isoform-specific mechanical linkages. *Nat Cell Biol*. 2015; 17: 1597–1606. <https://doi.org/10.1038/ncb3268> PMID: 26523364
12. Ringer P, Weiß A, Cost A-L, Freikamp A, Sabass B, Mehlich A, et al. Multiplexing molecular tension sensors reveals piconewton force gradient across talin-1. *Nat Methods*. 2017; 14: 1090–1096. <https://doi.org/10.1038/nmeth.4431> PMID: 28945706
13. Grashoff C, Hoffman BD, Brenner MD, Zhou R, Parsons M, Yang MT, et al. Measuring mechanical tension across vinculin reveals regulation of focal adhesion dynamics. *Nature*. 2010; 466: 263–266. <https://doi.org/10.1038/nature09198> PMID: 20613844
14. Borghi N, Sorokina M, Shcherbakova OG, Weis WI, Pruitt BL, Nelson WJ, et al. E-cadherin is under constitutive actomyosin-generated tension that is increased at cell-cell contacts upon externally applied stretch. *Proc Natl Acad Sci USA*. 2012; 109: 12568–12573. <https://doi.org/10.1073/pnas.1204390109> PMID: 22802638
15. Conway DE, Breckenridge MT, Hinde E, Gratton E, Chen CS, Schwartz MA. Fluid shear stress on endothelial cells modulates mechanical tension across VE-cadherin and PECAM-1. *Curr Biol*. 2013; 23: 1024–1030. <https://doi.org/10.1016/j.cub.2013.04.049> PMID: 23684974
16. Pandey P, Hawkes W, Hu J, Megone WV, Gautrot J, Anilkumar N, et al. Cardiomyocytes Sense Matrix Rigidity through a Combination of Muscle and Non-muscle Myosin Contractions. *Dev Cell*. 2018; 44: 326–336.e3. <https://doi.org/10.1016/j.devcel.2017.12.024> PMID: 29396114
17. Kumar A, Ouyang M, Van den Dries K, McGhee EJ, Tanaka K, Anderson MD, et al. Talin tension sensor reveals novel features of focal adhesion force transmission and mechanosensitivity. *J Cell Biol*. 2016; 213: 371–383. <https://doi.org/10.1083/jcb.201510012> PMID: 27161398
18. Lagendijk AK, Gomez GA, Baek S, Hesselson D, Hughes WE, Paterson S, et al. Live imaging molecular changes in junctional tension upon VE-cadherin in zebrafish. *Nat Commun*. 2017; 8: 1402. <https://doi.org/10.1038/s41467-017-01325-6> PMID: 29123087

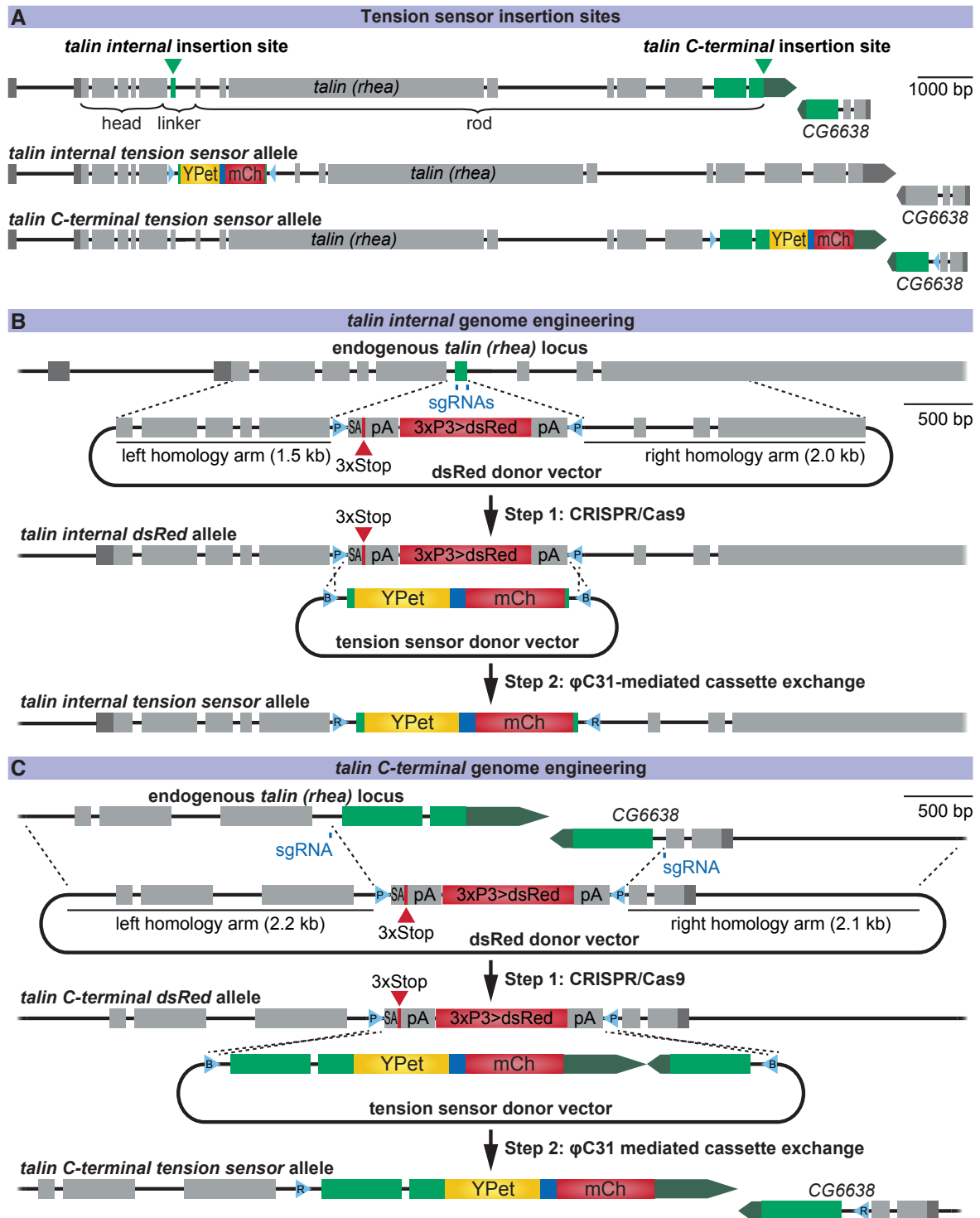
19. Krieg M, Dunn AR, Goodman MB. Mechanical control of the sense of touch by β -spectrin. *Nat Cell Biol.* 2014; 16: 224–233. <https://doi.org/10.1038/ncb2915> PMID: 24561618
20. Röper J-C, Mitrossilis D, Stirnemann G, Waharte F, Brito I, Fernandez-Sanchez M-E, et al. The major β -catenin/E-cadherin junctional binding site is a primary molecular mechano-transducer of differentiation in vivo. *eLife.* 2018; 7: 773. <https://doi.org/10.7554/eLife.33381> PMID: 30024850
21. Suzuki A, Badger BL, Haase J, Ohashi T, Erickson HP, Salmon ED, et al. How the kinetochore couples microtubule force and centromere stretch to move chromosomes. *Nat Cell Biol.* 2016; 18: 382–392. <https://doi.org/10.1038/ncb3323> PMID: 26974660
22. Bökel C, Brown NH. Integrins in development: moving on, responding to, and sticking to the extracellular matrix. *Dev Cell.* 2002; 3: 311–321. [https://doi.org/doi.org/10.1016/S1534-5807\(02\)00265-4](https://doi.org/doi.org/10.1016/S1534-5807(02)00265-4) PMID: 12361595
23. Sun Z, Guo SS, Fässler R. Integrin-mediated mechanotransduction. *J Cell Biol.* 2016; 215: 445–456. <https://doi.org/10.1083/jcb.201609037> PMID: 27872252
24. Weitkunat M, Kaya-Çopur A, Grill SW, Schnorrer F. Tension and force-resistant attachment are essential for myofibrillogenesis in *Drosophila* flight muscle. *Curr Biol.* 2014; 24: 705–716. <https://doi.org/10.1016/j.cub.2014.02.032> PMID: 24631244
25. Bunch TA, Salatino R, Engelsjerd MC, Mukai L, West RF, Brower DL. Characterization of mutant alleles of myospheroid, the gene encoding the beta subunit of the *Drosophila* PS integrins. *Genetics.* 1992; 132: 519–528. PMID: 1427041
26. Klapholz B, Brown NH. Talin—the master of integrin adhesions. *J Cell Sci.* 2017; jcs.190991–12. <https://doi.org/10.1242/jcs.190991> PMID: 28701514
27. Moser M, Legate KR, Zent R, Fässler R. The Tail of Integrins, Talin, and Kindlins. *Science.* 2009; 324: 895–899. <https://doi.org/10.1126/science.1163865> PMID: 19443776
28. Zhang X, Koolhaas WH, Schnorrer F. A versatile two-step CRISPR- and RMCE-based strategy for efficient genome engineering in *Drosophila*. *G3 (Bethesda).* 2014; 4: 2409–2418. <https://doi.org/10.1534/g3.114.013979> PMID: 25324299
29. Spletter ML, Barz C, Yeroslaviz A, Zhang X, Lemke SB, Bonnard A, et al. A transcriptomics resource reveals a transcriptional transition during ordered sarcomere morphogenesis in flight muscle. *eLife.* 2018; 7: e34058. <https://doi.org/10.7554/eLife.34058> PMID: 29846170
30. Schnorrer F, Schönbauer C, Langer CCH, Dietzl G, Novatchkova M, Schernhuber K, et al. Systematic genetic analysis of muscle morphogenesis and function in *Drosophila*. *Nature.* 2010; 464: 287–291. <https://doi.org/10.1038/nature08799> PMID: 20220848
31. Brown NH, Gregory SL, Rickoll WL, Fessler LI, Prout M, White RAH, et al. Talin is essential for integrin function in *Drosophila*. *Dev Cell.* 2002; 3: 569–579. [https://doi.org/doi.org/10.1016/S1534-5807\(02\)00290-3](https://doi.org/doi.org/10.1016/S1534-5807(02)00290-3) PMID: 12408808
32. Yuan L, Fairchild MJ, Perkins AD, Tanentzapf G. Analysis of integrin turnover in fly myotendinous junctions. *J Cell Sci.* 2010; 123: 939–946. <https://doi.org/10.1242/jcs.063040> PMID: 20179102
33. Perrimon N, Zirin J, Bai J. Primary cell cultures from *Drosophila* gastrula embryos. *J Vis Exp.* 2011. <https://doi.org/10.3791/2215> PMID: 21403631
34. Bai J, Sepp KJ, Perrimon N. Culture of *Drosophila* primary cells dissociated from gastrula embryos and their use in RNAi screening. *Nat Protoc.* 2009; 4: 1502–1512. <https://doi.org/10.1038/nprot.2009.147> PMID: 19798083
35. Bendig G, Grimmmler M, Huttner IG, Wessels G, Dahme T, Just S, et al. Integrin-linked kinase, a novel component of the cardiac mechanical stretch sensor, controls contractility in the zebrafish heart. *Genes Dev.* 2006; 20: 2361–2372. <https://doi.org/10.1101/gad.1448306> PMID: 16921028
36. Loison O, Weitkunat M, Kaya-Çopur A, Nascimento-Alves C, Matzat T, Spletter ML, et al. Polarization-resolved microscopy reveals a muscle myosin motor-independent mechanism of molecular actin ordering during sarcomere maturation. *PLoS Biol.* 2018; 16: e2004718. <https://doi.org/10.1371/journal.pbio.2004718> PMID: 29702642
37. Weitkunat M, Brasse M, Bausch AR, Schnorrer F. Mechanical tension and spontaneous muscle twitching precede the formation of cross-striated muscle in vivo. *Development.* 2017; 144: 1261–1272. <https://doi.org/10.1242/dev.140723> PMID: 28174246
38. Elliott PR, Goult BT, Kopp PM, Bate N, Grossmann JG, Roberts GCK, et al. The Structure of the talin head reveals a novel extended conformation of the FERM domain. *Structure.* 2010; 18: 1289–1299. <https://doi.org/10.1016/j.str.2010.07.011> PMID: 20947018
39. Wiseman PW, Brown CM, Webb DJ, Hebert B, Johnson NL, Squier JA, et al. Spatial mapping of integrin interactions and dynamics during cell migration by image correlation microscopy. *J Cell Sci.* 2004; 117: 5521–5534. <https://doi.org/10.1242/jcs.01416> PMID: 15479718

40. Plotnikov SV, Pasapera AM, Sabass B, Waterman CM. Force fluctuations within focal adhesions mediate ECM-rigidity sensing to guide directed cell migration. *Cell*. 2012; 151: 1513–1527. <https://doi.org/10.1016/j.cell.2012.11.034> PMID: 23260139
41. Bryantsev AL, Baker PW, Lovato TL, Jaramillo MS, Cripps RM. Differential requirements for Myocyte Enhancer Factor-2 during adult myogenesis in *Drosophila*. *Dev Biol*. 2012; 361: 191–207. <https://doi.org/10.1016/j.ydbio.2011.09.031> PMID: 22008792
42. Margadant F, Chew LL, Hu X, Yu H, Bate N, Zhang X, et al. Mechanotransduction in vivo by repeated talin stretch-relaxation events depends upon vinculin. *PLoS Biol*. 2011; 9: e1001223. <https://doi.org/10.1371/journal.pbio.1001223> PMID: 22205879
43. Rivas-Pardo JA, Eckels EC, Popa I, Kosuri P, Linke WA, Fernandez JM. Work Done by Titin Protein Folding Assists Muscle Contraction. *Cell Rep*. 2016; 14: 1339–1347. <https://doi.org/10.1016/j.celrep.2016.01.025> PMID: 26854230
44. del Rio A, Perez-Jimenez R, Liu R, Roca-Cusachs P, Fernandez JM, Sheetz MP. Stretching single talin rod molecules activates vinculin binding. *Science*. 2009; 323: 638–641. <https://doi.org/10.1126/science.1162912> PMID: 19179532
45. Yao M, Goult BT, Chen H, Cong P, Sheetz MP, Yan J. Mechanical activation of vinculin binding to talin locks talin in an unfolded conformation. *Sci Rep*. 2014; 4: 4610. <https://doi.org/10.1038/srep04610> PMID: 24714394
46. Yao M, Goult BT, Klapholz B, Hu X, Toseland CP, Guo Y, et al. The mechanical response of talin. *Nat Commun*. 2016; 7: 11966. <https://doi.org/10.1038/ncomms11966> PMID: 27384267
47. Wang X, Ha T. Defining single molecular forces required to activate integrin and notch signaling. *Science*. 2013; 340: 991–994. <https://doi.org/10.1126/science.1231041> PMID: 23704575
48. Wang X, Sun J, Xu Q, Chowdhury F, Roein-Peikar M, Wang Y, et al. Integrin Molecular Tension within Motile Focal Adhesions. *Biophys J*. 2015; 109: 2259–2267. <https://doi.org/10.1016/j.bpj.2015.10.029> PMID: 26636937
49. Chang AC, Mekhdjian AH, Morimatsu M, Denisin AK, Pruitt BL, Dunn AR. Single Molecule Force Measurements in Living Cells Reveal a Minimally Tensioned Integrin State. *ACS Nano*. 2016; 10: 10745–10752. <https://doi.org/10.1021/acs.nano.6b03314> PMID: 27779848
50. Ranganayakulu G, Schulz RA, Olson EN. Wingless signaling induces nautilus expression in the ventral mesoderm of the *Drosophila* embryo. *Dev Biol*. 1996; 176: 143–148. <https://doi.org/10.1006/dbio.1996.9987> PMID: 8654890
51. Millard TH, Martin P. Dynamic analysis of filopodial interactions during the zipper phase of *Drosophila* dorsal closure. *Development*. 2008; 135: 621–626. <https://doi.org/10.1242/dev.014001> PMID: 18184725
52. Schnorrer F, Kalchauer I, Dickson BJ. The transmembrane protein Kon-tiki couples to Dgrip to mediate myotube targeting in *Drosophila*. *Dev Cell*. 2007; 12: 751–766. <https://doi.org/10.1016/j.devcel.2007.02.017> PMID: 17488626
53. Förster D, Luschnig S. Src42A-dependent polarized cell shape changes mediate epithelial tube elongation in *Drosophila*. *Nat Cell Biol*. 2012; 14: 526–534. <https://doi.org/10.1038/ncb2456> PMID: 22446736
54. Venken KJT, Schulze KL, Haelterman NA, Pan H, He Y, Evans-Holm M, et al. MiMIC: a highly versatile transposon insertion resource for engineering *Drosophila melanogaster* genes. *Nat Methods*. 2011; 8: 737–743. <https://doi.org/10.1038/nmeth.1662> PMID: 21985007
55. Klapholz B, Herbert SL, Wellmann J, Johnson R, Parsons M, Brown NH. Alternative mechanisms for talin to mediate integrin function. *Curr Biol*. 2015; 25: 847–857. <https://doi.org/10.1016/j.cub.2015.01.043> PMID: 25754646
56. Dietzl G, Chen D, Schnorrer F, Su K-C, Barinova Y, Fellner M, et al. A genome-wide transgenic RNAi library for conditional gene inactivation in *Drosophila*. *Nature*. 2007; 448: 151–156. <https://doi.org/10.1038/nature05954> PMID: 17625558
57. Cong L, Ran FA, Cox D, Lin S, Barretto R, Habib N, et al. Multiplex Genome Engineering Using CRISPR/Cas Systems. *Science*. 2013; 339: 819–823. <https://doi.org/10.1126/science.1231143> PMID: 23287718
58. Böttcher R, Hollmann M, Merk K, Nitschko V, Obermaier C, Philippou-Massier J, et al. Efficient chromosomal gene modification with CRISPR/cas9 and PCR-based homologous recombination donors in cultured *Drosophila* cells. *Nucleic Acids Res*. 2014; 42: e89. <https://doi.org/10.1093/nar/gku289> PMID: 24748663
59. Weitkunat M, Schnorrer F. A guide to study *Drosophila* muscle biology. *Methods*. 2014; 68: 2–14. <https://doi.org/10.1016/j.ymeth.2014.02.037> PMID: 24625467
60. Schindelin J, Arganda-Carreras I, Frise E, Kaynig V, Longair M, Pietzsch T, et al. Fiji: an open-source platform for biological-image analysis. *Nat Methods*. 2012; 9: 676–682. <https://doi.org/10.1038/nmeth.2019> PMID: 22743772

61. Lemke SB, Schnorrer F. In Vivo Imaging of Muscle-tendon Morphogenesis in *Drosophila* Pupae. *J Vis Exp*. 2018;: e57312–e57312. <https://doi.org/10.3791/57312> PMID: [29443094](https://pubmed.ncbi.nlm.nih.gov/29443094/)
62. Mary H, Rueden C, Ferreira T. KymographBuilder: Release 1.2.4. 2016. <https://doi.org/10.5281/zenodo.56702>
63. Müller P, Schwille P, Weidemann T. PyCorrFit-generic data evaluation for fluorescence correlation spectroscopy. *Bioinformatics*. 2014; 30: 2532–2533. <https://doi.org/10.1093/bioinformatics/btu328> PMID: [24825612](https://pubmed.ncbi.nlm.nih.gov/24825612/)
64. Müller CB, Loman A, Pacheco V, Koberling F, Willbold D, Richtering W, et al. Precise measurement of diffusion by multi-color dual-focus fluorescence correlation spectroscopy. *Europhys Lett*. 2008; 83: 46001–6. <https://doi.org/10.1209/0295-5075/83/46001>
65. Weidemann T. Application of fluorescence correlation spectroscopy (FCS) to measure the dynamics of fluorescent proteins in living cells. *Methods Mol Biol*. 2014; 1076: 539–555. https://doi.org/10.1007/978-1-62703-649-8_24 PMID: [24108643](https://pubmed.ncbi.nlm.nih.gov/24108643/)
66. Weidemann T, Wachsmuth M, Knoch TA, Müller G, Waldeck W, Langowski J. Counting nucleosomes in living cells with a combination of fluorescence correlation spectroscopy and confocal imaging. *J Mol Biol*. 2003; 334: 229–240. <https://doi.org/10.1016/j.jmb.2003.08.063> PMID: [14607115](https://pubmed.ncbi.nlm.nih.gov/14607115/)
67. Steiert F, Petrov EP, Schultz P, Schwille P, Weidemann T. Photophysical Behavior of mNeonGreen, an Evolutionarily Distant Green Fluorescent Protein. *Biophys J*. 2018; 114: 2419–2431. <https://doi.org/10.1016/j.bpj.2018.04.013> PMID: [29706225](https://pubmed.ncbi.nlm.nih.gov/29706225/)
68. Reedy MC, Beall C. Ultrastructure of developing flight muscle in *Drosophila*. II. Formation of the myo-tendon junction. *Dev Biol*. 1993; 160: 466–479. <https://doi.org/10.1006/dbio.1993.1321> PMID: [8253278](https://pubmed.ncbi.nlm.nih.gov/8253278/)

Paper I – Supporting Figures

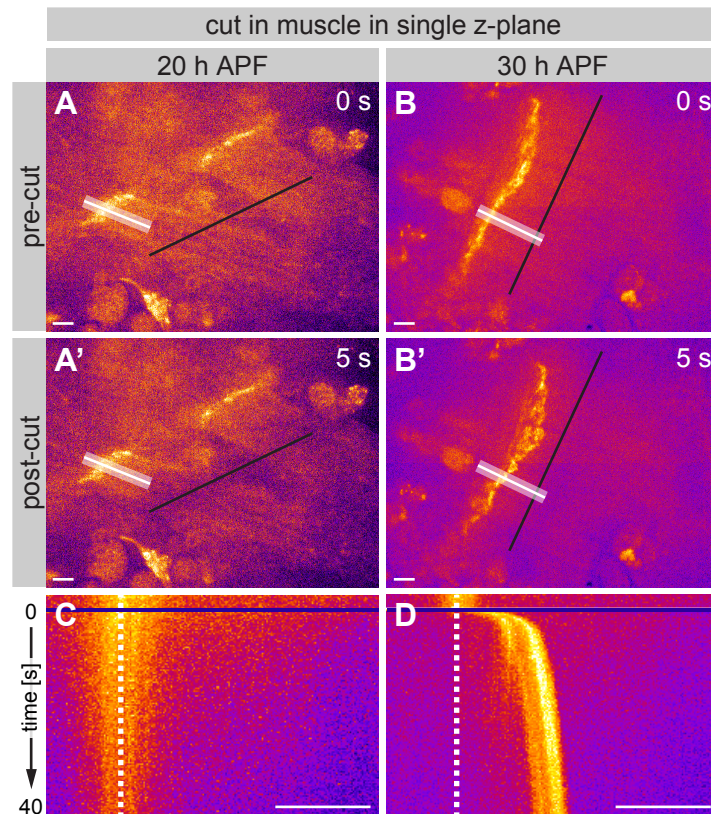
The following pages include the Supporting Figures of **Paper I** reproduced together with their original Figure legends from Lemke et al. (2019).



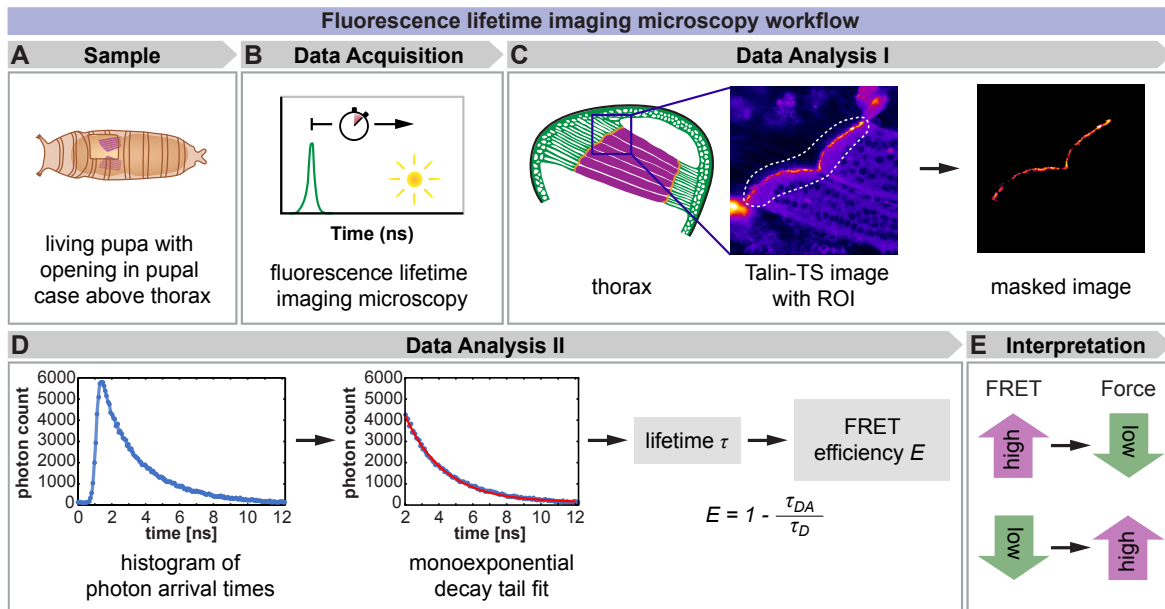
S1 Fig. Talin tension sensor genome engineering. **A.** Top: Gene model of *talin (rhea, isoform RF)* with the insertion sites (green) in the linker region between Talin head and rod (internal) and at the C-terminus. The gene *CG6638* immediately follows *talin* and therefore was also included. Middle: Tension sensor allele with the sensor module inserted into the
(legend continued on the next page)

(legend continued)

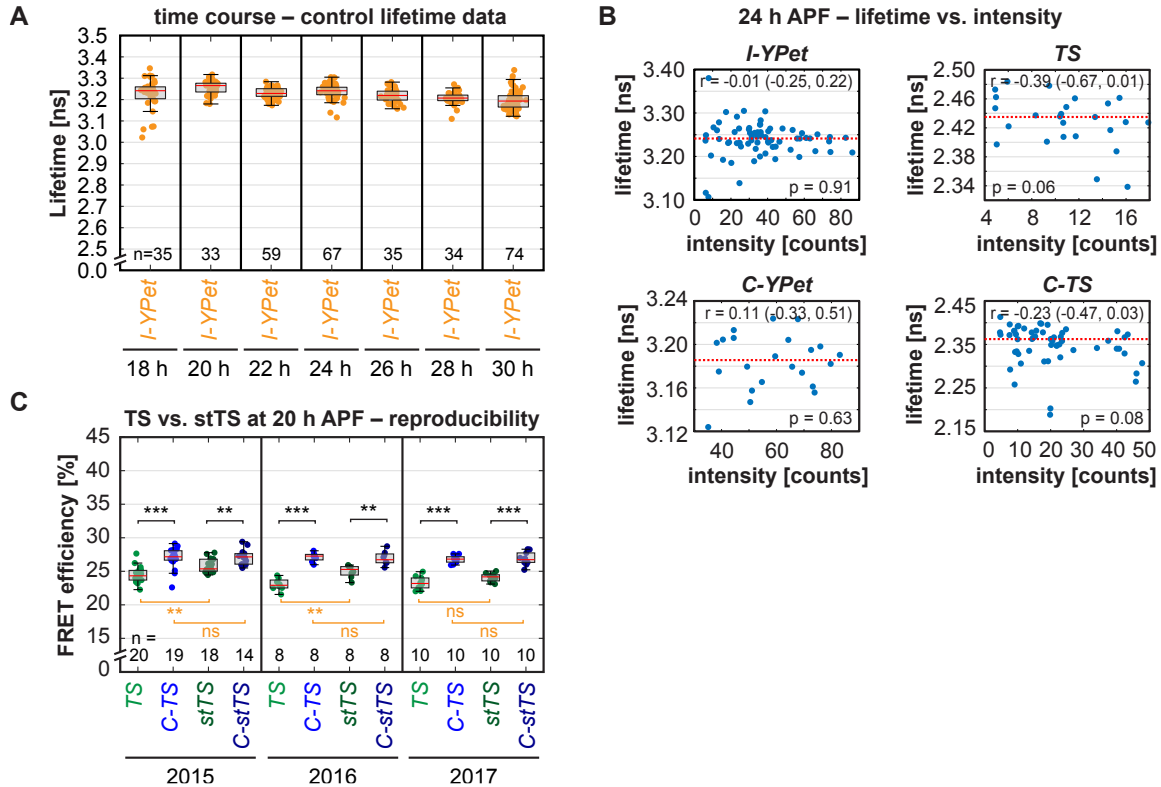
target exon in the linker region of Talin. attR sites left in the surrounding introns are shown in light blue. Bottom: C-terminal control sensor allele with the sensor module inserted at the C-terminus of Talin. Gene models are drawn to scale. **B.** Scheme showing how tension sensor alleles were generated. Step 1: The target exon in the linker region (green) was replaced by a splice acceptor (SA)-3xStop-SV40 terminator (pA)-3xP3>dsRed-pA cassette flanked by attP sites (P) using the CRISPR/Cas9 system. Specifically, a dsRed donor vector containing 1.5 to 2.0 kb homology arms was injected into *Act5C*-Cas9 expressing embryos (also carrying a *DNAIig4*¹⁶⁹ mutation to favor homology-directed repair over nonhomologous end-joining (Zhang et al., 2014a)) together with 2 in vitro-transcribed sgRNAs (target sites in blue). Successful targeting was identified by screening for fluorescent red eyes. Step 2: ϕ C31-mediated cassette exchange was performed to replace the dsRed cassette by the original target exon including a tension sensor module consisting of YPet, a flexible, calibrated, mechanosensitive linker peptide (dark blue), and mCherry (mCh). To this end, a tension sensor donor vector including flanking attB sites (B) was injected together with *vasa*- ϕ C31 plasmid. Thereby, the tension sensor was inserted seamlessly into the gene (after Talin amino acid 456) except for 2 attR sites (R) in the flanking introns. Successful exchange events were identified by screening for the absence of fluorescent red eyes (Zhang et al., 2014a). Control fly lines with 1 fluorophore and fly lines with different tension sensor modules were generated by repeating step 2 with different donor vectors. **C.** Scheme showing how C-terminal zero-force sensor alleles were generated using the same strategy. However, at the C-terminus, 3 exons (green) were replaced by the dsRed cassette in the first step, because the last intron in *talin* is small and the gene *CG6638* follows immediately after *talin*. All 3 exons were put back in the second step together with the sensor module resulting in 1 attR site in a *talin* intron and 1 in an *CG6638* intron. Respective controls with the individual fluorophores were also generated. CRISPR/Cas9, clustered regularly interspaced short palindromic repeats/CRISPR-associated protein 9; mCh, mCherry; sgRNA, single guide RNA.



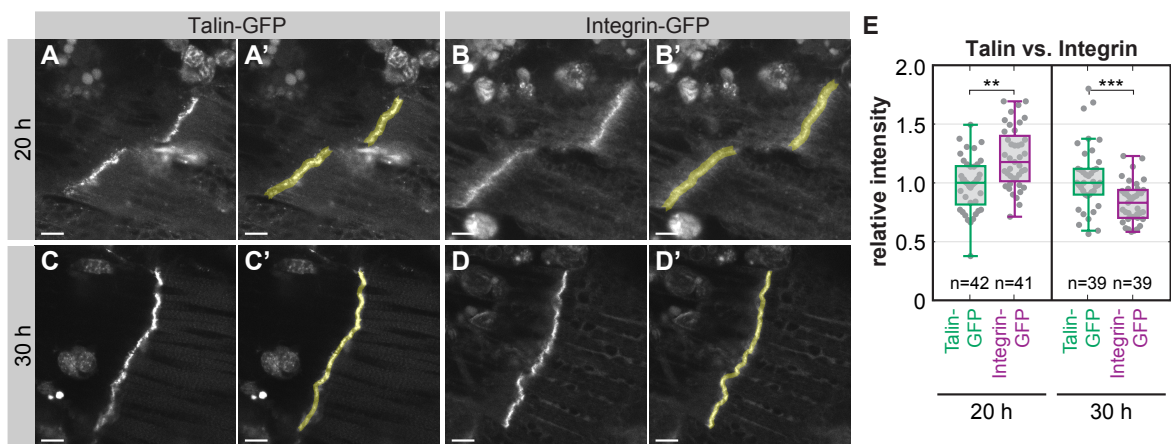
S2 Fig. Laser cutting induces contractions in 30 h APF flight muscles. A–B. Stills from movies of *talin-I-YPet* pupae before and after an incomplete cut of the muscle in a single z-plane. Black lines mark the position of the laser cuts, and white lines indicate areas analyzed in kymographs in C and D. C–D Kymographs showing muscle attachment movement. Dashed lines mark the position of the muscle attachments before the cut (at 0 s). Time resolution is 300 ms. Scale bars are 10 μm . See S4 and S5 Movies. h APF, hours after puparium formation.



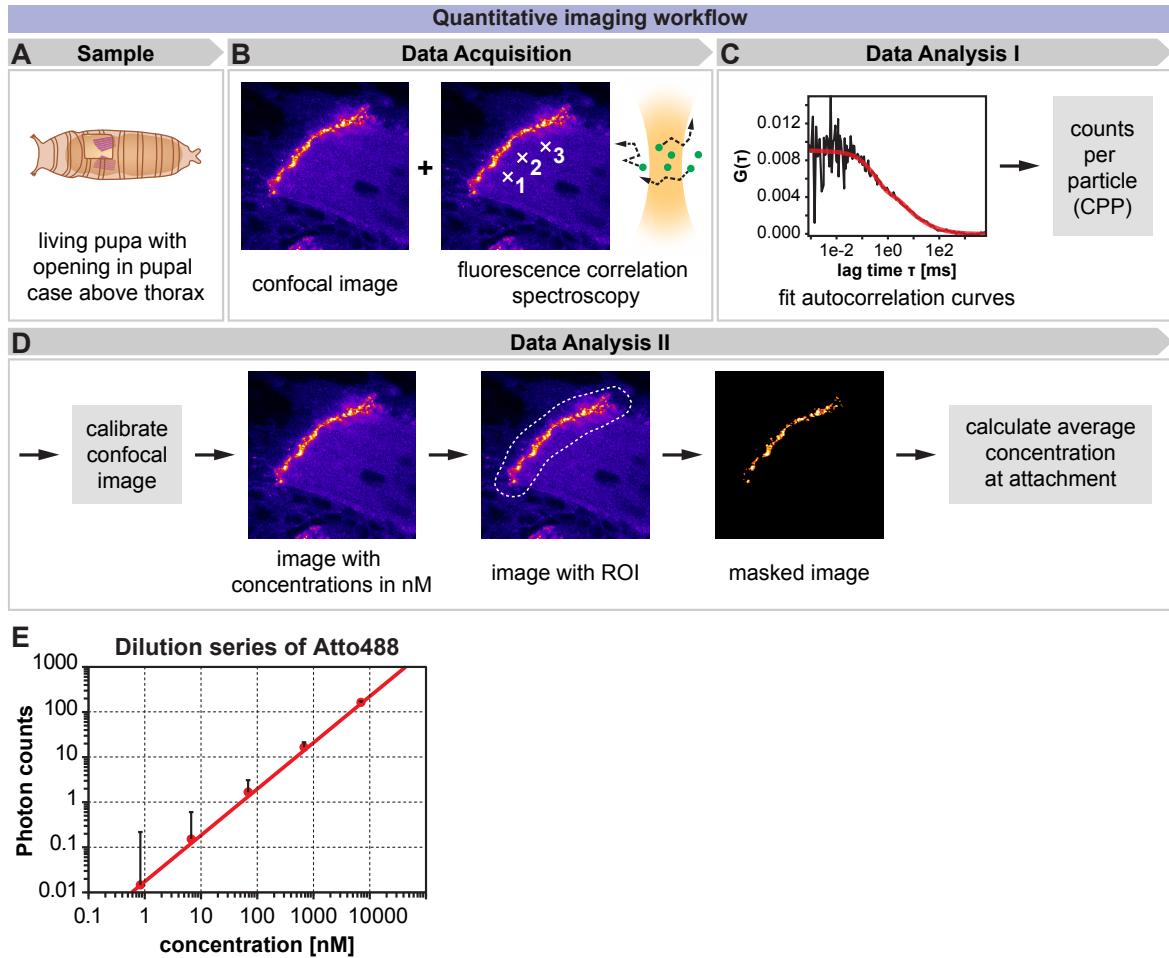
S3 Fig. FLIM workflow to determine FRET efficiencies. **A.** Living *talin-TS* or control pupae were prepared for imaging by opening a window in the pupal case above the thorax containing the developing flight muscles (magenta) (Lemke and Schnorrer, 2018). **B.** FLIM was performed on a confocal microscope equipped with a pulsed laser (indicated by green peak) for exciting the donor fluorophore (YPet) and a TCSPC detector for recording photon arrival times (indicated by yellow dot). **C.** A YPet intensity image created from the FLIM data was used to manually draw an ROI containing the anterior muscle attachment sites of the dorsal-longitudinal flight muscles close to the surface of the thorax. From this ROI, a mask for the muscle attachment sites was created by Multi-Otsu thresholding. **D.** Photon arrival times of all photons inside the mask were plotted in a histogram. The tail of the curve was fitted by a monoexponential decay to determine the lifetime τ . By comparing the lifetime of the Talin tension sensor τ_{DA} with the lifetime of respective donor-only control τ_D , the FRET efficiency E was calculated. **E.** Interpretation of FRET results: a high FRET efficiency indicates mostly closed sensor modules and therefore low force; vice versa, a low FRET efficiency indicates mostly open sensor modules and therefore high force. FLIM, fluorescence lifetime imaging microscopy; FRET, Förster resonance energy transfer; ROI, region of interest; TCSPC, time-correlated single photon counting; YPet, yellow fluorescent protein for energy transfer.



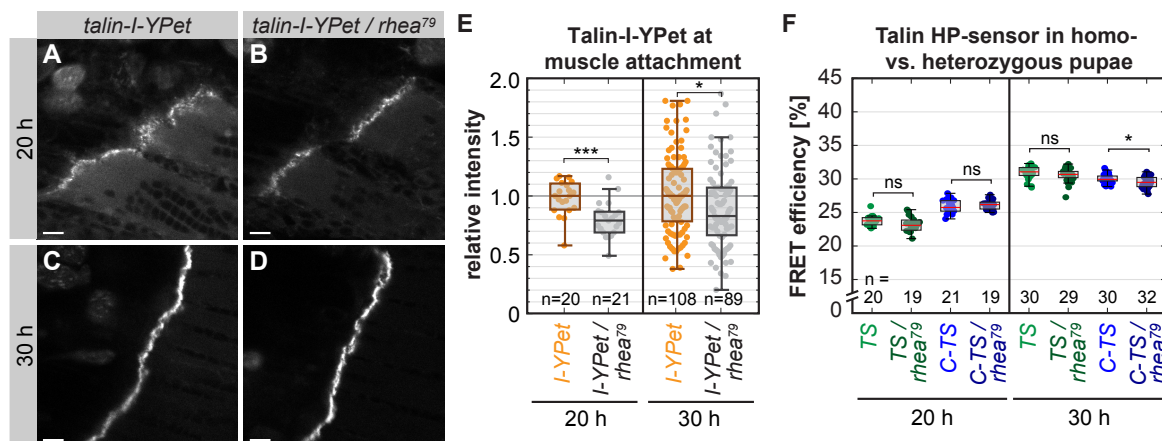
S4 Fig. Control measurements for Talin forces detected at muscle attachment sites in vivo. **A.** Lifetime data of donor-only controls at the internal position of Talin (I-YPet) **B.** Lifetime data for I-YPet, C-YPet, TS, and C-TS at 24h APF for each pupa plotted against the average intensity inside its muscle attachment site mask. Red dotted line represents median lifetime value. No correlation between lifetime and intensity could be detected (Pearson correlation coefficient r with 95% confidence interval and p-values are indicated). **C.** Reproducibility of FLIM-FRET measurements performed in different years: TS and its stable variant stTS show a reproducible decrease in FRET efficiency compared to the C-terminal zero-force controls C-TS and C-stTS at 20 h APF (Kolmogorov-Smirnov test, *** $p < 0.001$, ** $p < 0.01$, ns: $p > 0.05$). Underlying data can be found in S1 Data. C-TS, Talin control sensor with HP-sensor module; C-stTS, Talin control sensor with HPst-sensor module; C-YPet, Talin with C-terminal YPet; FLIM, fluorescence lifetime imaging microscopy; FRET, Förster resonance energy transfer; h APF, hours after puparium formation; HP, Villin headpiece; HPst, stable Villin headpiece; I-YPet, Talin with internal YPet; ns, nonsignificant; stTS, Talin tension sensor with HPst-sensor module; TS, Talin tension sensor with HP-sensor module; YPet, yellow fluorescent protein for energy transfer.



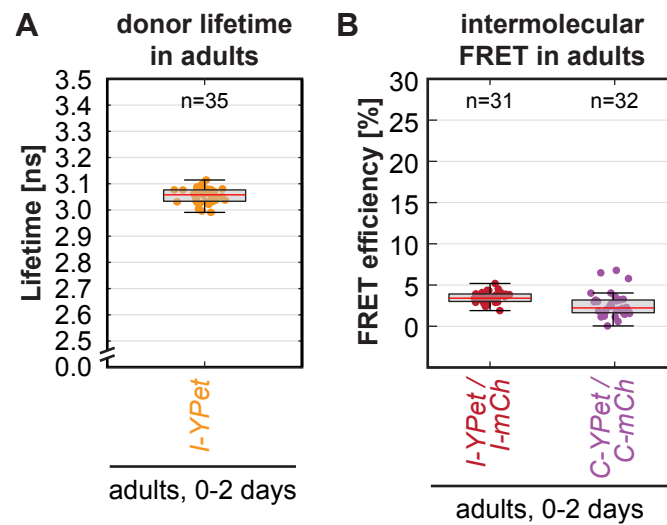
S5 Fig. Integrin levels are comparable to Talin levels at muscle attachment sites. **A–D.** Live imaging of flight muscle attachment sites at 20 h and 30 h APF. Pupae expressing Talin-GFP (A and C) were compared to pupae expressing Integrin-GFP (β PS-GFP) (B and D). Yellow shaded areas in A'–D' indicate attachment regions in which GFP intensity was quantified. Scale bars are 10 μ m. **E.** Quantification of Talin- and Integrin-GFP intensity at muscle attachment sites. Median Talin-GFP intensity was set to 1 for 20 h APF and 30 h APF. (Kolmogorov-Smirnov test, *** $p < 0.001$, ** $p < 0.01$). Underlying data can be found in S1 Data. GFP, green fluorescent protein; h APF, hours after puparium formation.



S6 Fig. Quantitative imaging workflow and control measurements for FCS. **A.** Living *talin-I-YPet* pupae were prepared for quantitative imaging by opening a window in the pupal case above the thorax containing the developing flight muscles (magenta) (Lemke and Schnorrer, 2018). **B.** A confocal image and 3 FCS measurements were acquired using the same detector on a confocal microscope. **C.** Autocorrelation curves from the FCS measurements were fit to obtain a CPP value for each pupa. **D.** The CPP value was used to calibrate each image resulting in a pixel-by-pixel concentration image. This image was used to manually draw an ROI around the muscle attachment site. From this ROI, a muscle attachment mask was created automatically by Multi-Otsu thresholding. Finally, the average concentration at the attachment was calculated from the pixel values inside the mask for each pupa. **E.** Pixel-by-pixel photon count values measured in confocal images of an Atto488 dye dilution series (mean with standard deviation). Note that the number of detected photons increases linearly with the concentration of the dye for the entire range measured. Thus, the high intensities at muscle attachment sites can be directly compared to low intensities in the muscle interior of the same confocal image. Underlying data can be found in S1 Data. CPP, counts per particle; FCS, fluorescence correlation spectroscopy; ROI, region of interest.



S7 Fig. Talin levels at muscle attachment sites are only slightly reduced in heterozygous pupae. **A–D.** Live imaging of flight muscle attachment sites of homozygous *talin-I-YPet* pupae (2 copies) and heterozygous *talin-I-YPet/rhea⁷⁹* pupae (1 copy). Scale bars are 10 μ m. **E.** Quantification of Talin-I-YPet (I-YPet) intensities at muscle attachment sites. Median intensity of homozygous pupae was set to 1 for 20 h and 30 h APF. Note that the Talin levels are only reduced to 80% and not 50% in heterozygous pupae. **F.** Talin force measurements in homozygous and heterozygous tension sensor (TS) and zero-force control (C-TS) pupae. (Kolmogorov-Smirnov test, *** $p < 0.001$, * $p < 0.05$; ns: $p > 0.05$). Underlying data can be found in S1 Data. C-TS, Talin control sensor with HP-sensor module; h APF, hours after puparium formation; HP, Villin headpiece; I-YPet, Talin with internal YPet; ns, nonsignificant; *rhea⁷⁹*, *talin* deficiency; TS, Talin tension sensor with HP-sensor module; YPet, yellow fluorescent protein for energy transfer.



S8 Fig. Control measurements for Talin forces detected at muscle attachment sites in adult flies. A. Lifetime data of donor-only control at the internal position of Talin (I-YPet) in adults. The measured lifetime is slightly lower than in pupae at 18–30 h APF (S4A Fig), likely due to the short background lifetime of the adult cuticle that is just above to the muscle attachment sites. **B.** Intermolecular FRET control data comparing heterozygous I-YPet/I-mCh or C-YPet/C-mCh pupae to homozygous I-YPet or C-YPet pupae, respectively. Underlying data can be found in S1 Data. C-mCh, Talin with C-terminal mCherry; C-YPet, Talin with C-terminal YPet; FRET, Förster resonance energy transfer; h APF, hours after puparium formation; I-mCh, Talin with internal mCherry; I-YPet, Talin with internal YPet; YPet, yellow fluorescent protein for energy transfer.



Review

Mechanical forces during muscle development

Sandra B. Lemke^a, Frank Schnorrer^{a,b,*}^a Muscle Dynamics Group, Max Planck Institute of Biochemistry, Am Klopferspitz 18, 82152 Martinsried, Germany^b Developmental Biology Institute of Marseille (IBDM), CNRS, UMR 7288, Aix-Marseille Université, Case 907, Parc Scientifique de Luminy, 13288 Marseille, France

ARTICLE INFO

Article history:

Received 25 September 2016

Received in revised form 20 November 2016

Accepted 21 November 2016

Available online 29 November 2016

Keywords:

Muscle
Tension
Force
Biomechanics
Sarcomere
Myofibrillogenesis
Self-organization
Integrin
Titin

ABSTRACT

Muscles are the major force producing tissue in the human body. While certain muscle types specialize in producing maximum forces, others are very enduring. An extreme example is the heart, which continuously beats for the entire life. Despite being specialized, all body muscles share similar contractile mini-machines called sarcomeres that are organized into regular higher order structures called myofibrils. The major sarcomeric components and their organizational principles are conserved throughout most of the animal kingdom. In this review, we discuss recent progress in the understanding of myofibril and sarcomere development largely obtained from *in vivo* models. We focus on the role of mechanical forces during muscle and myofibril development and propose a tension driven self-organization mechanism for myofibril formation. We discuss recent technological advances that allow quantification of forces across tissues or molecules *in vitro* and *in vivo*. Although their application towards muscle development is still in its infancy, these technologies are likely to provide fundamental new insights into the mechanobiology of muscle and myofibril development in the near future.

© 2016 The Authors. Published by Elsevier Ireland Ltd. This is an open access article under the CC BY-NC-ND license (<http://creativecommons.org/licenses/by-nc-nd/4.0/>).

Contents

| | |
|--|-----|
| 1. Introduction | 92 |
| 2. The muscle 'dimension problem' | 93 |
| 3. Muscle and myofibril development – a balance of forces | 94 |
| 4. Integrins – central force sensors at the muscle-tendon junction | 95 |
| 5. Titin – a force sensor with a tuneable spring at the heart of the sarcomere | 96 |
| 6. Force production – the usual suspects? | 97 |
| 7. Myofibrillogenesis model – tension driven self-organization. | 97 |
| 8. How experimentalists sense tension | 98 |
| 9. Conclusions and perspectives. | 99 |
| Competing interests | 99 |
| Acknowledgements | 100 |
| References. | 100 |

1. Introduction

Mature body muscles can produce very high forces. The 1992 Guinness Book of World Records reports an American with a masseter (jaw) muscle bite strength of 442 kg and at the 2016 Rio Olympics, a Georgian

managed to lift 258 kg in a technique called 'clean and jerk' to win a gold medal. These maximum forces can only be produced for a few seconds until the muscles fatigue. However, body muscles can also produce forces over long time periods enabling body posture, walking or lifelong heart beating. Similarly enduring muscle forces support the flight of animals. During *Drosophila* flight, the indirect flight muscles contract at 200 Hz and sustain an estimated power of about 80 W/kg muscle mass over many hours of flight (Dudley, 2000; Götz, 1987; Lehmann and Dickinson, 1997).

* Corresponding author at: Developmental Biology Institute of Marseille (IBDM), CNRS, UMR 7288, Aix-Marseille Université, Case 907, Parc Scientifique de Luminy, 13288 Marseille, France

E-mail address: frank.schnorrer@univ-amu.fr (F. Schnorrer).

Although different body muscle types differ significantly in their physiology (Schiaffino and Reggiani, 2011; Schönbauer et al., 2011; Spletter and Schnorrer, 2014), the molecular basis for force production is shared amongst all of them. The contractile unit of all muscles is the sarcomere, which shortens using a sliding mechanism: bipolar myosin thick filaments pull themselves into cross-linked actin thin filaments and thus shorten the sarcomere (Huxley and Niedergerke, 1954; Huxley and Hanson, 1954). Sarcomeres are arrayed in series into linear myofibrils, which span the entire muscle. Thus, coordinated contraction of all sarcomeres along a myofibril shortens the entire muscle and produces a mechanical force. Interestingly, not only the mechanism of muscle contraction, but also most of its molecular components are evolutionarily conserved from worms and flies to humans, hence the sarcomere is an ancient molecular machine (Ehler and Gautel, 2008; Vigoreaux, 2006).

While the identity and in many cases the function of the sarcomeric proteins during muscle contraction is known in molecular detail (Hill and Olson, 2012), the mechanisms of sarcomere assembly during muscle development are much less well understood. Here, we review recent advances in understanding muscle development, with a particular focus

on the role of mechanical forces in myofibril and sarcomere formation. We propose a tension-driven model of myofibrillogenesis and discuss recent technological advances to quantify mechanical forces *in vitro* or in developing muscles *in vivo*. These technologies should provide further mechanistic insight into how muscles are built during development to allow both the maximal strength and endurance observed in the amazing muscle performances during adult life.

2. The muscle 'dimension problem'

Mature skeletal muscles are connected at both ends via tendons to the skeleton (Fig. 1). This connection allows muscle contractions to move the skeleton of the animal, leading to locomotion. Large vertebrate muscles are generally composed of several hundred muscle fibers, which are the cellular units of the muscle. In humans, muscle fibers can be several centimeters long, and even in the small fruit fly *Drosophila*, the flight muscle fibers have a length of about 1 mm (Fig. 1). Every muscle fiber is filled with many myofibrils. Each myofibril linearly spans the entire length of the muscle fiber from one tendon attachment to the other. However, the sarcomeres, the repetitive units that build the

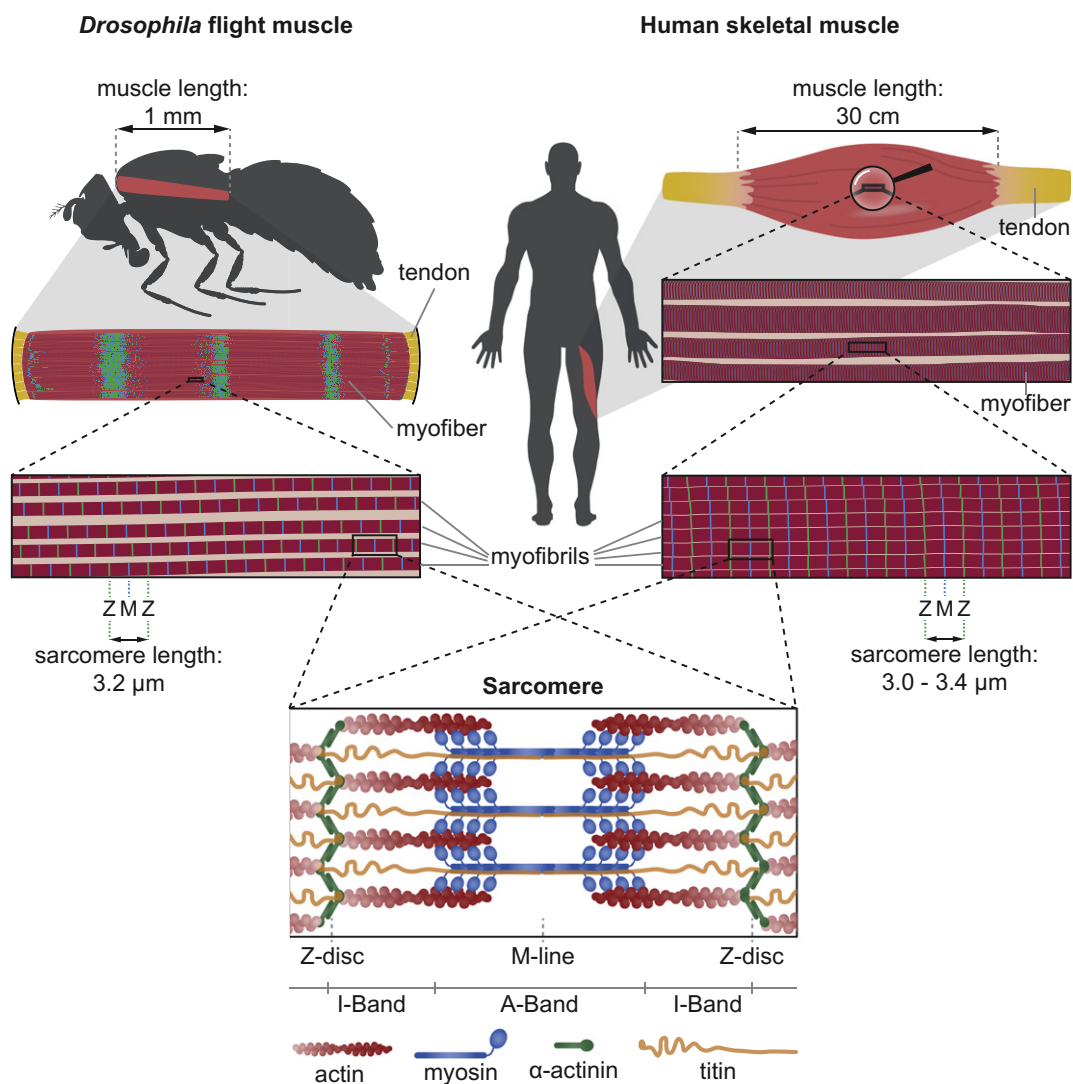


Fig. 1. The muscle dimension problem: structure and dimensions of muscles in fly versus human. **Top:** Schematic representation of *Drosophila* and human muscles in a series of magnifications. Each muscle fiber contains hundreds of myofibrils that span the entire length of the myofiber. Sarcomeres are several orders of magnitude shorter but must be assembled perfectly into a myofibril to connect both muscle-tendon attachments at the fiber ends. In fly and human, sarcomeres are similar in length (3.2 μm in flight muscles and 3.0 to 3.4 μm in relaxed human muscles) and many sarcomeric proteins are well conserved. **Bottom:** Schematic of the sarcomere. Polar actin filaments (also called thin filaments) are anchored at the Z-disc (Z, green) by α-actinin. Thick filaments comprised of myosin bundles are centred at the M-line (M, blue) and interact with actin with their myosin heads. Titin, a connecting filament, is anchored at the Z-disc and spans through the I-band all the way to the M-line.

myofibrils, are several orders of magnitude shorter than the muscle fiber. Depending on the muscle type, the sarcomere length in relaxed human skeletal muscle *in vivo* varies from 3.0 to 3.4 μm (Ehler and Gautel, 2008; Llewellyn et al., 2008; Regev et al., 2011), which is similar to the 3.2 μm sarcomere length of *Drosophila* indirect flight muscle (Vigoreaux, 2006). This creates a ‘dimension problem’: about 300 sarcomeres must be linearly arrayed to form one myofibril spanning the entire flight muscle fiber in *Drosophila*, whereas large vertebrate muscles can require 100,000 sarcomeres to build a sufficiently long myofibril (Fig. 1).

It is important to note that most relaxed muscles are under passive tension, even if they do not produce active contractile forces. The source of this passive tension are the myofibrils themselves (Magid and Law, 1985), with a major contribution from the gigantic elastic molecule titin, which – in vertebrates – extends across half a sarcomere from the Z-disc to the M-line (Fig. 1) and thus stably connects thin with thick filaments (Fürst et al., 1988; Gautel, 2011a; Gautel and Goulding, 1996; Linke et al., 1996; Maruyama et al., 1976; Tskhovrebova and Trinick, 2003). This property of titin coined the term ‘connecting filaments’ for titin filaments. In fact, the historical name for titin was connectin, which was originally isolated from rabbit muscle depleted of actin and myosin (Maruyama, 2002; Maruyama et al., 1977). The passive tension ensures that each myofibril spans the muscle fiber linearly, similar to a slackline spanned between two trees, with a sarcomere length that is optimal for the next active contraction. The challenging consequence is that a myofibril rupture is deleterious and cannot be repaired easily, as the passive tension prevents the myofibril from simply reattaching to the muscle end. Similarly, the entire myofiber faces a challenge during development, as the fiber cannot simply measure its length and then decide to assemble 10, 100, 1000 or 10,000 sarcomeres per myofibril. The requirement for passive tension also rules out the developmental strategy to just assemble one sarcomere after the next onto loose myofibril ends, as such a myofibril would immediately collapse. Thus, nature chose a smarter solution to solve the dimension problem.

3. Muscle and myofibril development – a balance of forces

Muscle development is a multi-step process beginning with the fate specification of myoblasts, which fuse to form a myotube. Each myotube elongates and stably attaches its ends to tendon cells. Only after attachment does the myotube assemble its myofibrils and thus transition to a muscle fiber. At each of these steps, mechanical forces and the actomyosin cytoskeleton play important roles. We refer the reader to excellent recent reviews detailing both myoblast patterning (Dobi et al., 2015) and myoblast fusion (Kim et al., 2015; Rochlin et al., 2010). Here, we focus on the later steps of myogenesis, starting with the elongating myotube.

During myotube elongation in *Drosophila*, both myotube tips extend towards their future tendon cells (Fig. 2A) (Schnorrer and Dickson, 2004; Schweitzer et al., 2010). During this phase, the myotube tips resemble leading edges of migratory cells with numerous dynamic filopodia extending in the direction of myotube elongation (Schnorrer and Dickson, 2004; Schnorrer et al., 2007; Weitkunat et al., 2014). The actin cytoskeleton is polarized along the long axis of the myotube and supposedly produces a force that drives myotube elongation towards the future tendon attachments. It is likely that similar principles enable myotube elongation across somites in vertebrates, in order to reach their future tendons at the somite borders (Gros et al., 2008; Schweitzer et al., 2010). However, tendon development in vertebrates is more complex and requires an interplay between myogenic and osteogenic cells (Brent and Schweitzer, 2003; Brent and Tabin, 2004; Schweitzer et al., 2001).

After myotube elongation, myotubes need to attach to tendons. Recent studies of myotube attachment using the large *Drosophila* flight muscles showed that the tendon cells are more active than initially thought. They also form dynamic filopodia on their basal side, which

interdigitate with the myotube filopodia to initiate myotube-tendon attachment (Fig. 2A and B). During the next few hours of development, filopodia formation at the myotube tips stops and the initially dynamic attachment matures. Interestingly, during this phase of attachment maturation, the myotube compacts in length while the tendon cells form long cellular extensions to maintain the stable connection with both myotube ends (Fig. 2B and C). These cellular extensions, which originate from the basal side of the tendon epithelium, appear as straight lines, indicating strong tissue tension produced by the compacting myotube. Indeed, *in vivo* laser cutting experiments demonstrated that after attachment initiation, mechanical tension within the muscle-tendon system is gradually built up as the attachment matures and the myotube compacts (Weitkunat et al., 2014). Importantly, the tension axis is aligned with the long muscle axis, which will be the future muscle contraction axis. Therefore, tension can act as a guiding compass to ensure that the myofibrils form along this axis and not in any other direction.

During attachment initiation, when attachments are dynamic and tension is low, primarily short actin filaments are present within the myotube (Fig. 2B). These dynamic actin filaments are preferentially oriented along the tension axis, but are not yet periodic or striated. When tissue tension is built up and the myotube is maximally compacted, the first periodic muscle myosin pattern arises within the myotube as it transitions to a myofiber. This periodic muscle myosin pattern is located on a continuous actin fibril that represents an immature myofibril (Fig. 2C). Importantly, live imaging showed that both the formation of these immature myofibrils as well as the periodic muscle myosin pattern occurs simultaneously across the entire muscle fiber. As a consequence, each myofibril spans the entire myofiber from one attached end to the other and is indistinguishable from its neighboring fibrils in terms of maturity (Weitkunat et al., 2014). This strongly implies that a self-organization mechanism transitions the actomyosin cytoskeleton from an unordered to an ordered state, somewhat similar to a phase transition from freely diffusing proteins in a liquid to a liquid crystal or gel-like state. In this state, the proteins are ordered and tend to keep the same neighboring proteins – at least for a while, similar to what has been observed in the mitotic spindle (Hyman et al., 2014; Shimamoto et al., 2011). Interestingly, if the tension build-up in the myotube is disturbed genetically or acutely by laser cutting, myofibrillogenesis is severely compromised, suggesting that tension coordinates the myofibril self-organization process (Weitkunat et al., 2014). Using such a mechanism guarantees that the developing myotube is properly attached to tendons, as only then tension can be built up. Additionally, it ensures that the immature myofibrils are already anchored at the myotube-tendon junctions and only there, thus setting the correct muscle contraction axis required for coordinated body movements.

Similar long periodic myofibrillar arrays were found during development of the zebrafish somites (Sanger et al., 2009) or recently, during differentiation of human cells into myofibers attached to culture dishes *in vitro* (Chal et al., 2015). In the mammalian heart, myofibrils are also attached during development. In this case, the myofibrils of the neighboring rather small cardiomyocytes are mechanically coupled by specialized adhesion structures across membranes to produce coordinated forces (Perriard et al., 2003). If this coupling is blocked *in vitro*, myofibrillogenesis is severely compromised (Marino et al., 1987). Together, these observations strongly suggest that a similar tension driven self-organization mechanism may also coordinate myofibrillogenesis in mammalian muscle.

Once built, the immature myofibrils grow in width as well as in length, with the sarcomeres refining to a regular pseudo-crystalline array and adopting their final size in the mature adult muscle fiber (Fig. 2D) (Spletter et al., 2015). During this maturation phase, the myofibrils further adjust to the needs of the muscle fiber type, e.g. being a more enduring or high force producing fiber-type, by incorporation of particular sarcomeric proteins or protein isoforms (Schiaffino and Reggiani, 2011; Spletter et al., 2015; Spletter and Schnorrer, 2014).

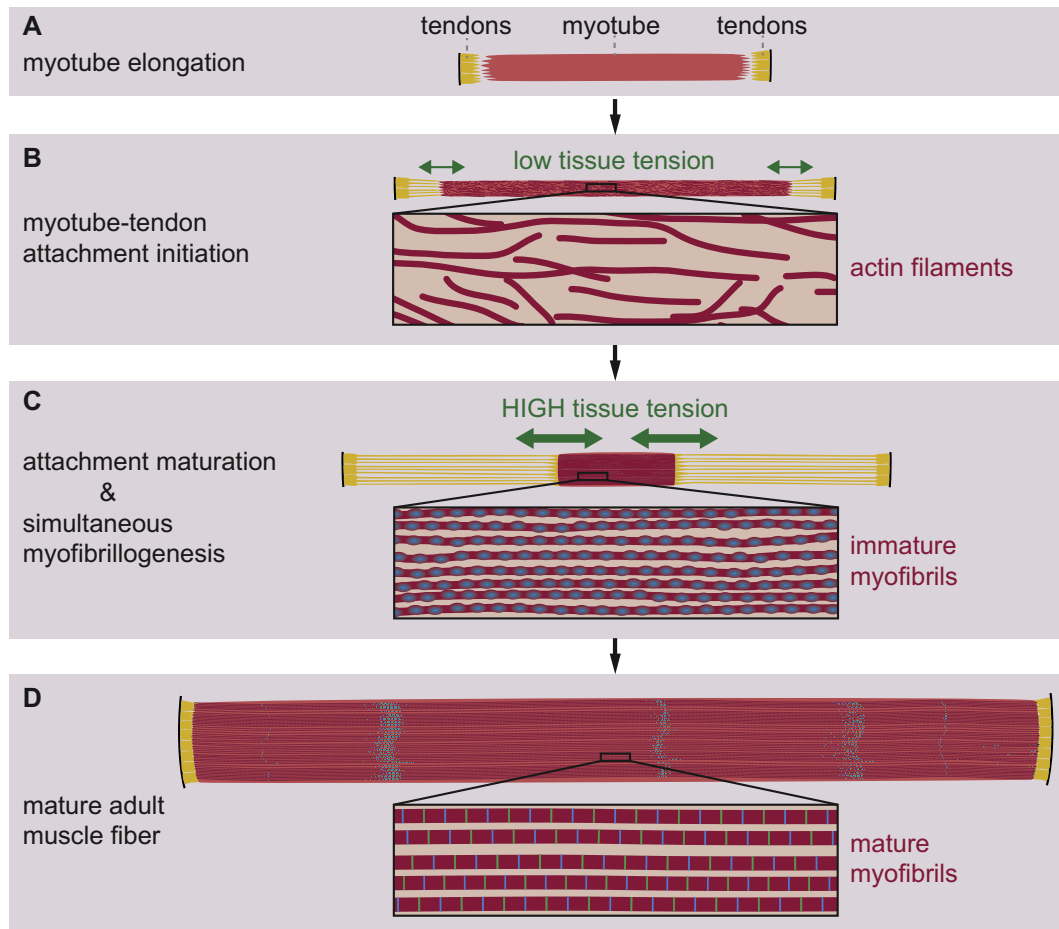


Fig. 2. Development of *Drosophila* indirect flight muscles. (A) The myotube (red) elongates towards its tendon targets (yellow). (B) The myotube initiates attachment to the tendon cells. Actin filaments in the myotube are short but preferentially oriented along the long muscle axis; tissue tension is low (green arrows). (C) During attachment maturation, the myotube compacts and high tissue tension is generated (green arrows). At the same time, immature myofibrils are formed simultaneously throughout the myotube. (D) The muscle fiber grows in length and width and the myofibrils mature to their final size.

Together, this generates muscle fibers that perfectly match the biomechanical demands of the animal.

4. Integrins – central force sensors at the muscle-tendon junction

How can cells – and myotubes in particular – sense mechanical tension molecularly and what molecular consequences does tension induce? The integrin family of receptors is likely to act as important force sensors. Integrins are essential for muscle-tendon attachment as mutations lead to round or detached muscles in worms and flies (Leptin et al., 1989; Williams and Waterston, 1994) and severe sarcomerogenesis defects in mice (Schwander et al., 2003). Integrins are α -, β -heterodimers, containing large extracellular domains, which interact with the extracellular matrix (ECM), and short cytoplasmic tails that bind to intracellular adaptor proteins such as talin and kindlin, which in turn link to the actin cytoskeleton (reviewed in Moser et al., 2009). Integrins are present both in the tendon cell membrane as well as the myotube tip membrane. They mediate muscle-tendon attachment by generating a force resistant muscle-ECM-tendon junction (reviewed in Brown, 2000).

Although forces across integrin molecules have not yet been measured *in vivo* at muscle-tendon junctions, the combination of several insights – partially gained in other systems – strongly suggest that integrin molecules at muscle-tendon junctions do bear forces. First, using cells plated on glass functionalized with a FRET-based molecular tension sensor attached to an artificial integrin ligand, individual integrin complexes were estimated to experience pulling forces in the

low piconewton (pN) range (Morimatsu et al., 2013). These values fit well with forces measured within focal adhesions of plated cells using a genetically encoded molecular tension sensor in the integrin adaptor protein talin (Austen et al., 2015). Second, *in vivo* evidence from talin mutant muscles showed a detachment of the actin cytoskeleton from the muscle-tendon junction, strongly suggesting that the assembling actin cytoskeleton is producing mechanical forces transmitted onto integrin tails by talin (Brown et al., 2002). Third, recent *in vivo* FRET analysis in *Drosophila* embryonic muscles confirmed that integrin tails bind to the talin head domain, while actin is binding along the rod domain, pulling talin into an extended conformation (Klapholz et al., 2015). Together, this is solid evidence that both integrins and talin are experiencing mechanical forces during muscle development *in vivo*.

What molecular consequences do these forces have for integrins and talin at the muscle-tendon junction? It appears that forces result in a stabilization and clustering of integrins at the muscle-tendon junction membrane (Fig. 3), similarly as proposed for focal adhesions (Kanchanawong et al., 2010; Legate et al., 2009). As a consequence, integrin levels increase during muscle-tendon attachment maturation and thus can counteract the higher forces. This model is supported by several *in vivo* observations. First, when flight muscles initiate attachment, mechanical tension is low and both integrin and talin levels at the junction are low. A few hours later, when tension is higher, attachments have matured and both integrin and talin are present in elevated amounts at the junction (Weitkunat et al., 2014). Second, *in vivo* fluorescence recovery after photobleaching (FRAP) experiments at the muscle-tendon junction demonstrated that higher contractile forces

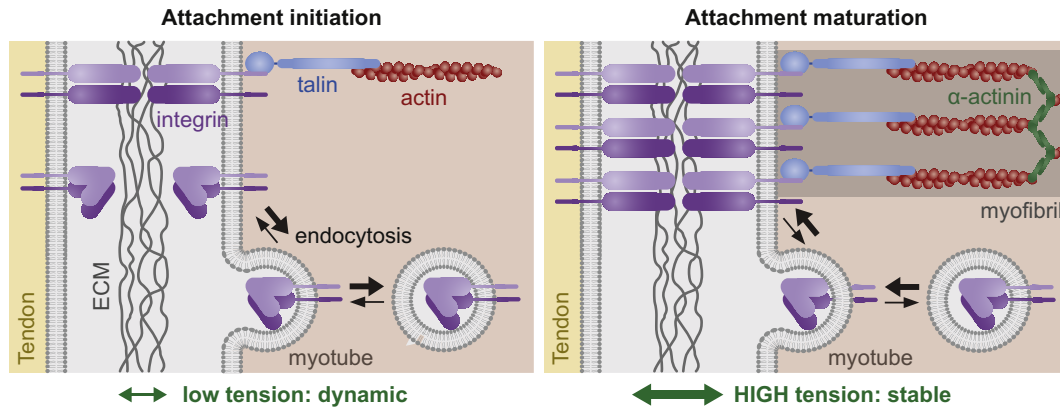


Fig. 3. Force-dependent integrin clustering and turnover at the muscle-tendon junction. During attachment initiation, tissue tension is low. The amount of integrin at the muscle-tendon junction bound to the extracellular matrix (ECM) is also low, whereas the mobile fraction of integrin is high. During attachment maturation and myofibrillogenesis, the tissue tension increases, resulting in reduced endocytosis. Therefore, integrin clusters are stabilized at the tips of myofibrils.

produced by the muscle correlate with lower integrin adhesion complex turnover by clathrin-mediated endocytosis (Pines et al., 2012). This suggests that forces can directly stabilize the clustered integrin complexes at the muscle-tendon junction (Fig. 3). Third, it was recently discovered in an elegant series of experiments that the Ilk-Pinch-Parvin (IPP) complex, a crucial regulator of integrin adhesion and integrin signalling (Legate et al., 2005), directly regulates integrin turnover in response to mechanical forces (Vakaloglou et al., 2016). If the IPP complex is mutated, integrins at the junction turn over faster than normal, resulting in an abnormally fuzzy muscle-tendon junction upon force. Interestingly, this morphological defect is rescued if muscle contraction is blocked, suggesting that the IPP complex reinforces integrin adhesion in response to muscle forces. Altogether, these and many other observations place integrins as central force sensors at the muscle-tendon junction that must integrate and adapt to dramatically dynamic forces during muscle development when the myofibrils assemble as well as during muscle function when the myofibrils contract.

5. Titin – a force sensor with a tuneable spring at the heart of the sarcomere

Not only muscle-tendon junctions experience forces. Tension is likely present homogeneously along developing and mature myofibrils. As a consequence, every assembling and mature sarcomere is under force, even in the relaxed muscle state. As mentioned above, this tension

is called passive tension and titin is one of its major sources. Titin is a gigantic protein larger than 3 MDa in size. Its modular architecture largely consists of immunoglobulin (Ig) and fibronectin type III (Fn3) domains, and in its fully extended state, titin is more than 1.5 μm long (Labeit and Kolmerer, 1995). This allows titin to span half a sarcomere, with its N-terminus embedded at the Z-disc and its C-terminus at the M-line (Fürst et al., 1988). It has been suggested to act as a molecular ruler or blue print for sarcomeric architecture (reviewed in Tskhovrebova and Trinick, 2003). Interestingly, the titin I-band region (between Z-disc and beginning of the thick filament, see Fig. 4) consists of different spring elements: the Ig-domain series and the so-called PEVK region. The latter largely consists of the amino acids Pro (P), Glu (E), Val (V) and Lys (K), which under low force form a coiled confirmation, stabilized by salt-bridges and hydrophobic interactions (Linke et al., 2002). If tension is applied on titin, these spring elements gradually extend; the Ig-domain series straightens (without unfolding any of the Ig-domains) and the PEVK domain gradually stretches, resulting in the elongation of the I-band region of the sarcomere under increasing strain (Gautel and Goulding, 1996; Linke et al., 1999) (Fig. 4). This mechanically induced elongation occurs at a low pN range and is fully reversible during the contraction cycle of a muscle (Linke et al., 2002). In a resting mature or developing muscle, titin is always present in a partially extended conformation and thus produces passive tension within the muscle-tendon system.

Importantly, the spring constant of titin is under tight regulation during muscle development and depends on the muscle type. Heart

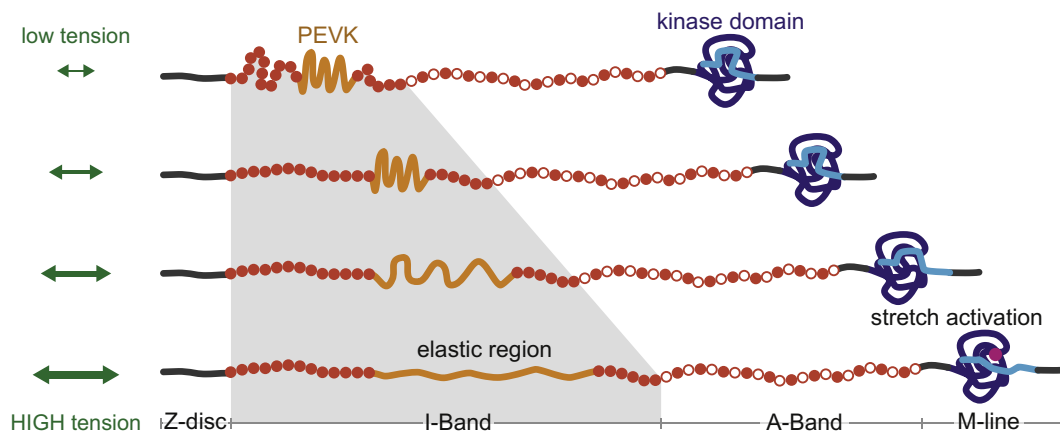


Fig. 4. Titin – a force sensor in the sarcomere. Schematic representation of titin and its response to increasing tension in the sarcomere (green arrows). Titin mainly consists of Immunoglobulin (Ig) and Fibronectin type III (Fn3) domains (red and white dots, respectively). The PEVK region (orange) is an elastic element that stretches with increasing tension, allowing the I-band region of titin to extend. The kinase domain of titin (blue) is thought to be activated upon stretch by the removal of a regulatory tail (light blue) allowing ATP binding (pink) at the active site. Therefore, titin can act as a stretch sensor in the sarcomere.

muscle is stiffer than skeletal muscle and the primary source of this difference is that skeletal muscle titin contains a significantly longer PEVK sequence as compared to heart muscle, making skeletal muscle titin more compliant (Gautel et al., 1996; Guo et al., 2010; Lange et al., 2006). As humans have only one titin gene, this isoform regulation occurs by alternative splicing (Bang et al., 2001). Misregulation of titin splicing, for example by a mutation in the RNA-binding protein RBM20, results in severe hereditary cardiomyopathies (Guo et al., 2012; Spletter and Schnorrer, 2014). Titin stiffness can also be fine-tuned by phosphorylation of the PEVK domain, which may play an important role during human heart failure (Kötter et al., 2013). Another important function of titin and its elasticity is that it can position the myosin filament centrally by pulling more strongly to one side, in case the filament is displaced (Agarkova et al., 2003). This balance of forces ensures that the myosin motor activity cannot cause a collapse of the sarcomere to one side and thus maintains symmetrical sliding between thin and thick filaments. Together, these data highlight the importance of titin's mechanical properties and their precise modulation for normal muscle development and function.

Beyond its role as a tuneable spring, titin was also proposed as an active force sensor that may regulate contractility or signalling in response to strain (reviewed in Gautel, 2011a, 2011b). This hypothesis is supported by the discovery of a C-terminally located autoinhibited kinase domain in titin (Mayans et al., 1998). The kinase domain could be activated *in vitro* by pulling on a titin fragment consisting of the kinase domain flanked by its neighboring Ig- and Fn-domains using an atomic force microscope (AFM). These pulling forces 'open' the kinase domain by pulling a regulatory tail away from the active site, enabling ATP binding to the kinase domain (Fig. 4) and thus supposedly kinase activity (Puchner et al., 2008). The forces required for ATP binding and kinase activation are within the physiological range and well below forces needed to unfold Ig-domains. These data suggest that the titin kinase may act as a biological force sensor *in vivo*. However, it is unclear if kinase activity is required for the function of the titin kinase domain. Recent data support the hypothesis of titin being a pseudokinase that may potentially act as a mechanically regulated scaffold to control protein turn-over (Bogomolovas et al., 2014; Lange et al., 2005). However unexpected for a pseudokinase, the catalytic core of titin is largely conserved (Gautel, 2011b) and also the insect titin kinases are active, at least *in vitro* (Fährmann et al., 2002). Thus, it remains an open question whether vertebrate titin is an active kinase or not and future research is required to fully understand how the gigantic sarcomeric force sensor titin communicates changes in tension with its partner proteins.

6. Force production – the usual suspects?

For many decades, it has been established that the motor activities of muscle myosin heavy chains produce the active forces responsible for sarcomere shortening during mature muscle contractions (reviewed in Cooke, 2004; Szent-Györgyi, 2004). Like all myosin II motors, muscle myosin is a hexamer consisting of two heavy chains, two essential light chains and two regulatory light chains (Howard, 2001). About 300 of these hexamers are assembled into surprisingly stereotyped 1.65 μm long bipolar myosin filaments present in mature sarcomeres of vertebrate muscles (Gokhin and Fowler, 2013; Tskhovrebova and Trinick, 2003). The pseudo-crystalline regularity of mature sarcomeres ensures that myosin motors only contact actin filaments of correct polarity to readily move towards their plus ends, which are anchored and cross-linked at the Z-discs (Fig. 1). Thus, the thick filaments can very efficiently produce forces along the axis of muscle contraction.

During muscle development and myofibril formation in particular, it is less clear how mechanical forces are being generated. At the early developmental stages, when myotubes elongate and myotube-tendon attachment is initiated, muscle myosin is not yet expressed at detectable levels (Spletter et al., 2015; M. Spletter & F.S. unpublished data). However, early myotubes do express nonmuscle myosin, which is

responsible for regulated force production in numerous cell types in various developmental contexts (reviewed in Howard, 2001). Evidence from cultured *Xenopus* myotubes suggests a role for nonmuscle myosin light chain kinase during myofibrillogenesis, both for correct myosin and titin assembly (Ferrari et al., 1998; Harris et al., 2005). Yet, mutations in nonmuscle myosin-IIA in mice only result in mild muscle phenotypes (Tullio et al., 1997), likely because other nonmuscle myosin isoforms compensate (Berg et al., 2001). In *Drosophila*, mutations in the single nonmuscle myosin heavy chain (*zipper*) present result in severe myofibrillogenesis defects in embryonic muscles (Bloor and Kiehart, 2001), supporting a direct role for nonmuscle myosin in myofibrillogenesis. Thus, it is possible that nonmuscle myosin is responsible for the observed tension before myofibrils start to assemble (Fig. 2C) (Weitkunat et al., 2014).

7. Myofibrillogenesis model – tension driven self-organization

Myotubes face the challenge of organizing myofibrils throughout their entire volume. This is different in epithelial cells forming a monolayer, which is one of the best models to study the requirement of actin-myosin contractility for tissue self-organization. In these cells, actomyosin is largely restricted to belt-like structures at the apical cell cortex (reviewed in Heisenberg and Bellaiche, 2013; Lecuit et al., 2011). In order to fill the entire myotube with myofibrils, it is likely that the actomyosin network is mechanically coupled across large areas, possibly across the entire myotube from one integrin attachment site to the other (Fig. 5). The subsequent mechanical tension across the myotube appears largely isotropic, as it does not result in obvious actomyosin flows (Weitkunat et al., 2014), contrasting observations from the cell cortex of polarizing cells (Mayer et al., 2010) or during epithelial spreading and remodelling (Behrmdt et al., 2012; Rauzi et al., 2010).

Historically, two distinct myofibrillogenesis models have been established. The premyofibril model, which is largely based on *ex vivo* culture data, suggests that short bipolar nonmuscle myosin filaments assemble with short α -actinin cross-linked actin filaments to form premyofibrils (Rhee et al., 1994; White et al., 2014). This is consistent with the observation of actin filaments *in vivo* before periodically patterned immature myofibrils are detected (Fig. 5A). The premyofibril model further suggests that nonmuscle myosin is gradually exchanged for muscle myosin in the mature myofibrils. Although observed in a dotted pattern on pre-myofibrils *in vitro* (White et al., 2014), it is unclear if nonmuscle myosin is present in a detectable periodic pattern *in vivo* during early steps of myofibrillogenesis (Bloor and Kiehart, 2001). By contrast to muscle myosin, nonmuscle myosin only forms bipolar mini-filaments with approximately 10 heads on each side (reviewed in Vicente-Manzanares et al., 2009) and thus a periodic spacing is unlikely to be detected with current microscopy techniques. The observation that muscle myosin is detectable *in vivo* as periodic dots on immature myofibrils (Weitkunat et al., 2014) suggests that the myosin exchange must occur at an early developmental stage (Fig. 5B). These myosin dots are also consistent with the second myofibrillogenesis model, which proposes that muscle myosin containing thick filaments (precursors) and titin containing α -actinin cross-linked actin filaments, termed I-Z-I bodies, are first built independently and only assemble to myofibrils in a second step (Ehler et al., 1999; Holtzer et al., 1997). Data supporting a coordinated assembly of prebuilt protein complexes during sarcomerogenesis have also been gained in *Drosophila* (Rui et al., 2010). In our opinion, both models are rather complementary and represent two aspects of the complex myofibrillogenesis process, both depending on mechanical tension caused by bipolar myosin filaments pulling on bipolar cross-linked actin filaments to self-organize immature periodically patterned myofibrils.

We integrate the old models with recent *in vivo* data to suggest the following revised tension-driven model for *in vivo* myofibril self-organization (see also Sparrow and Schöck, 2009). In a first phase (Fig. 5A), myotubes need to establish a stable integrin-mediated attachment to

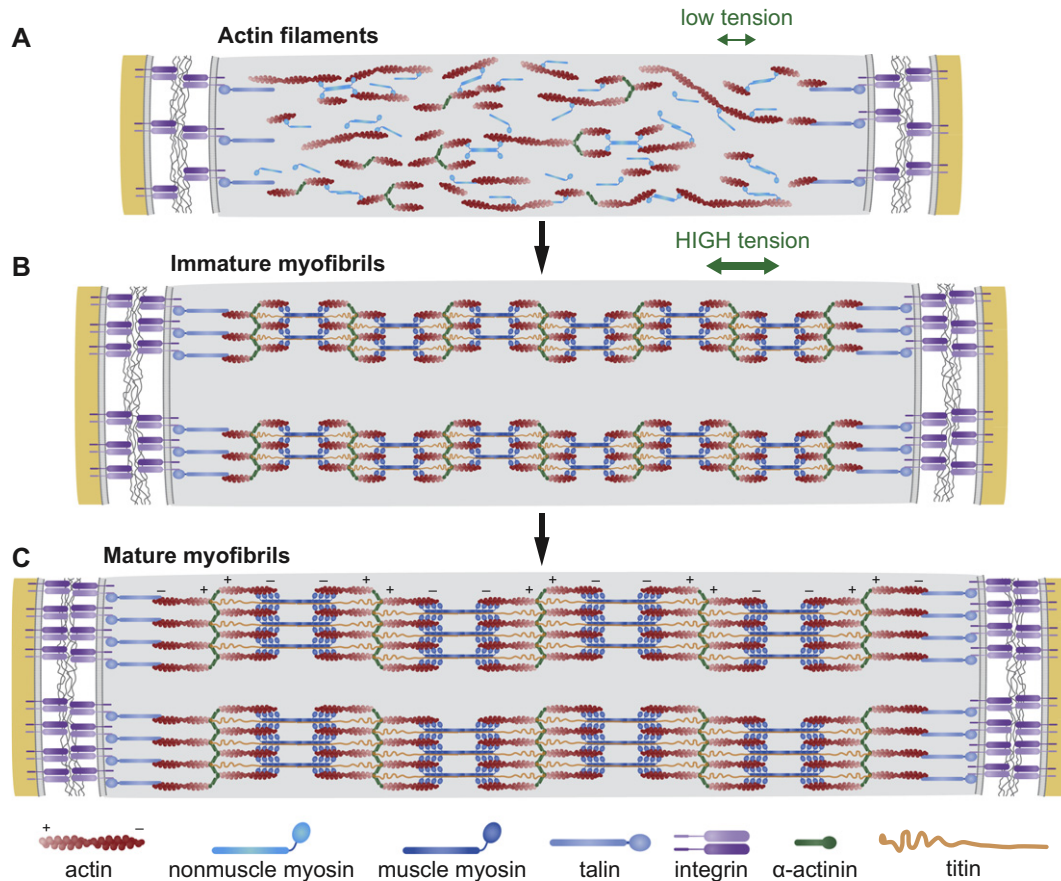


Fig. 5. Tension-dependent model of myofibril development. (A) Early in development when tissue tension is low (green arrows), bipolar non-muscle myosin (light blue) and actin filaments (red) are loosely and dynamically interacting. The actin filaments are oriented with respect to the muscle axis but not yet striated. (B) As development proceeds, tension increases and immature myofibrils form across the entire myofiber. Muscle myosin is expressed and forms larger bipolar filaments (dark blue) stably binding to bipolar actin filaments, cross-linked by α -actinin (red and green). Titin (orange) stably connects both. This creates a striated appearance of the immature myofibrils, each one anchored to the muscle-tendon junction by integrin and talin at both ends, allowing tension to be transmitted across the entire myofibril. (C) In a final step, myofibrils and sarcomeres grow both in length and thickness by incorporating additional molecules until they reach the mature size.

tendons at both myotube ends. During this phase, mechanical tension is initially low but steadily increases, likely through the pulling of nonmuscle myosin filaments on short cross-linked actin filaments. Here, tension fulfills two important roles: it locally orients the actin and myosin filaments towards each other along the muscle axis and it globally coordinates the assembly process across the entire myotube. As a consequence, the actin filament network orients along the muscle axis but is not yet periodic. In a second phase (Fig. 5B), muscle myosin and titin are expressed in high quantities and tension induces integrin clustering at the muscle ends. Together, this drives the simultaneous self-organization of periodic immature myofibrils, each of which spans the entire myofiber, thus mechanically linking both integrin attachments. These immature myofibrils contain muscle myosin and titin in a periodic pattern and require both myosin motor activity and the titin scaffold or its passive tension activity for their formation (Rui et al., 2010; Schnorrer et al., 2010; Weitkunat et al., 2014). In a third phase (Fig. 5C), this self-organization process continues and the myofibrils mature. Large amounts of actin, muscle myosin, α -actinin, titin and many other components are incorporated and form the final pseudo-crystalline sarcomere morphology.

8. How experimentalists sense tension

As discussed throughout this review, mechanical tension at the tissue and single molecule level is essential for muscle morphogenesis. The same is true for many other developmental processes: most cells

continuously probe the stiffness of their environment to instruct developmental decisions, e.g. myotubes only build myofibrils efficiently on a substrate that recapitulates the *in vivo* stiffness and is neither too soft nor too stiff (Engler, 2004). The experimentalist can take advantage of this continuous exploratory behaviour and measure the forces generated by cells *in vitro* by applying a technique called traction force microscopy (Fig. 6A). To achieve this, cells are plated on a micropillar substrate of defined stiffness. By determining the deflection angle of the micropillars, cellular pulling forces can be measured in a quantitative way and thus a traction map of the cell is acquired (reviewed in Ribeiro et al., 2016). A similar technique was successfully applied to measure substrate tension during myotube differentiation and myofibrillogenesis using the C2C12 myoblast cell line. Consistent with the *in vivo* observations, mechanical tension is present along the long axis of forming myotubes and tension significantly increases during myotube to myofiber differentiation (Li et al., 2008). Thus, traction force microscopy can measure global cellular forces *in vitro*.

A complementary method that allows determination of the biomechanical properties of individual proteins or protein domains at the single molecule level *in vitro* is single molecule atomic force microscopy (AFM) (reviewed in Hughes and Dougan, 2016). A protein of interest is purified and attached to a rigid substrate on one end and to the tip of a calibrated AFM cantilever on the opposite end. The deflection angle of a laser beam is used to quantify the forces applied as the cantilever moves away from the substrate and thus pulls and eventually unfolds the protein or peptide of interest (Fig. 6B). This technique was

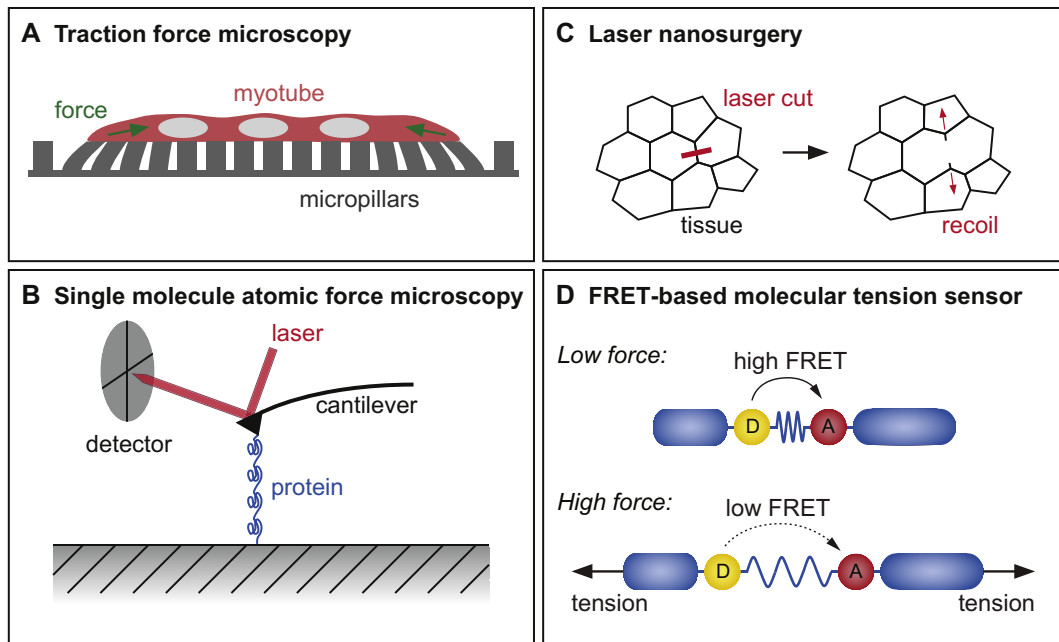


Fig. 6. How experimentalists sense tension. (A) **Traction force microscopy:** Cells are plated on a surface of stereotyped micropillars. Forces generated by the cells are calculated by measuring the deflection of the micropillars. (B) **Single molecule atomic force microscopy:** A single protein is attached to a surface and a cantilever. Bending of the cantilever can be detected as the cantilever is moved away from the surface and stretches the protein. This allows the quantification of forces needed to stretch and unfold protein domains. (C) **Laser nanosurgery:** Tissue tension is measured by severing of for example cell-cell edges with a pulsed UV-laser and quantifying the tissue recoil velocity. (D) **FRET-based molecular tension sensor:** A tension sensor module, consisting of a donor 'D' and an acceptor fluorescent protein 'A' connected by a flexible linker peptide, is inserted into a protein of choice. The higher the forces across a protein, the lower the FRET efficiency.

applied extensively to study the properties of individual titin fragments. It was shown that 150 to 300 pN forces are required to unfold individual titin Ig-domains *in vitro* (Rief et al., 1997). This appears higher than what an individual titin molecule may experience *in vivo*; however, the same study also showed that Ig-domain unfolding is reversible and thus may be a way to balance very high forces *in vivo* (Rief et al., 1997). Similar single molecule measurements established titin's PEVK domain as a flexible spring that elastically opens and closes at a much lower force range and thus likely contributes to the mechanical properties of the sarcomere *in vivo* (Li et al., 2001; Linke et al., 2002).

Measuring tension *in vitro* always has the disadvantage of being artificial. Thus, we need techniques that can also be applied *in vivo* within the intact developing organism. One technique widely used within recent years is *in vivo* laser nanosurgery or laser cutting (Fig. 6C). A pulsed UV laser (355 nm) or infrared laser is used to locally generate a low energy plasma and precisely sever protein connections, for example of the actin or microtubule cytoskeleton, without affecting the rest of the cell (Colombelli et al., 2009; Colombelli et al., 2005; Vogel et al., 2009). Laser cutting was also applied widely *in vivo* to sever cell-cell junctions or cortical actin networks. The velocity of the resulting recoil can be used to quantify relative tissue tension comparing different cells, mutants or developmental stages (Behrndt et al., 2012; Mayer et al., 2010; Weitkunat et al., 2014). Thus, laser nanosurgery is a powerful method to assess and quantify tissue tension *in vivo*.

A more challenging task is to determine forces across individual molecules in intact cells or even within an intact developing organism. One method that has gained significant interest in recent years uses genetically encoded Förster resonance energy transfer (FRET)-based molecular tension sensors. These sensors consist of a FRET donor-acceptor pair that is connected by a short flexible spring-like peptide that stretches or unfolds under force (Fig. 6D). Low forces applied to this peptide produce high FRET, whereas increasing forces reduce FRET. Various linker peptides were recently developed and calibrated using single molecule force spectroscopy to quantify forces in the range of 1 to 11 pN (reviewed in Freikamp et al., 2016). As these sensors are genetically encoded and can be inserted into proteins of choice,

piconewton forces across specific proteins can be quantified in cells and in principle also within organisms. Such tension sensors have been successfully applied to quantify forces across talin and the talin binding protein vinculin in focal adhesions of cells plated in a dish. These studies nicely showed that assembling focal adhesions experience larger forces than disassembling ones (Grashoff et al., 2010) and that talin molecules are subjected to forces ranging from 7 to 10 pN (Austen et al., 2015). Thus far, molecular tension sensors have not been used to investigate forces during muscle development *in vivo*, however, we believe developing muscles will be a fantastic system to test them and quantify forces across proteins that build the contractile sarcomere.

9. Conclusions and perspectives

Mechanical forces are important for many, if not most, morphogenetic processes that build a higher organism. In particular during muscle formation, the correct timing, location and magnitude of mechanical forces subjected onto cells and molecules are critical. We are only beginning to adapt techniques that were developed *in vitro* to measure forces *in vivo*. In many cases, we do not know the magnitude of forces that tissues or molecules encounter during animal development. It also remains a challenge to determine how many molecules within a given pool, for example at the muscle-tendon junction, do experience forces. Novel techniques such as FRET-based tension sensors may open new avenues to measure tension across proteins *in vivo*. It will be similarly challenging to manipulate forces *in vivo* in a controlled manner in order to assess their impact. Tackling and hopefully overcoming some of these challenges may eventually unravel the mechanisms muscles use to sense and interpret tension to form the highly ordered contractile apparatus that fits the biomechanical needs of each muscle type.

Competing interests

The authors declare that no competing interests exist.

Acknowledgements

We are grateful to Carsten Grashoff, Maria Spletter and Nuno Luis for insightful comments on this review. Work in the Schnorrer lab is supported by the EMBO Young Investigator Program (F.S.), the European Research Council under the European Union's Seventh Framework Programme (FP/2007–2013)/ERC Grant 310939 (F.S.), the Max Planck Society (S.B.L., F.S.), the Centre National de la Recherche Scientifique (CNRS) (F.S.) and the Boehringer Ingelheim Fonds (S.B.L.).

References

- Agarkova, I., Ehler, E., Lange, S., Schoenauer, R., Perriard, J.-C., 2003. M-band: a safeguard for sarcomere stability? *J. Muscle Res. Cell Motil.* 24, 191–203.
- Austen, K., Ringer, P., Mehlich, A., Chrostek-Grashoff, A., Kluger, C., Klingner, C., Sabass, B., Zent, R., Rief, M., Grashoff, C., 2015. Extracellular rigidity sensing by talin isoform-specific mechanical linkages. *Nat. Cell Biol.* 17:1597–1606. <http://dx.doi.org/10.1038/ncb3268>.
- Bang, M.L., Centner, T., Fornoff, F., Geach, A.J., Gotthardt, M., McNabb, M., Witt, C.C., Labeit, D., Gregorio, C.C., Granzier, H., Labeit, S., 2001. The complete gene sequence of titin, expression of an unusual approximately 700-kDa titin isoform, and its interaction with obscurin identify a novel Z-line to I-band linking system. *Circ. Res.* 89: 1065–1072. <http://dx.doi.org/10.1161/hh2301.100981>.
- Behrndt, M., Salbreux, G., Campinho, P., Hauschild, R., Oswald, F., Roensch, J., Grill, S.W., Heisenberg, C.P., 2012. Forces driving epithelial spreading in zebrafish gastrulation. *Science* 338:257–260. <http://dx.doi.org/10.1126/science.1224143>.
- Berg, J.S., Powell, B.C., Cheney, R.E., 2001. A millennial myosin census. *Mol. Biol. Cell* 12, 780–794.
- Bloor, J., Kiehart, D., 2001. Zipper nonmuscle myosin-II functions downstream of PS2 integrin during. *Dev. Biol.* 239 (2), 215–228.
- Bogomolovas, J., Gasch, A., Simkovic, F., Rigden, D.J., Labeit, S., Mayans, O., 2014. Titin kinase is an inactive pseudokinase scaffold that supports MuRF1 recruitment to the sarcomeric M-line. *Open Biol.* 4:140041. <http://dx.doi.org/10.1098/rsob.140041>.
- Brent, A., Schweitzer, R., Tabin, C., 2003. A somitic compartment of tendon progenitors. *Cell* 113, 235–248.
- Brent, A., Tabin, C., 2004. FGF acts directly on the somitic tendon progenitors through the Ets transcription factors Pea3 and Erm to regulate scleraxis expression. *Development* 131, 3885.
- Brown, N.H., 2000. Cell-cell adhesion via the ECM: integrin genetics in fly and worm. *Matrix Biol.* 19, 191–201.
- Brown, N.H., Gregory, S.L., Rickoll, W.L., Fessler, L.L., Prout, M., White, R.A.H., Fristrom, J.W., 2002. Talin is essential for integrin function in *Drosophila*. *Dev. Cell* 3, 569–579.
- Chal, J., Oginuma, M., Al Tanoury, Z., Gobert, B., Sumara, O., Hick, A., Bousson, F., Zidouni, Y., Mursch, C., Moncuquet, P., Tassy, O., Vincent, S., Miyazaki, A., Bera, A., Garnier, J.-M., Guevara, G., Hestini, M., Kennedy, L., Hayashi, S., Drayton, B., Cherrier, T., Gayraud-Morel, B., Gussone, E., Relaix, F., Tajbakhsh, S., Pourquie, O., 2015. Differentiation of pluripotent stem cells to muscle fiber to model Duchenne muscular dystrophy. *Nat. Biotechnol.* 33:962–969. <http://dx.doi.org/10.1038/nbt.3297>.
- Colombelli, J., Reynaud, E.G., Rietdorf, J., Pepperkok, R., Stelzer, E.H.K., 2005. In vivo selective cytoskeleton dynamics quantification in interphase cells induced by pulsed ultraviolet laser nanosurgery. *Traffic* 6:1093–1102. <http://dx.doi.org/10.1111/j.1600-0854.2005.00334.x>.
- Colombelli, J., Besser, A., Kress, H., Reynaud, E., Girard, P., Caussinus, E., Haselmann, U., Small, J., Schwarz, U., Stelzer, E., 2009. Mechanosensing in actin stress fibers revealed by a close correlation between force and protein localization. *J. Cell Sci.* 122, 1665.
- Cooke, R., 2004. The sliding filament model: 1972–2004. *J. Gen. Physiol.* 123:643–656. <http://dx.doi.org/10.1085/jgp.200409089>.
- Dobi, K.C., Schulman, V.K., Bayliss, M.K., 2015. Specification of the somatic musculature in *Drosophila*. *WIREs Dev. Biol.* <http://dx.doi.org/10.1002/wdev.182>.
- Dudley, R., 2000. *The Biomechanics of Insect Flight*. Princeton University Press.
- Ehler, E., Gautel, M., 2008. The sarcomere and sarcomerogenesis. *Adv. Exp. Med. Biol.* 642, 1–14.
- Ehler, E., Rothen, B.M., Hämmerle, S.P., Komiyama, M., Perriard, J.C., 1999. Myofibrillogenesis in the developing chicken heart: assembly of Z-disk, M-line and the thick filaments. *J. Cell Sci.* 112 (Pt 10), 1529–1539.
- Engler, A.J., 2004. Myotubes differentiate optimally on substrates with tissue-like stiffness: pathological implications for soft or stiff microenvironments. *J. Cell Biol.* 166: 877–887. <http://dx.doi.org/10.1083/jcb.200405004>.
- Fährmann, M., Fonk, I., Beinbrech, G., 2002. The kinase activity of the giant protein projectin of the flight muscle of *Locusta migratoria*. *Insect Biochem. Mol. Biol.* 32, 1401–1407.
- Ferrari, M.B., Ribbeck, K., Hagler, D.J., Spitzer, N.C., 1998. A calcium signaling cascade essential for myosin thick filament assembly in *Xenopus myocytes*. *J. Cell Biol.* 141, 1349–1356.
- Freikamp, A., Cost, A.-L., Grashoff, C., 2016. The piconewton force awakens: quantifying mechanics in cells. *Trends Cell Biol.* <http://dx.doi.org/10.1016/j.tcb.2016.07.005>.
- Fürst, D.O., Osborn, M., Nave, R., Weber, K., 1988. The organization of titin filaments in the half-sarcomere revealed by monoclonal antibodies in immunoelectron microscopy: a map of ten nonrepetitive epitopes starting at the Z line extends close to the M line. *J. Cell Biol.* 106, 1563–1572.
- Gautel, M., 2011a. The sarcomeric cytoskeleton: who picks up the strain? *Curr. Opin. Cell Biol.* 23:39–46. <http://dx.doi.org/10.1016/j.ccb.2010.12.001>.
- Gautel, M., 2011b. Cytoskeletal protein kinases: titin and its relations in mechanosensing. *Pflugers Arch. - Eur. J. Physiol.* 462:119–134. <http://dx.doi.org/10.1007/s00424-011-0946-1>.
- Gautel, M., Goulding, D., 1996. A molecular map of titin/connectin elasticity reveals two different mechanisms acting in series. *FEBS Lett.* 385, 11–14.
- Gautel, M., Lehtonen, E., Pietruschka, F., 1996. Assembly of the cardiac I-band region of titin/connectin: expression of the cardiac-specific regions and their structural relation to the elastic segments. *J. Muscle Res. Cell Motil.* 17, 449–461.
- Gokhin, D.S., Fowler, V.M., 2013. A two-segment model for thin filament architecture in skeletal muscle. *Nat. Rev. Mol. Cell Biol.* 14:113–119. <http://dx.doi.org/10.1038/nrm3510>.
- Götz, K.G., 1987. Course-control, metabolism and wing interference during ultralong tethered flight in *Drosophila melanogaster*. *J. Exp. Biol.* 128, 35–46.
- Grashoff, C., Hoffman, B.D., Brenner, M.D., Zhou, R., Parsons, M., Yang, M.T., Mclean, M.A., Sligar, S.G., Chen, C.S., Ha, T., Schwartz, M.A., 2010. Measuring mechanical tension across vinculin reveals regulation of focal adhesion dynamics. *Nature* 466:263–266. <http://dx.doi.org/10.1038/nature09198>.
- Gros, J., Serralbo, O., Marcelle, C., 2008. WNT11 acts as a directional cue to organize the elongation of early muscle fibres. *Nature* 457, 589–593.
- Guo, W., Bharmal, S.J., Esbona, K., Greaser, M.L., 2010. Titin diversity—alternative splicing gone wild. *J. Biomed. Biotechnol.* 2010:1–8. <http://dx.doi.org/10.1016/j.jbjmcc.2009.11.013>.
- Guo, W., Schafer, S., Greaser, M.L., Radke, M.H., Liss, M., Govindarajan, T., Maatz, H., Schulz, H., Li, S., Parrish, A.M., Dauksaite, V., Vakeel, P., Klaassen, S., Gerull, B., Thierfelder, L., Regitz-Zagrosek, V., Hacker, T.A., Saube, K.W., Dec, G.W., Ellinor, P.T., MacRae, C.A., Spallek, B., Fischer, R., Perrot, A., Zelik, C.O., Saar, K., Hubner, N., Gotthardt, M., 2012. RBM20, a gene for hereditary cardiomyopathy, regulates titin splicing. *Nat. Med.* 18:766–773. <http://dx.doi.org/10.1038/nm.2693>.
- Harris, B.N., Li, H., Terry, M., Ferrari, M.B., 2005. Calcium transients regulate titin organization during myofibrillogenesis. *Cell Motil. Cytoskeleton* 60:129–139. <http://dx.doi.org/10.1002/cm.20054>.
- Heisenberg, C.-P., Bellaiche, Y., 2013. Forces in tissue morphogenesis and patterning. *Cell* 153:948–962. <http://dx.doi.org/10.1016/j.cell.2013.05.008>.
- Hill, J., Olson, E., 2012. *Muscle*. Academic Press.
- Holtzer, H., Hijikata, T., Lin, Z.X., Zhang, Z.Q., Holtzer, S., Protasi, F., Franzini-Armstrong, C., Sweeney, H.L., 1997. Independent assembly of 1.6 microns long bipolar MHC filaments and I-Z-1 bodies. *Cell Struct. Funct.* 22, 83–93.
- Howard, J., 2001. *Mechanics of Motor Proteins & the Cytoskeleton*. Sinauer Associates Incorporated.
- Hughes, M.L., Dougan, L., 2016. The physics of pulling polyproteins: a review of single molecule force spectroscopy using the AFM to study protein unfolding. *Rep. Prog. Phys.* 79:076601. <http://dx.doi.org/10.1088/0034-4885/79/7/076601>.
- Huxley, H., Hanson, J., 1954. Changes in the cross-striations of muscle during contraction and stretch and their structural interpretation. *Nature* 173, 973–976.
- Huxley, A.F., Niedergerke, R., 1954. Structural changes in muscle during contraction; interference microscopy of living muscle fibres. *Nature* 173, 971–973.
- Hyman, A.A., Weber, C.A., Jülicher, F., 2014. Liquid-liquid phase separation in Biology. *Annu. Rev. Cell Dev. Biol.* 30:39–58. <http://dx.doi.org/10.1146/annurev-cellbio-100913-013325>.
- Kanchanawong, P., Shtengel, G., Pasapera, A.M., Ramko, E.B., Davidson, M.W., Hess, H.F., Waterman, C.M., 2010. Nanoscale architecture of integrin-based cell adhesions. *Nature* 468:580–584. <http://dx.doi.org/10.1038/nature09621>.
- Kim, J.H., Jin, P., Duan, R., Chen, E.H., 2015. Mechanisms of myoblast fusion during muscle development. *Curr. Opin. Genet. Dev.* 32:162–170. <http://dx.doi.org/10.1016/j.gde.2015.03.006>.
- Klapholz, B., Herbert, S.L., Wellmann, J., Johnson, R., Parsons, M., Brown, N.H., 2015. Alternative mechanisms for Talin to mediate integrin function. *Cell Biol.* <http://dx.doi.org/10.1016/j.cub.2015.01.043>.
- Kötter, S., Gout, L., Frieling-Salewsky, V.M., Müller, A.E., Helling, S., Marcus, K., Remedios, D.C., Linke, W.A., Krüger, M., 2013. Differential changes in titin domain phosphorylation increase myofibril stiffness in failing human hearts. *Cardiovasc. Res.* 99: 648–656. <http://dx.doi.org/10.1093/cvr/cvt144>.
- Labeit, S., Kolmerer, B., 1995. Titins: giant proteins in charge of muscle ultrastructure and elasticity. *Science* 270, 293–296.
- Lange, S., Ehler, E., Gautel, M., 2006. From A to Z and back? Multicompartments proteins in the sarcomere. *Trends Cell Biol.* 16, 11–18.
- Lange, S., Xiang, F., Yakovenko, A., Vihola, A., Hackman, P., Rostkova, E., Kristensen, J., Brandmeier, B., Franzen, G., Hedberg, B., Gunnarsson, L.G., Hughes, S.M., Marchand, S., Sejersten, T., Richard, I., Edström, L., Ehler, E., Udd, B., Gautel, M., 2005. The kinase domain of titin controls muscle gene expression and protein turnover. *Science* 308: 1599–1603. <http://dx.doi.org/10.1126/science.1110463>.
- Lecuit, T., Lenne, P.-F., Munro, E., 2011. Force generation, transmission, and integration during cell and tissue morphogenesis. *Annu. Rev. Cell Dev. Biol.* 27:157–184. <http://dx.doi.org/10.1146/annurev-cellbio-100109-104027>.
- Legate, K.R., Montanez, E., Kudlacek, O., Füssler, R., 2005. ILK, PINCH and parvin: the tIPP of integrin signalling. *Nat. Rev. Mol. Cell Biol.* 7:20–31. <http://dx.doi.org/10.1038/nrm1789>.
- Legate, K.R., Wickström, S.A., Fässler, R., 2009. Genetic and cell biological analysis of integrin outside-in signalling. *Genes Dev.* 23:397–418. <http://dx.doi.org/10.1101/gad.1758709>.
- Lehmann, F.-O., Dickinson, M.H., 1997. The changes in power requirements and muscle efficiency during elevated force production in the fruit fly *Drosophila melanogaster*. *J. Exp. Biol.* 200, 1133–1143.
- Leptin, M., Bogaert, T., Lehmann, R., Wilcox, M., 1989. The function of PS integrins during *Drosophila* embryogenesis. *Cell* 56, 401–408.
- Li, H., Oberhauser, A.F., Redick, S.D., Carrion-Vazquez, M., Erickson, H.P., Fernandez, J.M., 2001. Multiple conformations of PEVK proteins detected by single-molecule techniques. *Proc. Natl. Acad. Sci. U. S. A.* 98:10682–10686. <http://dx.doi.org/10.1073/pnas.191189098>.

- Li, B., Lin, M., Tang, Y., Wang, B., Wang, J.H.C., 2008. A novel functional assessment of the differentiation of micropatterned muscle cells. *J. Biomech.* 41:3349–3353. <http://dx.doi.org/10.1016/j.jbiomech.2008.09.025>.
- Linke, W.A., Ivemeyer, M., Olivieri, N., Kolmerer, B., Rüegg, J.C., Labeit, S., 1996. Towards a molecular understanding of the elasticity of titin. *J. Mol. Biol.* 261, 62–71.
- Linke, W.A., Rudy, D.E., Centner, T., Gautel, M., Witt, C., Labeit, S., Gregorio, C.C., 1999. I-band titin in cardiac muscle is a three-element molecular spring and is critical for maintaining thin filament structure. *J. Cell Biol.* 146, 631–644.
- Linke, W.A., Kulke, M., Li, H., Fujita-Becker, S., Neagoe, C., Manstein, D.J., Gautel, M., Fernandez, J.M., 2002. PEVK domain of titin: an entropic spring with actin-binding properties. *J. Struct. Biol.* 137:194–205. <http://dx.doi.org/10.1006/jsbi.2002.4468>.
- Llewellyn, M., Barretto, R., Delp, S., Schnitzer, M., 2008. Minimally invasive high-speed imaging of sarcomere contractile dynamics in mice and humans. *Nature* 454, 784–788.
- Magid, A., Law, D.J., 1985. Myofibrils bear most of the resting tension in frog skeletal muscle. *Science* 230:1280–1282. <http://dx.doi.org/10.1126/science.4071053>.
- Marino, T.A., Kuseryk, L., Lauva, I.K., 1987. Role of contraction in the structure and growth of neonatal rat cardiocytes. *Am. J. Phys.* 253, H1391–H1399.
- Maruyama, K., 2002. β -Actinin, cap Z, connectin and titin: what's in a name? *Trends Biochem. Sci.*
- Maruyama, K., Natori, R., Nonomura, Y., 1976. New elastic protein from muscle. *Nature* 262:58–60. <http://dx.doi.org/10.1038/262058a0>.
- Maruyama, K., Matsubara, S., Natori, R., Nonomura, Y., Kimura, S., 1977. Connectin, an elastic protein of muscle. *Charact. Funct. J. Biochem.* 82, 317–337.
- Mayans, O., Van der Ven, P.F., Wilm, M., Mues, A., Young, P., Fürst, D.O., Wilmanns, M., Gautel, M., 1998. Structural basis for activation of the titin kinase domain during myofibrillogenesis. *Nature* 395:863–869. <http://dx.doi.org/10.1038/27603>.
- Mayer, M., Depken, M., Bois, J.S., Jülicher, F., Grill, S.W., 2010. Anisotropies in cortical tension reveal the physical basis of polarizing cortical flows. *Nature* 467:617–621. <http://dx.doi.org/10.1038/nature09376>.
- Morimatsu, M., Mekhdjian, A.H., Adhikari, A.S., Dunn, A.R., 2013. Molecular tension sensors report forces generated by single integrin molecules in living cells. *Nano Lett.* 13:3985–3989. <http://dx.doi.org/10.1021/nl4005145>.
- Moser, M., Legate, K.R., Zent, R., Fassler, R., 2009. The tail of integrins, talin, and kindlins. *Science* 324:895–899. <http://dx.doi.org/10.1126/science.1163865>.
- Perriard, J.-C., Hirschy, A., Ehler, E., 2003. Dilated cardiomyopathy: a disease of the intercalated disc? *Trends Cardiovasc. Med.* 13:30–38. [http://dx.doi.org/10.1016/S1050-1738\(02\)00209-8](http://dx.doi.org/10.1016/S1050-1738(02)00209-8).
- Pines, M., Das, R., Ellis, S.J., Morin, A., Czerniecki, S., Yuan, L., Klose, M., Coombs, D., Tanentzapf, G., 2012. Mechanical force regulates integrin turnover in *Drosophila* in vivo. *Nat. Cell Biol.* 14:935–943. <http://dx.doi.org/10.1038/ncb2555>.
- Puchner, E.M., Alexandrovich, A., Kho, A.L., Hensen, U., Schäfer, L.V., Brandmeier, B., Gräter, F., Grubmüller, H., Gaub, H.E., Gautel, M., 2008. Mechanoenzymatics of titin kinase. *Proc. Natl. Acad. Sci.* 105:13385–13390. <http://dx.doi.org/10.1073/pnas.0805034105>.
- Rauzi, M., Lenne, P.-F., Lecuit, T., 2010. Nature09566. *Nature* 468:1110–1114. <http://dx.doi.org/10.1038/nature09566>.
- Regev, G.J., Kim, C.W., Tomiya, A., Lee, Y.P., Ghofrani, H., Garfin, S.R., Lieber, R.L., Ward, S.R., 2011. Psoas muscle architectural design, in vivo sarcomere length range, and passive tensile properties support its role as a lumbar spine stabilizer. *Spine* 36: E1666–E1674. <http://dx.doi.org/10.1097/BRS.0b013e31821847b3>.
- Rhee, D., Sanger, J.M., Sanger, J.W., 1994. The premyofibril: evidence for its role in myofibrillogenesis. *Cell Motil. Cytoskeleton* 28:1–24. <http://dx.doi.org/10.1002/cm.970280102>.
- Ribeiro, A.J.S., Denisin, A.K., Wilson, R.E., Pruitt, B.L., 2016. For whom the cells pull: hydrogel and micropost devices for measuring traction forces. *Methods* 94:51–64. <http://dx.doi.org/10.1016/j.ymeth.2015.08.005>.
- Rief, M., Gautel, M., Oesterhelt, F., Fernandez, J.M., Gaub, H.E., 1997. Reversible unfolding of individual titin immunoglobulin domains by AFM. *Science* 276, 1109–1112.
- Rochlin, K., Yu, S., Roy, S., Baylies, M., 2010. Myoblast fusion: when it takes more to make one. *Dev. Biol.* 341, 66–83.
- Rui, Y., Bai, J., Perrimon, N., 2010. Sarcomere formation occurs by the assembly of multiple latent protein complexes. *PLoS Genet.* 6, e1001208. <http://dx.doi.org/10.1371/journal.pgen.1001208>.
- Sanger, J.W., Wang, J., Holloway, B., Du, A., Sanger, J.M., 2009. Myofibrillogenesis in skeletal muscle cells in zebrafish. *Cell Motil. Cytoskeleton* 66:556–566. <http://dx.doi.org/10.1002/cm.20365>.
- Schiaffino, S., Reggiani, C., 2011. Fiber types in mammalian skeletal muscles. *Physiol. Rev.* 91:1447–1531. <http://dx.doi.org/10.1152/physrev.00031.2010>.
- Schnorrer, F., Dickson, B., 2004. Muscle building mechanisms of myotube guidance and attachment site selection. *Dev. Cell* 7, 9–20.
- Schnorrer, F., Kalchauer, I., Dickson, B., 2007. The transmembrane protein Kon-tiki couples to Dgrip to mediate myotube targeting in *Drosophila*. *Dev. Cell* 12, 751–766.
- Schnorrer, F., Schönbauer, C., Langer, C.C.H., Dietzl, G., Novatchkova, M., Schernhuber, K., Fellner, M., Azaryan, A., Radolf, M., Stark, A., Keleman, K., Dickson, B.J., 2010. Systematic genetic analysis of muscle morphogenesis and function in *Drosophila*. *Nature* 464:287–291. <http://dx.doi.org/10.1038/nature08799>.
- Schönbauer, C., Distler, J., Jähring, N., Radolf, M., Dodt, H.-U., Frasch, M., Schnorrer, F., 2011. Spalt mediates an evolutionarily conserved switch to fibrillar muscle fate in insects. *Nature* 479:406–409. <http://dx.doi.org/10.1038/nature10559>.
- Schwander, M., Leu, M., Stumm, M., Dorchie, O.M., Ruegg, U.T., Schittny, J., Müller, U., 2003. Beta1 integrins regulate myoblast fusion and sarcomere assembly. *Dev. Cell* 4, 673–685.
- Schweitzer, R., Chyung, J., Murtaugh, L., Brent, A., Rosen, V., Olson, E., Lassar, A., Tabin, C., 2001. Analysis of the tendon cell fate using scleraxis, a specific marker for tendons and ligaments. *Development* 128, 3855.
- Schweitzer, R., Zelzer, E., Volk, T., 2010. Connecting muscles to tendons: tendons and musculoskeletal development in flies and vertebrates. *Development* 137: 2807–2817. <http://dx.doi.org/10.1242/dev.047498>.
- Shimamoto, Y., Maeda, Y.T., Ishiwata, S., Libhaber, A.J., Kapoor, T.M., 2011. Insights into the Micromechanical Properties of the Metaphase Spindle. *Cell* 145:1062–1074. <http://dx.doi.org/10.1016/j.cell.2011.05.038>.
- Sparrow, J., Schöck, F., 2009. The initial steps of myofibril assembly: integrins pave the way. *Nat. Rev. Mol. Cell Biol.* 10, 293–298.
- Spletter, M.L., Schnorrer, F., 2014. Transcriptional regulation and alternative splicing cooperate in muscle fiber-type specification in flies and mammals. *Exp. Cell Res.* 321: 90–98. <http://dx.doi.org/10.1016/j.yexcr.2013.10.007>.
- Spletter, M.L., Barz, C., Yeroslaviz, A., Schönbauer, C., Ferreira, I.R.S., Sarov, M., Gerlach, D., Stark, A., Habermann, B.H., Schnorrer, F., 2015. The RNA-binding protein Arrest (Bruno) regulates alternative splicing to enable myofibril maturation in *Drosophila* flight muscle. *EMBO Rep.* 16:178–191. <http://dx.doi.org/10.15252/embr.201439791>.
- Szent-Györgyi, A.G., 2004. The early history of the biochemistry of muscle contraction. *J. Gen. Physiol.* 123:631–641. <http://dx.doi.org/10.1085/jgp.200409091>.
- Tskhovrebova, L., Trinick, J., 2003. Titin: properties and family relationships. *Nat. Rev. Mol. Cell Biol.* 4:679–689. <http://dx.doi.org/10.1038/nrm1198>.
- Tullio, A.N., Accili, D., Ferrans, V.J., Yu, Z.X., Takeda, K., Grinberg, A., Westphal, H., Preston, Y.A., Adelstein, R.S., 1997. Nonmuscle myosin II-B is required for normal development of the mouse heart. *Proc. Natl. Acad. Sci. U. S. A.* 94, 12407–12412.
- Vakaloglou, K.M., Chrysanthos, G., Zervas, C.G., 2016. IPP complex reinforces cell adhesion by relaying tension-dependent signals to inhibit integrin turnover. *Cell Rep.* 14: 2668–2682. <http://dx.doi.org/10.1016/j.celrep.2016.02.052>.
- Vicente-Manzanares, M., Ma, X., Adelstein, R.S., Horwitz, A.R., 2009. Non-muscle myosin II takes centre stage in cell adhesion and migration. *Nat. Rev. Mol. Cell Biol.* 10: 778–790. <http://dx.doi.org/10.1038/nrm2786>.
- Vigoreaux, J.O., 2006. Molecular Basis of Muscle Structure, in: *Muscle Development in Drosophila*, Molecular Biology Intelligence Unit. Springer, New York, New York, NY: pp. 143–156. http://dx.doi.org/10.1007/0-387-32963-3_12.
- Vogel, S.K., Pavin, N., Maghelli, N., Jülicher, F., Tolić-Nørrelykke, I.M., 2009. Self-organization of dynein motors generates meiotic nuclear oscillations. *PLoS Biol.* 7, e1000087. <http://dx.doi.org/10.1371/journal.pbio.1000087>.
- Weitkunat, M., Kaya-Copur, A., Grill, S.W., Schnorrer, F., 2014. Tension and force-resistant attachment are essential for myofibrillogenesis in *Drosophila* flight muscle. *Curr. Biol.* 24:705–716. <http://dx.doi.org/10.1016/j.cub.2014.02.032>.
- White, J., Barro, M.V., Makarenkova, H.P., Sanger, J.W., Sanger, J.M., 2014. Localization of sarcomeric proteins during myofibril assembly in cultured mouse primary skeletal myotubes. *Anat. Rec.* 297:1571–1584. <http://dx.doi.org/10.1002/ar.22981>.
- Williams, B.D., Waterston, R.H., 1994. Genes critical for muscle development and function in *Caenorhabditis elegans* identified through lethal mutations. *J. Cell Biol.* 124, 475–490.

Video Article

In Vivo Imaging of Muscle-tendon Morphogenesis in *Drosophila* PupaeSandra B. Lemke¹, Frank Schnorrer^{1,2}¹Muscle Dynamics Group, Max Planck Institute of Biochemistry²Aix Marseille University, CNRS, IBDMCorrespondence to: Sandra B. Lemke at lemke@biochem.mpg.de, Frank Schnorrer at frank.schnorrer@univ-amu.frURL: <https://www.jove.com/video/57312>DOI: [doi:10.3791/57312](https://doi.org/10.3791/57312)Keywords: Developmental Biology, Issue 132, Live imaging, *Drosophila*, pupal development, muscle, tendon, sarcomere, myofibril, attachment, self-organization

Date Published: 2/6/2018

Citation: Lemke, S.B., Schnorrer, F. *In Vivo* Imaging of Muscle-tendon Morphogenesis in *Drosophila* Pupae. *J. Vis. Exp.* (132), e57312, doi:10.3791/57312 (2018).**Abstract**

Muscles together with tendons and the skeleton enable animals including humans to move their body parts. Muscle morphogenesis is highly conserved from animals to humans. Therefore, the powerful *Drosophila* model system can be used to study concepts of muscle-tendon development that can also be applied to human muscle biology. Here, we describe in detail how morphogenesis of the adult muscle-tendon system can be easily imaged in living, developing *Drosophila* pupae. Hence, the method allows investigating proteins, cells and tissues in their physiological environment. In addition to a step-by-step protocol with helpful tips, we provide a comprehensive overview of fluorescently tagged marker proteins that are suitable for studying the muscle-tendon system. To highlight the versatile applications of the protocol, we show example movies ranging from visualization of long-term morphogenetic events – occurring on the time scale of hours and days – to visualization of short-term dynamic processes like muscle twitching occurring on time scale of seconds. Taken together, this protocol should enable the reader to design and perform live-imaging experiments for investigating muscle-tendon morphogenesis in the intact organism.

Video LinkThe video component of this article can be found at <https://www.jove.com/video/57312/>**Introduction**

The muscle-tendon apparatus allows animals including humans to move their body parts. The molecular building blocks of the muscle-tendon system are highly conserved. Therefore, concepts of muscle-tendon development relevant for human muscle biology, for example muscle morphogenesis, muscle-tendon attachment and myofibril self-organization, can be studied using *Drosophila melanogaster* as an easily accessible model system. The *Drosophila* pupal system has several experimental advantages. First, at the pupal stage – when the adult muscles are formed – the organism is sessile and therefore easy to image on a microscope over a period of hours or even days. Second, many muscles form close enough underneath the pupal surface so that they can be imaged inside the intact, partially translucent organism. Third, the muscles can be investigated in their natural environment, where they are connected to the forming exoskeleton via tendon cells and tissue tension is built up. This is not possible in muscle cell culture systems. And finally, a plethora of genetic tools is available in *Drosophila*. Among these are many fluorescently tagged markers that allow labeling of specific cell types or subcellular structures for imaging *in vivo*.

Table 1 summarizes the most important markers used for studying muscle-tendon morphogenesis. It includes markers overexpressed using the GAL4-UAS-system¹ and endogenously tagged protein markers^{2,3,4}. The advantage of the GAL4-UAS-system is that the markers are generally expressed at high levels, resulting in a strong signal that can easily be imaged in whole-mount pupae. In addition, tissue specificity can be achieved by choosing GAL4 drivers carefully. The advantage of fusion proteins expressed under endogenous control is that the dynamics of the respective proteins can be studied *in vivo*, while they can also be used as markers for different cell types or specific subcellular structures, for example, β PS-Integrin-GFP for muscle attachment sites. Together, these markers provide high flexibility in experimental design and choice of research problems that can be solved now and in the future.

| Labeled structure | Marker | Expression and localization | Class | Stock number | Comment | Ref. |
|-------------------|---|--|---|----------------------|--|------|
| Muscle | <i>Mef2</i> -GAL4 | all myoblasts and all muscles at all stages | GAL4 line | BL 27390 | | 5 |
| | <i>1151</i> -GAL4 | adult muscle precursors and early myotubes until ≈24 h APF | GAL4 line, enhancer trap | - | | 6 |
| | <i>Act79B</i> -GAL4 | jump muscle upon differentiation | GAL4 line | - | | 7 |
| | <i>Act88F</i> -GAL4 | indirect flight muscles starting ≈14 h APF | GAL4 line | - | | 7 |
| | <i>Act88F</i> -Cameleon 3.1 | indirect flight muscles starting ≈14 h APF | Act88F enhancer/promoter driving Cameleon 3.1 | - | Ca ²⁺ indicator | 8 |
| | <i>Act88F</i> -GFP | indirect flight muscles starting ≈14 h APF | GFP-fusion (fly TransgeneOme line) | fTRG78 and fTRG10028 | | 4 |
| | <i>Him</i> -nls-GFP | adult muscle precursors, nuclear, until ≈24 h APF in indirect flight muscles | enhancer/promoter with nls-GFP reporter | - | 1.5 kb enhancer fragment | 9 |
| | <i>Mhc</i> -Tau-GFP | microtubules in DLM templates and in differentiating muscles | enhancer/promoter with Tau-GFP reporter | BL 53739 | | 10 |
| | βTub60D-GFP | microtubules in myotubes (e.g. in indirect flight muscles from ≈14 h APF, strongly decreasing after ≈48 h APF) | GFP-fusion (fly TransgeneOme line) | fTRG958 | | 4 |
| | <i>Mhc</i> -GFP (<i>weeP26</i>) | sarcomeres (thick filament) in all body muscles (e.g. in indirect flight muscles starting from ≈30 h APF) | GFP-trap | - | use heterozygous, labels an isoform subset | 11 |
| | <i>Sls</i> -GFP | sarcomeres (Z-disc) in all body muscles (e.g. in indirect flight muscles starting from ≈30 h APF) | GFP-trap (FlyTrap line) | - | G53, use heterozygous | 2 |
| | <i>Zasp66</i> -GFP | Z-disc in all body muscles | GFP-trap (FlyTrap line) | BL 6824 | ZCL0663 | 2,12 |
| | <i>Zasp52</i> -GFP | Z-disc in all body muscles | GFP-trap (FlyTrap line) | BL 6838 | G00189 | 2,12 |
| | <i>Hts</i> -GFP | actin binding; expressed in epithelium, myoblasts and myotubes | GFP-fusion (fly TransgeneOme line) | fTRG585 | | 4 |
| <i>Dlg1</i> -GFP | epithelial cell junctions, myoblasts and membranes in muscles at all stages | GFP-fusion (fly TransgeneOme line) | fTRG502 | | 4 | |

| | | | | | | |
|-------------------------------|--------------------------|---|------------------------------------|--------------------------------|---|----|
| Muscle attachment site | βPS-Integrin-GFP | muscle attachment sites (e.g., starting ≈18 h AFP in indirect flight muscles) | GFP-knock-in | - | | 13 |
| | Talin-GFP and -mCherry | muscle attachment sites (e.g., starting ≈18 h AFP in indirect flight muscles) | GFP-trap (MiMIC line) | - | | 3 |
| | Talin-GFP | muscle attachment sites (e.g., starting ≈18 h AFP in indirect flight muscles) | GFP-fusion (fly TransgeneOme line) | fTRG587 | | 4 |
| | Ilk-GFP | muscle attachment sites (e.g., starting ≈18 h AFP in indirect flight muscles) | GFP-trap (FlyTrap line) | Kyoto 110951 (ZCL3111) | ZCL3111, ZCL3192 | 2 |
| | Vinc-GFP and -RFP | muscle attachment sites (e.g., starting ≈18 h AFP in indirect flight muscles) | GFP-fusion (transgene) | - | | 13 |
| Tendon | <i>sr</i> -GAL4 | thorax tendon cells, throughout pupal stage | GAL4 line, enhancer trap | BL 26663 | homozygous lethal | 14 |
| Muscle and Tendon | <i>Duf</i> -GAL4 | muscles and epithelia, early onset | GAL4 line | BL 66682 | kirre-rP298, founder cell marker | 15 |
| UAS-reporters | <i>UAS</i> -GFP-Gma | actin binding | UAS line | BL 31776 | actin binding domain of Moesin fused to GFP | 16 |
| | <i>UAS</i> -mCherry-Gma | actin binding | UAS line | - | Gma fused to mCherry | 17 |
| | <i>UAS</i> -Lifeact-GFP | actin binding | UAS line | BL 35544 | | 18 |
| | <i>UAS</i> -Lifeact-Ruby | actin binding | UAS line | BL 35545 | | 18 |
| | <i>UAS</i> -CD8-GFP | membrane binding | UAS line | various stocks, e.g.: BL 32184 | | 19 |
| | <i>UAS</i> -CD8-mCherry | membrane binding | UAS line | BL 27391 and 27392 | | 20 |
| | <i>UAS</i> -palm-mCherry | membrane binding through palmitoylation | UAS line | BL 34514 | <i>UAS</i> -brainbow | 21 |

Table 1: Fluorescently tagged protein markers suitable for studying muscle-tendon morphogenesis *in vivo*.

Here, we describe in detail how imaging of muscle-tendon morphogenesis in living pupae can be performed easily and successfully (**Figure 1**). Alternatively, pupae can be fixed, dissected and immunostained, which allows using antibodies to also label proteins for which no live markers are available²². In this case, the imaging quality is generally higher because there is no movement and the structure of interest can be placed in close proximity to the coverslip. However, dissection and fixation can lead to damage and molecular or tissue dynamics, for example, muscle twitching, can only be studied in the living organism.

Protocol

1. Stage Pupae

1. Set up a cross with 20 - 40 virgin females and about 20 males per bottle of fly food (**Figure 1A**). Alternatively, if stocks will be used, flip each stock into new bottles. To get enough pupae, consider setting up two bottles per genotype.
2. Incubate the bottles at 25 °C (or 27 °C according to the experimental design) for five to six days (**Figure 1B**).
NOTE: Keep flipping the flies every two to three days to avoid overcrowding and to ensure a continuous supply of pupae.
3. Use a wet brush to collect white prepupae from the walls of the bottles and transfer them to the glass slides (**Figure 1C**). Time the staging such that the pupae reach the desired age when starting live imaging under the microscope.
NOTE: These prepupae look like older pupae in terms of their shape, but they are still white like larvae. The onset of the prepupal stage is defined as 0 h after puparium formation (0 h APF).

4. Remove clumps of fly food sticking to the pupae with a wet brush and orient the ventral side of the pupae towards the glass slide using a stereomicroscope (**Figure 1D**). Discard pupae that are still moving (too young) or that have started to turn brown (too old). This ensures that all pupae have the same age (0 - 1 h APF).
5. Label the slides with genotype, date and time of collection. Transfer the glass slides to one petri dish each and add a wet tissue to prevent the pupae from drying out (**Figure 1E**).
6. Store the pupae in an incubator at 25 °C or 27 °C until they reach the desired age. Continue with the next steps 1 h before imaging, so that the pupae have the desired age when starting live imaging (step 3), for example at 13 h APF for the movie shown in **Figure 2A-D**.
NOTE: The earliest feasible starting time point is after head-eversion of the pupae occurring at 8 - 10 h APF at 27 °C.

2. Prepare Pupae for Imaging

1. Ensure that the pupae now stick to the glass slide just like they naturally stick to the walls of the bottles because of residual fly food. No extra glue is required. If the pupae do not stick well enough because of high humidity, open the petri dish for a few min to let them dry. Alternatively, transfer them to double-sided tape on a glass slide, but usually, this is not necessary.
2. **Open window in the pupal case for imaging of indirect flight muscles (Figure 1F; Skip to section 2.3 for imaging of abdominal muscles.)**
 1. Orient the pupae sticking to the glass slide with the anterior facing away from the researcher under a stereomicroscope. Adjust the zoom to 2X.
 2. Using one end of biology grade #5 forceps, gently poke a hole into the pupal case dorsal to the wing where the abdomen ends, and the thorax begins.
 3. To slice open the pupal case, gently move the forceps to the anterior end of the thorax along the wing but avoid damaging the vulnerable wing tissue.
NOTE: If fluid leaks from the pupa, it is damaged; discard it and start over with a different pupa.
 4. Lift up the section of the pupal case above the thorax with the forceps and then cut this section off with fine, sharp scissors on the opposite side of the dorsal midline.
3. **Open window in pupal case for imaging of abdominal muscles (Figure 1G)**
 1. Orient the pupae sticking to the glass slide with the anterior facing towards the researcher under a stereomicroscope. Adjust the zoom to 2X.
 2. Using one end of biology grade #5 forceps, gently poke a hole into the pupal case dorsal to the wing where the thorax ends, and the abdomen begins.
 3. To slice open the pupal case, gently move the forceps towards the posterior end of the abdomen.
NOTE: If fluid leaks from the pupa, it is damaged; discard it and start over with a different pupa.
 4. Lift up the section of the pupal case above the abdomen with the forceps and then cut this section off with fine, sharp scissors on the opposite side of the dorsal midline.
4. **Mount Pupae (Figure 1H)**
 1. Use a wet brush to transfer up to five pupae to a plastic slide with a groove (custom-built, reusable, see discussion and list of materials). Add one or two spacer coverslips to each side depending on the depth of the groove and the thickness of the pupae. Put a small drop of water underneath each spacer coverslip to make it stick to the slide and leave some space between the groove and the spacer coverslips on each side.
NOTE: The spacer coverslips can also be permanently attached to the slide with super glue, in advance.
 2. Orient the pupae such that the opening in the pupal case faces upwards using the brush. Ensure careful positioning of the pupae at the correct angle for good imaging quality. Optimize the angle for each tissue and developmental time point.
NOTE: A small amount of water in the groove makes positioning of the pupae easier. Drain excess water with the brush afterward to avoid drowning.
 3. Hold a coverslip (18 x 18 mm) above the pupae without touching them. Place small droplets (about 0.5 µL) of 50% glycerol solution above each pupal case opening onto the coverslip using a 20 µL pipette.
NOTE: This procedure ensures that the droplets have the same spacing as the pupae.
 4. Turn the coverslip over and position it above the pupae by hand or using forceps (standard #5) while resting one side of the coverslip on the spacer coverslips next to the pupae. Next, gently drop the coverslip onto the pupae. Ensure that the pupal case openings are properly covered with 50% glycerol for good imaging quality and to prevent the pupae from drying out.
 5. Fold over one end of a piece of adhesive tape and grab it with forceps (standard #5) at that end. Gently place the tape such that it covers one edge of the top coverslip, the spacer coverslip(s), and the plastic slide on one side. Do not press down the tape, yet. First, turn the slide around and repeat for the other side.
 6. Use both index fingers to press down the tape simultaneously on both sides. This procedure ensures that the pupae are not displaced.
 7. Check whether the pupae are well in contact with the coverslip. For optimal imaging quality the pupae should be gently squeezed underneath the coverslip. Adjust the number of spacer coverslips if necessary.
 8. Label the slide by writing on the sticky tape.

3. Live Imaging of Pupae

1. The mounting method allows imaging of the pupae both on inverted microscopes (**Figure 1I**) and on upright microscopes (**Figure 1J**). Especially suitable for live imaging are scanning confocal microscopes, two-photon microscopes and spinning disc confocal microscopes irrespective of whether they are inverted or upright. For long-term movies, use a temperature-controlled stage if available.
2. Using the ocular and a UV lamp or transmission light, locate a pupa and focus inside the pupa.
3. Using the camera, find the desired structure and adjust the zoom level.

- For long-term movies, define a z-stack that encompasses the structure of interest well (for example, the indirect flight muscles, their attachment sites, the tendon cells or a combination the aforementioned) and choose a time interval. Consider doing averaging for better image quality. For high-speed, short-term movies, choose a single z-plane to achieve a high frame rate.
- Adjust the laser power to give the best possible signal but little saturation. However, too high laser power can damage the pupa over time.
- Start imaging and return from time to time to check the movie and readjust the z-stack positioning if necessary.

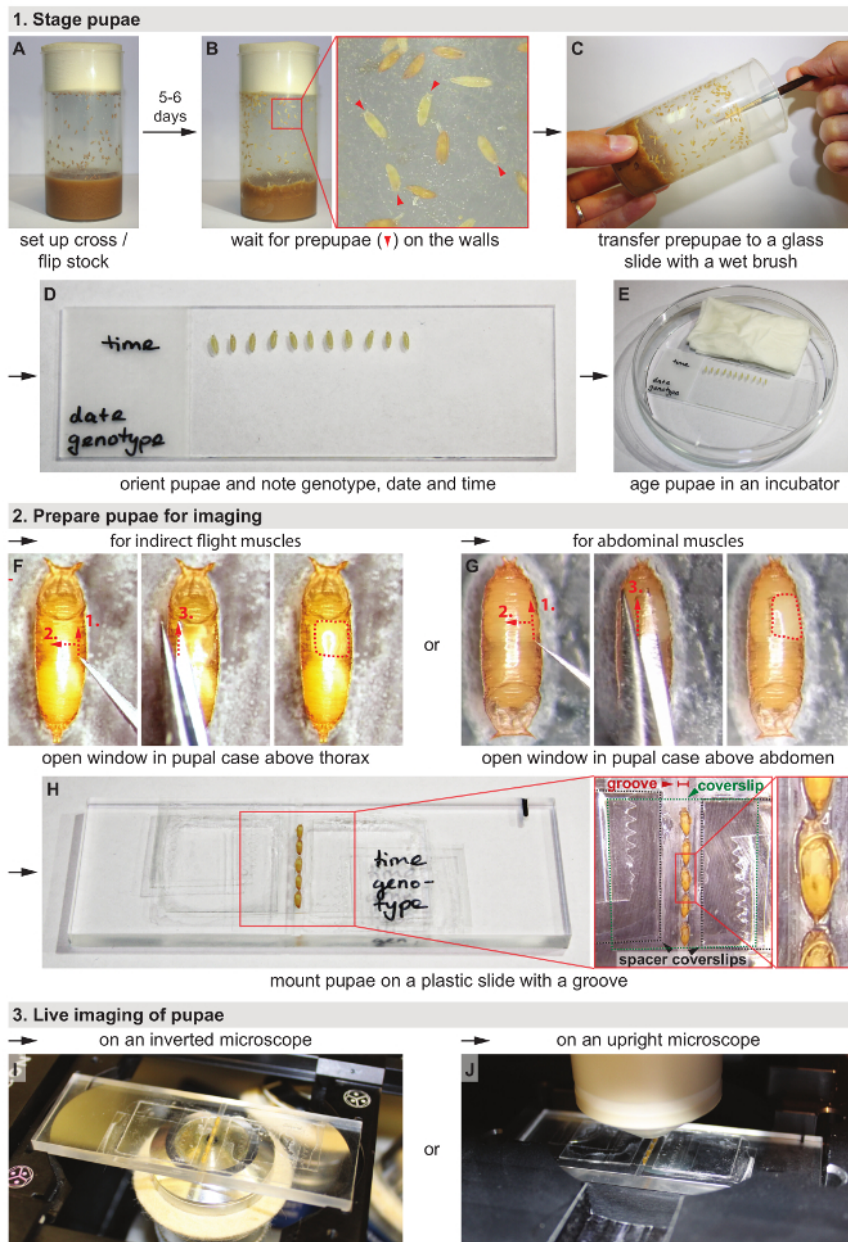


Figure 1: Workflow for live imaging of muscle-tendon morphogenesis in *Drosophila* pupae. See protocol for details. [Please click here to view a larger version of this figure.](#)

Representative Results

Various tissues can be imaged *in vivo* in developing fly pupae, making them an ideal model system to study morphogenesis of adult organs. Among these are the indirect flight muscles, the thorax epithelium including the tendon cells, the wing epithelium, abdominal muscles and the heart^{22,23,24,25,26,27}. Here, we focus on live imaging of muscle and tendon morphogenesis. For a detailed description of indirect flight muscle and abdominal muscle morphogenesis and additional methods for studying muscle biology in *Drosophila*, we refer the reader to Weitkunat and Schnorrrer 2014²².

Live imaging of indirect flight muscles

For studying the long-term development of the indirect flight muscles consisting of the dorsolongitudinal muscles (DLMs) and the dorsoventral muscles (DVMs), globular Moesin actin-binding domain tagged with GFP (*UAS-GFP-Gma*) was expressed in all muscles using the *Myocyte enhancer factor 2 (Mef2)*-GAL4 driver (**Figure 2A-D, Movie S1**). Prior to imaging, a window in the pupal case was opened above the thorax as shown in **Figure 1F**. On a two-photon microscope, z-stacks were acquired every 20 min for 21 h starting at ≈ 11 h after puparium formation (11 h APF). In this time frame, the DLMs (green overlays in **Figure 2A'-D'**) first initiate attachment to the tendon cells (**Figure 2A**) and then split while the muscle attachments mature (**Figure 2B**). Next, the myotubes shorten (**Figure 2C**) until they finally reach the maximally compacted stage at 30 h APF (**Figure 2D**). Taken together, this movie highlights the dramatic changes in muscle morphology that occur on the time scale of hours.

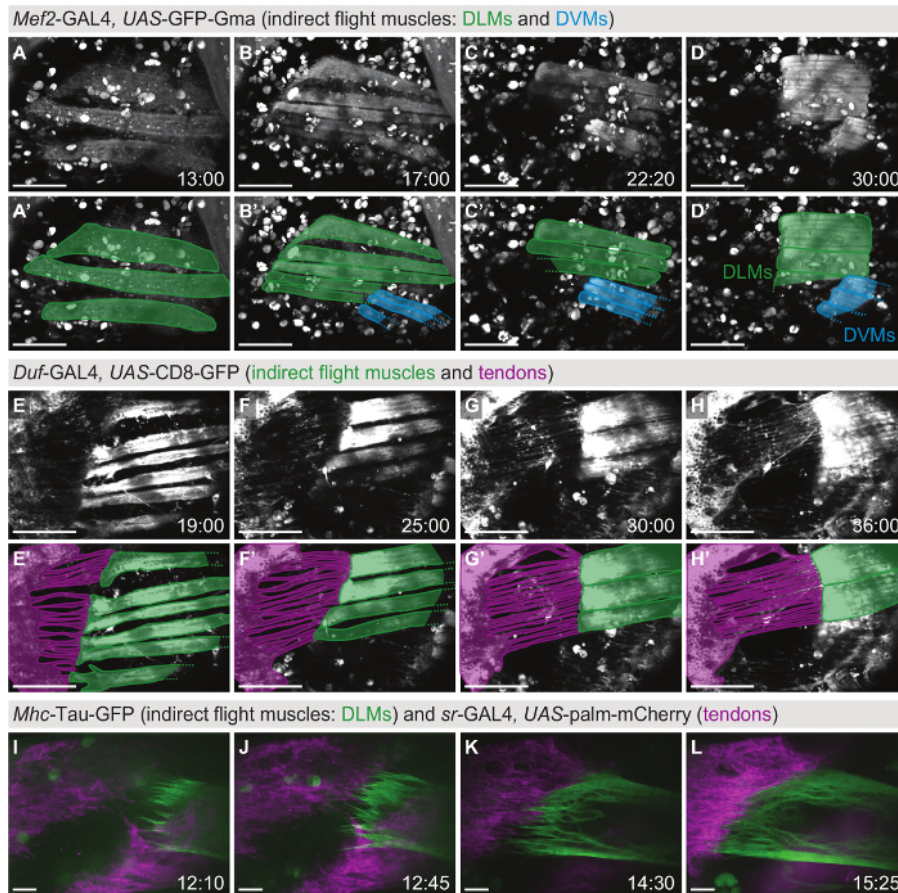


Figure 2: Live imaging of indirect flight muscle and tendon morphogenesis. (A-D) Time points from a two-photon movie (Movie S1) using *Mef2*-GAL4, *UAS-GFP-Gma* as a marker for actin in the indirect flight muscles consisting of the dorsolongitudinal muscles (DLMs, highlighted in green in A'-D') and the dorsoventral muscles (DVMs, highlighted in blue in A'-D'). Scale bars are 100 μ m. (E-H) Time points from a two-photon movie (Movie S2) using *Duf*-GAL4, *UAS-CD8-GFP* as a marker for indirect flight muscles and the thorax epithelium including tendon cells. Panels E'-H' show an overlay with a model of the muscle-tendon system at each time point, highlighting the long cellular extensions formed by the tendon epithelium (magenta) in contact with the muscles (green). Scale bars are 100 μ m (estimated from size of imaged structures). (I-L) Time points from a two-color, spinning disc confocal movie (Movie S3) focusing on muscle-tendon attachment initiation. The tendon cells are labeled with *sr*-GAL4, *UAS-palm-mCherry* (magenta) and the dorsolongitudinal indirect flight muscles with *Mhc*-Tau-GFP (green). Scale bars are 10 μ m. Time is indicated as hh:mm after puparium formation (APF). Note that not all movies were acquired on a temperature-controlled stage, therefore, developmental timing may diverge. [Please click here to view a larger version of this figure.](#)

For studying tendon and muscle morphogenesis at the same time, membrane-bound GFP (*UAS-CD8-GFP*) was expressed using *Dumbfounded (Duf)*-GAL4 as a driver, which is expressed both in the tendon cells and the indirect flight muscles (**Figure 2E-H, Movie S2**). A z-stack was taken on a two-photon microscope every 20 min starting at 16 h APF for 20 h. While the myotubes compact (green overlay in **Figure 2E'-H'**), the tendon cells form long cellular extensions that elongate with time (magenta overlay in **Figure 2E'-H'**). Taken together, this movie highlights the close interplay between the tendon and muscle cells *in vivo*.

To investigate muscle-tendon interaction in more detail, two-color, high-magnification imaging was performed. Pupae with *myosin heavy chain (Mhc)*-Tau-GFP in the DLMs and *UAS-palmitoylated-mCherry (UAS-palm-mCherry)* driven by *stripe (sr)*-GAL4 in the tendons were imaged every 5 min starting at 12 h APF for 4.5 h on a spinning disc confocal microscope (**Figure 2I-L, Movie S3**). At 12 h APF, the myotubes migrate towards their tendon target cells while forming long filopodia at their tips (**Figure 2I**). Subsequently, the muscle and tendon tissues interdigitate (**Figure 2J, K**) to form a stable attachment. As the attachment matures, fewer filopodia form and the muscle-tendon interface smoothens (**Figure 2L**). Thus, two-color, high-magnification imaging can be used to reveal cellular dynamics in detail in the living organism.

Live imaging of abdominal muscles

For live imaging of the abdominal muscles (Figure 3, Movie S4), *Mef2-GAL4>UAS-CD8-GFP* was used as a marker and a window was opened above the abdomen in the pupal case as detailed in Figure 1G. Similar to the indirect flight muscle movie represented in Figure 2A-D, the formation and growth of the abdominal muscles can be followed over many hours of development (55 h in Movie S4). During this time, the myoblasts fuse to form growing myotubes (Figure 3A). The myotube tips migrate to their tendon targets, and after attaching to the tendon cells, the contractile units of the muscles, the sarcomeres, are formed (Figure 3B-D).

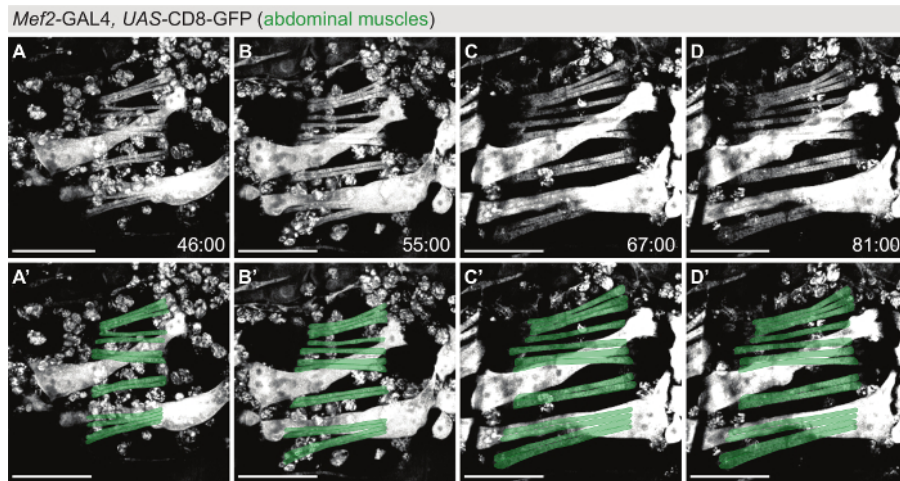


Figure 3: Live imaging of abdominal muscle morphogenesis. (A-D) Time points from a movie (Movie S4) using *Mef2-GAL4, UAS-CD8-GFP* as a marker to follow abdominal muscle morphogenesis. Panels A'-E' show overlays with models of an abdominal muscle set (green) that forms *de novo* during the pupal stage. Scale bars are 100 μ m. Time is indicated as hh:mm APF. The movie was acquired at room temperature. [Please click here to view a larger version of this figure.](#)

Live imaging of twitching muscles

In contrast to Figure 2 and Figure 3, Figure 4 shows muscle dynamics occurring on the time scale of seconds: the live recording of muscle contractions. Pupae expressing β PS-Integrin-GFP under endogenous control were imaged with a time resolution of 0.65 s in a single z-plane on a confocal microscope (Movie S5). In the example displayed in Figure 4, the attachment sites of three DVMs (Figure 4A) were imaged for 10 min starting at 42 h APF. During this time, five twitch events were observed (Figure 4B-F), showing that the sarcomeres are already assembled well enough to support coordinated contractions at this time point in development. Hence, imaging of muscle twitching can be used as a functional read-out for sarcomerogenesis already during indirect flight muscle development²⁸, as opposed to for example flight tests, which can only be performed after eclosion.

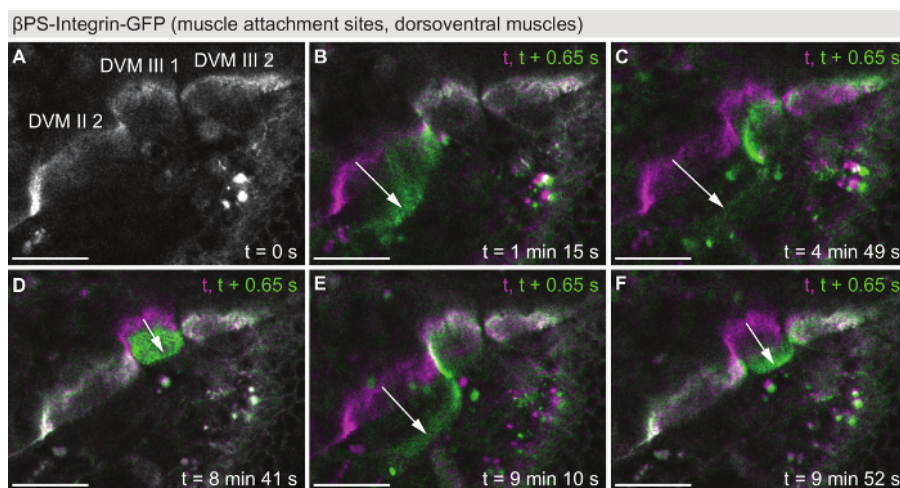


Figure 4: Live imaging of twitching muscles. (A) First time-point from a movie (Movie S5) showing twitching of dorsoventral indirect flight muscles at 42 h APF using β PS-Integrin-GFP as a marker. In the field of view are the muscle attachment sites of DVM II 2, DVM III 1 and DVM III 2. (B-F) Color overlays of five individual twitch events, each showing the frame before the twitch (magenta) and the first frame of the twitch event (green). Note that the individual muscle fibers twitch independently from each other. Arrows highlight the twitching motion. The time resolution of the movie is 0.65 s. Scale bars are 25 μ m. [Please click here to view a larger version of this figure.](#)

Live imaging of endogenously tagged proteins

Similar to β PS-Integrin-GFP, a large collection of fusion proteins expressed in *Drosophila* under endogenous control has been generated^{2,3,4}. These fly lines can be used to study for example the subcellular localization or the expression profiles of proteins of interest. The collection is especially helpful if specific antibodies are not available or protein dynamics need to be investigated *in vivo* without fixation. **Figure 5** shows three examples of endogenously expressed fusion proteins from the fly TransgeneOme (fTRG) library, Hu li tai shao (Hts)-GFP (**Figure 5A, B**), Talin-GFP (**Figure 5C, D**) and β Tubulin60D-GFP (**Figure 5E, F**). The expression of these proteins can be studied in all tissues that express them naturally. Here, we show the thorax epithelium (**Figure 5A, C, E**) and the indirect flight muscles or their attachment sites (**Figure 5B, D, F**) as examples.

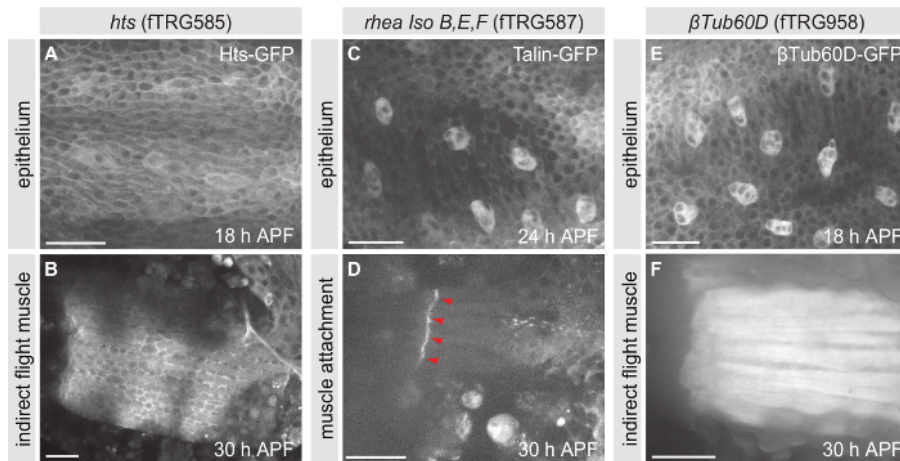


Figure 5: Live imaging of endogenously tagged proteins. (A, B) Maximum projections of z-stacks taken of pupae expressing Hts-GFP. (C, D) Maximum projections of z-stacks taken of pupae expressing Talin-GFP. (E, F) Maximum projections of z-stacks taken of pupae expressing β Tubulin60D-GFP. Panels A, C and E show the thorax epithelium at 18, 24 and 18 h APF, respectively, and panels B, D and F show the indirect flight muscles or their attachment sites at 30 h APF. Scale bars are 25 μ m. [Please click here to view a larger version of this figure.](#)

Discussion

The presented protocol describes how to image muscle-tendon morphogenesis in living *Drosophila* pupae using a variety of fluorescently tagged proteins. This *in vivo* imaging strategy can be used to study developmental processes in their natural environment of the entire organism.

It is crucial for a successful experiment to find the correct developmental time point to analyze. For example, dorsolongitudinal indirect flight muscles initiate attachment to their tendon targets at ≈ 16 h APF²³ while abdominal muscles develop later and attach on both ends only between 30 and 40 h APF²⁶. Consequently, previously published literature should be used to find the right time points of development to analyze or, if the tissue or structure of interest has not been studied in detail before, the overall development has to be characterized first.

For mounting pupae successfully on the custom-built plastic slides, it is important that the grooves have suitable dimensions: The grooves need to be 1.0 - 1.5 mm wide and 0.3 - 0.4 mm deep. This depth allows adjusting the precise distance to the top coverslip with spacer coverslips as needed. However, at least one spacer coverslip should be used to avoid draining the 50% glycerol away from the sample by capillary forces. The correct positioning of the pupae in the groove requires some experience and should be optimized such that the structure of interest is as close as possible to the coverslip.

If a large number of pupae is supposed to be imaged in one microscope session, they can all be mounted beforehand and then stored in an incubator until imaging to ensure proper developmental timing. The pupae should survive the entire procedure and also at least try to eclose if kept on the slide after imaging. The survival rate can be used as a readout to check whether the imaging conditions harm the pupae.

The imaging settings should be chosen carefully according to the experimental requirements. For short-term movies, a high frame rate versus a high signal-to-noise ratio needs to be balanced, while relatively high laser power can be used without damaging the pupae too much. However, for long-term movies, the laser power has to be kept at a moderate level and the pupae should not be imaged continuously but rather at certain time points, for example, every 20 min. To ensure that the structure of interest does not move out of the field of view, it might be necessary to readjust the positioning of the z-stack between time points. To our knowledge, the opening of the pupal case per se does not affect developmental timing. However, a temperature-controlled stage should be used for long-term movies to ensure proper developmental timing. Keeping these considerations in mind, highly informative movies can be acquired.

The presented protocol can be used to visualize not only muscle-tendon morphogenesis but also other developing tissues, for example, the wing epithelium²⁹. Only three modifications to this protocol are required: (1) opening of the pupal case above the wing instead of the thorax or abdomen, (2) positioning of pupae with the wing towards the top coverslip, and (3) the use of different fluorescent marker proteins. With the advancement of the CRISPR/Cas9-technology, more and more endogenously tagged fluorescent proteins will be available, because it has become more straightforward to target endogenous loci in *Drosophila*^{30,31,32}. In the future, this will allow elucidating the dynamics of numerous proteins, cells and entire tissues in their physiological environment in detail.

Disclosures

The authors have nothing to disclose.

Acknowledgements

We thank Manuela Weitkunat for the acquisition of Movie S3. We are grateful to Reinhard Fässler for generous support. This work was supported by the EMBO Young Investigator Program (F.S.), the European Research Council under the European Union's Seventh Framework Programme (FP/2007-2013)/ERC Grant 310939 (F.S.), the Max Planck Society (S.B.L., F.S.), the Centre National de la Recherche Scientifique (CNRS) (F.S.), the excellence initiative Aix-Marseille University AMIDEX (F.S.), the LabEX-INFORM (F.S.) and the Boehringer Ingelheim Fonds (S.B.L.).

References

- Brand, A. H., & Perrimon, N. Targeted gene expression as a means of altering cell fates and generating dominant phenotypes. *Development*. **118** (2), 401-415, (1993).
- Morin, X., Daneman, R., Zavortink, M., & Chia, W. A protein trap strategy to detect GFP-tagged proteins expressed from their endogenous loci in *Drosophila*. *P. Natl. Acad. Sci. USA*. **98** (26), 15050-15055 (2001).
- Venken, K. J. T. *et al.* MiMIC: a highly versatile transposon insertion resource for engineering *Drosophila melanogaster* genes. *Nat. Meth.* **8** (9), 737-743 (2011).
- Sarov, M. *et al.* A genome-wide resource for the analysis of protein localisation in *Drosophila*. *eLife*. **5**, e12068 (2016).
- Ranganayakulu, G., Schulz, R. A., & Olson, E. N. Wingless signaling induces nautilus expression in the ventral mesoderm of the *Drosophila* embryo. *Dev. Biol.* **176** (1), 143-148 (1996).
- Roy, S., & Raghavan, K. V. Homeotic genes and the regulation of myoblast migration, fusion, and fibre-specific gene expression during adult myogenesis in *Drosophila*. *Development (Cambridge, England)*. **124** (17), 3333-3341, (1997).
- Bryantsev, A. L., Baker, P. W., Lovato, T. L., Jaramillo, M. S., & Cripps, R. M. Differential requirements for Myocyte Enhancer Factor-2 during adult myogenesis in *Drosophila*. *Dev. Biol.* **361** (2), 191-207 (2012).
- Gordon, S., & Dickinson, M. H. Role of calcium in the regulation of mechanical power in insect flight. *P. Natl. Acad. Sci. USA*. **103** (11), 4311-4315 (2006).
- Jin, H. *et al.* Genome-Wide Screens for In Vivo Tinman Binding Sites Identify Cardiac Enhancers with Diverse Functional Architectures. *PLoS Genet.* **9** (1), e1003195 (2013).
- Chen, E. H., & Olson, E. N. Antisocial, an intracellular adaptor protein, is required for myoblast fusion in *Drosophila*. *Dev. Cell.* **1** (5), 705-715, (2001).
- Clyne, P. J., Brotman, J. S., Sweeney, S. T., & Davis, G. Green Fluorescent Protein Tagging *Drosophila* Proteins at Their Native Genomic Loci With Small P Elements. *Genetics*. **165** (3), 1433-1441, (2003).
- Katzemich, A., Liao, K. A., Czerniecki, S., & Schöck, F. Alp/Enigma Family Proteins Cooperate in Z-Disc Formation and Myofibril Assembly. *PLoS Genet.* **9** (3), e1003342 (2013).
- Klapholz, B. *et al.* Alternative mechanisms for talin to mediate integrin function. *Curr. Biol.* **25** (7), 847-857 (2015).
- Schnorrer, F., Kalchauer, I., & Dickson, B. J. The transmembrane protein Kon-tiki couples to Dgrip to mediate myotube targeting in *Drosophila*. *Dev. Cell.* **12** (5), 751-766 (2007).
- Menon, S. D., & Chia, W. *Drosophila* rolling pebbles: a multidomain protein required for myoblast fusion that recruits D-Titin in response to the myoblast attractant Dumbfounded. *Dev. Cell.* **1** (5), 691-703, (2001).
- Bloor, J. W., & Kiehart, D. P. zipper Nonmuscle myosin-II functions downstream of PS2 integrin in *Drosophila* myogenesis and is necessary for myofibril formation. *Dev. Biol.* **239** (2), 215-228 (2001).
- Millard, T. H., & Martin, P. Dynamic analysis of filopodial interactions during the zipper phase of *Drosophila* dorsal closure. *Development (Cambridge, England)*. **135** (4), 621-626 (2008).
- Hatan, M., Shinder, V., Israeli, D., Schnorrer, F., & Volk, T. The *Drosophila* blood brain barrier is maintained by GPCR-dependent dynamic actin structures. *J. Cell Biol.* **192** (2), 307-319 (2011).
- Lee, T., & Luo, L. Mosaic Analysis with a Repressible Cell Marker for Studies of Gene Function in Neuronal Morphogenesis. *Neuron*. **22** (3), 451-461 (1999).
- Roy, S., Huang, H., Liu, S., & Kornberg, T. B. Cytoskeleton-mediated contact-dependent transport of the *Drosophila* decapentaplegic signaling protein. *Science*. **343** (6173), 1244624-1244624 (2014).
- Förster, D., & Luschig, S. Src42A-dependent polarized cell shape changes mediate epithelial tube elongation in *Drosophila*. *Nat. Cell Biol.* **14** (5), 526-534 (2012).
- Weitkunat, M., & Schnorrer, F. A guide to study *Drosophila* muscle biology. *Methods*. **68** (1), 2-14 (2014).
- Weitkunat, M., Kaya-Çopur, A., Grill, S. W., & Schnorrer, F. Tension and force-resistant attachment are essential for myofibrillogenesis in *Drosophila* flight muscle. *Curr. Biol.* **24** (7), 705-716 (2014).
- Guirao, B. *et al.* Unified quantitative characterization of epithelial tissue development. *eLife*. **4**, e08519 (2015).
- Etournay, R. *et al.* Interplay of cell dynamics and epithelial tension during morphogenesis of the *Drosophila* pupal wing. *eLife*. **4**, e07090 (2015).
- Weitkunat, M., Brasse, M., Bausch, A. R., & Schnorrer, F. Mechanical tension and spontaneous muscle twitching precede the formation of cross-striated muscle in vivo. *Development (Cambridge, England)*. **144** (7), 1261-1272 (2017).
- Sellin, J., Albrecht, S., Kölsch, V., & Paululat, A. Dynamics of heart differentiation, visualized utilizing heart enhancer elements of the *Drosophila melanogaster* bHLH transcription factor Hand. *Gene Expr. Patterns*. **6** (4), 360-375 (2006).
- Lemke, S. B., & Schnorrer, F. Mechanical forces during muscle development. *Mech. Develop.* **144** (Pt A), 92-101 (2017).

29. Classen, A.-K., Aigouy, B., Giangrande, A., & Eaton, S. Imaging *Drosophila* pupal wing morphogenesis. *Methods Mol. Biol.* **420**, 265-275 (2008).
30. Gratz, S. J. *et al.* Genome engineering of *Drosophila* with the CRISPR RNA-guided Cas9 nuclease. *Genetics.* **194** (4), 1029-1035 (2013).
31. Zhang, X., Koolhaas, W. H., & Schnorrer, F. A versatile two-step CRISPR- and RMCE-based strategy for efficient genome engineering in *Drosophila*. *G3 (Bethesda).* **4** (12), 2409-2418 (2014).
32. Port, F., Chen, H.-M., Lee, T., & Bullock, S. L. Optimized CRISPR/Cas tools for efficient germline and somatic genome engineering in *Drosophila*. *P. Natl. Acad. Sci. USA.* **111** (29), E2967-76 (2014).

A transcriptomics resource reveals a transcriptional transition during ordered sarcomere morphogenesis in flight muscle

Maria L Spletter^{1,2*}, Christiane Barz¹, Assa Yeroslaviz³, Xu Zhang^{1,4,5}, Sandra B Lemke¹, Adrien Bonnard^{4,6}, Erich Brunner⁷, Giovanni Cardone⁸, Konrad Basler⁷, Bianca H Habermann^{3,4,6}, Frank Schnorrer^{1,4*}

¹Muscle Dynamics Group, Max Planck Institute of Biochemistry, Martinsried, Germany; ²Biomedical Center, Physiological Chemistry, Ludwig-Maximilians-Universität München, Martinsried, Germany; ³Computational Biology Group, Max Planck Institute of Biochemistry, Martinsried, Germany; ⁴Aix Marseille Univ, CNRS, IBDM, Marseille, France; ⁵School of Life Science and Engineering, Foshan University, Guangdong, China; ⁶Aix Marseille Univ, INSERM, TAGC, Marseille, France; ⁷Institute of Molecular Life Sciences, University of Zurich, Zurich, Switzerland; ⁸Imaging Facility, Max Planck Institute of Biochemistry, Martinsried, Germany

Abstract Muscles organise pseudo-crystalline arrays of actin, myosin and titin filaments to build force-producing sarcomeres. To study sarcomerogenesis, we have generated a transcriptomics resource of developing *Drosophila* flight muscles and identified 40 distinct expression profile clusters. Strikingly, most sarcomeric components group in two clusters, which are strongly induced after all myofibrils have been assembled, indicating a transcriptional transition during myofibrillogenesis. Following myofibril assembly, many short sarcomeres are added to each myofibril. Subsequently, all sarcomeres mature, reaching 1.5 μm diameter and 3.2 μm length and acquiring stretch-sensitivity. The efficient induction of the transcriptional transition during myofibrillogenesis, including the transcriptional boost of sarcomeric components, requires in part the transcriptional regulator Spalt major. As a consequence of Spalt knock-down, sarcomere maturation is defective and fibers fail to gain stretch-sensitivity. Together, this defines an ordered sarcomere morphogenesis process under precise transcriptional control – a concept that may also apply to vertebrate muscle or heart development.

DOI: <https://doi.org/10.7554/eLife.34058.001>

***For correspondence:**

maria.spletter@bmc.med.lmu.de (MLS);
frank.schnorrer@univ-amu.fr (FS)

Competing interests: The authors declare that no competing interests exist.

Funding: See page 28

Received: 04 December 2017

Accepted: 26 May 2018

Published: 30 May 2018

Reviewing editor: K

VijayRaghavan, National Centre for Biological Sciences, Tata Institute of Fundamental Research, India

© Copyright Spletter et al. This article is distributed under the terms of the [Creative Commons Attribution License](https://creativecommons.org/licenses/by/4.0/), which permits unrestricted use and redistribution provided that the original author and source are credited.

Introduction

Sarcomeres are the stereotyped force producing mini-machines present in all striated muscles of bilaterians. They are built of three filament types arrayed in a pseudo-crystalline order: actin filaments are cross-linked with their plus ends at the sarcomeric Z-disc and face with their minus ends towards the sarcomere center. In the center, symmetric bipolar muscle myosin filaments, anchored at the M-line, can interact with the actin filaments. Myosin movement towards the actin plus ends thus produces force during sarcomere shortening. Both filament types are permanently linked by a third filament type, the connecting filaments, formed of titin molecules (*Gautel and Djinić-Carugo, 2016; Lange et al., 2006*). A remarkable feature of sarcomeres is their stereotyped size, ranging from 3.0 to 3.4 μm in relaxed human skeletal muscle fibers (*Ehler and Gautel, 2008; Llewellyn et al., 2008; Regev et al., 2011*). Even more remarkable, the length of each bipolar myosin filament is 1.6 μm in all mature sarcomeres of vertebrate muscles, requiring about 300 myosin hexamers to assemble per filament (*Gokhin and Fowler, 2013; Tskhovrebova and Trinick, 2003*).

eLife digest Animals may have different types of muscles but they all have one thing in common: molecular machines called sarcomeres that produce a pulling force. Conserved from fruit flies to humans, these structures line up end-to-end inside muscle cells, forming long cables called myofibrils. Some of the myofibrils in a human can reach several centimetres in length, which is much longer than those in a fruit fly. However, individual sarcomeres are the same length in both humans and flies.

To build the parts of the sarcomere, an animal cell first copies the relevant genes into intermediate molecules known as mRNAs, which are then translated to build new sarcomere proteins. Developing muscle cells later tune their sarcomeres to make them sensitive to stretching. This tweaks the power and force of the mature muscle, but the details of this developmental process are not fully understood.

Now, Spletter et al. have counted all the mRNAs in the developing flight muscles of fruit flies, with the aim of generating a resource that catalogues the changes in gene activity, or expression, that occur as muscles develop. This revealed that sarcomeres form in three phases. First, the cells assembled all their myofibrils. Then, they added short sarcomeres to the ends of their myofibrils. Finally, the sarcomeres matured to their full length and diameter, and became sensitive to stretching.

Fruit fly muscles had 40 patterns of gene expression, with most of the sarcomere components having one of two specific patterns. The expression of these genes dramatically rose after the young muscle cells had finished assembling all their myofibrils, suggesting muscles express different genes when their sarcomeres mature. A protein called spalt-major helped the cell to know when to make the transition, allowing the sarcomeres to grow in length and width.

Losing spalt-major late in muscle development stopped sarcomere growth and prevented the tuning process. The sarcomeres failed to become sensitive to stretching, a crucial feature of mature muscle. Muscles without spalt-major contracted too much and without coordination, like a muscle spasm.

The similarities between fruit fly and human sarcomeres suggest this developmental sequence may also occur in human muscles too. Understanding these steps may help to improve repair after injury or muscle growth during exercise. The next step is to test whether regenerating or growing muscles develop in the same way.

DOI: <https://doi.org/10.7554/eLife.34058.002>

Human muscle fibers can be several centimetres in length and both ends of each fiber need to be stably connected to tendons to achieve body movements. As sarcomeres are only a few micrometres in length, many hundreds need to assemble into long linear myofibrils that span from one muscle end to the other and thus enable force transmission from the sarcomeric series to the skeleton (*Lemke and Schnorrer, 2017*). Thus far, we have a very limited understanding of how sarcomeres initially assemble into long immature myofibrils during muscle development to exactly match the length of the mature muscle fiber (*Sparrow and Schöck, 2009*). In particular, we would like to understand how such sarcomeres mature to the very precise stereotyped machines present in mature muscle fibers.

Across evolution, both the pseudo-crystalline regularity of sarcomeres as well as their molecular components are well conserved (*Ehler and Gautel, 2008; Vigoreaux, 2006*). Thus, *Drosophila* is a valid model to investigate the biogenesis of sarcomeres as well as their maturation. In particular, the large indirect flight muscles (IFMs) that span the entire fly thorax are an ideal model system to investigate mechanisms of myofibrillogenesis. They contain thousands of myofibrils consisting of 3.2 μm long sarcomeres (*Schönbauer et al., 2011; Spletter et al., 2015*).

Like all *Drosophila* adult muscles, IFMs are formed during pupal development from a pool of undifferentiated myoblasts called adult muscle precursors (AMPs) (*Bate et al., 1991*). From 8 hr after puparium formation (APF), these AMPs either fuse with themselves (for the dorso-ventral flight muscles, DVMs) or with remodelled larval template muscles (for the dorso-longitudinal flight muscles, DLMs) to form myotubes (*Dutta et al., 2004; Fernandes et al., 1991*). These myotubes

develop dynamic leading edges at both ends and initiate attachment to their respective tendon cells at 12 to 16 hr APF (Weitkunat et al., 2014). These attachments mature and mechanical tension is built up in the myotubes, followed by the formation of the first immature periodic myofibrils at 30 hr APF when the muscle fibers are about 150 μm in length. These immature myofibrils contain the earliest sarcomeres, which are about 1.8 μm in length (Weitkunat et al., 2014). During the remaining 3 days of pupal development, the muscle fibers grow to about 1 mm to fill the entire thorax and sarcomere length increases to a final length of about 3.2 μm in adult flies (Orfanos et al., 2015; Reedy and Beall, 1993).

After myoblasts have fused to myotubes, the flight muscle specific selector gene *spalt major* (*spalt*, *salm*) is turned on in the developing flight muscle myotubes. Spalt major is responsible for the correct fate determination and development of the flight muscles, which includes the fibrillar flight muscle morphology and the stretch-activated muscle contraction mode (Schönbauer et al., 2011; Syme and Josephson, 2002). It does so by controlling the expression of more than 700 flight muscle specific genes or gene isoforms during development (Spletter and Schnorrer, 2014; Spletter et al., 2015). However, how the interplay between all these isoforms instructs the formation of highly regular, pseudo-crystalline sarcomeres in the flight muscle is not understood.

Here, we studied the transcriptional dynamics of flight muscle development in detail. We performed a systematic mRNA-Seq time-course of isolated muscle tissue at eight time points from the myoblast stage until the mature adult muscle stage, generating a transcriptomics resource of developing flight muscle. Bioinformatic analysis of expression dynamics identified two gene clusters that are strongly enriched for sarcomeric genes. The temporal dynamics of these clusters identified a transcriptional transition that is required for sarcomere morphogenesis. We define sarcomere morphogenesis in three sequential although overlapping phases. First, immature myofibrils assemble simultaneously; second, short sarcomeres are added to each myofibril; and third, all sarcomeres mature to their final length and diameter and acquire stretch-sensitivity. Interestingly, the number of myofibrils remains constant, suggesting that every sarcomere progresses through sarcomere maturation. We show that the flight muscle selector gene *spalt major* contributes to the observed transcriptional transition, suggesting that muscle fiber type-specific transcription is continuously required during sarcomere formation and maturation. Together, these findings indicate that precise transcriptional control of the sarcomeric components enables their ordered assembly into sarcomeres and their maturation to pseudo-crystalline regularity.

Results

A time-course of indirect flight muscle development

To better understand muscle morphogenesis in general and myofibrillogenesis in particular, we focused on the *Drosophila* indirect flight muscles (IFMs). We hypothesised that major morphological transitions during IFM development may be induced by transcriptional changes, thus we aimed to generate a detailed developmental mRNA-Seq dataset from IFMs. IFMs are built from AMPs that adhere to the hinge region of the wing disc epithelium and are labelled with GFP-Gma under *Him* control (Figure 1A) (Soler and Taylor, 2009). At 16 hr APF, many of these myoblasts have fused to larval template muscles to build the dorsal-longitudinal flight muscle (DLM) myotubes, which initiate attachment to their tendons. At this stage, the DLM myotubes of fibers 3 and 4 have a length of about 300 μm (Figure 1B). Fusion ceases at about 24 hr APF (Figure 1C) and attachment matures until 32 hr APF, coinciding with the strong recruitment of βPS -Integrin and the spectraplaklin homolog Shortstop (Shot) to the attachment sites. At this stage the myofibers have built up mechanical tension and compacted to a length of about 150 μm , coinciding with the appearance of long Shot-positive tendon extensions that anchor the muscles within the thorax. This important developmental transition is highlighted by the assembly of immature myofibrils visualised by strong F-actin staining throughout the entire muscle fiber (Figure 1D) (Weitkunat et al., 2014).

After 32 hr APF, the myofibers undergo another developmental transition and begin to grow dramatically. They elongate 3-fold to reach a length of about 480 μm by 48 hr APF (Figure 1E) and about 590 μm by 56 hr APF (Figure 1F). Concomitantly, the tendon extensions shrink with the myofibers being directly connected to the basal side of the tendon cell epithelium by 72 hr APF

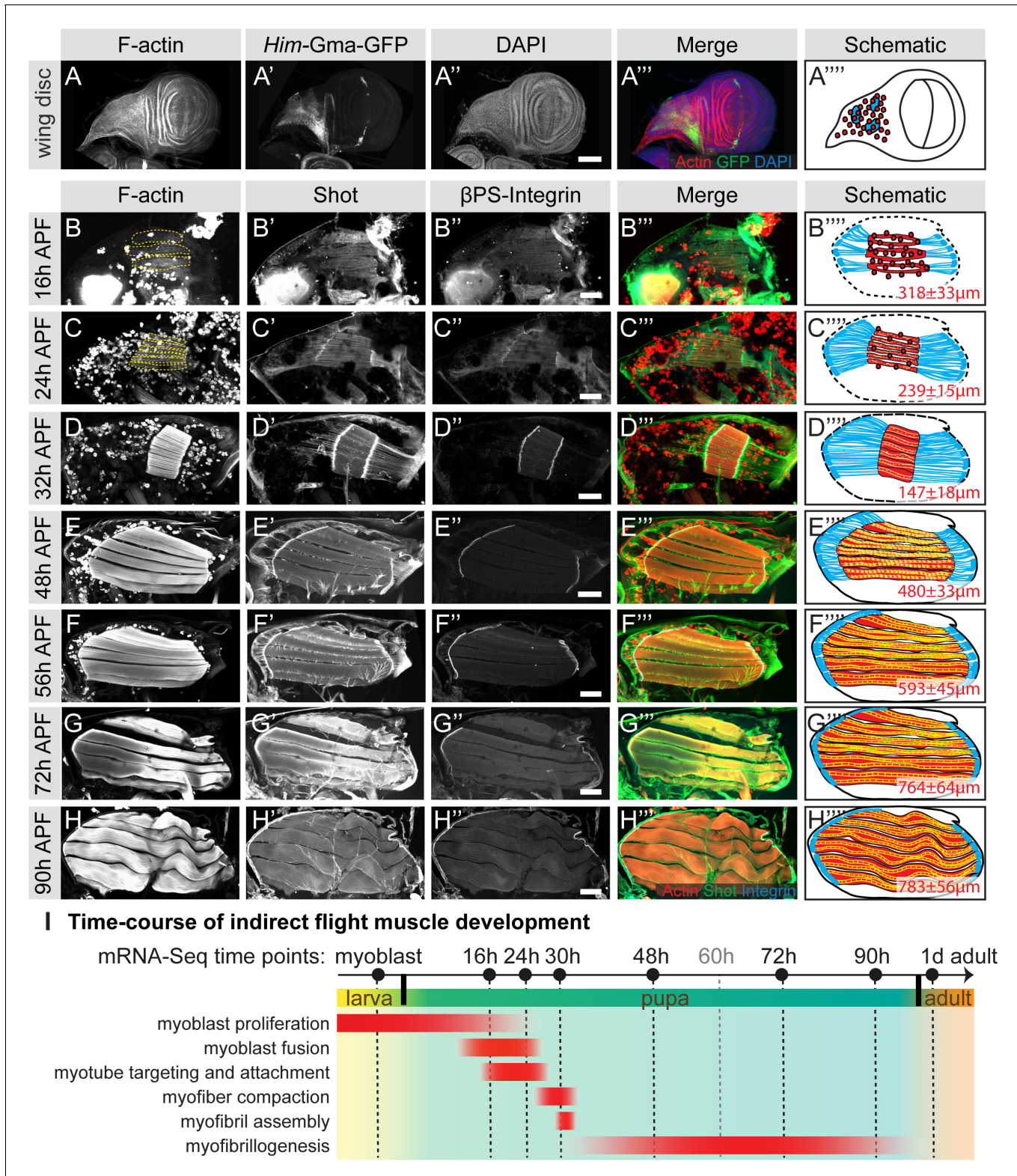


Figure 1. Development of the dorsal longitudinal indirect flight muscles. (A–H) Time-course of DLM development. (A) Myoblasts adhering to the hinge of the larval wing disc were visualised with *Him-GFP-Gma* (green), F-actin was stained with phalloidin (red) and nuclei with DAPI (blue). (B–H) Time-course of DLM and myotendinous junction development at 16 hr (B), 24 hr (C), 32 hr (D), 48 hr (E), 56 hr (F), 72 hr (G) and 90 hr APF (H). F-actin was stained with phalloidin (red), Shot (green) and β PS-Integrin (blue). DLMs are highlighted in dashed yellow lines in B and C. (A'''–C''') Scheme of the

Figure 1 continued on next page

Figure 1 continued

respective developmental stages with myoblasts and muscles in red, tendon cells in blue and wing disc or pupal thorax outline in black. The length of the muscle fibers is indicated in red. For details see text. Scale bar represents 100 μm . (I) Temporal summary of known events during myogenesis (red). Samples for mRNA-Seq were collected at time points noted in black.

DOI: <https://doi.org/10.7554/eLife.34058.003>

The following source data is available for figure 1:

Source data 1. This table includes the length measurements of the indirect flight muscle fibers at the indicated stage.

DOI: <https://doi.org/10.7554/eLife.34058.004>

(**Figure 1G**). At the end of pupal development (90 hr APF), wavy muscle fibers with a length of about 780 μm containing mature myofibrils (**Figure 1H**) are present within the thorax.

A transcriptomics resource of indirect flight muscle development

To quantify transcriptional dynamics across the entire developmental time-course, we focused on the major developmental transitions and isolated mRNA from dissociated myoblasts of dissected or mass-isolated third instar wing discs and from hand-dissected IFMs at 16, 24, 30, 48, 72 and 90 hr APF pupae, and adult flies 1 day after eclosion (**Figure 1I**). We performed mRNA-Seq using at least two biological replicates for each time point (see Materials and methods). To identify genes with similar temporal expression profiles, we used Mfuzz (*Kumar and Futschik, 2007*) to cluster standard normalized read counts from all genes expressed above background (12,495 of 13,322 genes). This allowed us to confidently identify 40 distinct genome-wide clusters (**Figure 2—figure supplement 1**), each of which contains a unique gene set ranging from 155 to 703 members (**Supplementary file 1**). These clusters represent various temporal expression dynamics, with high expression at early (myoblast proliferation and fusion), mid (myotube attachment and myofibril assembly) or late (myofiber growth) myogenesis stages or a combination thereof (**Figure 1I, Figure 2—figure supplement 1**). These distinct patterns suggest a precise temporal transcriptional regulation corresponding to observed morphological transition points.

To verify the mRNA-Seq and cluster analysis, we selected a number of ‘indicator’ genes with available antibodies or GFP fusion proteins whose expression correlates with important developmental transitions. Twist (*Twi*) is a myoblast nuclear marker at larval stages and its expression needs to be down-regulated after myoblast fusion in pupae (*Anant et al., 1998*). We find *twi* mRNA in Mfuzz cluster 27, with high expression in myoblasts until 16 hr APF and a significant down-regulation from 24 hr APF, which we were able to verify with antibody stainings (**Figure 2A–C**). The flight muscle fate selector gene *spalt major* (*salm*) (*Schönbauer et al., 2011*) and its target, the IFM splicing regulator *arrest* (*aret, bruno*) (*Spletter et al., 2015*) are members of cluster 26 and 14, respectively. Expression of both clusters is up-regulated after myoblast fusion at 16 hr APF, which we were able to verify with antibody stainings (**Figure 2D–F, Figure 2—figure supplement 2A–C**). The apparent *salm* mRNA peak at 72 hr APF, which does not appear to cause a further protein increase, represents a mere 1.3 fold increase in expression and would need further confirmation as *Salm*, like many transcription factors, is expressed at low levels. For the initiation of muscle attachment, we selected Kon-tiki (*Kon*) (*Schnorrer et al., 2007; Weitkunat et al., 2014*), member of cluster 15, which is transiently up-regulated after myoblast fusion, before it is down-regulated again after 30 hr APF. Consistently, we found Kon-GFP present at muscle attachment sites at 30 hr APF but not at 72 hr APF (**Figure 2G–I**). A similar expression peak shifted to slightly later time points is found in cluster 34, which contains β -tubulin 60D (β Tub60D) (*Leiss et al., 1988*). Consistently, we find β -Tub60D-GFP (*Sarov et al., 2016*) expression in IFMs at 30 and 48 hr but not 72 hr APF (**Figure 2J–L**). After attachment is initiated, the attachments need to mature and be maintained. As expected, we found the essential attachment components β PS-Integrin (*mys*) and Talin (*rhea*) in clusters that are up-regulated after myoblast fusion until adulthood (clusters 7 and 25, respectively). This is consistent with continuous high protein expression of β PS-Integrin-GFP and Talin-GFP at muscle attachment sites (**Figure 2M–O, Figure 2—figure supplement 2D–F**). Taken together, these semi-quantitative protein localisation data nicely validate the temporal mRNA dynamics found in the mRNA-Seq data, confirming our methodology.

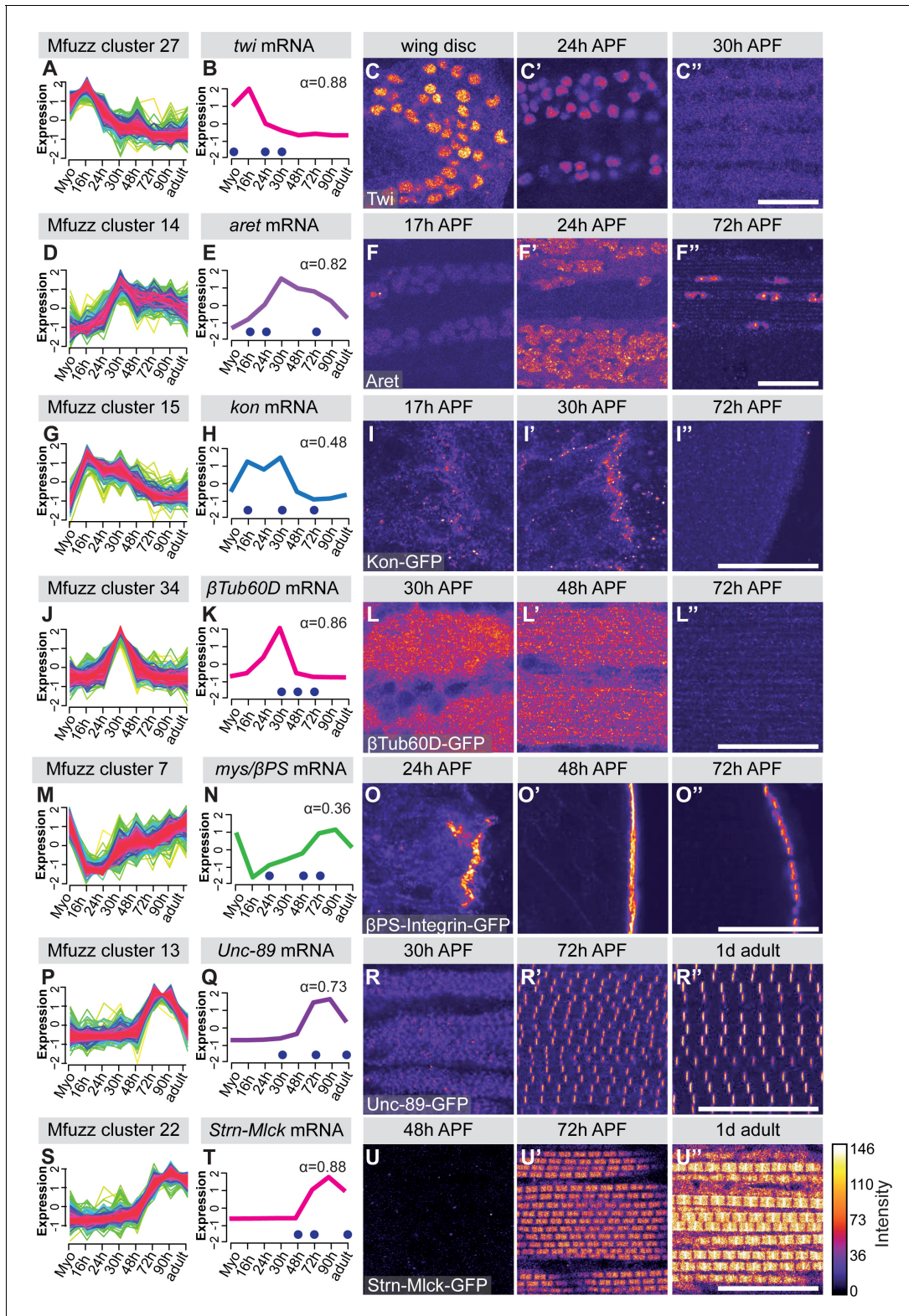


Figure 2. Verification of mRNA-Seq time-course by 'indicator' gene expression. (A,D,G,J,M,P,S) Temporal expression dynamics were evaluated by clustering standard-normal mRNA-seq counts using Mfuzz. Temporal expression profiles are plotted with high membership values in warm colours (red, pink), and lower membership values in cool colours (blue, green). (B,E,H,K,N,Q,T) The profile of one 'indicator' gene from each cluster is shown and coloured based on the Mfuzz membership value α . (C,F,I,L,O,R,U). Protein expression and localisation dynamics were visualised by antibody staining
 Figure 2 continued on next page

Figure 2 continued

against *Twi* (C) and *Aret* (F) or against GFP for GFP tagged fosmid reporters for *Kon* (I), β -Tub60D (L), β PS-Integrin (*mys*) (O), *Unc-89* (Obscurin) (R) and *Strn-Mlck* (U). Images for the same protein were acquired using the same settings, and pseudo-coloured based on intensity. Note the close correlation between mRNA and protein expression dynamics. Time points are indicated by blue dots on the mRNA expression profile. Scale bars represent 20 μ m.

DOI: <https://doi.org/10.7554/eLife.34058.005>

The following figure supplements are available for figure 2:

Figure supplement 1. Forty distinct temporal mRNA-Seq expression profiles.

DOI: <https://doi.org/10.7554/eLife.34058.006>

Figure supplement 2. Additional examples of ‘indicator’ gene expression.

DOI: <https://doi.org/10.7554/eLife.34058.007>

A transcriptional transition after 30 hr APF

Hierarchical clustering of the core expression profiles from the 40 identified Mfuzz clusters defines eight temporally ordered groups (**Figure 3**) that show progressive expression dynamics as muscle development proceeds. A time-dependent shift in gene ontology (GO) term enrichments is apparent between the eight groups, reflecting the different stages of IFM development. GO-Elite analysis (**Zambon et al., 2012**) for gene set enrichment identified GO terms related to cell proliferation and development as enriched in the early clusters (such as the *twi* cluster 27 or the *kon* cluster 15), whereas terms related to actin filament dynamics are more enriched in the middle clusters (such as the β PS-Integrin cluster seven and the Talin cluster 25), reassuring that the clustering approach is valid (**Figure 3, Supplementary file 2**). Strikingly, the only two clusters that display a strong enrichment for genes important for sarcomere organisation are clusters 13 and 22, both of which are late up-regulated clusters (**Figure 3**). Members of both clusters just become detectable at 30 hr APF (*Unc-89*/*Obscurin*-GFP, *Act88F*-GFP, *Mhc*-GFP) or even later at 48 hr APF (*Strn-Mlck*-GFP, *Mf*-GFP). In all cases, we could confirm the strong up-regulation from 30 hr to 72 hr APF in the mRNA-Seq data at the protein level using GFP fusion proteins under endogenous control (**Figure 2P–U, Figure 2—figure supplement 2J–P**) (**Sarov et al., 2016**). We additionally verified the late up-regulation of *Flightin* (*Fln*), a member of cluster 3, which is detectable at 72 hr but not at 30 hr APF (**Figure 2—figure supplement 2G–I**).

At late stages of flight muscle development, mitochondrial density strongly increases (**Clark et al., 2006**). Using GO-Elite, we found a strong enrichment for mitochondrial related pathways in four late up-regulated clusters, namely 3, 28, 39 as well as the sarcomere cluster 22 (**Figure 3**). By comparing the clusters to systematic functional data acquired at all stages of *Drosophila* muscle development (**Schnorrer et al., 2010**), we find enrichments in clusters throughout the time-course. Interestingly, genes highly expressed in flight muscle compared to other muscle types, identified as ‘*salm*-core genes’ (**Spletter et al., 2015**), are also enriched in the late clusters, including the mitochondrial enriched clusters 3, 28, 39 and the sarcomere enriched cluster 22 (**Figure 3**). These data highlight the changes in biological process enrichments that parallel expression dynamics, with a particular transition happening during later stages of muscle development after 30 hr APF. This corresponds to a time period after immature myofibrils have been assembled, which thus far remained largely unexplored.

To examine the temporal expression dynamics in more detail, we performed a principle component analysis (PCA) of the mRNA-Seq time points and Mfuzz clusters and found that the major variance is developmental time, with a notable change after 30 hr APF (**Figure 4A, Figure 4—figure supplement 1A**). There are a large number of genes being up-regulated as well as down-regulated between 30 and 48 hr and between 48 and 72 hr APF, with major differences between the sets of genes expressed at early (16–30 hr APF) versus late (72–90 hr APF) stages of development (**Figure 4B, Figure 4—figure supplement 1B**). Thus, we focused our attention on the transcriptional transition between 30 and 72 hr APF, which correlates with major growth of the flight muscle fibers (**Figure 1**).

A large number of genes are significantly up- or down-regulated from 30 hr to 72 hr APF, as visualized on a volcano plot displaying \log_2 fold changes (FC) (**Figure 4C**), suggesting a major change in gene expression. In particular, many sarcomeric genes are strongly up-regulated. To identify fine details in expression dynamics, we took all genes significantly up-regulated between 30 and 72 hr

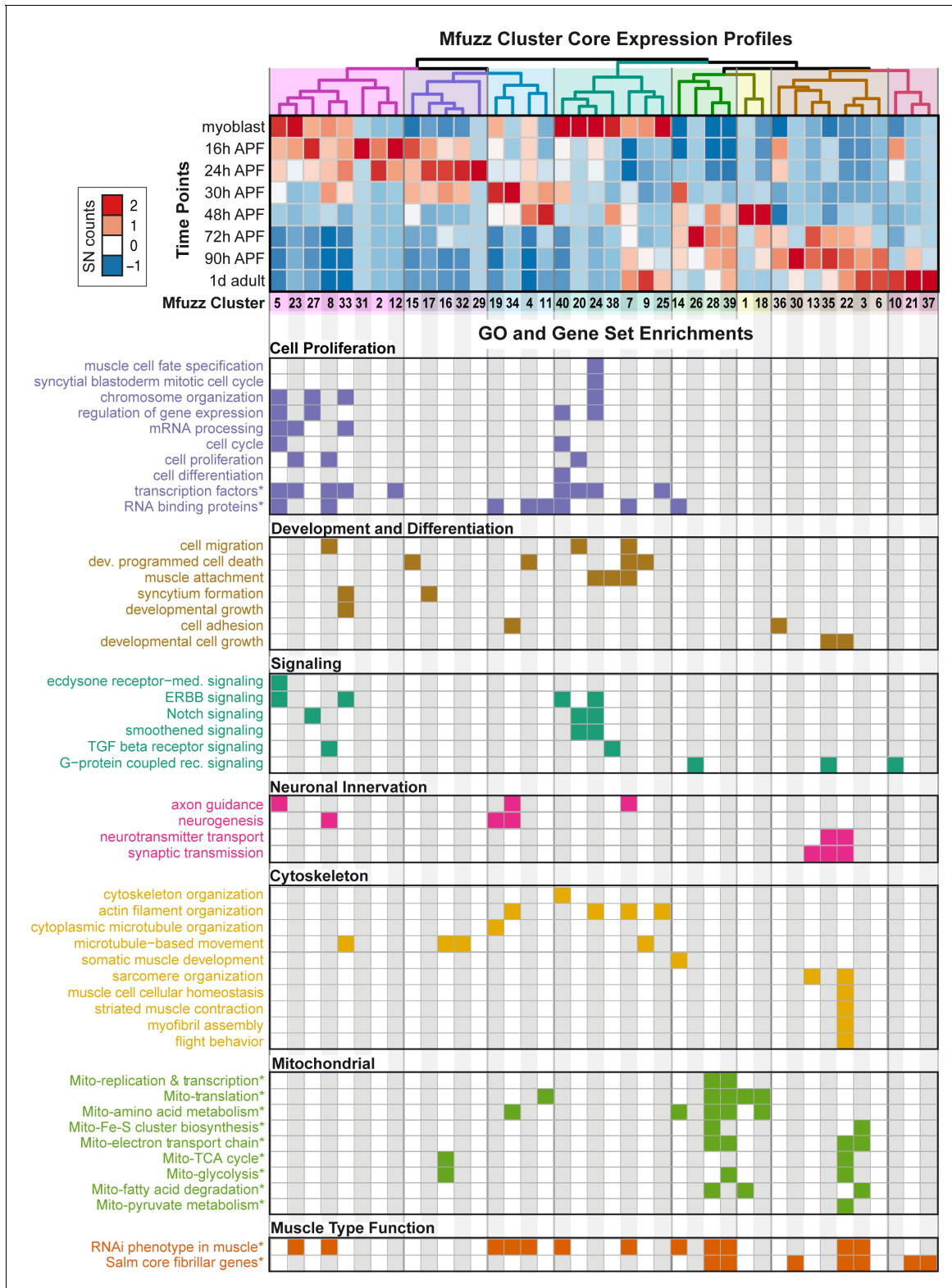


Figure 3. Expression dynamics reveal a temporal ordering of biological processes during muscle morphogenesis. (Top) Heat map of Mfuzz cluster core expression profiles. Standard-normal count values for all genes with a membership value $\alpha > 0.8$ were averaged to generate the core expression profile for each cluster. Mfuzz expression profiles fall into eight groups (coloured dendrogram leaves) based on hierarchical clustering of their temporal expression dynamics. Time points and Mfuzz clusters are labelled. Colour scale of standard-normal count values ranges from blue (stable/no) to red (high).
 Figure 3 continued on next page

Figure 3 continued

expression) to red (high expression). (Bottom) GO Biological Process and user-defined gene set (marked with *) enrichments calculated with GO-Elite. Note that proliferation, development and differentiation terms are enriched at early time points, while mitochondrial and sarcomere terms are enriched at late time points. A coloured box indicates a significant enrichment of a given term in the specified cluster (see **Supplementary file 2** for details).

DOI: <https://doi.org/10.7554/eLife.34058.008>

APF and performed hierarchical clustering of their DESeq2 normalized counts values (**Figure 4D**). We noted that many genes are turned on from 30 hr to 72 hr APF, whereas others are already expressed at 30 hr and strongly increase their expression until 72 hr (**Figure 4D**), suggesting a transcriptional transition after 30 hr APF. Consistently, we found GO-terms of cell proliferation, cell cycle and Notch signalling down-regulated, whereas actin cytoskeleton, sarcomere, muscle function and mitochondrial related gene sets are strongly up-regulated from 30 hr to 72 hr APF (**Figure 4E**). Finally, the genes up-regulated from 30 hr to 72 hr APF are enriched for sarcomeric proteins and the 'salm core genes' (**Figure 4—figure supplement 1C,D**), and the Mfuzz gene clusters with the most up-regulated members are the mitochondrial and both sarcomeric gene containing clusters 13 and 22 (**Figure 4F**). Together, these data suggest that in particular expression of the sarcomeric and mitochondrial genes is strongly induced after 30 hr APF.

Ordered phases during sarcomere morphogenesis

The strong up-regulation of sarcomeric gene expression after immature myofibrils have been assembled (**Figure 1**) (**Weitkunat et al., 2014**) caught our interest and prompted us to more closely investigate the later stages of myofibrillogenesis during which myofibers grow dramatically (**Figure 1**). We stained the myofibers with phalloidin to reveal myofibril morphology and with the titin isoform Kettin (an isoform of the *sallimus* gene) to label the developing Z-discs and systematically quantified sarcomere length and myofibril width (see Materials and methods) (**Figure 5A, Supplementary file 3**). By measuring the total muscle fiber length, we calculated the total number of sarcomeres per myofibril at a given stage. We found that the sarcomere length and width remain relatively constant at about 2.0 and 0.5 μm , respectively until 48 hr APF (**Figure 5B,C, Supplementary file 3**). However, the number of sarcomeres per myofibril dramatically increases from about 100 at 34 hr to about 230 at 48 hr APF. After 48 hr only a few more sarcomeres are added, resulting in about 270 sarcomeres per myofibril at 60 hr APF. This number remains constant until the fly ecloses (**Figure 5D, Supplementary file 3**). Moreover, by analysing fiber cross-sections we found that the growth of the individual myofibril diameter correlates with growth of the entire muscle fiber. Both fiber diameter and myofibril diameter remain constant from 30 hr to 48 hr APF. After 48 hr the myofibril diameter grows nearly 3-fold from 0.46 μm to 1.43 μm in adult flies (**Figure 5E–G**), while fiber cross-sectional area grows nearly 4-fold from 1,759 μm^2 to 6,970 μm^2 . Strikingly, during the entire time period from 30 hr APF to adults, the total number of myofibrils per muscle fiber remains constant (about 2000 per muscle fiber, **Figure 5H**). Taken together, these quantitative data lead us to propose ordered but somewhat overlapping phases of sarcomere morphogenesis: (1) During the sarcomere assembly phase, about 100 immature sarcomeres self-assemble within each immature myofibril. (2) Many short sarcomeres are added to each myofibril increasing its length. (3) The short sarcomeres grow in length and thickness to reach the mature pseudo-crystalline pattern. No new myofibrils are built after the initial myofibril assembly phase.

We gained additional evidence to support this ordered myofibrillogenesis model on both the molecular and functional levels. First, the initial assembly versus the later sarcomere maturation complement the transition in gene expression we observe from 30 hr to 72 hr APF. Using members of the late induced Mfuzz clusters that contain sarcomeric components, we found that indeed a subset of sarcomeric proteins, such as Unc-89/Obscurin and Mhc, are already detectable in a periodic pattern on immature myofibrils at 30 hr. By contrast, other important components, including Fln, Myofilin (Mf) and Strn-Mlck, are only incorporated into myofibrils from 48 hr APF, showing high levels by 72 hr APF (**Figure 5—figure supplement 1**). Second, to investigate muscle function, we used Talin-YPet as a muscle attachment marker and quantified the number of spontaneous muscle contractions in intact pupae (see Materials and methods). Interestingly, we found that immature myofibrils already start to spontaneously contract at 30 hr APF. These spontaneous contractions increase in strength

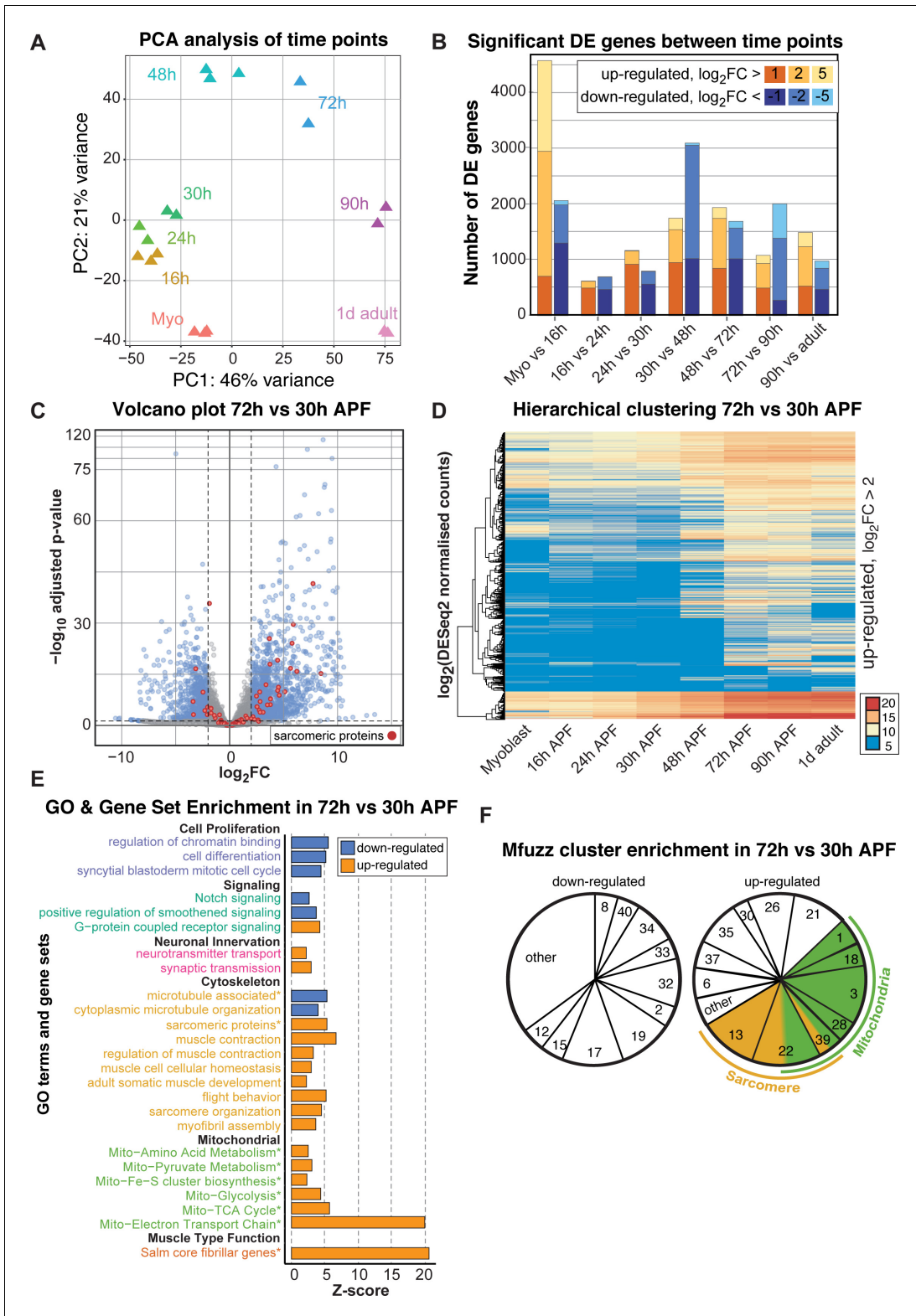


Figure 4. A major transition in gene expression after 30 hr APF. (A) DESeq2 principle components analysis (PCA) of all mRNA-Seq libraries. Each triangle represents a different biological replicate coloured by time point. Note that individual replicates for a given time point cluster together. PC1 divides early (≤ 48 hr APF) from late (≥ 72 hr) stages. (B) Stacked box plot of the number of significantly differentially expressed genes up-regulated (reds) or down-regulated (blues) between sequential time points with a p-value < 0.05 and a \log_2FC (fold change) of > 1 (dark), > 2 (medium) or > 5 (light). Figure 4 continued on next page

Figure 4 continued

The large differences between myoblast to 16 hr APF reflect muscle specification. A second large shift in expression is evident between 30 and 72 hr APF. (C) Volcano plot illustrating the strong up-regulation of sarcomeric proteins (red) from 30 hr to 72 hr APF. Significantly up- or down-regulated genes are in blue (p -value <0.05 and $\text{abs}(\log_2\text{FC})>2$). (D) Hierarchical clustering of \log_2 transformed DESeq2 normalized counts for all genes that are significantly up-regulated between 30 and 72 hr APF. Note that they are either strongly induced at 48 or 72 hr APF (from yellow to red), or only turned on at 48 or 72 hr APF (blue to yellow/red), suggesting a major transition in gene expression after 30 hr APF. Colour scale of \log_2 count values ranges from blue (not expressed) to red (highly expressed). (E) GO-Elite and user-defined gene set (marked with *) enrichments in up- (red) and down- (blue) regulated genes from 30 hr to 72 hr APF. Note the strong enrichment of mitochondrial and sarcomere terms in the up-regulated genes. (F) Pie charts showing the proportion of genes belonging to an enriched Mfuzz cluster in the sets of genes either up- or down-regulated from 30 hr to 72 hr APF. Note that a large proportion of genes up-regulated 30 hr to 72 hr belong to cluster 22, as well as Mfuzz clusters enriched for sarcomere (yellow) or mitochondrial (green) terms.

DOI: <https://doi.org/10.7554/eLife.34058.009>

The following figure supplement is available for figure 4:

Figure supplement 1. Additional evidence supporting a transition in gene expression between 30 and 72 hr APF.

DOI: <https://doi.org/10.7554/eLife.34058.010>

and frequency until 48 hr APF, but then cease, producing no detectable spontaneous contractions at 72 hr APF (**Figure 5I,J**, **Figure 5—video 1**). This demonstrates that during the sarcomere assembly phase, immature contractile myofibrils are generated, which then likely acquire stretch-sensitivity as the immature myofibrils mature and thus cease contracting.

Salm contributes to the transcriptional transition after 30 hr APF

How does the transcriptional transition of the various sarcomeric components instruct myofibrillogenesis? As the identified sarcomeric clusters 13 and 22 are enriched for 'salm-core genes' (**Spletter et al., 2015**) (**Figure 3**), we chose to investigate gene expression in developing *spalt*-major knock-down (*salmIR*) flight muscles compared to wild type (**Supplementary file 4**). *salmIR* IFM shows a strong down-regulation in gene expression, notably of mRNAs coding for sarcomeric and mitochondrial components at 24 and 30 hr APF, and in particular at 72 hr APF (**Figure 6A–C**, **Figure 6—figure supplement 1A–D**). The genes down-regulated in *salmIR* IFM are enriched for GO terms associated with sarcomere assembly, flight behaviour and mitochondrial genes, as well as for the mitochondrial Mfuzz clusters 3, 28, 39 and the sarcomeric Mfuzz clusters 13 and 22 (**Figure 6—figure supplement 1E–G**). Interestingly, members of cluster 22, which is strongly enriched for sarcomeric and mitochondrial genes, are not only down-regulated at 72 hr APF in *salmIR* (**Figure 6B**) but are also less strongly induced from 30 hr to 72 hr APF in *salmIR* muscle compared to wild type (**Figure 6D**), suggesting that *salm* in addition to other factors is indeed required for the strong induction of sarcomeric protein expression after 30 hr APF.

Salm is expressed shortly after myoblast fusion and constitutive knock-down of *salm* with *Mef2-GAL4* results in a major shift of muscle fiber fate (**Schönbauer et al., 2011**), which may indirectly influence transcription after 30 hr APF. Hence, we aimed to reduce *Salm* levels only later in development, to directly address its role during sarcomere maturation. To this end, we knocked-down *salm* with the flight muscle specific driver *Act88F-GAL4*, which is expressed from about 18 hr APF and requires *salm* activity for its expression (**Bryantsev et al., 2012**; **Spletter et al., 2015**). This strategy enabled us to reduce *Salm* protein levels at 24 hr APF resulting in undetectable *Salm* levels at 72 hr APF (**Figure 6—figure supplement 2**). To test if *Salm* contributes to the transcriptional boost of sarcomeric components after 30 hr APF, we performed quantitative imaging using unfixed living flight muscles expressing GFP fusion proteins under endogenous control. We used green fluorescent beads to normalise the GFP intensity between different samples, and could verify the induction of Mhc, Unc-89, Fln and Strn-Mlck on the protein level from 30 hr to 72 hr APF (**Figure 6—figure supplement 3**). While overall sarcomere morphology is not strongly affected in *Act88F >> salmIR* muscles, we found that the levels of Strn-Mlck, Fln and Mhc proteins are strongly reduced at 90 hr as compared to wild-type controls (**Figure 6D–H**). This suggests that *salm* indeed contributes to the transcriptional transition that boosts the expression of a number of sarcomeric proteins after 30 hr APF.

To investigate the consequences of late *salm* knock-down, we quantified the myofibril and sarcomere morphology from 48 hr onwards. The myofibrils display a fibrillar morphology, confirming that

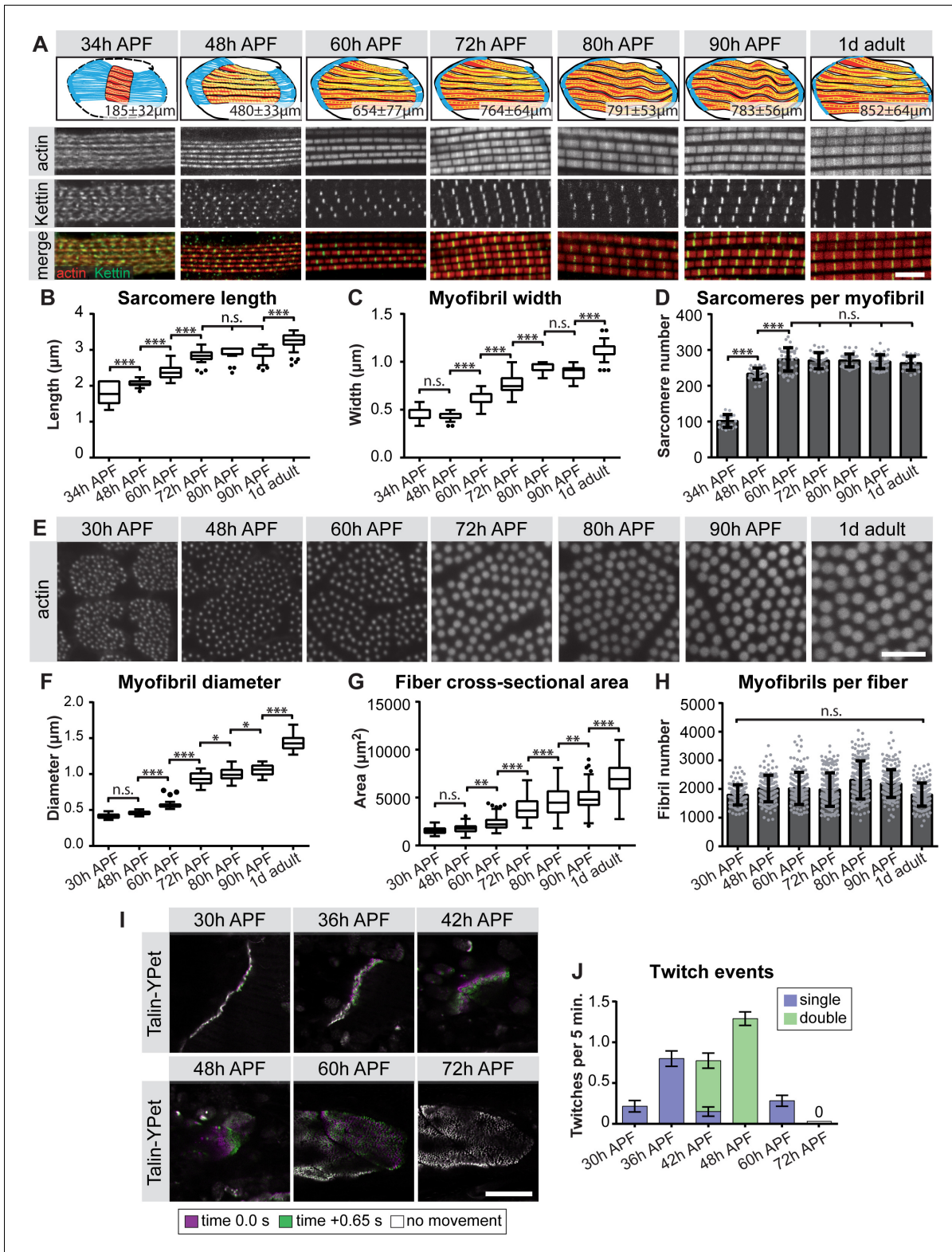


Figure 5. Sequential phases of sarcomere morphogenesis in flight muscles. (A) Scheme of hemi-thoraces at 34, 48, 60, 72, 80, 90 hr APF and 1 day adults (muscle in red, tendon in blue, sarcomeres in yellow) with indicated muscle fiber length. Myofibrils and sarcomeres at these time points were stained for phalloidin (F-actin, red) and Kettin (Z-disc, green). Scale bar represents 5 μm. (B,C) Tukey box and whisker plot of sarcomere length and myofibril width. Box extends from 25 to 75%, line marks median, whiskers extend to 25/75% plus 1.5 times the interquartile range. (D) Histogram of Figure 5 continued on next page

Figure 5 continued

sarcomere number per myofibril. Error bars represent SD. Note the sarcomere assembly at 34 hr, followed by sarcomere addition until ~48 hr and sarcomere maturation after ~48 hr APF. (E) Cross-sections of the DLMs at 30, 48, 60, 72, 80, 90 hr APF and 1 day adult. Scale bar represents 5 μm . (F,G) Tukey box and whisker plot of myofibril diameter and myofiber cross-sectional area. Note the lack of growth in diameter or area from 30 hr to 48 hr. (H) Histogram of the number of myofibrils per myofiber. Error bars represent SD. Note that all myofibrils are already present at 30 hr APF. Tukey's multiple comparison p-value < 0.05*, .01**, .001***, n.s. = not significant. N > 10 for each individual time point. (I) Stills of live movies of DLMs at 30, 36, 42, 48, 60 and 72 hr APF. Scale bar represents 50 μm . For live movies see **Figure 5—video 1**. Stills are a time 0.0 s image (magenta) overlaid with a time +0.65 s image (green), where a perfect overlap (white) shows no movement. (J) Quantification of spontaneous contraction events per fiber per 5 min, with single twitches in blue and double twitches in green. Fibers are first contractile at 30 hr APF, reach peak contractility at 48 hr and stop all spontaneous contraction shortly after 60 hr APF.

DOI: <https://doi.org/10.7554/eLife.34058.011>

The following video, source data, and figure supplement are available for figure 5:

Source data 1. This table includes calculation of the number of sarcomeres per myofibril in wild type flight muscles at the indicated stage.

DOI: <https://doi.org/10.7554/eLife.34058.013>

Source data 2. This table includes the sarcomere length in wild type flight muscles measured at the indicated stage.

DOI: <https://doi.org/10.7554/eLife.34058.014>

Source data 3. This table includes the sarcomere/myofibril width in wild type flight muscles measured at the indicated stage.

DOI: <https://doi.org/10.7554/eLife.34058.015>

Source data 4. This table includes the myofiber cross-sectional area measured in wild type flight muscle fibers or only fibers 3 and four at the indicated stage.

DOI: <https://doi.org/10.7554/eLife.34058.016>

Source data 5. This table includes the number of myofibrils per myofiber calculated for either all wild type flight muscle fibers or only fibers 3 and four at the indicated stage.

DOI: <https://doi.org/10.7554/eLife.34058.017>

Source data 6. This table includes the myofibril diameter measured in wild type flight muscles at the indicated stage.

DOI: <https://doi.org/10.7554/eLife.34058.018>

Source data 7. This table includes the muscle twitch events per wild-type fiber per 5 min recorded at the indicated stage.

DOI: <https://doi.org/10.7554/eLife.34058.019>

Figure supplement 1. Expression and localisation of thin- and thick-filament structural proteins.

DOI: <https://doi.org/10.7554/eLife.34058.012>

Figure 5—video 1. Twitching time-course in developing DLMs.

DOI: <https://doi.org/10.7554/eLife.34058.020>

the early function of *Salm* to determine IFM fate was unaffected by our late knock-down. At 72 hr APF and more prominently at 90 hr APF and in adults, *Act88F* >> *salmIR* myofibrils showed actin accumulations at broadened Z-discs (**Figure 7A–H**), which are often a landmark of nemaline myopathies (*Sevdali et al., 2013; Wallgren-Pettersson et al., 2011*). The myofibril width was not significantly different in these myofibrils (**Figure 7I**). However, the sarcomeres of *Act88F* >> *salmIR* muscles displayed a strong defect in sarcomere length growth after 48 hr APF (**Figure 7J, Supplemental File 3**), with sarcomeres only obtaining a length of 2.8 μm in adult flies, demonstrating that *Salm* in addition to other factors is required for normal sarcomere maturation.

Salm function contributes to gain of stretch-activation during sarcomere maturation

Given the defects in sarcomere length and sarcomere gene expression in *Act88F* >> *salmIR* muscles, we explored the function of these abnormal muscle fibers. As expected, *Act88F* >> *salmIR* flies are flightless (**Figure 7—figure supplement 1A**) and we observed rupturing of the adult muscle fibers within 1d after eclosion (**Figure 7—figure supplement 1B–G**), demonstrating the importance of proper sarcomere maturation to prevent muscle atrophy. Based on our finding that spontaneous flight muscle contractions stop by 72 hr APF, we hypothesized that if *Salm* truly regulates sarcomere maturation, we may see spontaneous contraction defects during development. At 48 hr APF, *Act88F* >> *salmIR* fibers twitch, but less often than and without the double twitches observed in control fibers (**Figure 7K,L,O; Figure 7—video 1**). Strikingly, at 72 hr APF *salmIR* fibers fail to stop contracting and moreover show frequent and uncoordinated spontaneous contractions in which different myofibril bundles of the same fiber twitch at different times (**Figure 7M–O, Figure 7—**

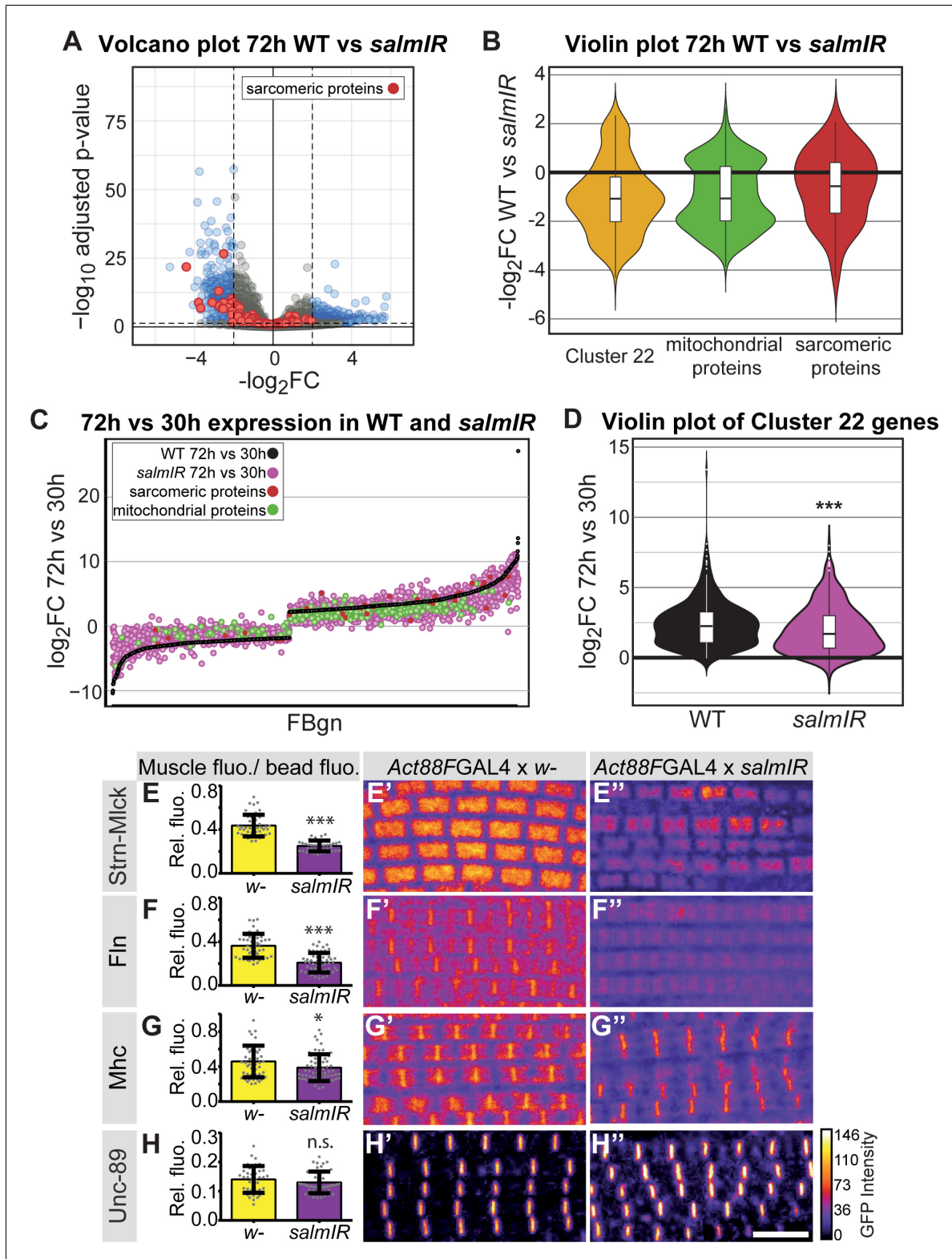


Figure 6. *salm* contributes to the transition in gene expression after 30 hr APF. (A) Volcano plot of mRNA-Seq comparison of wild-type (WT) versus *salmIR* IFMs at 72 hr APF. Note the significant down-regulation of genes in *salmIR*, especially sarcomeric protein coding genes (red). Significantly differentially expressed (DE) genes ($abs(\log_2 FC) > 2$, $p < 0.05$) are in blue. (B) Violin plot showing down-regulation of sarcomeric proteins (in red), mitochondrial proteins (in green) and members of Mfuz cluster 22 (in yellow) in *salmIR* compared to wild type at 72 hr APF. Box plots indicate the Figure 6 continued on next page

Figure 6 continued

median of the data as well as the first and third quartile in the box, outliers are the dots. (C) WT mRNA-Seq fold change values of all genes significantly DE from 30 hr to 72 hr APF are ordered from lowest to highest (black). The corresponding *salmIR* fold change is shown in yellow. Both sarcomeric (red) and mitochondrial protein coding genes (blue) are less strongly up- or down-regulated in *salmIR* across the 30 hr to 72 hr APF transition. Note that many genes in *salmIR* (yellow dots) are not as strongly induced or even repressed compared to WT (below and above the black WT line, respectively). (D) Violin plot comparing the \log_2FC over the 30 hr to 72 hr transition in WT (in black) and *salmIR* IFM (in magenta) for members of Mfuzz Cluster22. Box plots indicate the median of the data as well as the first and third quartile in the box, outliers are the dots. Note the significant decrease in induction to 72 hr APF in the *salmIR* sample. ***Student's t-test p-value<0.0005. (E–H) *salm* is required for the induction of some but not all sarcomeric proteins. *Act88F* >> *salmIR* in the background of GFP-tagged Strn-Mlck-IsoR (E), Fln (F), Mhc (G) and Unc-89 (H). Quantitative changes in live GFP fluorescence at 90 hr APF were measured by quantitative confocal microscopy relative to standard fluorescent beads, revealing significant decreases in induction for Strn-Mlck, Fln and Mhc between wild type control (shown in yellow, *Act88F-GAL4* crossed to *w¹¹¹⁸*) and *Act88F* >> *salmIR* (shown in purple). Scale bar represents 5 μ m. Error bars represent SEM, Student's t-test p-value<0.05*, 0.001***, n.s. = not significant. N > 10 for each individual sample. (E'–H') Intensity-coded GFP fluorescence at 90 hr APF in confocal images of fixed myofibrils.

DOI: <https://doi.org/10.7554/eLife.34058.021>

The following source data and figure supplements are available for figure 6:

Source data 1. This table includes the fiber divided by bead fluorescence intensity measurements for quantification of the indicated fosmid-GFP or UAS-GFP-Gma expression levels at the indicated stage.

DOI: <https://doi.org/10.7554/eLife.34058.025>

Source data 2. This table includes the fiber divided by bead fluorescence intensity measurements for various fosmid-GFPs in the *Act88F* >> *salmIR* or control *Act88F-Gal4* x w- background at 90 hr APF.

DOI: <https://doi.org/10.7554/eLife.34058.026>

Figure supplement 1. *salm* regulates gene expression during flight muscle development.

DOI: <https://doi.org/10.7554/eLife.34058.022>

Figure supplement 2. *Act88F-GAL4* driven knock-down of *salm* is efficient.

DOI: <https://doi.org/10.7554/eLife.34058.023>

Figure supplement 3. Expression of sarcomeric proteins strongly increases from 30 hr to 72 hr APF.

DOI: <https://doi.org/10.7554/eLife.34058.024>

video 2), demonstrating that sarcomere maturation is indeed disrupted, with the likely consequence that myofibrils fail to acquire normal stretch-activation sensitivity.

To directly test the function of a sarcomeric component during the sarcomere maturation phase, we investigated the role of the prominently induced *Salm* target *Strn-Mlck*. *Strn-Mlck* is only expressed after 30 hr APF and is largely incorporated during sarcomere maturation (**Figure 5—figure supplement 1E**, **Figure 6—figure supplement 3E**), and thus is also a bone-fide example of a gene regulated during the transcriptional transition. In *Strn-Mlck* mutants, sarcomere and myofibril morphology, including myofibril width, is initially normal. However, at 80 hr APF the sarcomeres overgrow, consistently reaching lengths of more than 3.5 μ m and resulting in slightly longer muscle fibers at 80 hr APF (**Figure 8**). After overgrowing, sarcomeres appear to hyper-contract resulting in short, thick sarcomeres in 1-day-old adults (**Figure 8E,J,K,L**). Like *Act88F* >> *salmIR* flies, *Strn-Mlck* mutant adults are flightless (**Figure 7—figure supplement 1A**) and display ruptured fibers during the first days of life (**Figure 7—figure supplement 1K–M**) (Spletter et al., 2015). Together, these data demonstrate that sarcomere maturation must be precisely controlled at the transcriptional level to enable the precise growth of sarcomeres to their final mature size. This ensures the lifelong function of the contractile apparatus of muscle fibers.

Discussion

A developmental muscle transcriptomics resource

In this study, we generated a systematic developmental transcriptomics resource from *Drosophila* flight muscle. The resource quantifies the transcriptional dynamics across all the major stages of muscle development over five days, starting with stem cell-like myoblasts and attaching myotubes to fully differentiated, stretch-activatable muscle fibers. We have specifically focused on the transcriptional regulation of sarcomere and myofibril morphogenesis; however, the data we provide cover all other expected dynamics, such as mitochondrial biogenesis, T-tubule morphogenesis, neuromuscular junction formation, tracheal invagination, etc. Thus, together with the available systematic

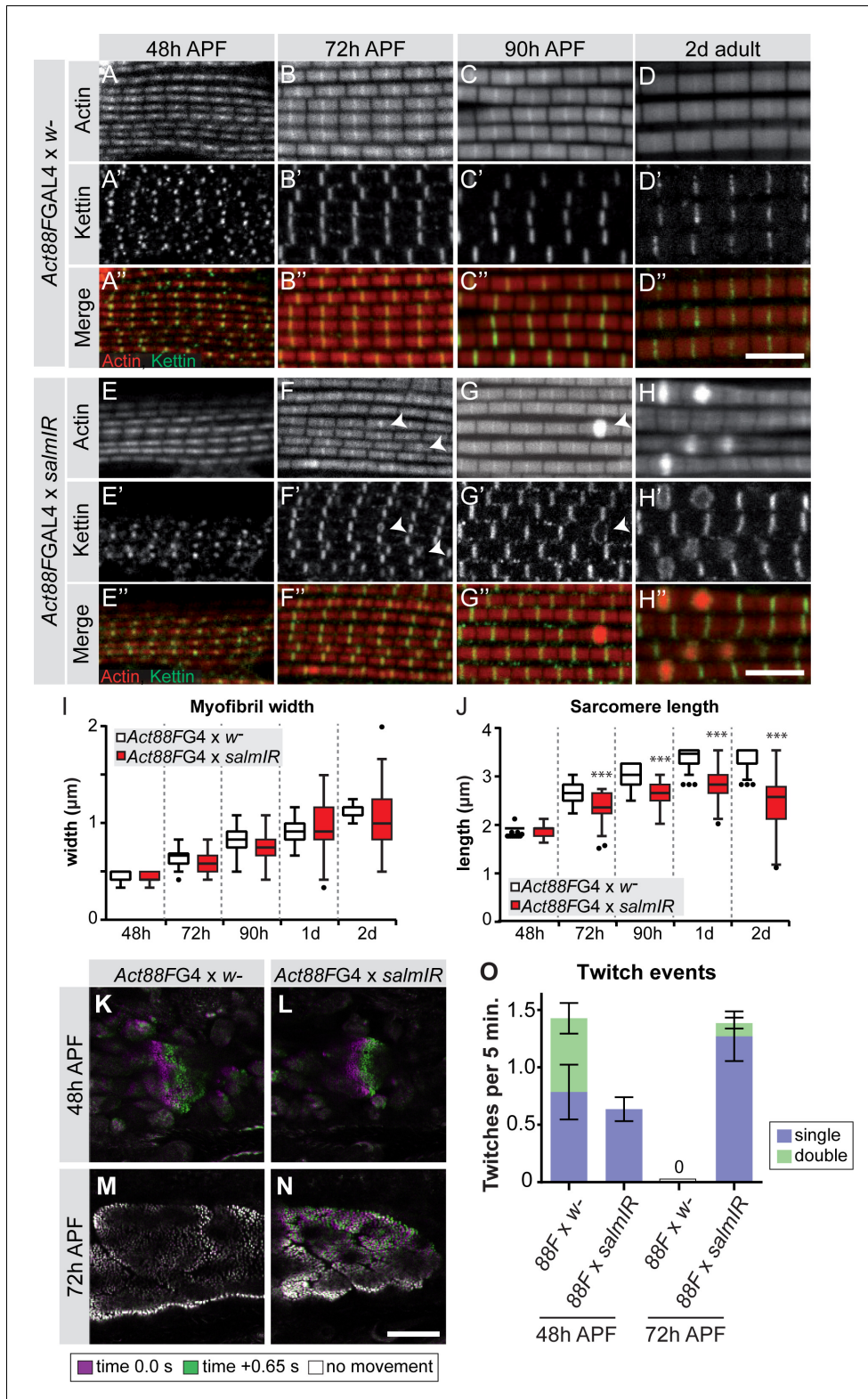


Figure 7. *salm* is required for normal sarcomere maturation and function. (A–H) Myofibrils of *Act88F-GAL4* / + (A–D) or *Act88F* >> *salmIR* (E–H). Note that *salmIR* DLM remains fibrillar and appears normal at 48 hr APF (E), but at 72 hr APF (F) 90 hr APF (G) and 2 day adult (H) Z-discs widen and show actin accumulations (arrowheads). (I, J) Tukey box and whisker plot of myofibril width (I) and sarcomere length (J) in *Act88F-GAL4* / + and *Act88F* >> *salmIR* (red). Tukey's multiple comparison p-value < 0.001***. N > 10 for each individual time point. Scale bars represent 5 μm. (K–O) Stills Figure 7 continued on next page

Figure 7 continued

from live movies of developing DLMs at 48 and 72 hr APF in *Act88F*-GAL4 / + (K, M) and *Act88F* >> *salmIR* (L, N). Scale bar represents 50 μ m. Coloured as in **Figure 5**. (O) Quantification of spontaneous contraction events per fiber per 5 min, with single twitches in blue and double twitches in green. Error bars represent SEM. *salmIR* fibers continue spontaneously contracting at 72 hr APF.

DOI: <https://doi.org/10.7554/eLife.34058.027>

The following video, source data, and figure supplement are available for figure 7:

Source data 1. This table includes the muscle twitch events per *Act88F* >> *salmIR* fiber per 5 min and the respective controls recorded at the indicated stage.

DOI: <https://doi.org/10.7554/eLife.34058.029>

Source data 2. This table includes the sarcomere length measured in *Act88F* >> *salmIR* flight muscles and the respective controls at the indicated stage.

DOI: <https://doi.org/10.7554/eLife.34058.030>

Source data 3. This tables includes the sarcomere/myofibril width measured in *Act88F* >> *salmIR* flight muscles and the respective controls at the indicated stage.

DOI: <https://doi.org/10.7554/eLife.34058.031>

Figure supplement 1. *Act88F* >> *salmIR* and *Strn-Mlck* mutant flies are flightless and IFM fibers rupture in adult flies.

DOI: <https://doi.org/10.7554/eLife.34058.028>

Figure 7—video 1. Twitching in developing *Act88F*-GAL4 / + and *Act88F* >> *salmIR* DLMs at 48 hr APF.

DOI: <https://doi.org/10.7554/eLife.34058.032>

Figure 7—video 2. Twitching in developing *Act88F*-GAL4 / + and *Act88F* >> *salmIR* DLMs at 72 hr APF.

DOI: <https://doi.org/10.7554/eLife.34058.033>

functional data of *Drosophila* muscle development (**Schnorrer et al., 2010**), our data should be a versatile resource for the muscle community. It nicely complements existing systematic data from vertebrate muscle, which thus far are largely restricted to postnatal stages (**Brinegar et al., 2017; Drexler et al., 2012; Lang et al., 2017; Zheng et al., 2009**). Furthermore, *Drosophila* flight muscle contains a single muscle fiber type, in contrast to the mixed fiber types found in mammals (**Schiaffino and Reggiani, 2011; Spletter and Schnorrer, 2014**). Hence, in this model the transcriptional dynamics of a single fiber type muscle can be followed with unprecedented precision.

A transcriptional transition correlating with ordered sarcomere morphogenesis

Earlier work has shown that the flight muscle myotubes first attach to tendon cells and then build-up mechanical tension. This tension triggers the simultaneous assembly of immature myofibrils, converting the myotube to an early myofiber (**Weitkunat et al., 2014**). This suggested a tension-driven self-organisation mechanism of myofibrillogenesis (**Lemke and Schnorrer, 2017**). Here we discovered that myofibrillogenesis is not only regulated mechanically, but to a large extent also transcriptionally. This enabled us to extend our model for ordered myofibrillogenesis also to later developmental stages and to define three sequential although somewhat overlapping phases (**Figure 9**). During the sarcomere self-assembly phase at about 30 hr APF, a large number of genes coding for sarcomeric proteins, including Mhc, *Act88F* and *Unc-89/Obsecrin*, become up-regulated to enable the self-organization of short, immature sarcomeres within thin, immature myofibrils. Strikingly, all of the about 2000 myofibrils assemble during this phase.

This is followed by a sarcomere addition phase during which a transcriptional transition is initiated and the expression of the sarcomeric proteins increases. Concomitantly, the muscle fibers grow in length by addition of new sarcomeres to all the immature myofibrils, increasing the sarcomere number from about 80 to 230 per fibril at 48 hr APF. These sarcomeres are contractile, but remain short and thin (**Figure 9**).

After the transcriptional transition, myofibrillogenesis enters the final sarcomere maturation phase. Proteins present in immature myofibrils like Mhc, *Act88F* and *Unc-89/Obsecrin* are expressed to even higher levels, and additional, often flight-muscle specific proteins like Mf, Fln and the titin-related isoform *Strn-Mlck*, begin to be expressed at high levels and are incorporated into the maturing sarcomeres. This facilitates a dramatic growth of all immature sarcomeres in length and particularly in diameter with all 2000 myofibrils reaching a pseudo-crystalline regularity within about two days of development (**Figure 9**). Importantly, these matured sarcomeres no longer contract

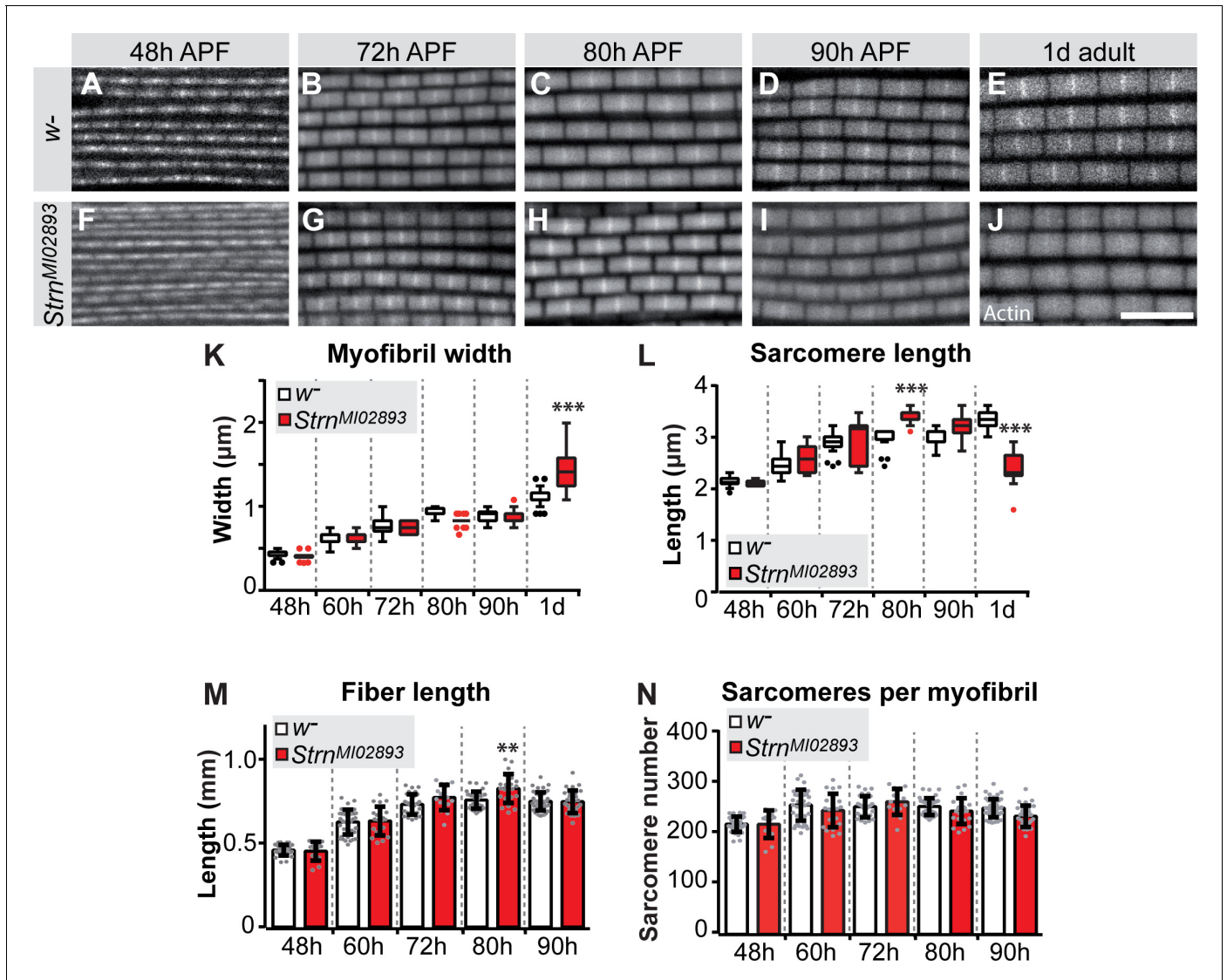


Figure 8. *Strn*-*Mlck* contributes to sarcomere length regulation during sarcomere maturation. (A–J) Wild type (A–E) and *Strn*^{M102893} mutant (F–J) sarcomere development at 48, 72, 80, 90 hr APF and 1 day adult. (K–N) Tukey box and whisker plot of myofibril width (K) and sarcomere length (L) in wild type and *Strn*^{M102893} mutant (red). Tukey’s multiple comparison p-value<0.001***. N > 10 for each individual time point. Histogram of fiber length (M) and number of sarcomeres per myofibril (N). Error bars represent SEM. Tukey’s multiple comparison p-value<0.01**, N > 10 for each individual time point. Note that a normal number of sarcomeres are formed in *Strn*^{M102893} mutants, but they grow too long at 80 hr APF and hyper-contract in 1 day adult.

DOI: <https://doi.org/10.7554/eLife.34058.034>

The following source data is available for figure 8:

Source data 1. This table includes the numbers of sarcomeres calculated per *strn-mlck* mutant myofibril and the respective control at the indicated stage.

DOI: <https://doi.org/10.7554/eLife.34058.035>

Source data 2. This table includes the length measurements of the indirect flight muscle fibers at the indicated stage for *strn-mlck* mutants and wild-type controls.

DOI: <https://doi.org/10.7554/eLife.34058.036>

Source data 3. This table includes the calculated numbers of sarcomeres per myofibril at the indicated stage for *strn-mlck* mutants.

DOI: <https://doi.org/10.7554/eLife.34058.037>

Source data 4. This table includes the sarcomere length measured in *strn-mlck* mutant flight muscles at the indicated stage.

DOI: <https://doi.org/10.7554/eLife.34058.038>

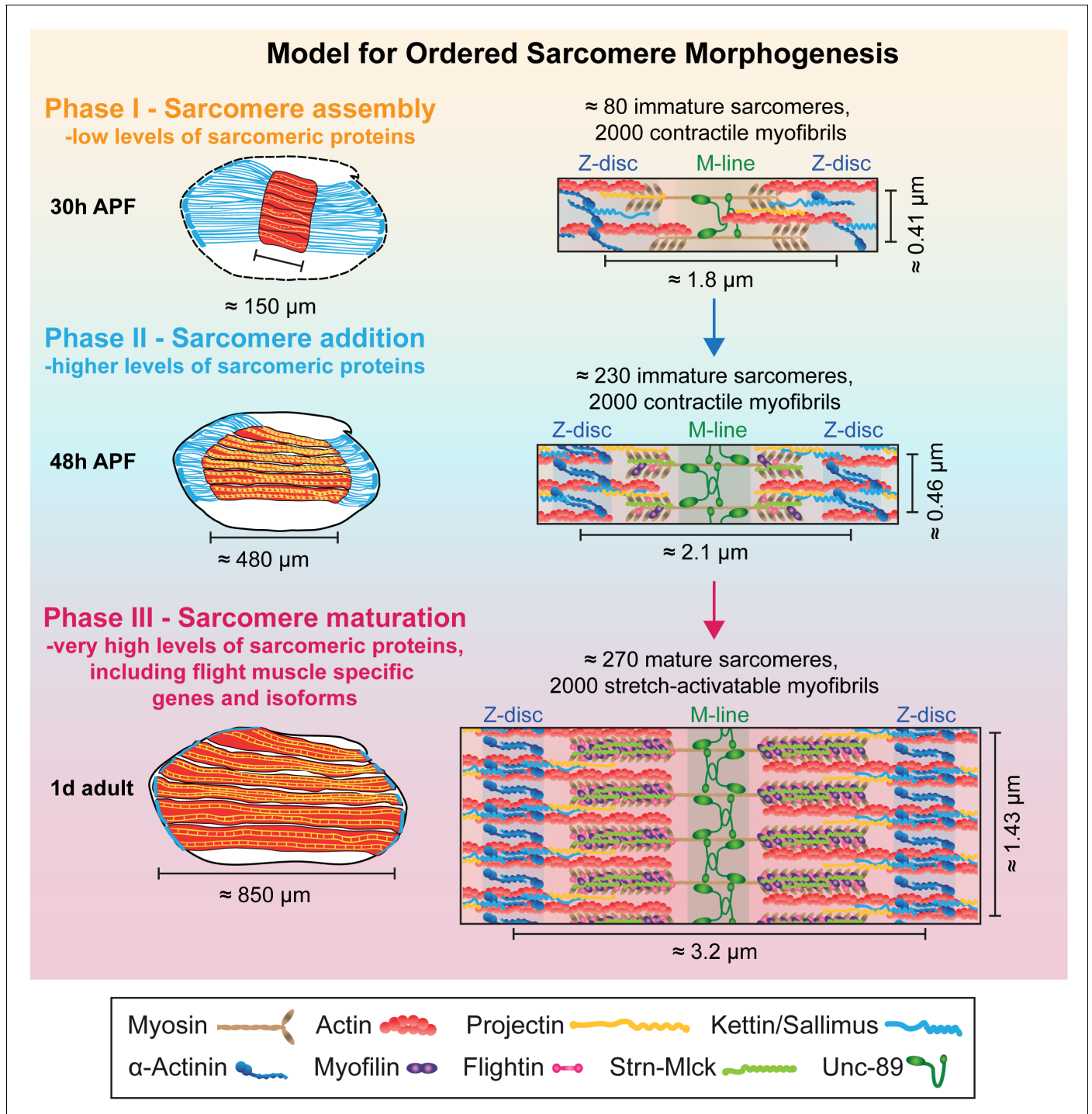


Figure 9. Model for ordered sarcomere morphogenesis. Phase 1 - Sarcomere assembly: Sarcomeric proteins are expressed at low levels, enabling the self-assembly of immature sarcomeres and myofibrils at around 30 hr APF. Each of the 2000 myofibrils contains about 80 immature sarcomeres. Phase 2 - Sarcomere addition: Sarcomere protein expression increases and each immature myofibril incorporates many new sarcomeres until about 48 hr APF. These immature sarcomeres contract spontaneously. Phase 3 - Sarcomere maturation: After 48 hr APF, sarcomere protein expression increases even more, including flight muscle specific proteins/isoforms, and all sarcomeres strongly grow in width and length. This enables the flight muscle to gain stretch-activation. Muscles are shown in red, tendons in blue. Structural proteins are illustrated as cartoons and are not drawn to scale. Induction of Actin, Mhc, Myofilin, Flightin, Strn-Mlck and Unc-89/Obscurin is shown here, expression of αActinin, Projectin and Kettin/Sallimus was shown by others (Bullard et al., 2006; Burkart et al., 2007; Katzemich et al., 2013; Orfanos et al., 2015; Weitkunat et al., 2014).

DOI: <https://doi.org/10.7554/eLife.34058.039>

spontaneously, likely because they acquired the stretch-activated mechanism of contraction described for mature *Drosophila* flight muscles (Bullard and Pastore, 2011; Josephson, 2006).

Our ordered sarcomere morphogenesis model is strongly supported by the observation that the number of myofibrils remains largely constant during the entire sarcomere morphogenesis period, suggesting that in flight muscles no new myofibrils are added after the initial assembly of immature myofibrils at about 30 hr APF. As all sarcomeres are present shortly after 48 hr APF, they all need to mature simultaneously to achieve their final pseudo-crystalline regularity.

Our model is further supported by previous studies. We and others found that immature myofibrils have a width of about 0.5 μm (Weitkunat et al., 2014), which corresponds to about four thick filaments across each myofibril at the EM level at 42 hr APF (at 22°C) (Reedy and Beall, 1993). This 'core' myofibril structure built until 48 hr APF, when most sarcomeres have formed, is expanded dramatically after 48 hr APF, reaching a mature width of 1.5 μm , corresponding to about 35 thick filaments across each myofibril at the EM-level (Reedy and Beall, 1993). Recent data showed that the 'core' myofibril structure built until 48 hr APF contains already highly ordered actin filaments, which gain even higher order to reach their pseudo-crystalline regularity at 90 hr APF (Loison et al., 2018). In total, each adult myofibril contains around 800 thick filaments per sarcomere (Gajewski and Schulz, 2010). The 'core' myofibril structure was also revealed by the preferential recruitment of over-expressed actin isoforms (Röper et al., 2005) and more importantly, by selective incorporation of a particular Mhc isoform that is only expressed at mid-stages of flight muscle development (Orfanos and Sparrow, 2013). This Mhc isoform expression switch coincides with the global transition in sarcomeric gene expression between the sarcomere assembly and the sarcomere maturation phases that we defined here. It also fits with the recent discovery that the formin family member Fhos is selectively required for actin filament elongation and recruitment of new actin filaments and thus myofibril diameter growth after 48 hr APF (Shwartz et al., 2016). Expression of Fhos is also induced after 30 hr APF. Fhos is a member of Mfuzz Cluster 28, another strongly induced cluster, underscoring the general relevance of the transcriptional transition for ordered sarcomerogenesis.

Regulated active sarcomere contractions

Mature indirect flight muscles employ a stretch-activated mechanism of muscle contraction, thus Ca^{2+} is not sufficient to trigger muscle contractions without additional mechanical stretch (Bullard and Pastore, 2011; Josephson, 2006). This is different to cross-striated body muscles of flies or mammals that contract synchronously with Ca^{2+} influx. Hence, it is intriguing that immature flight muscle myofibrils do in fact contract spontaneously, with the contraction frequencies and intensities increasing until 48 hr APF. It was recently proposed in *Drosophila* cross-striated abdominal muscles and in developing cross-striated zebrafish muscles that spontaneous contractions are important for the proper formation of the cross-striated pattern (Mazelet et al., 2016; Weitkunat et al., 2017). A similar role for contractions was found in C2C12 cells by stimulating the contractions optogenetically (Asano et al., 2015). This shows that spontaneous contractions are a necessary general feature for the assembly of cross-striated muscle fibers across species.

However, flight muscles are not cross-striated in the classical sense, but have a fibrillar organisation in which each myofibril remains isolated and is not aligned with its neighbouring myofibrils (Figure 5) (Josephson, 2006; Schönbauer et al., 2011). We can only speculate about the mechanism that prevents alignment of the myofibrils in the flight muscles, but it is likely related to their stretch-activated contraction mechanism. This mechanism prevents spontaneous twitching due to increased Ca^{2+} levels, because it additionally requires mechanical activation that can only occur during flight in the adult. Thus, flight muscle sarcomeres not only grow and mature their sarcomere structure, they also gain their stretch-activatability.

Continuous maintenance of muscle type-specific fate

We identified an important transition in gene expression between the early sarcomere assembly and the late sarcomere maturation phases. Similar large scale transcriptome changes have also been observed during postnatal stages of mouse (Brinegar et al., 2017), chicken (Zheng et al., 2009) and pig (Zhao et al., 2015) skeletal muscle development or during regeneration after injury in fish (Montfort et al., 2016) and mouse muscles (Warren et al., 2007), indicating that muscle maturation generally correlates with large scale transcriptional changes.

It is well established that general myogenic transcription factors, in particular Mef2, are continuously required in muscles for their normal differentiation (Sandmann et al., 2006; Soler et al., 2012). Mef2 regulates a suit of sarcomeric proteins in fly, fish and mouse muscle important for correct sarcomere assembly and maturation (Hinits and Hughes, 2007; Kelly et al., 2002; Potthoff et al., 2007; Stronach et al., 1999). In *Drosophila*, Mef2 cooperates with tissue-specific factors, such as CF2, to induce and fine-tune expression of structural genes (Gajewski and Schulz, 2010; García-Zaragoza et al., 2008; Tanaka et al., 2008). General transcriptional regulators, such as E2F, further contribute to high levels of muscle gene expression during myofibrillogenesis, in part through regulation of Mef2 itself (Zappia and Frolov, 2016). However, it is less clear if muscle type-specific identity genes are continuously required to execute muscle type-specific fate. Spalt major (Salm) is expressed after myoblast fusion in flight muscle myotubes and is required for all flight muscle type-specific gene expression: in its absence the fibrillar flight muscle is converted to tubular cross-striated muscle (Schönbauer et al., 2011; Spletter et al., 2015). Here we demonstrated that Salm is continuously required for correct sarcomere morphogenesis, as late *salm* knock-down leads to defects in sarcomere growth during the late sarcomere maturation phase, causing severe muscle atrophy in adults. It might do so by modifying the cooperation between Mef2 and E2F or by changing chromatin states, as vertebrate spalt homologs are recently discussed as epigenetic regulators (Yang, 2018; Zhang et al., 2015). However, Salm cannot be solely responsible for the transcriptional transition after 30 hr APF, as the transition still partially occurs in its absence.

Ordered sarcomere morphogenesis – a general mechanism?

Here we defined ordered phases of sarcomere morphogenesis in *Drosophila* flight muscles. Is this a general concept for sarcomere morphogenesis? Reviewing the literature, one finds that in other *Drosophila* muscle types which display a tubular cross-striated myofibril organisation, such as the fly abdominal muscles, the striated sarcomeres also first assemble and then grow in length (Pérez-Moreno et al., 2014; Weitkunat et al., 2017), suggesting a conserved mechanism. In developing zebrafish skeletal muscles, young myofibers present in younger somites show a short sarcomere length of about 1.2 μm , which increases to about 2.3 μm when somites and muscle fibers mature (Sanger et al., 2017; Sanger et al., 2009). Interestingly, sarcomere length as well as thick filament length increase simultaneously during fish muscle maturation, indicating that as in flight muscles, the length of all sarcomeres in one large muscle fiber is homogenous at a given time (Sanger et al., 2009). Similar results were obtained in mouse cardiomyocytes measuring myosin filament length at young (two somite) and older (13 somite) stages (Du et al., 2008) and even in human cardiomyocytes, in which myofibrils increase nearly threefold in width and become notably more organized and contractile from 52 to 127 days of gestation (Racca et al., 2016). These data suggest that sarcomeres generally may go through a series of ordered but overlapping developmental phases.

Interestingly, these changes in sarcomere morphology correlate with a switch in myosin heavy chain isoform expression changing from embryonic to neonatal to adult during skeletal muscle development (Schiaffino et al., 2015). Importantly, mutations in embryonic myosin (MYH3 in humans) result in severe congenital disorders characterised by multiple facial and limb contractures (Toydemir et al., 2006). As a similar ordered expression of myosin isoforms is also found during muscle regeneration after injury in adults (Ciciliot and Schiaffino, 2010; Schiaffino et al., 2015), we hypothesize that our sequential sarcomere morphogenesis model may also be applicable to vertebrate skeletal and possibly heart muscles. It will be a future challenge to identify possible feedback mechanisms that indicate the successful end of the sarcomere assembly phase or a possible re-entry into the sarcomere assembly phase during muscle regeneration or exercise induced muscle fiber growth. It is enticing to speculate that the assembling cytoskeleton itself would measure its assembly status and provide a mechanical feedback signal to modify the activity of muscle-specific transcription factors.

Materials and methods

Key resources table

Continued on next page

Continued

| Reagent type (species) or resource | Designation | Source or reference | Identifiers | Additional information |
|---|------------------------------|---------------------|---|-------------------------------------|
| Gene (<i>Drosophila melanogaster</i>) | spalt major; salm | NA | FLYB:FBgn0261648 | |
| Gene (<i>D. melanogaster</i>) | Stretchin-Mlck; Strn-Mlck | NA | FLYB:FBgn0265045 | |
| Genetic reagent (<i>D. melanogaster</i>) | w[1118] | Bloomington | BDSC:3605; FLYB:FBst0003605; RRID:BDSC_3605 | |
| Genetic reagent (<i>D. melanogaster</i>) | salmIR | PMID: 22094701 | VDRC:13302; FLYB:FBst0450930 | Flybase symbol: VDRC:v13302 |
| Genetic reagent (<i>D. melanogaster</i>) | KK101052 | PMID: 17625558 | VDRC:101052 | |
| Genetic reagent (<i>D. melanogaster</i>) | Act88F-GAL4 | PMID: 22008792 | | Source: Richard Cripps |
| Genetic reagent (<i>D. melanogaster</i>) | Strn-Mlck-MiMIC | Bloomington | FLYB:FBal0264439 | Flybase symbol:Strn-MlckMI02893 |
| Genetic reagent (<i>D. melanogaster</i>) | Strn-Mlck-IR | PMID: 21460824 | BDSC:31891; FLYB:FBti0130299; RRID:BDSC_31891 | Flybase symbol:P{TRiP.JF02170}attP2 |
| Genetic reagent (<i>D. melanogaster</i>) | Strn-Mlck-GFP, Isoform R | PMID: 25532219 | | Symbol: Strn4; |
| Genetic reagent (<i>D. melanogaster</i>) | Mhc-GFP | PMID: 26896675 | VDRC:318471 | Symbol: fTRG500; |
| Genetic reagent (<i>D. melanogaster</i>) | Mf-GFP | PMID: 26896675 | VDRC:318132 | Symbol: fTRG501; |
| Genetic reagent (<i>D. melanogaster</i>) | rhea-GFP | PMID: 26896675 | VDRC:318486 | Symbol: fTRG587; |
| Genetic reagent (<i>D. melanogaster</i>) | Fln-GFP | PMID: 26896675 | VDRC:318238 | Symbol: fTRG876; |
| Genetic reagent (<i>D. melanogaster</i>) | mys-GFP | PMID: 26896675 | VDRC:318285 | Symbol: fTRG932; |
| Genetic reagent (<i>D. melanogaster</i>) | β Tub60D-GFP | PMID: 26896675 | VDRC:318309 | Symbol: fTRG958; |
| Genetic reagent (<i>D. melanogaster</i>) | unc-89-GFP | PMID: 26896675 | VDRC:318326 | Symbol: fTRG1046; |
| Genetic reagent (<i>D. melanogaster</i>) | Act88F-GFP | PMID: 26896675 | VDRC:318362 | Symbol:fTRG10028; |
| Genetic reagent (<i>D. melanogaster</i>) | Him-nuc-eGFP | PMID: 19324085 | | Source: Michael V. Taylor |
| Genetic reagent (<i>D. melanogaster</i>) | Him-GAL4 | this paper | | |
| Genetic reagent (<i>D. melanogaster</i>) | UAS-BBM | PMID: 22446736 | | |
| Genetic reagent (<i>D. melanogaster</i>) | Him-GFP-Gma | this paper | | |
| Genetic reagent (<i>D. melanogaster</i>) | rhea-YPet | this paper | | |
| Genetic reagent (<i>D. melanogaster</i>) | kon-GFP | this paper | | |
| Genetic reagent (<i>D. melanogaster</i>) | Mef2-GAL4 | Bloomington | BDSC:27390; RRID:BDSC_27390 | |

Continued on next page

Continued

| Reagent type (species) or resource | Designation | Source or reference | Identifiers | Additional information |
|--|---|--------------------------------------|--------------------------|---|
| Genetic reagent (<i>D. melanogaster</i>) | UAS-GFP-Gma | PMID: 12324971 | | Source: Don Kiehart; Description |
| Antibody | guinea pig anti-Shot | PMID: 9832554 | | (1:500); Source: Talila Volk |
| Antibody | rat anti-Kettin (MAC155/Klg16) | Babraham Bioscience Technologies | Babraham: MAC_155(P6689) | (1:50) |
| Antibody | rabbit anti-GFP (ab290) | Abcam | Abcam:ab290 | (1:1000) |
| Antibody | rat anti-Bruno | PMID: 12591598 | | (1:500); Source: Anne Ephrussi |
| Antibody | rabbit anti-Salm | PMID: 7905822 | | (1:50); Source: Reinhard Schuh |
| Antibody | mouse anti- β PS-integrin (CF.6G11) | Developmental Studies Hybridoma Bank | DSHB:CF.6G11 | (1:500) |
| Antibody | rabbit anti-Twi | PMID: 2688897 | | (1:1000); Source: Siegfried Roth |
| Antibody | rabbit anti-Fln | PMID: 11134077 | | (1:50); Source: Jim Vigoreaux |
| Commercial assay or kit | fluorescent beads | ThermoFisher (Molecular Probes) | | OrderID: InSpeckTM Green Kit I-7219 |
| Commercial assay or kit | Dynabeads | Invitrogen | | OrderID: #610.06 |
| Commercial assay or kit | Superscript III First-Strand Synthesis System | Invitrogen | | OrderID: #18080-051 |
| Chemical compound, drug | Fluoroshield with DAPI | Sigma | | OrderID: #F6057 |
| Chemical compound, drug | Vectashield with DAPI | Biozol | | OrderID: VEC-H-1200 |
| Chemical compound, drug | Tissue-Tek O.C.T. | Weckert Labortechnik | | OrderID: 4583; Sakura Finetek |
| Chemical compound, drug | TriPure reagent | Roche | | OrderID: #11667157001 |
| Software, algorithm | Fiji (Image J) | PMID: 22743772 | | |
| Software, algorithm | MyofibrilJ | this paper | 1dbb0d4 | Source: https://imagej.net/MyofibrilJ |
| Software, algorithm | STAR | PMID: 23104886 | | |
| Software, algorithm | SAMtools | PMID: 19505943 | | |
| Software, algorithm | featureCounts | PMID: 24227677 | | |
| Software, algorithm | DESeq2 | PMID: 25516281 | | |
| Software, algorithm | R | R Project for Statistical Computing | RRID:SCR_001905 | |
| Software, algorithm | ComplexHeatmap | PMID: 27207943 | | |
| Software, algorithm | corrplot | GitHub | | Source: https://github.com/taiyun/corrplot |
| Software, algorithm | VennDiagram | PMID: 21269502 | | |
| Software, algorithm | plyr | DOI: 10.18637/jss.v040.i01 | | |
| Software, algorithm | reshape2 | DOI: 10.18637/jss.v021.i12 | | |
| Software, algorithm | ggplot2 | ISBN:978-0-387-98140-6 | | |
| Software, algorithm | RColorBrewer | Author: Erich Neuwirth; | | Source: https://cran.r-project.org/web/packages/RColorBrewer/index.html |
| Software, algorithm | Mfuzz | PMID: 16078370 | | |
| Software, algorithm | GO-Elite | PMID: 22743224 | | |

Fly strains

Fly stocks were maintained using standard culture conditions. Characterization of normal IFM sarcomere and fiber growth was performed in *w¹¹¹⁸* grown at 27°C. *salml* RNAi was performed with previously characterized GD3029 (referred to as *salmlR*) and KK181052 (Schönbauer et al., 2011) from VDRC (<http://stockcenter.vdrc.at>) (Dietzl et al., 2007) at 25°C using *Act88F-GAL4* to induce knock-down after 24 hr APF. *Act88F-GAL4* x *w¹¹¹⁸* served as control. The *Strn-Mlck-MiMIC* insertion MI02893 into IFM-specific IsoR (Bloomington stock 37038) and TRiP hairpin JF02170 were obtained from Bloomington (Ni et al., 2011). The *salml-EGFP* line was used to sort wing discs (Marty et al., 2014). Tagged genomic fosmid reporter fly lines include *strn4* (*Strn-Mlck-GFP*, Isoform R) (Spletter et al., 2015), fTRG500 (*Mhc-GFP*, Isoforms K, L, M), fTRG501 (*Mf-GFP*, Isoforms A, G, N), fTRG587 (*Rhea-GFP*, Isoforms B, E, F, G), fTRG876 (*Fln-GFP*), fTRG932 (*mys-GFP*), fTRG958 (*βTub60D-GFP*), fTRG1046 (*unc-89-GFP*), and fTRG10028 (*Act88F-GFP*) (Sarov et al., 2016).

To label myoblasts, we utilized the enhancer for *Holes-in-muscle* (*Him*), which is expressed in dividing myoblasts and promotes the progenitor fate. *Him-nuc-eGFP* flies were a gift of M. Taylor (Soler and Taylor, 2009). *Him-GAL4* flies were created by cloning an EcoRI to SacII fragment of the *Him* enhancer (Liotta et al., 2007) upstream of GAL4 into pStinger. UAS-BBM (UAS-palmCherry) (Förster and Luschnig, 2012) was driven with *Him-GAL4* to label myoblasts. *Him-GFP-Gma* flies were created by PCR amplifying GFP-Gma with Ascl and Pacl overhangs and then cloning downstream of the *Him* enhancer in pStinger to generate a gypsy insulator-*Him^{enh}*-Gma-GFP-SV40-gypsy insulator cassette.

The *rhea-YPet* line used to label muscle ends for live imaging of twitch events was generated by CRISPR-mediated gene editing at the endogenous locus (S.B.L and F.S., details will be published elsewhere). The *kon-GFP* line was generated by inserting GFP into the *kon* locus after its transmembrane domain using the genomic fosmid FlyFos021621, which was integrated using Φ-C31 into VK00033 (I. Ferreira and F.S., details will be published elsewhere).

Flight tests

Flight tests were performed as previously described (Schnorrer et al., 2010). *Act88F-GAL4* crosses were kept at 25°C, as higher temperatures negatively impacted flight ability, because of the very high GAL4 expression levels in this strain. Adult males were collected on CO₂ and recovered at least 24 hr at 25°C before testing. Flies were introduced into the top of a 1 m long cylinder divided into five zones. Those that landed in the top two zones were considered 'normal fliers', those in the next two zones 'weak fliers' and those that fell to the bottom of the cylinder 'flightless'.

Immuno-staining

Wing-discs were dissected from 3rd instar wandering larvae in 1x PBS and fixed in 4% PFA in PBS-T. Discs were stained as described below for anti-GFP. Adult and pupal flight muscles were dissected and stained as previously described (Weitkunat and Schnorrer, 2014). Briefly, early pupae (16–60 hr APF) were freed from the pupal case, fixed for 20 min. in 4% PFA in relaxing solution and washed in 0.5% PBS-Triton-X100 (PBS-T). 72 hr APF and older samples were cut sagittally with a microtome blade. All samples were blocked for at least 1 hr at RT in 5% normal goat serum in PBS-T and stained with primary antibodies overnight at 4°C. Primary antibodies include: guinea pig anti-Shot 1:500 (gift of T. Volk), rat anti-Kettin 1:50 (MAC155/Klg16, Babraham Institute), rabbit anti-GFP 1:1000 (ab290, Abcam), rat anti-Bruno 1:500 (Filardo and Ephrussi, 2003), rabbit anti-Salm 1:50 (Kühnlein et al., 1994), mouse anti-βPS-integrin 1:500 (CF.6G11, DSHB), rabbit anti-Twi 1:1000 (gift of Siegfried Roth) and rabbit anti-Fln 1:50 (Reedy et al., 2000) (gift of Jim Vigoreaux). Samples were washed three times in 0.5% PBS-T and incubated overnight at 4°C with secondary conjugated antibodies (1:500) from Invitrogen (Molecular Probes) including: Alexa488 goat anti-guinea pig IgG, Alexa488 donkey anti-rat IgG, Alexa488 goat anti-mouse IgG, Alexa488 goat anti-rabbit IgG, rhodamine-phalloidin, Alexa568 goat anti-rabbit IgG and Alexa633 goat anti-mouse IgG. Samples were washed three times in 0.5% PBS-T and mounted in Vectashield containing DAPI.

Cryosections

Head, wings and abdomen were removed from one day old *w¹¹¹⁸* flies and thoraxes were fixed overnight at 4°C in 4% PFA. For 30–90 hr APF samples, pupae were freed from the pupal case, poked 3–

5 times with an insect pin in the abdomen and fixed overnight at 4°C in 4% PFA. Thoraxes or pupae were then sunk in 30% sucrose in 0.5% PBS-T overnight at 4°C on a nutator. Thoraxes or pupae were embedded in Tissue-Tek O.C.T. (Sakura Finetek) in plastic moulds (#4566, Sakura Finetek) and frozen on dry ice. Blocks were sectioned at 30 µm on a cryostat (Microm vacutome). Sections were collected on glass slides coated with 1% gelatin +0.44 µM chromium potassium sulfate dodecahydrate to facilitate tissue adherence. Slides were post-fixed for 1 min. in 4% PFA in 0.5% PBS-T at RT, washed in 0.5% PBS-T, incubated with rhodamine-phalloidin for 2 hr at RT, washed three times in 0.5% PBS-T and mounted in Fluoroshield with DAPI (#F6057, Sigma).

Microscopy and image analysis

Images were acquired with a Zeiss LSM 780 confocal microscope equipped with an α Plan-APO-CHROMAT 100x oil immersion objective lens (NA 1.46). To compare if indicator protein expression replicates the mRNA-Seq expression dynamics, we imaged three time points from each expression profile with the same confocal settings. Laser gain and pinhole settings were set on the brightest sample and reused on remaining time points in the same imaging session. All samples were additionally stained with the same antibody mix on the same day and if possible in the same tube. Images were processed with Fiji (*Schindelin et al., 2012*) and Photoshop, and displayed using the 'Fire' look-up table.

Fiber length and fiber cross-sectional area were measured with freehand drawing tools in Fiji based on rhodamine-phalloidin staining. Sarcomere length, myofibril width, and myofibril diameter were measured automatically using a custom Fiji plug-in, MyofibrilJ, available from <https://imagej.net/MyofibrilJ> and code from <https://github.com/giocard/MyofibrilJ> (*Cardone, 2018*; copy archived at <https://github.com/elifesciences-publications/MyofibrilJ>). All measurements are based on rhodamine-phalloidin staining, except 34 hr APF sarcomere lengths, which are based on both rhodamine-phalloidin and Unc-89-GFP staining. 'Sarcomeres per fibril' was calculated as average individual fiber length divided by sarcomere length for fiber 3 or 4. 'Fibrils per fiber' was calculated as average number of fibrils per unit area multiplied by individual fiber cross sectional area.

For determining myofibril diameter, samples were imaged using a 3x optical zoom (50 nm pixel size). At least 20 cross-section images from different fibers for >10 flies were acquired for each time point. The number of fibrils per section and fibril diameter were determined with the tool 'analyze myofibrils crosswise' from MyofibrilJ (<https://imagej.net/MyofibrilJ>). In this tool, an initial estimate of the diameter is obtained by finding the first minimum in the radial average profile of the autocorrelation (*Goodman, 1996*) of the image. This estimate is used to calibrate the optimal crop area around all the cross-sections in the image, their position previously detected by finding the local intensity peaks. All of the detected cross-sections are then combined to obtain a noise-free average representation of the fibril section. Finally, the diameter is calculated by examining the radial profile of the average and measuring the full width where the intensity is 26% of the maximum range.

For determining sarcomere length and myofibril width, for each experiment between 10 and 25 images were acquired from more than 10 individual flies. From each image, nine non-overlapping regions of interest were selected, which were rotated to orient fibrils horizontally, when necessary. The tool 'analyze myofibrils lengthwise' from MyofibrilJ reports the sarcomere length (indicated as repeat) and myofibril width (indicated as thickness). Because of the periodic nature of sarcomere organization, their length is estimated by means of Fourier analysis, identifying the position of the peaks on the horizontal axis of the Fourier transformed imaged. Quality of the estimate was evaluated by visual inspection of the Fourier transformed image, overlaid with the peaks detected, as generated by the plug-in. Myofibrils width is estimated from the position of the first minimum in the vertical intensity profile of the autocorrelation of the image.

Live imaging of developmental spontaneous contractions was performed on a Leica SP5 confocal microscope. Prior to imaging, a window was cut in the pupal case, and pupae were mounted in slotted slides as previously described (*Lemke and Schnorner, 2018*; *Weitkunat and Schnorner, 2014*). At the specified developmental time point, IFMs were recorded every 0.65 s for 5 min. General movement within the thorax was distinguished from IFM-specific contraction, and each sample was scored for the number of single or double contractions observed per 5 min time window. Data were recorded in Excel and ANOVA was performed in GraphPad Prism to determine significant differences. Movies were assembled in Fiji (Image J), cropped and edited for length to highlight a selected twitch event.

Quantitative imaging of fosmid reporter intensity was performed at 30 hr APF, 48 hr APF, 72 hr APF, 90 hr APF and in 1 day adult in live IFM by normalizing to fluorescent beads (ThermoFisher (Molecular Probes), InSpeck Green Kit I-7219). IFMs were dissected from five flies, mounted with fluorescent microspheres (0.3% or 1% relative intensity, depending on the reporter intensity) in the supplied mounting medium and immediately imaged (within 20 min). Intensity measurements were obtained at 40x for at least 10 flies in regions where both IFM and at least three beads were visible. Control *Act88F-GAL4;; fosmid-GFP x w¹¹¹⁸* and *Act88F-GAL4;; fosmid-GFP x salmIR* (fossids used included *Strn-Mlck-GFP*, *Mhc-GFP*, *Fln-GFP*, and *Unc-89-GFP*) were imaged in the same imaging session. Relative fluorescence fiber to beads was calculated for each image in Fiji by averaging intensity for three fiber ROIs and three bead ROIs. Data were recorded in Excel and Student's t-test for significance and plotting were performed in GraphPad Prism.

mRNA-Seq

We previously published mRNA-Seq analysis of dissected IFMs from *Mef2-GAL4, UAS-GFP-Gma x w¹¹¹⁸* at 30 hr APF, 72 hr APF and 1d adult, and *Mef2-GAL4, UAS-GFP-Gma x salmIR* in 1d adult (Spletter et al., 2015). We expanded this analysis in the present study to include myoblasts from third instar larval wing discs (see below) and dissected IFMs from *Mef2-GAL4, UAS-GFP-Gma x w¹¹¹⁸* at 16, 24, 30, 48, 72, 90 hr APF and from 1 day adults as well as IFMs from *Mef2-GAL4, UAS-GFP-Gma x salmIR* flies at 24, 30, 72 hr APF and from 1 day adults. IFMs were dissected from groups of 15 flies in 30 min to minimize changes to the transcriptome, spun down in PBS for 5 min at 7500 rpm and immediately frozen in 100 μ l TriPure reagent (#11667157001, Roche) on dry ice. RNA was isolated after combining IFMs from 150 to 200 flies, with biological duplicates or triplicates for each time point.

Poly(A)+mRNA was purified using Dynabeads (#610.06, Invitrogen) and integrity was verified on a Bioanalyzer. mRNA was then fragmented by heating to 94°C for 210 s in fragmentation buffer (40 mM TrisOAc, 100 mM KOAc, 30 mM MgOAc₂). First-strand cDNA synthesis was performed with the Superscript III First-Strand Synthesis System (#18080-051, Invitrogen) using random hexamers. The second strand was synthesized with dUTP and submitted to the Vienna Biocenter Core Facilities (VBCF, <http://www.vbcf.ac.at>) for stranded library preparation according to standard Illumina protocols and sequenced as SR100 on an Illumina HiSeq2500. Libraries were multiplexed two to four per lane using TrueSeq adaptors.

Wing disc sorting and myoblast isolation

To perform mRNA-Seq on fusion competent myoblasts that will form the IFMs, we first dissected wing discs from wandering third instar larvae and manually cut the hinge away from the wing pouch. mRNA was isolated in TriPure reagent and sequenced as described above. We estimate this sample (Myo1) is ~50% myoblast, as the myoblasts form a nearly uniform layer over the underlying epithelial monolayer. To obtain a purer myoblast sample, we performed large-scale imaginal disc sorting followed by dissociation. We used particle sorting to isolate imaginal discs from *Him-GAL4, UAS-BBM* (UAS-palmCherry); *salm-EGFP* flies based on the green fluorescent signal. 10–12 ml of larvae in PBS were disrupted using a GentleMACS mixer (Miltenyl Biotec) and discs were collected through a mesh sieve (#0278 in, 25 opening, 710 μ m). Fat was removed by centrifugation for 10 min. at 1000 rpm at 4°C, discs were rinsed in PBS and then re-suspended in HBSS. Discs were further purified on a Ficoll gradient (25%:16%). Discs were then sorted on a Large Particle Flow Cytometer (BioSorter (FOCA1000), Union Biometrica, Inc.), obtaining 600–1000 discs per sample. Discs were spun for 5 min at 600 rcf in a Teflon Eppendorf tube and then re-suspended in the dissociation mixture (200 μ l of 10x Trypsin, 200 μ l HBSS, 50 μ l collagenase (10 mg/mL), 50 μ l dispase (10 mg/ml)). The tube was incubated for 10 min. at RT and then transferred to a thermal shaker for 30 min. at 25°C at 650 rpm. Myoblasts were filtered through a 35 μ m tube-cap filter and spun at 600 rcf for 5 min. to pellet the cells. Cells were re-suspended in HBSS for evaluation or frozen in TriPure reagent for RNA extraction. We obtained samples with ~90% purity based on counting the number of red fluorescent cells/non fluorescent+green fluorescent cells in three slide regions. mRNA was isolated in TriPure reagent and sequenced as described above, generating the Myo2 and Myo3 samples.

Analysis of RNA-Seq data

FASTA files were de-multiplexed and base called using Illumina software. Reads were trimmed using the FASTX-toolkit. Sequences were mapped using STAR (Dobin et al., 2013) to the *Drosophila* genome (BDGP6.80 from ENSEMBL). Mapped reads were sorted and indexed using SAMtools (Li et al., 2009), and then bam files were converted to bigwig files. Libraries were normalized based on library size and read-counts uploaded to the UCSC Browser for visualization (http://genome.ucsc.edu/cgi-bin/hgTracks?hgS_doOtherUser=submit&hgS_otherUserName=Ayeroslaviz&hgS_otherUserSessionName=IFMTP.leg.TCpaperHub1; http://genome.ucsc.edu/cgi-bin/hgTracks?hgS_doOtherUser=submit&hgS_otherUserName=Ayeroslaviz&hgS_otherUserSessionName=AretSalmIFMTP.TCpaperHub2).

Mapped sequences were run through featureCounts (Liao et al., 2014) and differential expression analysis was performed on the raw counts using DESeq2 (Love et al., 2014). We performed all pairwise comparisons across the time-course as well as between wild-type and *salmIR* samples (Supplementary file 1 and 4). All original and processed data can be found as supplemental data or in the Gene Expression Omnibus submission (accession number GSE107247). R packages employed in the analysis include ComplexHeatmap (Gu et al., 2016), CorrPlot (<https://github.com/taiyun/corr-plot>), VennDiagram (Chen and Boutros, 2011), plyr (Wickham, 2011), reshape2 (Wickham, 2007), ggplot2 (Wickham, 2009) and RColorBrewer (Neuwirth, 2015).

Genome-wide soft clustering was performed in R with Mfuzz (Futschik and Carlisle, 2005), using the DESeq2 normalized count values. We filtered the dataset to include all genes expressed at one time point or more, defining expression as >100 counts after normalization. We then set all count values < 100 to 0, to remove noise below the expression threshold. DESeq2 normalized data was standardized in Mfuzz to have a mean value of zero and a standard deviation of one, to remove the influence of expression magnitude and focus on the expression dynamics. We tested 'k' ranging from 10 to 256. We then performed consecutive rounds of clustering to obtain three independent replicates with similar numbers of iterations, ultimately selecting a final k = 40 clusters with iterations equal to 975, 1064 and 1118. We calculated a 'stability score' for each cluster by calculating how many genes are found in the same cluster in each run (Supplementary file 1). Figures are from the 1064 iterations dataset. Mfuzz cluster core expression profiles were calculated as the average standard-normal expression of all genes with a membership value greater than or equal to 0.8, and then core profiles were clustered in R using Euclidean distance and complete linkage.

Enrichment analysis was performed with GO-Elite (Zambon et al., 2012) using available Gene Ontology terms for *Drosophila*. We additionally defined user provided gene lists for transcription factors, RNA binding proteins, microtubule associated proteins, sarcomeric proteins, genes with an RNAi phenotype in muscle (Schnorrer et al., 2010), mitochondrial genes (<http://mitoXplorer.biochem.mpg.de>) and *salm* core fibrillar genes (Spletter et al., 2015). Full results and gene lists are available in Supplementary file 2. These user-supplied lists allowed us to define more complete gene sets relevant to a particular process or with a specific localization than available in existing GO terms. Analysis was performed with 5000 iterations to generate reliable significance values.

Data availability

Processed data from DESeq2, Mfuzz and GO-Elite are available in Supplementary file 1, 2, 4. mRNA-Seq data are publicly available from NCBI's Gene Expression Omnibus (GEO) under accession number GSE107247. mRNA-Seq read counts are further publicly accessible as track hubs in the UCSC Genome Browser at the following links: [1] (wild-type IFM time course) http://genome.ucsc.edu/cgi-bin/hgTracks?hgS_doOtherUser=submit&hgS_otherUserName=Ayeroslaviz&hgS_otherUserSessionName=IFMTP.leg.TCpaperHub1 and [2] (*salm* timecourse) http://genome.ucsc.edu/cgi-bin/hgTracks?hgS_doOtherUser=submit&hgS_otherUserName=Ayeroslaviz&hgS_otherUserSessionName=AretSalmIFMTP.TCpaperHub2. Fiji scripts for analysis of sarcomere length, myofibril width and myofibril diameter are available from <https://imagej.net/MyofibrilJ>. Raw data used to generate all plots presented in figure panels are available in the source data files for Figures 1, 5, 6, 7 and 8. Data on statistical test results are presented in Supplementary file 5.

Acknowledgements

We thank Irene Ferreira for constructing the tagged *kon-tiki* allele and the Bloomington and VDRC stock centers for fly stocks. We are grateful to Reinhard Fässler and Andreas Ladurner for generous support and to Bettina Stender for excellent technical assistance. We thank Elena Nikonova for initial analysis of the *Act88F-GAL4 x salmIR* phenotype and Sandra Esser for testing the *salm* KK181052 hairpin. We acknowledge the VBCF (Vienna, AT) for mRNA-sequencing and the Core Facility Bioimaging at the Max Planck Institute for Biochemistry and the LMU Biomedical Center (Martinsried, DE) for help with confocal image analysis. We thank Florian Marty for help with the BioSorter, and Alexander Stark for help setting-up the mRNA-sequencing. We thank Aynur Kaya-Copur and Wouter Koolhaas for helpful discussions, and Nuno Luis and Vincent Loreau for insightful comments on the manuscript. Our work was supported by the Max Planck Society and the CNRS; postdoctoral Humboldt, EMBO long-term (688–2011), and NIH-NRSA (5F32AR062477) fellowships (MLS), the Friedrich-Bauer Stiftung (MLS), the Center for Integrated Protein Science München (MLS), the Boehringer Ingelheim Fonds (SBL), a Career Development Award from the Human Frontier Science Program (FS), the EMBO Young Investigator Program (FS) and the European Research Council under the European Union's Seventh Framework Programme (FP/2007–2013)/ERC Grant 310939 (FS), the excellence initiative Aix-Marseille University AMIDEX (ANR-11-IDEX-0001–02) (FS), the ANR-ACHN (FS) and the LabEX-INFORM (ANR-11-LABX-0054) (FS) and France Bioimaging (ANR-10-INBS-04–01) (FS).

Additional information

Funding

| Funder | Grant reference number | Author |
|---|--------------------------------|---|
| Max-Planck-Gesellschaft | | Maria L Spletter Christiane Barz Assa Yeroslaviz Xu Zhang Sandra B Lemke Giovanni Cardone Bianca H Habermann Frank Schnorrer |
| European Molecular Biology Organization | EMBO-LTR 688-2011 | Maria L Spletter |
| Alexander von Humboldt-Stiftung | | Maria L Spletter |
| National Institute for Health Research | 5F32AR062477 | Maria L Spletter |
| Centre National de la Recherche Scientifique | | Xu Zhang Adrien Bonnard Bianca H Habermann Frank Schnorrer |
| Boehringer Ingelheim Fonds | | Sandra B Lemke |
| Center for Integrated Protein Science München | the Boehringer Ingelheim Fonds | Sandra B Lemke |
| Aix-Marseille Université | ANR-11-IDEX-0001-02 | Bianca H Habermann Frank Schnorrer |
| H2020 European Research Council | ERC Grant 310939 | Frank Schnorrer |
| Agence Nationale de la Recherche | ANR-11-LABX-0054 | Frank Schnorrer |
| European Molecular Biology Organization | EMBO-YIP | Frank Schnorrer |
| Agence Nationale de la Recherche | ANR-10-INBS-04- 01 | Frank Schnorrer |

Agence Nationale de la Recherche ANR ACHN

Frank Schnorrer

The funders had no role in study design, data collection and interpretation, or the decision to submit the work for publication.

Author contributions

Maria L Spletter, Data curation, Formal analysis, Validation, Investigation, Visualization, Methodology, Writing—original draft, Writing—review and editing; Christiane Barz, Data curation, Investigation; Assa Yeroslaviz, Software, Formal analysis, Visualization, Methodology, Writing—review and editing; Xu Zhang, Sandra B Lemke, Data curation, Formal analysis, Investigation, Writing—review and editing; Adrien Bonnard, Formal analysis, Investigation, Visualization; Erich Brunner, Investigation, Methodology; Giovanni Cardone, Software, Writing—review and editing; Konrad Basler, Funding acquisition, Methodology, Writing—review and editing; Bianca H Habermann, Software, Formal analysis, Funding acquisition, Validation, Visualization, Methodology, Writing—review and editing; Frank Schnorrer, Conceptualization, Supervision, Funding acquisition, Validation, Writing—original draft, Writing—review and editing

Author ORCIDs

Maria L Spletter  <http://orcid.org/0000-0002-2068-3350>

Xu Zhang  <http://orcid.org/0000-0002-1628-9895>

Sandra B Lemke  <http://orcid.org/0000-0002-3817-4351>

Giovanni Cardone  <http://orcid.org/0000-0003-4712-1451>

Bianca H Habermann  <http://orcid.org/0000-0002-2457-7504>

Frank Schnorrer  <http://orcid.org/0000-0002-9518-7263>

Decision letter and Author response

Decision letter <https://doi.org/10.7554/eLife.34058.051>

Author response <https://doi.org/10.7554/eLife.34058.052>

Additional files

Supplementary files

- Supplementary file 1. mRNA-Seq raw data The file includes multiple tabs containing the raw or input counts data from bioinformatics analysis, as well as a key to all original data provided in the supplementary tables. This table includes mRNA-Seq counts data, DESeq2 normalized counts data and standard normal counts data used for Mfuzz clustering for wild-type and *salmIR* IFM time points. The averaged core expression profiles for each Mfuzz cluster are also listed.

DOI: <https://doi.org/10.7554/eLife.34058.040>

- Supplementary file 2. GO-Elite analysis data. This table includes multiple tabs containing the GO-Elite analysis of enrichments in Mfuzz clusters as well as genes up- or down-regulated from 30–72 hr APF and between wild-type and *salmIR* IFM. It also contains a complete list of all genes included in the 'User Defined' gene sets.

DOI: <https://doi.org/10.7554/eLife.34058.041>

- Supplementary file 3. Summary of sarcomere and myofibril quantifications This table includes a numerical summary of quantification values reported graphically in **Figures 5, 7 and 8**. Quantifications of sarcomere length, myofibril width and myofibril diameter were performed with the MyofibrilJ script (see Materials and methods). Fiber length and cross-sectional area measurements were performed in Fiji/Image J.

DOI: <https://doi.org/10.7554/eLife.34058.042>

- Supplementary file 4. DESeq2 pairwise differential expression analysis This table contains multiple tabs containing the output data from DESeq2 differential expression analysis between sequential IFM development time points, from 30 to 72 hr APF as well as between WT and *salmIR* IFM.

DOI: <https://doi.org/10.7554/eLife.34058.043>

- Supplementary file 5. Statistical Data This table includes multiple tabs containing the statistical and calculation data for the different panels of **Figures 1, 5, 6, 7 and 8**.

DOI: <https://doi.org/10.7554/eLife.34058.044>

- Transparent reporting form

DOI: <https://doi.org/10.7554/eLife.34058.045>

Data availability

Processed data from DESeq2, Mfuzz and GO-Elite are available in Supplementary Files 1, 2, 4. mRNA-Seq data are publicly available from NCBI's Gene Expression Omnibus (GEO) under accession number GSE107247. Fiji scripts for analysis of sarcomere length, myofibril width and myofibril diameter are available from <https://imagej.net/MyofibrilJ>. Raw data used to generate all plots presented in figure panels are available in the source data files for Figures 1, 5, 6, 7 and 8. Data on statistical test results are presented in Supplementary File 5.

The following dataset was generated:

| Author(s) | Year | Dataset title | Dataset URL | Database, license, and accessibility information |
|--|------|--|---|---|
| Spletter ML, Schnorrer F, Yeroslaviz A, Stark A, Habermann B | 2017 | Systematic transcriptomics reveals a biphasic mode of sarcomere morphogenesis in flight muscles regulated by Spalt | https://www.ncbi.nlm.nih.gov/geo/query/acc.cgi?acc=GSE107247 | Publicly available at the NCBI Gene Expression Omnibus (accession no: GSE107247). |

The following previously published dataset was used:

| Author(s) | Year | Dataset title | Dataset URL | Database, license, and accessibility information |
|---|------|--|---|--|
| Spletter ML, Schnorrer F, Gerlach D, Stark A, Yeroslaviz A, Habermann B | 2014 | The RNA binding protein Arrest (Aret) regulates myofibril maturation in Drosophila flight muscle | https://www.ncbi.nlm.nih.gov/geo/query/acc.cgi?acc=GSE63707 | Publicly available at the NCBI Gene Expression Omnibus (accession no: GSE63707). |

References

- Anant S, Roy S, VijayRaghavan K. 1998. Twist and notch negatively regulate adult muscle differentiation in *Drosophila*. *Development* **125**:1361–1369. PMID: 9502718
- Asano T, Ishizuka T, Morishima K, Yawo H. 2015. Optogenetic induction of contractile ability in immature C2C12 myotubes. *Scientific Reports* **5**:8317. DOI: <https://doi.org/10.1038/srep08317>, PMID: 25661648
- Bate M, Rushton E, Currie DA. 1991. Cells with persistent twist expression are the embryonic precursors of adult muscles in *Drosophila*. *Development* **113**:79–89. PMID: 1765010
- Brinegar AE, Xia Z, Loehr JA, Li W, Rodney GG, Cooper TA. 2017. Extensive alternative splicing transitions during postnatal skeletal muscle development are required for calcium handling functions. *eLife* **6**:e27192. DOI: <https://doi.org/10.7554/eLife.27192>, PMID: 28826478
- Bryantsev AL, Baker PW, Lovato TL, Jaramillo MS, Cripps RM. 2012. Differential requirements for myocyte enhancer Factor-2 during adult myogenesis in *Drosophila*. *Developmental Biology* **361**:191–207. DOI: <https://doi.org/10.1016/j.ydbio.2011.09.031>, PMID: 22008792
- Bullard B, Burkart C, Labeit S, Leonard K. 2006. The function of elastic proteins in the oscillatory contraction of insect flight muscle. *Journal of Muscle Research and Cell Motility* **26**:479–485. DOI: <https://doi.org/10.1007/s10974-005-9032-7>
- Bullard B, Pastore A. 2011. Regulating the contraction of insect flight muscle. *Journal of Muscle Research and Cell Motility* **32**:303–313. DOI: <https://doi.org/10.1007/s10974-011-9278-1>, PMID: 22105701
- Burkart C, Qiu F, Brendel S, Benes V, Hååg P, Labeit S, Leonard K, Bullard B. 2007. Modular proteins from the *Drosophila* sallimus (sls) gene and their expression in muscles with different extensibility. *Journal of Molecular Biology* **367**:953–969. DOI: <https://doi.org/10.1016/j.jmb.2007.01.059>, PMID: 17316686
- Cardone G. 2018. *MyofibrilJ*. GitHub. 033d83c. <https://github.com/giocard/MyofibrilJ>
- Chen H, Boutros PC. 2011. VennDiagram: a package for the generation of highly-customizable venn and Euler diagrams in R. *BMC Bioinformatics* **12**:35. DOI: <https://doi.org/10.1186/1471-2105-12-35>, PMID: 21269502
- Ciciliot S, Schiaffino S. 2010. Regeneration of mammalian skeletal muscle. basic mechanisms and clinical implications. *Current Pharmaceutical Design* **16**:906–914. PMID: 20041823

- Clark IE, Dodson MW, Jiang C, Cao JH, Huh JR, Seol JH, Yoo SJ, Hay BA, Guo M. 2006. Drosophila pink1 is required for mitochondrial function and interacts genetically with parkin. *Nature* **441**:1162–1166. DOI: <https://doi.org/10.1038/nature04779>, PMID: 16672981
- Dietzl G, Chen D, Schnorrer F, Su KC, Barinova Y, Fellner M, Gasser B, Kinsey K, Oettel S, Scheiblaue S, Couto A, Marra V, Keleman K, Dickson BJ. 2007. A genome-wide transgenic RNAi library for conditional gene inactivation in Drosophila. *Nature* **448**:151–156. DOI: <https://doi.org/10.1038/nature05954>, PMID: 17625558
- Dobin A, Davis CA, Schlesinger F, Drenkow J, Zaleski C, Jha S, Batut P, Chaisson M, Gingeras TR. 2013. STAR: ultrafast universal RNA-seq aligner. *Bioinformatics* **29**:15–21. DOI: <https://doi.org/10.1093/bioinformatics/bts635>, PMID: 23104886
- Drexler HC, Ruhs A, Konzer A, Mendler L, Bruckskotten M, Looso M, Günther S, Boettger T, Krüger M, Braun T. 2012. On marathons and sprints: an integrated quantitative proteomics and transcriptomics analysis of differences between slow and fast muscle fibers. *Molecular & Cellular Proteomics* **11**:M111.010801. DOI: <https://doi.org/10.1074/mcp.M111.010801>, PMID: 22210690
- Du A, Sanger JM, Sanger JW. 2008. Cardiac myofibrillogenesis inside intact embryonic hearts. *Developmental Biology* **318**:236–246. DOI: <https://doi.org/10.1016/j.ydbio.2008.03.011>, PMID: 18455713
- Dutta D, Anant S, Ruiz-Gomez M, Bate M, VijayRaghavan K. 2004. Founder myoblasts and fibre number during adult myogenesis in Drosophila. *Development* **131**:3761–3772. DOI: <https://doi.org/10.1242/dev.01249>, PMID: 15262890
- Ehler E, Gautel M. 2008. The sarcomere and sarcomerogenesis. *Advances in Experimental Medicine and Biology* **642**:1–14. PMID: 19181089
- Fernandes J, Bate M, VijayRaghavan K. 1991. Development of the indirect flight muscles of Drosophila. *Development* **113**:67–77. PMID: 1765009
- Filardo P, Ephrussi A. 2003. Bruno regulates gurken during Drosophila oogenesis. *Mechanisms of Development* **120**:289–297. DOI: [https://doi.org/10.1016/S0925-4773\(02\)00454-9](https://doi.org/10.1016/S0925-4773(02)00454-9), PMID: 12591598
- Förster D, Luschnig S. 2012. Src42A-dependent polarized cell shape changes mediate epithelial tube elongation in Drosophila. *Nature Cell Biology* **14**:526–534. DOI: <https://doi.org/10.1038/ncb2456>, PMID: 22446736
- Futschik ME, Carlisle B. 2005. Noise-robust soft clustering of gene expression time-course data. *Journal of Bioinformatics and Computational Biology* **03**:965–988. DOI: <https://doi.org/10.1142/S0219720005001375>
- Gajewski KM, Schulz RA. 2010. CF2 represses actin 88F gene expression and maintains filament balance during indirect flight muscle development in Drosophila. *PLoS ONE* **5**:e10713. DOI: <https://doi.org/10.1371/journal.pone.0010713>, PMID: 20520827
- García-Zaragoza E, Mas JA, Vivar J, Arredondo JJ, Cervera M. 2008. CF2 activity and enhancer integration are required for proper muscle gene expression in Drosophila. *Mechanisms of Development* **125**:617–630. DOI: <https://doi.org/10.1016/j.mod.2008.03.003>, PMID: 18448314
- Gautel M, Djinić-Carugo K. 2016. The sarcomeric cytoskeleton: from molecules to motion. *Journal of Experimental Biology* **219**:135–145. DOI: <https://doi.org/10.1242/jeb.124941>, PMID: 26792323
- Gokhin DS, Fowler VM. 2013. A two-segment model for thin filament architecture in skeletal muscle. *Nature Reviews Molecular Cell Biology* **14**:113–119. DOI: <https://doi.org/10.1038/nrm3510>
- Goodman JW. 1996. *Introduction to Fourier Optics*. 2nd. McGraw-Hill.
- Gu Z, Eils R, Schlesner M. 2016. Complex heatmaps reveal patterns and correlations in multidimensional genomic data. *Bioinformatics* **32**:2847–2849. DOI: <https://doi.org/10.1093/bioinformatics/btw313>, PMID: 27207943
- Hinitz Y, Hughes SM. 2007. Mef2s are required for thick filament formation in nascent muscle fibres. *Development* **134**:2511–2519. DOI: <https://doi.org/10.1242/dev.007088>, PMID: 17537787
- Josephson R. 2006. Comparative Physiology of Insect Flight Muscle. In: Josephson R (Ed). *Nature's Versatile Engine: Insect Flight Muscle Inside and Out*. Georgetown, TX: Landes Bioscience. p. 35–43.
- Katzemich A, Liao KA, Czerniecki S, Schöck F. 2013. Alp/Enigma family proteins cooperate in Z-disc formation and myofibril assembly. *PLoS Genetics* **9**:e1003342. DOI: <https://doi.org/10.1371/journal.pgen.1003342>, PMID: 23505387
- Kelly KK, Meadows SM, Cripps RM. 2002. Drosophila MEF2 is a direct regulator of Actin57B transcription in cardiac, skeletal, and visceral muscle lineages. *Mechanisms of Development* **110**:39–50. DOI: [https://doi.org/10.1016/S0925-4773\(01\)00586-X](https://doi.org/10.1016/S0925-4773(01)00586-X), PMID: 11744367
- Kumar L, Futschik M. 2007. Mfuzz: a software package for soft clustering of microarray data. *Bioinformatics* **23**:5–7. DOI: <https://doi.org/10.1093/bioinformatics/btl100>, PMID: 18084642
- Kühnlein RP, Frommer G, Friedrich M, Gonzalez-Gaitan M, Weber A, Wagner-Bernholz JF, Gehring WJ, Jäckle H, Schuh R. 1994. Spalt encodes an evolutionarily conserved zinc finger protein of novel structure which provides homeotic gene function in the head and tail region of the Drosophila embryo. *The EMBO Journal* **13**:168–179. PMID: 7905822
- Lang F, Aravamudan S, Nolte H, Türk C, Hölper S, Müller S, Günther S, Blaauw B, Braun T, Krüger M. 2017. Dynamic changes in the mouse skeletal muscle proteome during denervation-induced atrophy. *Disease Models & Mechanisms* **10**:881–896. DOI: <https://doi.org/10.1242/dmm.028910>, PMID: 28546288
- Lange S, Ehler E, Gautel M. 2006. From A to Z and back? multicompartment proteins in the sarcomere. *Trends in Cell Biology* **16**:11–18. DOI: <https://doi.org/10.1016/j.tcb.2005.11.007>, PMID: 16337382
- Leiss D, Hinz U, Gasch A, Mertz R, Renkawitz-Pohl R. 1988. Beta 3 tubulin expression characterizes the differentiating mesodermal germ layer during Drosophila embryogenesis. *Development* **104**:525–531. PMID: 3077351
- Lemke SB, Schnorrer F. 2017. Mechanical forces during muscle development. *Mechanisms of Development* **144**:92–101. DOI: <https://doi.org/10.1016/j.mod.2016.11.003>, PMID: 27913119

- Lemke SB**, Schnorrer F. 2018. In vivo imaging of Muscle-tendon morphogenesis in *Drosophila* pupae. *Journal of Visualized Experiments: JoVE*:e57312. DOI: <https://doi.org/10.3791/57312>
- Li H**, Handsaker B, Wysoker A, Fennell T, Ruan J, Homer N, Marth G, Abecasis G, Durbin R, 1000 Genome Project Data Processing Subgroup. 2009. The Sequence Alignment/Map format and SAMtools. *Bioinformatics* **25**:2078–2079. DOI: <https://doi.org/10.1093/bioinformatics/btp352>
- Liao Y**, Smyth GK, Shi W. 2014. featureCounts: an efficient general purpose program for assigning sequence reads to genomic features. *Bioinformatics* **30**:923–930. DOI: <https://doi.org/10.1093/bioinformatics/btt656>, PMID: 24227677
- Liotta D**, Han J, Elgar S, Garvey C, Han Z, Taylor MV. 2007. The him gene reveals a balance of inputs controlling muscle differentiation in *Drosophila*. *Current Biology* **17**:1409–1413. DOI: <https://doi.org/10.1016/j.cub.2007.07.039>, PMID: 17702578
- Llewellyn ME**, Barretto RP, Delp SL, Schnitzer MJ. 2008. Minimally invasive high-speed imaging of sarcomere contractile dynamics in mice and humans. *Nature* **454**:784–788. DOI: <https://doi.org/10.1038/nature07104>, PMID: 18600262
- Loison O**, Weitkunat M, Kaya-Çopur A, Nascimento Alves C, Matzat T, Spletter ML, Luschnig S, Brasselet S, Lenne PF, Schnorrer F. 2018. Polarization-resolved microscopy reveals a muscle myosin motor-independent mechanism of molecular actin ordering during sarcomere maturation. *PLOS Biology* **16**:e2004718. DOI: <https://doi.org/10.1371/journal.pbio.2004718>, PMID: 29702642
- Love MI**, Huber W, Anders S. 2014. Moderated estimation of fold change and dispersion for RNA-seq data with DESeq2. *Genome Biology* **15**:550. DOI: <https://doi.org/10.1186/s13059-014-0550-8>, PMID: 25516281
- Marty F**, Rockel-Bauer C, Simigdala N, Brunner E, Basler K. 2014. Large-scale imaginal disc sorting: a protocol for "omics"-approaches. *Methods* **68**:260–264. DOI: <https://doi.org/10.1016/j.ymeth.2014.04.005>, PMID: 24736056
- Mazelet L**, Parker MO, Li M, Arner A, Ashworth R. 2016. Role of active contraction and tropomodulins in regulating actin filament length and sarcomere structure in developing zebrafish skeletal muscle. *Frontiers in Physiology* **7**:91. DOI: <https://doi.org/10.3389/fphys.2016.00091>, PMID: 27065876
- Montfort J**, Le Cam A, Gabillard JC, Rescan PY. 2016. Gene expression profiling of trout regenerating muscle reveals common transcriptional signatures with hyperplastic growth zones of the post-embryonic myotome. *BMC Genomics* **17**:810. DOI: <https://doi.org/10.1186/s12864-016-3160-x>, PMID: 27756225
- Neuwirth E**. 2015. Package "RColorBrewer". 1–5.
- Ni JQ**, Zhou R, Czech B, Liu LP, Holderbaum L, Yang-Zhou D, Shim HS, Tao R, Handler D, Karpowicz P, Binari R, Booker M, Brennecke J, Perkins LA, Hannon GJ, Perrimon N. 2011. A genome-scale shRNA resource for transgenic RNAi in *Drosophila*. *Nature Methods* **8**:405–407. DOI: <https://doi.org/10.1038/nmeth.1592>, PMID: 21460824
- Orfanos Z**, Leonard K, Elliott C, Katzemich A, Bullard B, Sparrow J. 2015. Sallimus and the dynamics of sarcomere assembly in *Drosophila* flight muscles. *Journal of Molecular Biology* **427**:2151–2158. DOI: <https://doi.org/10.1016/j.jmb.2015.04.003>, PMID: 25868382
- Orfanos Z**, Sparrow JC. 2013. Myosin isoform switching during assembly of the *Drosophila* flight muscle thick filament lattice. *Journal of Cell Science* **126**:139–148. DOI: <https://doi.org/10.1242/jcs.110361>, PMID: 23178940
- Pérez-Moreno JJ**, Bischoff M, Martín-Bermudo MD, Estrada B. 2014. The conserved transmembrane proteoglycan perdido/Kon-tiki is essential for myofibrillogenesis and sarcomeric structure in *Drosophila*. *Journal of Cell Science* **127**:3162–3173. DOI: <https://doi.org/10.1242/jcs.150425>, PMID: 24794494
- Potthoff MJ**, Arnold MA, McAnally J, Richardson JA, Bassel-Duby R, Olson EN. 2007. Regulation of skeletal muscle sarcomere integrity and postnatal muscle function by Mef2c. *Molecular and Cellular Biology* **27**:8143–8151. DOI: <https://doi.org/10.1128/MCB.01187-07>, PMID: 17875930
- Racca AW**, Klaiman JM, Pioner JM, Cheng Y, Beck AE, Moussavi-Harami F, Bamshad MJ, Regnier M. 2016. Contractile properties of developing human fetal cardiac muscle. *The Journal of Physiology* **594**:437–452. DOI: <https://doi.org/10.1113/JP271290>, PMID: 26460603
- Reedy MC**, Beall C. 1993. Ultrastructure of developing flight muscle in *Drosophila*. I. assembly of myofibrils. *Developmental Biology* **160**:443–465. DOI: <https://doi.org/10.1006/dbio.1993.1320>, PMID: 8253277
- Reedy MC**, Bullard B, Vigoreaux JO. 2000. Flightin is essential for thick filament assembly and sarcomere stability in *Drosophila* flight muscles. *The Journal of Cell Biology* **151**:1483–1500. DOI: <https://doi.org/10.1083/jcb.151.7.1483>, PMID: 11134077
- Regev GJ**, Kim CW, Tomiya A, Lee YP, Ghofrani H, Garfin SR, Lieber RL, Ward SR. 2011. Psoas muscle architectural design, in vivo sarcomere length range, and passive tensile properties support its role as a lumbar spine stabilizer. *Spine* **36**:E1666–E1674. DOI: <https://doi.org/10.1097/BRS.0b013e31821847b3>, PMID: 21415810
- Röper K**, Mao Y, Brown NH. 2005. Contribution of sequence variation in *Drosophila* actins to their incorporation into actin-based structures in vivo. *Journal of Cell Science* **118**:3937–3948. DOI: <https://doi.org/10.1242/jcs.02517>, PMID: 16105877
- Sandmann T**, Jensen LJ, Jakobsen JS, Karzynski MM, Eichenlaub MP, Bork P, Furlong EE. 2006. A temporal map of transcription factor activity: mef2 directly regulates target genes at all stages of muscle development. *Developmental Cell* **10**:797–807. DOI: <https://doi.org/10.1016/j.devcel.2006.04.009>, PMID: 16740481
- Sanger JW**, Wang J, Fan Y, White J, Mi-Mi L, Dube DK, Sanger JM, Pruyne D. 2017. Assembly and maintenance of myofibrils in striated muscle. *Handbook of Experimental Pharmacology* **235**:39–75. DOI: https://doi.org/10.1007/164_2016_53, PMID: 27832381

- Sanger JW, Wang J, Holloway B, Du A, Sanger JM. 2009. Myofibrillogenesis in skeletal muscle cells in zebrafish. *Cell Motility and the Cytoskeleton* **66**:556–566. DOI: <https://doi.org/10.1002/cm.20365>, PMID: 19382198
- Sarov M, Barz C, Jambor H, Hein MY, Schmied C, Suchold D, Stender B, Janosch S, KJ VV, Krishnan RT, Krishnamoorthy A, Ferreira IR, Ejsmont RK, Finkl K, Hasse S, Kämpfer P, Plewka N, Vinis E, Schloissnig S, Knust E, et al. 2016. A genome-wide resource for the analysis of protein localisation in *Drosophila*. *eLife* **5**:e12068. DOI: <https://doi.org/10.7554/eLife.12068>, PMID: 26896675
- Schiaffino S, Reggiani C. 2011. Fiber types in mammalian skeletal muscles. *Physiological Reviews* **91**:1447–1531. DOI: <https://doi.org/10.1152/physrev.00031.2010>, PMID: 22013216
- Schiaffino S, Rossi AC, Smerdu V, Leinwand LA, Reggiani C. 2015. Developmental myosins: expression patterns and functional significance. *Skeletal Muscle* **5**:22. DOI: <https://doi.org/10.1186/s13395-015-0046-6>, PMID: 26180627
- Schindelin J, Arganda-Carreras I, Frise E, Kaynig V, Longair M, Pietzsch T, Preibisch S, Rueden C, Saalfeld S, Schmid B, Tinevez JY, White DJ, Hartenstein V, Eliceiri K, Tomancak P, Cardona A. 2012. Fiji: an open-source platform for biological-image analysis. *Nature Methods* **9**:676–682. DOI: <https://doi.org/10.1038/nmeth.2019>, PMID: 22743772
- Schnorrer F, Kalchauer I, Dickson BJ. 2007. The transmembrane protein Kon-tiki couples to dgrip to mediate myotube targeting in *Drosophila*. *Developmental Cell* **12**:751–766. DOI: <https://doi.org/10.1016/j.devcel.2007.02.017>, PMID: 17488626
- Schnorrer F, Schönbauer C, Langer CC, Dietzl G, Novatchkova M, Schernhuber K, Fellner M, Azaryan A, Radolf M, Stark A, Keleman K, Dickson BJ. 2010. Systematic genetic analysis of muscle morphogenesis and function in *Drosophila*. *Nature* **464**:287–291. DOI: <https://doi.org/10.1038/nature08799>, PMID: 20220848
- Schönbauer C, Distler J, Jährling N, Radolf M, Dodt HU, Frasch M, Schnorrer F. 2011. Spalt mediates an evolutionarily conserved switch to fibrillar muscle fate in insects. *Nature* **479**:406–409. DOI: <https://doi.org/10.1038/nature10559>, PMID: 22094701
- Sevdali M, Kumar V, Peckham M, Sparrow J. 2013. Human congenital myopathy actin mutants cause myopathy and alter Z-disc structure in *Drosophila* flight muscle. *Neuromuscular Disorders* **23**:243–255. DOI: <https://doi.org/10.1016/j.nmd.2012.11.013>, PMID: 23294764
- Shwartz A, Dhanyasi N, Schejter ED, Shilo B-Z. 2016. The *Drosophila* formin fhos is a primary mediator of sarcomeric thin-filament array assembly. *eLife* **5**:D786. DOI: <https://doi.org/10.7554/eLife.16540>
- Soler C, Han J, Taylor MV. 2012. The conserved transcription factor Mef2 has multiple roles in adult *Drosophila* musculature formation. *Development* **139**:1270–1275. DOI: <https://doi.org/10.1242/dev.077875>, PMID: 22357930
- Soler C, Taylor MV. 2009. The him gene inhibits the development of *Drosophila* flight muscles during metamorphosis. *Mechanisms of Development* **126**:595–603. DOI: <https://doi.org/10.1016/j.mod.2009.03.003>, PMID: 19324085
- Sparrow JC, Schöck F. 2009. The initial steps of myofibril assembly: integrins pave the way. *Nature Reviews Molecular Cell Biology* **10**:293–298. DOI: <https://doi.org/10.1038/nrm2634>, PMID: 19190670
- Spletter ML, Barz C, Yeroslaviz A, Schönbauer C, Ferreira IR, Sarov M, Gerlach D, Stark A, Habermann BH, Schnorrer F. 2015. The RNA-binding protein arrest (Bruno) regulates alternative splicing to enable myofibril maturation in *Drosophila* flight muscle. *EMBO Reports* **16**:178–191. DOI: <https://doi.org/10.15252/embr.201439791>, PMID: 25532219
- Spletter ML, Schnorrer F. 2014. Transcriptional regulation and alternative splicing cooperate in muscle fiber-type specification in flies and mammals. *Experimental Cell Research* **321**:90–98. DOI: <https://doi.org/10.1016/j.yexcr.2013.10.007>, PMID: 24145055
- Stronach BE, Renfranz PJ, Lilly B, Beckerle MC. 1999. Muscle LIM proteins are associated with muscle sarcomeres and require dMEF2 for their expression during *Drosophila* myogenesis. *Molecular Biology of the Cell* **10**:2329–2342. DOI: <https://doi.org/10.1091/mbc.10.7.2329>, PMID: 10397768
- Syme DA, Josephson RK. 2002. How to build fast muscles: synchronous and asynchronous designs. *Integrative and Comparative Biology* **42**:762–770. DOI: <https://doi.org/10.1093/icb/42.4.762>, PMID: 21708773
- Tanaka KK, Bryantsev AL, Cripps RM. 2008. Myocyte enhancer factor 2 and chorion factor 2 collaborate in activation of the myogenic program in *Drosophila*. *Molecular and Cellular Biology* **28**:1616–1629. DOI: <https://doi.org/10.1128/MCB.01169-07>, PMID: 18160709
- Toydemir RM, Rutherford A, Whitby FG, Jorde LB, Carey JC, Bamshad MJ. 2006. Mutations in embryonic myosin heavy chain (MYH3) cause Freeman-Sheldon syndrome and Sheldon-Hall syndrome. *Nature Genetics* **38**:561–565. DOI: <https://doi.org/10.1038/ng1775>, PMID: 16642020
- Tskhovrebova L, Trinick J. 2003. Titin: properties and family relationships. *Nature Reviews Molecular Cell Biology* **4**:679–689. DOI: <https://doi.org/10.1038/nrm1198>, PMID: 14506471
- Vigoreaux JO. 2006. Molecular Basis of Muscle Structure. In: *Muscle Development in Drosophila*. New York, NY: Springer New York. p. 143–156.
- Wallgren-Pettersson C, Sewry CA, Nowak KJ, Laing NG. 2011. Nemaline myopathies. *Seminars in Pediatric Neurology* **18**:230–238. DOI: <https://doi.org/10.1016/j.spen.2011.10.004>, PMID: 22172418
- Warren GL, Summan M, Gao X, Chapman R, Hulderman T, Simeonova PP. 2007. Mechanisms of skeletal muscle injury and repair revealed by gene expression studies in mouse models. *The Journal of Physiology* **582**:825–841. DOI: <https://doi.org/10.1113/jphysiol.2007.132373>, PMID: 17478534
- Weitkunat M, Brasse M, Bausch AR, Schnorrer F. 2017. Mechanical tension and spontaneous muscle twitching precede the formation of cross-striated muscle *in vivo*. *Development* **144**:1261–1272. DOI: <https://doi.org/10.1242/dev.140723>, PMID: 28174246

- Weitkunat M**, Kaya-Çopur A, Grill SW, Schnorrer F. 2014. Tension and force-resistant attachment are essential for myofibrillogenesis in *Drosophila* flight muscle. *Current Biology* **24**:705–716. DOI: <https://doi.org/10.1016/j.cub.2014.02.032>, PMID: 24631244
- Weitkunat M**, Schnorrer F. 2014. A guide to study *Drosophila* muscle biology. *Methods* **68**:2–14. DOI: <https://doi.org/10.1016/j.ymeth.2014.02.037>, PMID: 24625467
- Wickham H**. 2007. Reshaping data with the reshape package. *Journal of Statistical Software* **21**:1–20.
- Wickham H**. 2009. *ggplot2: Elegant Graphics for Data Analysis*. Springer.
- Wickham H**. 2011. The Split-Apply-Combine strategy for data analysis. *Journal of Statistical Software* **40**:1–29. DOI: <https://doi.org/10.18637/jss.v040.i01>
- Yang J**. 2018. SALL4 as a transcriptional and epigenetic regulator in normal and leukemic hematopoiesis. *Biomarker Research* **6**:1. DOI: <https://doi.org/10.1186/s40364-017-0115-6>, PMID: 29308206
- Zambon AC**, Gaj S, Ho I, Hanspers K, Vranizan K, Evelo CT, Conklin BR, Pico AR, Salomonis N. 2012. GO-Elite: a flexible solution for pathway and ontology over-representation. *Bioinformatics* **28**:2209–2210. DOI: <https://doi.org/10.1093/bioinformatics/bts366>, PMID: 22743224
- Zappia MP**, Frolov MV. 2016. E2F function in muscle growth is necessary and sufficient for viability in *Drosophila*. *Nature Communications* **7**:10509. DOI: <https://doi.org/10.1038/ncomms10509>, PMID: 26823289
- Zhang X**, Yuan X, Zhu W, Qian H, Xu W. 2015. SALL4: an emerging cancer biomarker and target. *Cancer Letters* **357**:55–62. DOI: <https://doi.org/10.1016/j.canlet.2014.11.037>, PMID: 25444934
- Zhao Y**, Li J, Liu H, Xi Y, Xue M, Liu W, Zhuang Z, Lei M. 2015. Dynamic transcriptome profiles of skeletal muscle tissue across 11 developmental stages for both tongcheng and Yorkshire pigs. *BMC Genomics* **16**:377. DOI: <https://doi.org/10.1186/s12864-015-1580-7>, PMID: 25962502
- Zheng Q**, Zhang Y, Chen Y, Yang N, Wang XJ, Zhu D. 2009. Systematic identification of genes involved in divergent skeletal muscle growth rates of broiler and layer chickens. *BMC Genomics* **10**:87. DOI: <https://doi.org/10.1186/1471-2164-10-87>, PMID: 19232135